Structuration and Integration of Magnetic Molecules and Nanoparticles on Surfaces and Devices by Direct-write AFM Lithography

Elena Bellido Vera

Doctoral Thesis

Estudi de doctorat en Química

Supervised by Dr. Daniel Ruiz Molina

Departament de Química
Facultat de Ciències

2011

Memòria presentada per aspirar al Grau de Doctor per Elena Bellido Vera

Vist i plau,

Dr. Daniel Ruiz Molina

Bellaterra, 20 d'Octubre del 2011

Daniel RUIZ MOLINA, Investigador del CSIC en el Centre d'Investigació en Nanociència i Nanotecnologia (CIN2-CSIC)

CERTIFICA

Que **Elena BELLIDO VERA**, Màster en Ciència i Tecnologia Químiques i Llicenciada en Química, va realitzar sota la seva direcció el treball d'investigació portant el títol: **"Structuration and Integration of Magnetic Molecules and Nanoparticles on Surfaces and Devices by Direct-write AFM Lithography"**. Aquest treball s'ha desenvolupat en el marc del programa de doctorat en Química del Departament de Química de la Universitat Autònoma de Barcelona.

I perquè consti, signa el present certificat.

Dr. Daniel Ruiz Molina

Bellaterra, 20 d'Octubre del 2011

Abbreviations

AFM	Atomic Force Microscopy
APTES	3-Aminopropyltriethoxysilane
ATR-FTIR	Attenuated Total Reflectance Fourier Transform Infrared
CNT	Carbon Nanotube
Co-NP	Cobalt Nanoparticle
DMF	Dimethylformamide
EBL	Electron Beam Lithography
EDX	Energy Dispersive X-ray Spectroscopy
ErW_{10}	$[Er(W_5O_{18})_2]^{9-}$
FE-SEM	Field Emission Scanning Electron Microscopy
FET	Field-Effect Transistor
FIB	Focused Ion Beam
HR-TEM	High Resolution -Transmission Electron Microscopy
LFM	Lateral Force Microscopy
LON	Local Oxidation Nanolithography
MHA	16-Mercaptohexadecanoic Acid
Mn_{12}	$[Mn_{12}O_{12}(O_2CR)_{16}(H_2O)_4]$
Mn_{12}ac	$[Mn_{12}O_{12}(O_2CCH_3)_{16}(H_2O)_4]$
Mn_{12}biph	$[Mn_{12}O_{12}(O_2CC_6H_4C_6H_5)_{16}(H_2O)_4]$
Mn_{12}bz	$[Mn_{12}O_{12}(O_2CC_6H_5)_{16}(H_2O)_4]$
MP tip	M-type Pen tip
NCH tip	Non-Contact High-resonance frequency tip
NP	Nanoparticle
o-DCB	*ortho*-Dichlorobenzene
ODT	1-Octadecanethiol
PBS	Phosphate Buffered Saline
POM	Polyoxometalate
SAED	Selected-Area Electron Diffraction
SAM	Self-Assembled Monolayer
SEM	Scanning Electron Microscopy
SMM	Single Molecule Magnet
SP tip	Single Pen tip
SPM	Scanning Probe Microscopy
SQUID	Superconducting Quantum Interference Device
STM	Scanning Tunneling Microscopy
$TbPc_2$	bis(phthalocyaninato) Terbium(III)
TEM	Transmission Electron Microscopy
ToF-SIMS	Time-of-Flight Secondary Ion Mass Spectrometry
UHV	Ultra High Vacuum
XPS	X-ray Photoelectron Microscopy
XRD	X-ray Diffraction
μCP	microContact Printing
2DEG	2-Dimensional Electron Gas

Synopsis

The reduction of magnetic materials to the nanometric scale has opened in the last decades new perspectives in material science. Nanosized materials exhibit unique properties, which can considerably differ from the properties of the corresponding bulk materials, opening a new wide range of phenomenologies and therefore of technological applications. Among them, the demand of higher density in information storage media most likely has constituted the fundamental motivation for the fabrication of smaller and smaller magnetic nanostructures (for a detailed review see ref.[1] and references therein). Two of the most prospective fields in this area over the last years have been magnetic nanoparticles (NPs) and molecular materials. These systems are prepared through a bottom-up approach by chemical methods allowing the tuning of their properties, sizes and morphologies.

Magnetic NPs represent an important class of nanostructured materials with potential use in many applications such as magnetic storage media,[2-4] spin transport devices,[5] medical drug delivery[6-8] Magnetic Resonance Imaging (MRI)[9, 10] or innovative cancer therapies,[11] among others. The magnetic properties of NPs are dominated by finite size and surface effects which gives rise to various special features, such as superparamagnetism or enhancement of the magnetic anisotropy.[12] In this sense, the application of such nanostructured materials in the fields listed above have motivated an intensive research devoted to the development of synthetic and structuring methods specifically aimed to control diverse parameters, such as the average particle size, particle size distribution, composition, crystalline structure, chemical environment, stability and spatial arrangement of the particles.[12-14]

Research on magnetic molecular materials as an alternative and complementary approach to reproduce the magnetic properties of inorganic solids started to raise attention more than 30 years ago.[15, 16] Molecular materials exhibit very homogeneous dimensions with sizes over a few nanometers or even below, an enormous monodispersivity, can be obtained in large quantities in a reproducible way, can be manipulated in a large variety of solvents and matrices and finally, can be obtained at very reasonable low costs. Most of the work reported over this time has been devoted to study the magnetic behavior of single crystals as well as amorphous and polycrystalline samples.[17, 18] This includes innovative research on stable pure organic materials that show magnetic ordering albeit being traditionally diamagnetic,[19-21] switchable magnetic molecules[22] or molecular clusters that exhibit single molecule magnet (SMM) behavior,[23] among others. SMMs is the family of magnetic molecules most widely studied over the last ten years. Since their discovery in the early 1990s, SMMs have been the focus of many investigations, motivated by the fact that these molecular exchange-coupled transition metal clusters show slow relaxation of the magnetization and magnetic hysteresis of purely molecular origin, thanks to the combination of large-spin ground states and high axial magnetic anisotropy.[24, 25] These new materials have been translated into new and pioneer advances such as the possibility to use them as perfect monodispersed model systems to study quantum phenomenologies, such as quantum tunneling of the macroscopic magnetic moment,[26-28] as

solvent magnetic nanosensors[29] or even as molecular switches.[30, 31] For all the above mentioned reasons, magnetic molecular materials have been proposed as potential candidates for several applications such as high-density magnetic storage,[32] classical and quantum computing applications,[33-36] spintronics[37] or magnetic cooling at low temperatures.[38]

In both cases, magnetic molecules and NPs, there has also been a broad development of proper techniques for their structuration on surfaces with control over their positioning, geometry and organization.[39, 40] Such advances can fuel the detailed understanding of their individual and collective properties by having the possibility to study them at the individual (or few of them) level. This would allow for instance the study of a detailed structure dependence of their magnetic properties as well as the magnetic interaction between them at a desired interparticle distance and organization. These studies require the development of strategies to evolve from bulk to their integration into sensors without compromising their properties. For instance, surface effects as well as interaction with the substrate can completely change the characteristic magnetic behavior observed in bulk, either increasing its magnetic anisotropy or completely removing it. To assess the structuration effect on the properties of these magnetic materials, new magnetic characterization tools that fulfill the required sensitivity and nanometric resolution are needed.[39] With this aim, common surface characterization techniques with atomic resolution such as scanning tunneling microscopy (STM) have been applied to detect and study magnetic moments of molecules on different surfaces.[41] The main limitation at the moment for the use of STM comes from the need to use robust enough systems and suitable deposition techniques to work in ultrahigh vacuum conditions (UHV).[42] Other alternative surface magnetic characterization techniques commonly applied for the study of thin films such as X-ray Magnetic Circular Dichroism (XMCD) have successfully been used as well.[32, 43, 44]

Nevertheless, one of the approximations that is attracting more attention and probably more results is that of typical magnetic characterization techniques for bulk crystalline samples such as superconducting quantum interference devices (SQUID) or Hall magnetometer sensors. These systems have been miniaturized to increase their sensitivity down to a single magnetic or NP moment, involving the need for the development of specific deposition and structuration techniques to integrate the magnetic materials into the sensors with the required control on positioning and quantity of material.[45] Another advantage is that integration into sensors is not only useful for the measurement of these systems down to the molecular level but also they represent themselves the first step towards the fabrication of useful devices.[46]

The aim of this Thesis has been to demonstrate the viability of direct-write atomic force microscopy (AFM) lithography as a very useful technique to overcome most of the challenges that implies such integration. For this, different experimental approaches have been explored ranging from the functionalization and nature of the tips, control on the number of units deposited or strategies for the controlled deposition with (sub)micrometric resolution.

Table of Content

Chapter 1

General introduction

In the first part of this introduction we will review the pioneering approaches so far followed for the integration of magnetic molecular materials and NPs into sensors. On the second part we will review recent advances on the state-of-the-art of direct-write AFM lithography, which is the technique of choice of this Thesis for the integration of the nanostructures into sensors, emphasizing all the advantages that it and benefits. Finally, in the last section we will concentrate more in detail on the three families of materials and sensors chosen for the development of this work.

1.1 Advances on integration of magnetic materials into sensors

In this section we will review the different approaches so far reported up to the moment of writing the present manuscript to integrate magnetic NPs and molecular materials into sensors with special attention to SQUID and Hall sensors. Our aim is to provide the reader an overview of the state-of-the-art in integration strategies.

1.1.1 SQUID sensors

SQUIDs have been successfully employed in high sensitive magnetic flux detection.[47] Typically, a SQUID is a ring of superconductor interrupted by one or more Josephson junctions,[47] whose ultimate goal will be measuring the magnetization reversal of an individual magnetic particle or molecule.[45, 48] In this context, it has been demonstrated that the sensitivity for such measurements is enhanced as the SQUID loop dimensions that pick up the signal from the material is shrinking down toward the dimensions of the particle itself and the cross section of the Josephson junction is also reduced.[49-52]

One of the first examples of such miniature SQUID sensors was reported by Ketchen *et col.*[53, 54] In this case, the SQUID loop consisted of two pickup coils ~ 15 μm in diameter (**Figure 1.1**a). The sensitivity of the sensor enabled to investigate the superconducting transition of a single 5 μm tin particle deposited onto one of the pickup coils. Much effort has been dedicated since then towards the further miniaturization of such sensors.[55-57] Wernsdorfer *et col.* fabricated 'miniature' SQUIDs with a loop diameter of ~ 1 μm and demonstrated the ability to detect the magnetization reversal of individual 20–50 nm cobalt clusters with a magnetic moment of about 2200 μ_B (Figure 1.1b).[58] Thanks to the recent progress in nanotechnology, it is possible to fabricate SQUIDs having a loop diameter less than 100 nm with an adequate sensitivity to detect the magnetic response of small spin populations.[59, 60] The device shown in Figure 1.1c represents the first fully nanosized SQUID reported by Lam and Tilbrook.[61] They designed and fabricated a nanoSQUID with a hole size of 200 nm x 200 nm and shunted Nb nanojunctions, with a sensitivity suitable to detect 250 μ_B.

To profit the sensitivity of these micro- and nanoSQUID sensors, a sample should be located within the SQUID loop. In this case, the magnetic flux variation $\Delta\Phi$ detected is proportional to the magnetization change ΔM associated with the reversal of the magnetic moments according to $\Delta\Phi = \alpha\ \Delta M$, where α is the flux coupling factor defined by the geometry of the sensor and sample, and by the location of the sample on the sensor.[62] So, in order to detect the magnetization reversal of an individual magnetic particle or molecule, it is necessary not only to increase the SQUID sensitivity up to single molecule level, but also to place the magnetic sample close to the edges of the loop to maximize the flux coupling factor as well.[63] It has been shown that the best inductive coupling of a nanomagnet to a nanoSQUID is achieved when the magnet is in direct proximity to one of the junctions, especially in the limit of very narrow bridges.[62] Other calculations estimate that atomic spin sensitivity can be achieved for a nanoSQUID with a loop radius of few nanometers coupled to an isolated magnetic dipole at its center.[64]

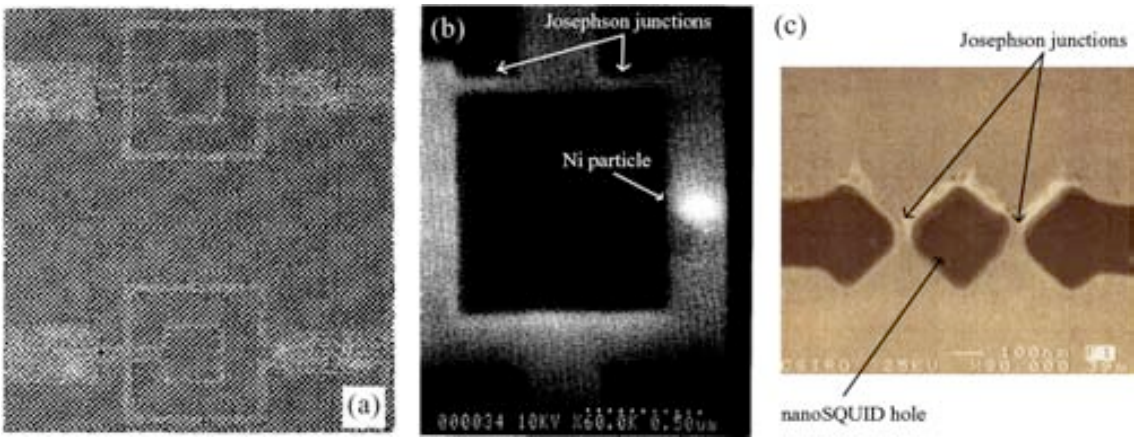

Figure 1.1 (a) Image of a microSQUID fabricated using photolithographic techniques. The image show the two pickup coils (~ 15 μm in diameter) surrounded by larger coils on a quartz substrate. (b) Scanning electron microscopy (SEM) image of microSQUID. The SQUID and the particle were patterned by electron beam lithography (EBL). Ni particle is placed on the SQUID wire. SQUID loop diameter is ~ 1 μm. (c) SEM image of SQUID loop fabricated using EBL and reactive ion etching. Hole size is 200 nm x 200 nm. Panels **a**, **b** and **c** are reproduced from ref.[54], [58] and [61], respectively.

The challenge of integrating a controlled number of particles or molecules into SQUIDs with accuracy and high flux coupling factor has been addressed by diverse strategies. The simplest method initially used consists in a random deposition of particles onto an array of sensors. This deposition was done either by drop casting, placing a drop of a dispersed solution of the target particles on a chip containing some hundreds of sensors,[65] or synthesizing the particles by spray pyrolisis and removing from the gas stream to precipitate them on the chip.[66] After deposition, the particles are physisorbed onto the chip, but only the ones falling in the sensitive zones of the sensors such as the Josephson junction of the SQUID loop, have enough flux coupling with the sensor to be detected. Those sensors are then selected for the magnetic measurements. In all these cases, the position and morphology of the particles was determined by scanning electron microscopy (SEM) only after magnetization measurements were done. Typically, parameters such as particle concentration or evaporation time are adjusted to ensure a dilute (sub)monolayer distribution on the sensors array. This procedure was used by Wernsdorfer *et col.* for the successful integration of individual nanosized nickel wires as well as magnetic NPs of different types and sizes in the range of tens of nanometers onto microSQUID detectors (**Figure 1.2**a).[65, 67, 68] The major drawback of this methodology relies on the implicit poor control on the exact particle position.

To date, diverse strategies have been developed to improve the control on the positioning of the magnetic samples on well-defined sites of SQUIDs. Among them, the use of probes emerges as a very promising approach. In these sense, Ketchen *et col.* have used a quartz fiber (tip ~ 10 μm across) mounted in a micromanipulator to guide a ~ 5 μm spherical tin particle into one of the pickup coils ~ 17.5 μm in diameter of a microSQUID sensor.[53] It is well known that the tip of the scanning probe microscopies (SPMs) can be used not only for imaging but also as a tool for the accurate positioning of single molecules and clusters along smooth surfaces in desired locations with nanoscale precision.[57, 69-73] Pakes *et col.* demonstrated the control on the positioning of a single particle by mechanical pushing of an individual ferritin protein with an AFM tip on a flat Si/SiO_2 surface.[73] In this way, Schleicher *et col.* made use of an AFM tip in

order to manipulate individual NPs (down to 10 nm in size) in a controlled way and relocate them on the SQUID loop (**Figure 1.3**).[66, 72]

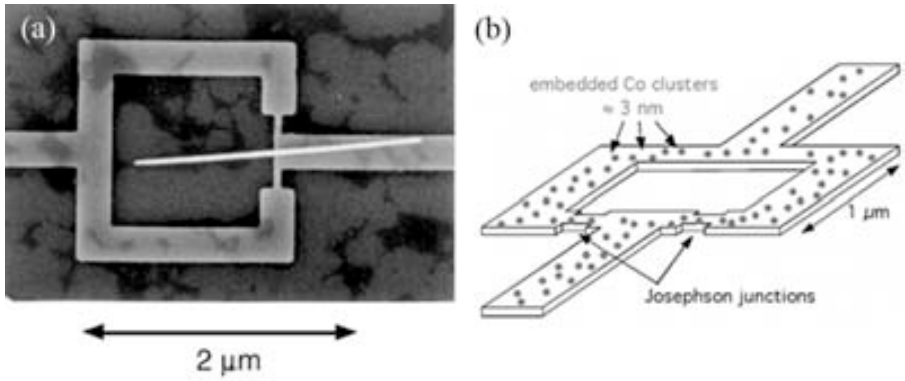

Figure 1.2 (a) SEM image of a Nb nanobridge-dc-SQUIDs fabricated by electron beam lithography (EBL). A Ni wire of ~ 65 nm in diameter was deposited on the microSQUID of 2 x 2 μm^2 by drop casting. (a) Schematic illustration of a nanobridge-dc-SQUID which is patterned out of a 20 nm thick superconducting Nb film containing a low density of 3 nm cobalt clusters (black dots). Panels **a** and **b** reproduced from ref.[67] and [74], respectively.

More recently, Faucher *et col.* exploited the potential of AFM to optimize the flux coupling between a nanoSQUID and a magnetic NP.[75] For this, they locally oxidized a surface using a voltage-biased tip to create a SQUID loop and Josephson junctions accurately positioned with respect to an existing iron dot previously grown by self-assembly process on the surface. Another recent example of the use of probes has been reported by Hao *et col.*[76] They used a SEM together with a sharpened probe (i.e. a carbon fiber) controlled by a micromanipulator to lift and position reversibly a ~ 150 nm FePt nanobead directly onto a nanoSQUID loop in a reversible and accurate way.

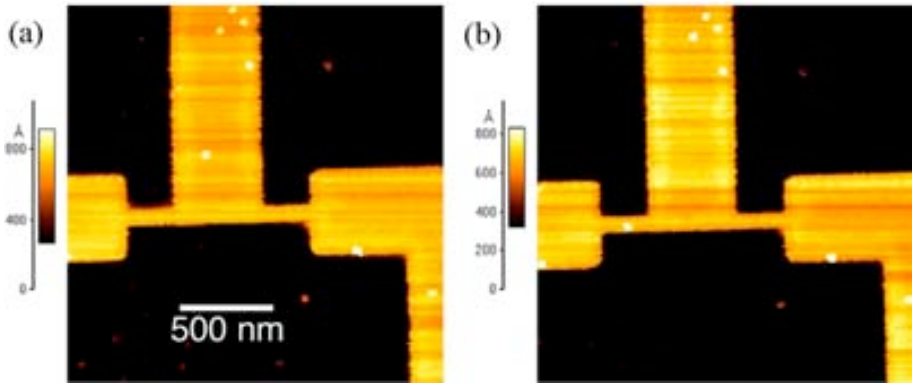

Figure 1.3 AFM images of the manipulation of metallic aerosol particles (Fe_3O_4) on a microSQUID using the AFM tip (a) before and (b) after moving one of the particles onto the junction. The method utilized the non-contact mode both for locating and moving the 15 nm nanoparticles. Reproduced from ref.[45].

Beyond the use of probes, other approaches were investigated. Jamet *et col.* developed a method where the NPs were directly embedded in the Josephson junction to both further improve the flux coupling and avoid NP oxidation.[74] Single 1000 atom cobalt clusters of about 3 nm diameter were directly embedded into the Nb junctions of the microSQUID (Figure 1.2b). In

this way, the coupling factor was highly improved, and they were able to detect the magnetization reversal of individual cobalt clusters.

Finally, we would like to mention a recently reported approach that used the nanosensor developed by Lam and Tilbrook shown in **Figure 1.4**a to perform the first measurement of the magnetization reversal of a single ferritin entity. Vohralik and Lam detected the magnetization reversal of native horse spleen ferritin (natural ferritin) with a magnetic moment of $\mu < 300\ \mu_B$.[77] In this case, in order to optimize the flux coupling, they attached a small number of ferritins directly over the nanojunction with a method combining monolayer self-assembling with electron beam lithography (EBL) (Figure 1.4).[78] First a 200 nm x 200 nm window in the polymethylmethacrylate (PMMA) resist deposited onto the Au overlayer of the Nb nanoSQUID was opened directly over the nanojunction by EBL. Then, in a second step, organic linker molecules were deposited directly over the exposed part of the Au and used to attach the ferritin proteins to the nanoSQUID sensor.

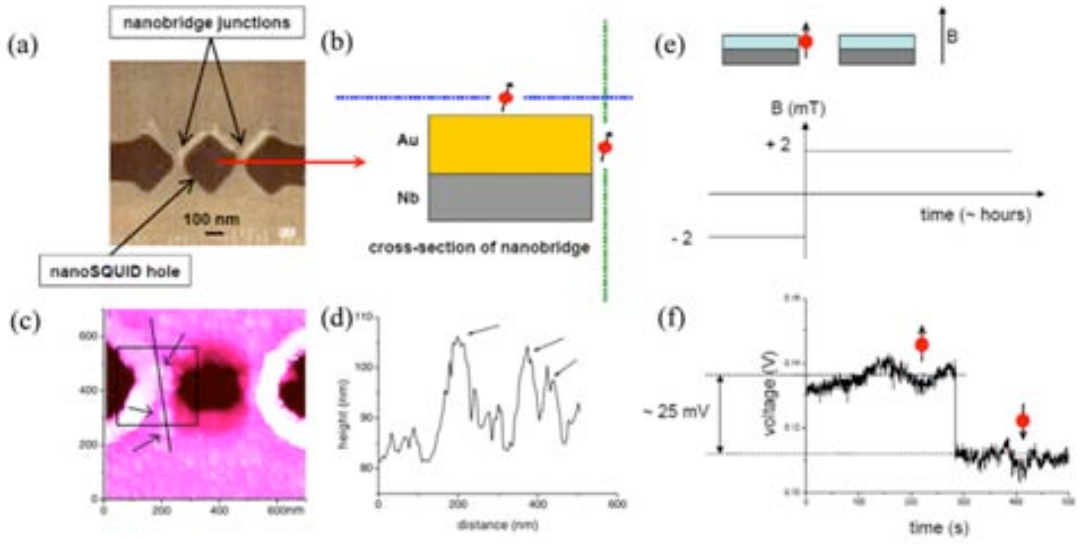

Figure 1.4 (a) SEM image of the nanoSQUID hole with two nanobridged junctions. (b) Idealized schematic cross section of one of the nanobridge junctions, showing a ferritin entity attached on top of the Au overlayer or on the sides. (c) AFM image of the nanoSQUID with a scan area of 700 nm x 700 nm. Arrows indicate the positions of the ferritins and the square shows the approximate location of the PMMA window used for the attachment. (d) Topography data for a line scan across the three ferritin particles indicated by arrows in panel **c**. (e) Schematic showing the main features of the sensor for the measurement, having attached ferritin to the nanoSQUID. The sample was cooled down to 4.2 K in zero field and then the applied field was adjusted to the desired value and the bias current was optimized. Keeping the field constant, the SQUID output voltage was recorded for a number of hours, (f) in addition to slow drifts in the signal and a fairly constant level noise, larger jumps were also observed. These jumps may be the result of reversals of the magnetic moments of attached ferritin entities (as illustrated in the diagram). Panels **a**, **b**, **e** and **f** are reproduced from ref.[77]. Panels **c** and **d** are reproduced from ref.[78].

1.1.2 Carbon nanotube-based SQUIDs and field-effect transistors

A second generation of nanoSQUIDs emerges with molecular Josephson junctions made out of a carbon nanotube (CNT) placed between two superconducting electrodes (**Figure 1.5**a).[55] The first SQUID with molecular Josephson junctions made out of CNT was presented by Cleziou *et*

col.,[79] to be used as a detector for magnetization switching of the magnetic moment of a single molecule. The comparable size of the CNT junction, which has a cross section of about 1 nm^2, with a molecule placed on top of the CNT, is expected to significantly optimize the flux coupling factor (Figure 1.5c). If feasible, this may allow the detection of the magnetization reversal of a single SMM placed on top of the CNT, as theoretically estimated by Bouchiat.[62] Apart from the CNT-based SQUID sensors, CNT-based field-effect transistors (FETs) are also of increasing interest. In these devices, the presence of a molecule grafted on the CNT locally perturbs the electronic states of the semiconductor CNT modifying the transport properties of the hybrid sensor. CNT-FETs are demonstrated to have single molecule sensitivity.[80] Very recently, it has been shown the localized magnetic moment of a SMM laterally coupled to a single-walled CNT also leads to a magnetic field dependence of the electrical transport through the CNT, thus permitting the electrical detection of the magnetization switching of the molecule.[81] However, optimization of such CNT-based spintronic schemes requires the improvement of integration methods of the magnetic entities onto the CNT, being a topic of great interest nowadays.[82]

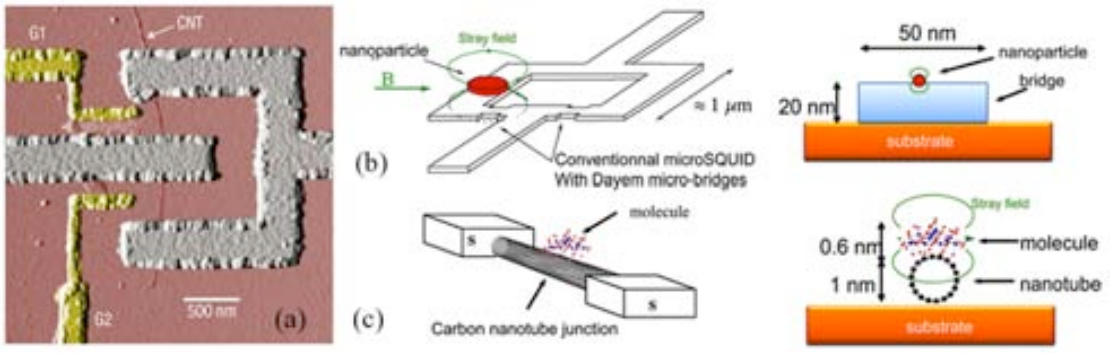

Figure 1.5 (a) AFM topography image of a CNT-SQUID sensor with two lateral gates (G1 and G2). The SQUID loop (grey) is interrupted by the two CNT Josephson junctions with a length of about 200 nm. The single-walled CNT with a diameter of about 1 nm was located using an AFM and Pd/Al (3/50 nm) aligned electrodes were deposited over the tube using EBL. (b,c) Schemes of the flux coupling between a magnetic entity and a nanoSQUID. (b) Left: NP placed on a nanobridge fabricated using nanolithography and thin film deposition. Right: Cross section (50 × 20 nm^2) of a nanobridge junction on which a 3 nm sized particle is placed. The flux coupling is rather poor because of the large mismatch between the particle size and the junction cross section. (c) Left: Molecular magnet grafted on a CNT nanobridge. Right: Cross section of a single-walled CNT junction (1 nm^2) on which a 0.6 nm sized molecule is placed. The flux coupling is optimized because the molecule size and the junction cross section are comparable. Panel **a** is reproduced from ref.[79]. Panels **b** and **c** are reproduced from ref.[62].

To date, several functionalization methods have been developed to decorate the walls of CNTs with diverse entities in solution.[83-85] Still, CNT-based sensors require the sequential addition of a small and controlled number of nanomagnets as well as grafting strategies that minimize the presence of scattering sites, such as the use of non-covalent bonds.[86] To avoid the limitation in the performance of the CNT-based sensors due to defects, Bogani and Wernsdorfer highlighted the fabrication steps needed for obtaining molecular magnets@CNT hybrids that shall be strongly considered when developing strategies for CNT-based sensors.[82] Great efforts have been devoted so far to the non-covalent decoration of the CNTs walls in solution with magnetic materials. For instance, Mallah *et col.* reported the direct assembly of a SMM polyoxometalate

(POM) of formula $[Fe_4(H_2O)_2(FeW_9O_{34})_2]^{10-}$ (Fe_6-POM) on single-wall CNTs though non-covalent grafting while preserving the chemical integrity and SMM behavior of the POM upon the assembly process.[87] Bogani *et col.* used non-covalent π-stacking interactions to graft pyrene-functionalized tetrairon (III) SMM $[Fe_4(L)_2(dpm)_6]$ (Hdpm=dipivaloylmethane) onto the walls of CNTs.[80] This strategy was followed for the functionalization of CNT-based FETs by immersing the sensors into a solution of the SMM, followed by extensive washing. The grafting was reiterated and after each treatment the progressive addition of SMMs was followed by the CNT-based sensor response, demonstrating the single-SMM sensitivity of CNT-based FETs. Even though the π-stacking strategy has been successfully used to graft molecules on the walls of CNTs in solution, the efficacy of this strategy when operating in conditions compatible to the fabrication of electronic sensors remains undisclosed. In particular, the authors reported that after each treatment, a few SMMs were found to stick onto the CNT, while some others were also located on the surrounding surface of the device, showing only limited specificity of the pyrene-substituted SMM for the CNTs. This inconvenient was overcome later on by Bogani *et col.*, who used van der Waals interactions from ligands containing long alkyl chains to self-assemble magnetic NPs of $CoFe_2O_4$ of ~ 6 nm in diameter onto CNTs, and studied the sequential grafting of the NPs on the transport properties of CNT-based FET sensors (**Figure 1.6**).[88] The hybrids were produced by repeating immersions of CNT-based sensors into a dispersion of the NPs. Moreover, the use of hydrophobic tails seemed more suited for a controlled and selective grafting, and allowed an appealing unprecedented sequential grafting of a controlled number of NPs to the CNTs.

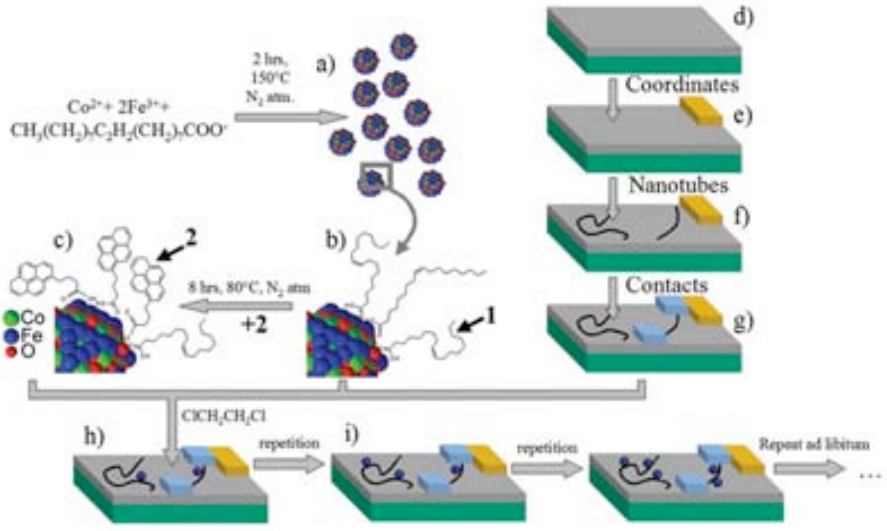

Figure 1.6 Scheme of the assembly of the CNT-based FET sensors with $CoFe_2O_4$ NPs. (a) Synthesis of $CoFe_2O_4$ NPs. (b) The NP surface is functionalized either with oleic acid or (c) with 4-(1-pyrenyl)butanoic acid. (d) Si wafers (green) covered with a SiO_2 layer (gray) (e) are used to fabricate gold electrodes (yellow). (f) CNTs are deposited and located with an AFM (g) Individual CNTs are connected with Pd leads (blue) spaced by 300 nm. (h) Hybrids are assembled by selective grafting of NPs on CNT. (i) Successive depositions allow control over the number of NPs in the hybrid. Reproduced from ref.[88].

In some cases, CNT-based sensors are built with already decorated CNTs. For instance, Rod *et col*. proposed three experimental methods to fabricate nanoscale sensors with a CNT bridging metallic electrodes and decorated with magnetic iron/iron oxide nanocubes ~ 18 nm in size.[89]

The decoration of the CNT walls with nanocubes was performed in solution and then the functionalized CNTs were deposited and aligned into the sensor by (i) nanomanipulation, where sharpened carbon fiber was used to pick-and-place nanocube@CNT hybrid on gold electrodes, (ii) random deposition by drop casting a droplet of a strongly diluted dispersion of nanocube@CNTs onto a specially designed array of gold electrodes and (iii) a technique based on ac-dielectrophoresis to align small single wall CNT bundles with the nanocubes attached to their surface.

Finally, a promising *in situ* deposition technique compatible with UHV characterization techniques uses a spray (or electrospray) to deposit materials on surfaces. This method has already been used for different purposes,[90-92] and Wernsdorfer *et col.* recently proposed to adapt it to deposit molecules directly onto the CNT junction of a CNT-based sensor.[45] In this strategy, the molecular vapor was directed into the dilution refrigerator, and as soon as a molecule landed on one of the two CNT junctions, the conductivity of the latter changed and the sample holder was closed. Then, the magnetization measurements established whether the molecule was magnetic or not.

1.1.3 Hall sensors

MicroHall magnetometry, based on the Hall response of a charge current to a small dipole field from the magnetic entities, has been widely used for the measurement of a large variety of materials including superconductors,[93] ferromagnetic particles,[94] and patterned submicron- or nanomagnets.[95-97] Typically, Hall probes are made of semiconductors (usually InSb for room temperature applications and GaAs/AlGaAs two dimensional electron gas (2DEG) for low temperatures). These materials are chosen for the special combination of low density of charge carriers and high mobility. Marked improvement in magnetic moment resolution was realized by using Hall gradiometry in which an empty Hall cross with opposite current flow is employed to circumvent the difficulty of measuring a tiny signal on top of a much larger background.[94, 98] In this case, the magnetic sample should be placed directly on the sensing area of the sensor, which corresponds to one of the Hall crosses, while the closely spaced reference cross is kept empty. Therefore, the most critical step in such an experiment is the alignment of the magnetic sample with the Hall cross.

The first Hall gradiometry measurement of NPs was performed on arrays of iron particles (~10^2–10^3 particles, 10^5–10^6 μ_B per particle) grown on Hall crosses of a few μm linewidth. For this, Kent *et col.* fabricated arrays of iron deposits with a variety of shapes and sizes down to nanometer scale by using STM assisted chemical vapor deposition.[94] The deposits were fabricated using a STM tip to decompose a metalorganic precursor iron pentacarbonyl $Fe(CO)_5$ by applying a bias voltage directly onto one of the cross sections of the sensor.[99] The tip was then progressively moved to different spots over the cross area to create the array. High precision alignment of the deposits was accomplished by previous imaging by STM the device in order to locate the target cross area and align the tip precisely to the desired position. Wirth *et col.* reported that the sensitivity of the measurements could be significantly improved by

matching the areas of the Hall cross and the array grown onto it (**Figure 1.7**a).[100] Later on, the sensitivity was further increased to the point of measuring the magnetization switching of a single magnetic NP with a magnetic moment of ~ 10^6 μ_B by shrinking the size of Hall probes to submicron range. In those experiments, Li *et col.* were able to fabricate a single magnetic NP directly onto the cross section 600 × 600 nm^2 in size of the sensor with high accuracy by STM assisted chemical vapor deposition (Figure 1.7b,c).[98] Further miniaturization of such sensors gives to nanometer-sized Hall magnetometers, which have been proposed as a promising candidate for single electron spin sensor though requires further control on the deposition of the magnetic entities with nanometric accuracy.[101-104]

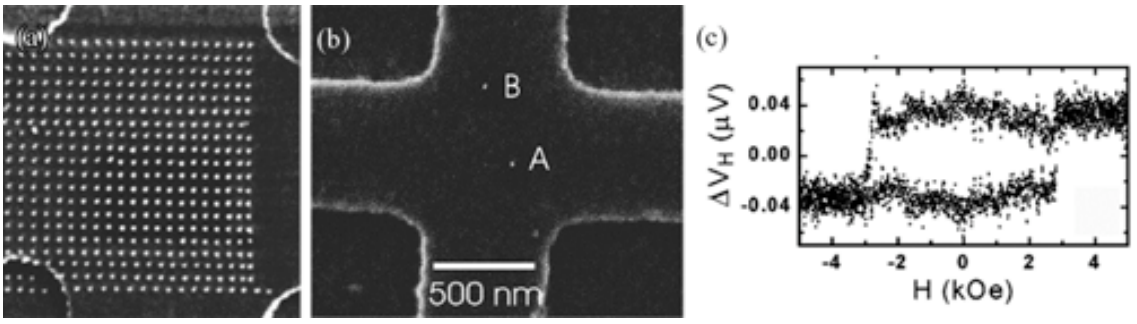

Figure 1.7 Growth of Fe deposits on the sensing areas of microHall gradiometers by combining STM and chemical vapor deposition. (a) SEM image of an array of 420 particles grown onto a Hall cross. The etched Hall cross of about 3.2 × 2.8 μm^2 is clearly visible. The image shows an area of 4.5 × 4.5 μm^2. (b) SEM image of a 600 × 600 nm^2 Hall cross with one particle in the sensing area (indicated in the image as A). Particle B is about 0.35 mm from the center, and has negligible contribution to the Hall signal. (c) Hall gradiometry measurement of a single iron NP (A) shown in panel **b** at 45 K. Panel **a** is reproduced from ref.[100]. Panels **b** and **c** are reproduced from ref.[98].

Finally, we should mention that Hall sensors are especially appealing for applications in biosensing for the detection of magnetically labeled biomolecules (*i.e.* using magnetic beads) due to its exceptional magnetic moment sensitivity over a large dynamic field range.[105-108] A necessary step in realizing biosensing is the integration of chemical and biological (soft) molecules. Typically, the sensing area of the sensor is decorated with linker molecules and in this way, they provide selective biomolecular binding to the specific target. Recently, Xiong *et col.* reported the unique capability of direct-write AFM lithography for the highly specific assembly of biological molecules onto the sensing area (1 × 1 μm^2) of microHall sensors with nanoscale precision and registry (**Figure 1.8**).[109]. They reported an indirect patterning approach where first the AFM tip was used to functionalize the sensing area with organic linkers. Then, the organic molecular template was used in a second step to guide in solution the site-selective attachment of biotin to the pre-functionalized area. Note that in these experiments the rest of Au surface needed to be passivated using a different organic molecule to avoid non-selective adsorption of biotin. Specific binding of complementarily functionalized streptavidin-coated superparamagnetic beads to the Hall crosses occurred via molecular recognition, and magnetic detection of the assembled beads was achieved at room temperature using microHall magnetometry.

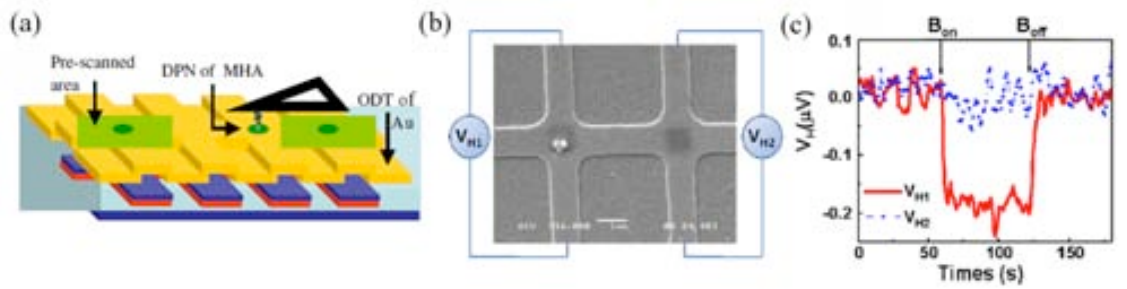

Figure 1.8 (a) Schematic illustration of molecular functionalization of microHall sensors using direct-write AFM lithography. To confine the organic linker molecule deposition exclusively to one of the Hall crosses, the two crosses at the edges were first scanned with an organic molecule coated AFM tip to register the coordinates of the device. Without losing contact with the substrate the tip was brought to the center of the other Hall crosses to generate organic molecular patterns. (b) SEM image of a microHall sensor. The molecular linker molecule was patterned as depicted in panel **a** and then biotinylated as is evidenced as dark squares in the central regions of the Hall crosses; the surrounding surface was passivated. In the left cross we can observe three streptavidin-coated magnetic beads assembled on the biotinylated region of the cross. (b) ac Hall voltage as a function of time for the two Hall crosses shown in panel **b**. Due to the presence of magnetic beads on the left cross, the ac Hall voltage V_{H1} (red) decreased by ~ 0.19 μV when a dc magnetic field B = 70.6 mT was applied. In contrast, no change in Hall voltage V_{H2} (blue) was observed when B was applied to the empty cross. Reproduced from ref.[109].

1.1.4 Graphene-based sensors

Similar to the interest grown on CNTs, graphene has turned up into a promising material to perform different types of improved devices based on its fascinating electrical, optical, thermal and mechanical features.[110-113] In this sense, several initiatives to design devices based on graphene can be found in the literature, though few of them include examples of real measurements on molecular materials. Just as it happens with CNTs, the integration of molecules on graphene surfaces must be done carefully, since the presence of covalent bonds for example could induce scattering sites that seriously perturb the desired electrical properties of graphene. Some of the designed tiny sensors are graphene-based SQUIDs,[114] graphene-based microHall[115] and also graphene-based FETs.[116]

A new type of SQUID formed by a single graphene sheet contacted with electrodes in the geometry of a loop has been suggested with potential high sensitivity to detect single nanomagnets.[114] One of the main advantages is the direct exposure of the sensing -conducting- area to the external world, being directly accessible to be functionalized with the magnetic materials. In this sense, graphene-based sensors as SQUIDs should be devices with high sensitivity and suitable to easily integrate a wide range of magnetic materials. Graphene can also be an excellent alternative to increase the sensitivity of Hall sensors, where an important issue to improve is the distance between the nanomagnet and the 2DEG sensing channel. Indeed, such channel is typically located beneath the capping and insulating layers 20 nm or more below the sensor surface. The atomic dimensions of graphene sense layer that is exposed directly in contact with the magnetic material can be used to overcome such limitations.

One of the open issues in these sensors is the integration of the magnetic material into the graphene-based micro- or nanostructure without modifying the graphene intrinsic structure and properties. Even more, the integration into Hall gradiometers is an experimental challenge since

it requires that the deposition is performed with the necessary resolution in positioning in order to place the material on one Hall cross while keeping the other free of material as a reference. However, the integration strategies described so far typically involves the blanket deposition of the magnetic material on the graphene-based sensor without any specificity to the sensing region of the sensor. This approach was followed by Lopes *et col.* to measure the electron transport properties of graphene-based FETs functionalized with pyrene-substituted bis(phthalocyaninato) Terbium(III) ($TbPc_2$) SMMs.[116] For this, the molecule was deposited *in situ* by drop casting a solution containing different $TbPc_2$ concentrations onto the sensor. One of the phthalocyanine ligands of the $TbPc_2$ molecule was substituted by a pyrene group and alkyl chains since both are well-known to exhibit an attractive interaction with sp^2 carbon materials, maximizing the intermolecular van der Waals interactions. They observed the shift of the minimum of the conductance toward lower gate voltages on increasing SMM concentrations up to a certain point, which suggested an electron transfer from the $TbPc_2$ molecules to the graphene, though no significant disorder seemed to be induced. Still, for higher concentrations, the presence of clusters and crystallites induce defects and diffusion sites on the graphene sheet, degrading progressively the mobility of graphene. More recently, an improved sensor made by a graphene nanoconstriction decorated with pyrene-substituted $TbPc_2$ SMMs has been successfully used to electrically detect the magnetization reversal of this molecule in the proximity of graphene (**Figure 1.9**).[117] In this case, the magnetic molecules were also deposited by drop casting method with an estimated average number of ten molecules deposited on the constriction. After deposition, changes of magnetoconductivity of the graphene sensor together with hysteresis with the magnetic field were observed due to the magnetization reversal of the SMM molecules placed on the graphene nanoconstriction, demonstrating the ability of hybrid spintronic graphene based nanodevices to detect magnetization properties at single molecule level.

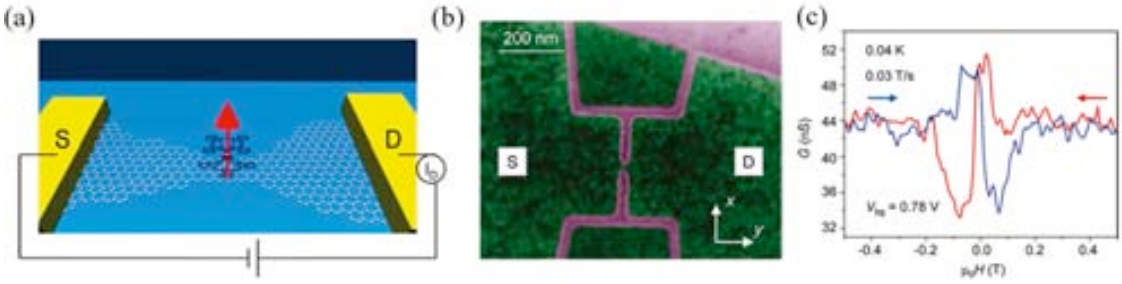

Figure 1.9 (a) Schematic illustration of the sensor showing the pyrene-substituted $TbPc_2$ SMM attached to graphene in the nanoconstriction contacted by source (S) and drain (D) electrodes. (b) False-color SEM image of the device. SiO_2 substrate and etched graphene are colored in purple. Graphene conductive regions are colored in green. Source and drain electrodes are indicated as S and D, respectively. (c) The magnetoconductivity curve G(H) represents the variation of conductivity when applying a magnetic field in the device (graphene plus $TbPc_2$ SMM) obtained at a fixed backgate voltage (V_{bg} is fixed at a conducting resonance). The blue curve represents the magnetoconductivity under increasing field (trace), while for the red curve the field is decreasing (retrace). The observed hysteresis is given by the magnetization reversal of the $TbPc_2$ SMMs deposited on the graphene constrictions. Reproduced from ref.[117].

1.1.5 Overview of the general context

In this section a brief summary of all the examples described in the previous section within the context of the present Thesis, from to its beginning to nowadays, is given.

Significant advances have been made in recent years for the integration of magnetic materials, both molecules and NPs into sensors. Integration techniques must advance together with the continuous miniaturization of devices, requiring a major precision on the deposition and control on both the amount of material deposited and how it is organized on the surface. In addition, the integration procedure must ensure the integrity of the nanomaterial as well as minimize at all the time the impact over the sensor. Only in this way, these advances can fuel the detailed understanding of the individual and collective magnetic behavior of particles and molecules, by having the possibility to study them at the individual (or few of them) level.

From the works above reviewed, two main tendencies for the integration of magnetic materials can be distinguished. The first strategy consisted on the random deposition of the sample onto an array of sensors. The advantages of random integration are mainly the straightforward application of well-known blank deposition techniques such as drop casting. A few examples using this approach for the deposition of NPs and molecules into microSQUIDs as well as graphene-based sensors have been given.[65, 67, 68, 116, 118] Structuration is simple and many sensors can be functionalized in a single experiment. The major drawback of this methodology relies on the implicit poor control for the exact particle position. Tens or even hundreds of experiments must be done before an optimal sensor with one or very few particles placed in the right position is found. While this fact favors the obtaining of statistics over the operational properties, it can also be very expensive and time-consuming.

Random decoration of CNT walls is itself a structuration process less demanding in terms of nanoscale location though more technologically challenging. It requires grafting strategies that permit the sequential addition of a small and controlled number of entities while minimizing the presence of scattering sites. Typically, the hybrids are produced by drop casting a solution containing the nanomaterial on a wafer of CNT-based sensors[81] or by directly immersing the sensor in the solution.[88] In some cases, CNT-based sensors are built with already decorated CNTs.[89] In this alternative methodology, the functionalization of the CNTs is performed in solution and then further efforts are needed to align the hybrid into the device.

By contrast to the random distribution, the second approach based on the site-selective deposition uses structuration and functionalization methods with nanometric control and accuracy over the localization. Site-selective integration arises in specific cases, as for example, when the coupling factor between the particle or molecule and the sensor needs to be optimized. It is also highly required when the deposition must take place at specific sensing areas while keeping other background areas on its original state to be used as reference. Even though diverse structuration techniques have been developed with this aim as described in the previous sections, such a controlled integration remains extremely challenging. One possibility is the procedure reported by Lam *et col.* that combines monolayer self-assembling with EBL for attaching a small number of ferritin entities over the junction of a nanoSQUID.[78] Even if successful, this strategy is an indirect deposition of the target material and hence it involves

several steps and a previous functionalization of the sensor surface with organic linkers. Such functionalization is not only prompted to modify the sensor characteristics but the presence of a linker between the nanomaterial and the sensor surface may also prevent an optimum flux coupling.

Nevertheless, among the different experimental techniques used with this aim, we would like to focus on the great potential of SPM tips as a tool for the direct manipulation and accurate positioning of nanomaterials. A few examples had already been reported before starting the present Thesis in 2007, which inspired us to achieve the objectives described in this manuscript. For instance, AFM tips were applied to improve the control on the integration of particles previously deposited *via* random method by moving them on the SQUID loop in a controlled way and pushing them to the desired spot.[66, 72] The integration of NPs into microHall sensors was accomplished using STM combined with chemical vapor deposition to directly grown nanometric deposits onto well-defined positions of one Hall cross of the sensor.[99, 119] Single structures and well-defined arrays of dots (by progressively moving the tip to different spots over the Hall cross) were accurately positioned on the sensing areas with nanometric resolution using this approach.

The exceptional results obtained following these approaches arise from combining both tip positioning and *in situ* imaging capabilities of SPM techniques in order to manipulate matter at the nanometer scale. In this sense, at the moment of initiating the present Thesis, direct-write AFM lithography emerged as one of the most promising SPM techniques to further exploit these features. This technique uses an AFM tip to directly deliver nanomaterials on a substrate through the meniscus formed at the point-of-contact between the tip and the substrate surface.[120, 121] First experiments using this approach were reported in the 1990s.[120, 122, 123] (A description and state-of-the-art of the technique will be described in detail in the next section). Since then, direct-write AFM lithography has been established as a very attractive tool to pattern a wide variety of materials, such as small organic molecules, polymers, NPs and biomolecules.[124] It is also important to remark that this technique can be virtually used on any type of substrate allowing control of the feature shape, dot size and line width by simply adjusting the tip movement over the surface, tip-substrate contact time and scan speed, respectively. These capabilities together with the tip positioning, ease of use and accessibility of AFM systems are strong potential advantages of this technique towards the integration of magnetic materials into sensors. To the best of our knowledge, at the moment of writing the present manuscript no previous works exploiting this direct deposition capability of direct-write AFM lithography to deliver magnetic molecules or NPs on the sensitive areas of sensors without the need of any previous modification of the sensor surface have been reported.

In fact, along the elaboration of the present Thesis, some excellent works have been published further emphasizing the strong potential envisioned for using SPM techniques as an integration tool. For instance, in 2009 Faucher *et col.* optimized the flux coupling between a nanoSQUID and a magnetic NP by local oxidation using a voltage-biased tip.[75] In the same year, a very notable contribution that demonstrate the unique capabilities of direct-write AFM lithography as integration tool was reported by Xiong *et col.*[109] The authors success on selectively attaching streptavidin-coated superparamagnetic beads on the sensing area of a microHall sensor with

high precision. It should be noticed that even if successful, this integration strategy shows some disadvantages intrinsic to an indirect approach such as the need to passivate the rest of the device surface to avoid non-specific adsorption and therefore kept the second Hall cross of the sensor empty.

1.2 Introduction to direct-write AFM lithography

SPM comprises a family of techniques in which a sharp probe is scanned across a surface while monitoring and compiling tip–sample interactions in order to measure surface topography and properties at nanometric scale.[125] Additionally, probes can be applied not only to characterize sample surfaces but also to develop methods for nanometer scale modification and patterning of surfaces.[126-129] These methods descend from the invention of STM in the early 1980s by IBM researchers Binnig and Rohrer, for which were awarded the Nobel Prize in Physics in 1986.[130] STM technique uses the tunneling current which flows between a biased tip and a sample, which significantly limits the materials that can be studied to only electrical conductive samples. This requirement led to the development in 1986 of the AFM by Binnig, Quate and Gerber.[131] Since its invention, AFM has emerged as a very powerful technique because of its ability to image at (sub)nanometric resolution almost any type of surface, including polymers, ceramics, composites, glass, and biological samples such as DNA and proteins.[132-137] Atomic resolution images of several semiconductor and insulator samples have also been reported.[138, 139] Even more AFM requires neither any special sample preparation nor a vacuum environment, and can be used in either ambient or liquid environment.

1.2.1 Atomic Force Microscopy

The working principle of AFM performance is relatively straightforward and is depicted in **Figure 1.10**a. The main component is the AFM probe which has a very sharp tip (often less than 10 nm in diameter at the apex) located at the end of a microscale cantilever. The tip is scanned over the sample surface while sensing changes in force between tip and surface. Several forces typically erase from the tip-substrate interaction depending on the distance regime, i.e. the tip-surface spacing (Figure 1.10b). The AFM can be operated in a number of modes, depending on its application. In general, the primary modes of AFM can be divided into contact and dynamic modes where the cantilever is vibrating.

In the contact mode the tip is brought into gentle contact with the sample and then scanned across the sample surface. As the tip is traced across the surface, repulsive forces coming from overlapping electron orbitals between tip and sample atoms cause the cantilever to bend to accommodate changes in topography. In addition to the repulsive force, other forces are also present in this contact regime, generally being the capillary force exerted by the thin liquid layer often present on the sample surface in an ambient environment, and the force exerted by the

cantilever itself. The changes on tip deflection during the scanning process are in turn monitored by the displacement of a laser beam from the back of the cantilever into a position-sensitive photodiode detector. The signal is then used through a feedback system to maintain a constant deflection of the tip by adjusting tip–sample separation through the movement of a piezoelectric actuator along the axial position. It is typical to use contact mode to image deflection, friction and/or topography. Alternatively, AFM can also be operated at constant height mode, where the distance of the tip with respect to the surface is fixed as it scans. This operation mode is often used for high resolution imaging of very flat surfaces.

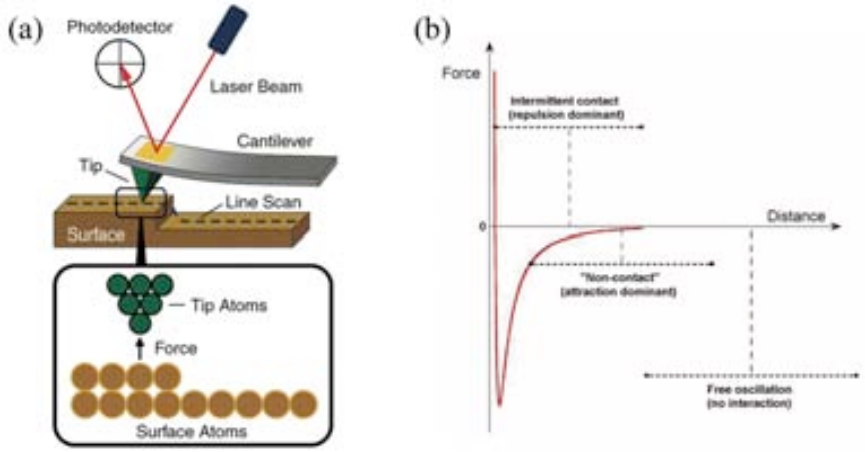

Figure 1.10 (a) Schematic illustration of the basic AFM principle. (b) Zones of interaction as the tip approaches the surface sample. As the tip and the sample are gradually brought together, their atoms begin to weakly attract each other. This attraction increases until the atoms are so close together that their electron clouds begin to repel each other. This electrostatic repulsion progressively weakens the attractive force as the separation continues to decrease. The total force goes through zero and finally becomes positive (repulsive). Reproduced from ref.[140].

In dynamic mode, also known as AC mode, the cantilever is driven to oscillate at or near one of its resonance frequencies.[141] The interaction of the tip with the surface causes changes in resonant frequency, amplitude and phase shift of the oscillating tip. Any of them can be used as a feedback parameter to track the topography of the surface. Dynamic mode operates in either the non-contact regime or the intermittent contact regime. In the non-contact regime, the tip is oscillating in the attractive regime (see Figure 1.10b). The feedback system monitors either the resonant frequency or vibration amplitude of the cantilever and keeps it constant by adjusting tip-sample separation in response to changes. The use of non-contact mode allows scanning without influencing the sample due to the tip contact. Alternatively, in intermittent contact regime, the oscillating tip is brought close to the sample so that it slightly contacts the surface at the bottom of its travel, causing the disruption of the dynamics of the vibrating tip (see Figure 1.10b). Typically, in this regime, the oscillation amplitude is used as feedback parameter to obtain the topography of the sample surface (this mode of operation is also known as Tapping Mode™). Additionally, variations in material properties can be mapped by simultaneously collecting the phase shift between the external excitation (i.e. driving force) and the tip oscillation. Intermittent contact mode eliminates lateral forces that can both damage the sample surface and reduce imaging resolution as well as it inherently prevents the tip from sticking.

To date, many variations of the described primary AFM modes have been developed including lateral force microscopy (LFM),[142] magnetic force microscopy (MFM),[143] electrostatic force microscopy (EFM),[144] Kelvin force microscopy (KFM)[145] and scanning thermal microscopy (SThM).[146] The development of new operating modes in order to collect more and more information from the matter at the (sub)nanometer scale is continuously in progress.

1.2.2 AFM-based lithographic techniques

Beyond its use as imaging tool, the basic operating principle of AFM provides the potential to directly manipulate matter at the nanometer scale thanks to its high resolution and *in situ* imaging capabilities. Therefore AFM-based lithographic techniques have emerged as one of the most powerful tools to create site-specific and localized structures in the field of Nanoscience and Nanotechnology. In the last two decades numerous AFM-based lithographic techniques using different writing mechanisms have emerged for the structuration of a wide variety of materials, such as small organic molecules,[120, 147] polymers,[148] NPs,[149-151] biomolecules[152-155] and inorganic compounds[156] with features sizes ranging from a few to hundred of nanometers (**Figure 1.11**).

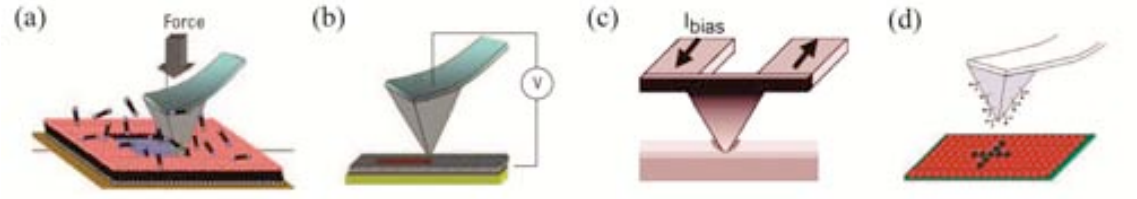

Figure 1.11 Schematic illustrations of representative examples of AFM-based lithographies: (a) nanografting, (b) local oxidation nanolithography, (c) termomechanical writing and (d) catalytic-probe nanolithography. Panels **a**, **b** and **d** reproduced from ref.[157]. Panel **c** reproduced from ref.[158].

Nanografting, scratching and AFM nanoscale manipulation are typical methods used in AFM to fabricate structures through mechanical interaction of the tip with the substrate (Figure 1.11a). In particular, nanografting uses a tip in order to displace nanometer scale selected portions of a thin film, such as a self-assembled monolayer (SAM).[159] As the tip plough through the thin film, molecules are removed and replaced by the reactive molecules in solution. In scratching method, also known as nanoshaving, the tip is also used for applying force but this time to directly displace material from the sample surface (such as surfaces of metals, semiconductors or polymers), creating pits or trenches surrounded by walls consisting of the initial substrate material.[160] Also, the tip can be applied for mechanically cut, push and move materials, such as biomolecules,[73, 161] CNTs[162] and nanocrystals[163] to form a given pattern on a substrate. In this sense, the smallest structure manipulated by a AFM tip is a single atom as reported by Sugimoto *et col.*, who created artificial atomic patterns by laterally rearranging the atoms with the tip.[164]
Alternatively, in local oxidation nanolithography (LON), also known as local anodic oxidation, scanning probe oxidation or nano-oxidation,[126] a suitable bias voltage is applied to a conductive tip, what makes the water meniscus formed in the tip-substrate gap to be dissociated and the

oxidative ions to react with the substrate leaving localized oxide nanostructures with a resolution of only few nanometers. This technique has been used for the direct fabrication of patterns and templates as well as for the local modification of the terminal groups of SAMs, among others (Figure 1.11b).[126, 129] A completely different approach is the termomechanical writing that combines the heat and mechanical force of a resistively heated probe to soften a polymer in the point-of-contact between the tip and the surface, thus facilitating the writing of data bits in a storage medium (Figure 1.11c).[158] One last example is the catalytic-probe nanolithography, where the scanning tip is modified with catalytic agents that react with terminal functional groups of a given SAM (Figure 1.11d).[165] As the tip touches localized areas of the surface, the molecular coating of the tip induces a catalytic reaction to write nanopatterns by chemically changing the terminal groups of the SAM.

Even though these techniques present high resolution and excellent capabilities for the fabrication of patterns onto well-defined locations of a surface, they show some disadvantages that limits their use for the integration of magnetic particles and molecules into sensor. As already mentioned, the AFM tip can effectively be used to move and relocate magnetic particles previously deposited *via* a random method to a specific spot on a SQUID loop (see section 1.1). However, the rest of techniques will require the use of indirect deposition approaches for the deposition of magnetic nanomaterials into the sensing areas of a sensor. That is, these techniques can be used to create templates onto well-defined positions on a surface for guiding the site-selective deposition of the magnetic material. Even if successful, the fabrication of templates using these techniques rely on the elimination or modification of surface components through the delivery of energy (e.g. force, current or heat) or chemical reactions which limits the type of sensor surface on which can be applied and can modify somehow the sensor characteristics. In addition, it limits also the type and number of different magnetic materials that can be deposited. In this context, direct-write AFM lithography emerges as a very attractive integration tool which deals with the above mentioned limitations by using the tip as a carrier and nanoscale delivery system for the direct and constructive patterning of functional materials onto well-defined positions. In the next section, we will introduce the main principles of this AFM-based lithographic technique.

1.2.3 Direct-write AFM lithography

The most natural idea about writing is the application of ink to paper. Direct-write AFM lithography resembles this process in which the AFM tip is used as “pen”, a solid-state substrate as “paper” and a solution containing the material as “ink”. In reviewing this strategy, the first example for transferring molecules from a tip to a substrate was reported in 1995 by Jaschke and Butt.[122] This was demonstrated by depositing aggregates of ODT in irregular-shaped structures with homogeneous heights of 1.2 nm onto freshly cleaved mica. Two years later, Piner and Mirkin reported how water was transported to and from polymer and mica substrates by the capillary formed between the AFM tip and sample.[123] The authors concluded that this transport occurred via the meniscus formed at the point-of-contact between tip and sample.

Although the goal of this work was to characterize the effects of water on LFM measurements, the authors recognized that, controlling the water transport process, this effect could be used for lithography and set the stage for the subsequent development of the direct-write AFM lithography technique.

The experimental procedure of direct-write AFM lithography is relatively simple and the fundamental scheme is diagrammed in **Figure 1.12**. In this writing method, the molecules or nanostructures that act as inks are coated on the tip and transported to the surface by engaging and traversing the tip over the surface in the form of the desired pattern. In most of the cases, the transport of the ink material from the tip to the substrate is mediated by a water meniscus which is formed through capillary condensation, as shown in Figure 1.12. It is generally accepted that ink transport process occurs in the presence of water between the tip and substrate even under dry conditions (0 % relative humidity) due to residual water that moves to the point-of-contact between tip and sample.[166, 167]

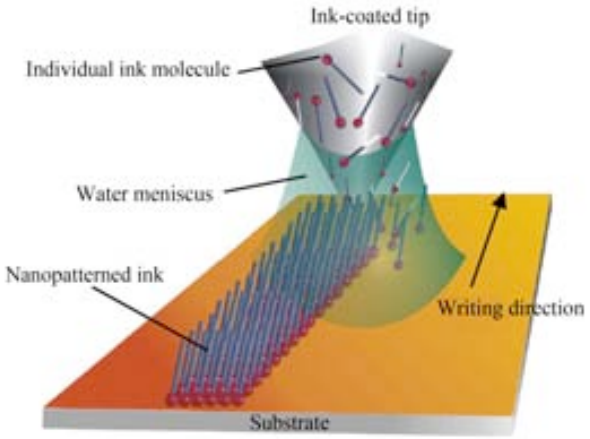

Figure 1.12 Schematic illustration of the writing mechanism of direct-write AFM lithography. A molecule-coated AFM tip deposits ink via a water meniscus onto a substrate. Reproduced from ref.[168].

In 1999, Mirkin *et col.* reported a pioneering work that demonstrated the enormous potential of direct-write AFM lithography by using alkanethiol molecules as ink.[120] These molecules were delivered onto a Au surface and arranged into well-defined SAMs with high resolution (down to 12 nm).[169] Importantly, the same authors also demonstrated the capability of the method to fabricate multi-component nanostructures made of monolayers of different alkanethiols down to a 5 nm separation.[169, 170] These results led to the invention of a commercialized process called dip pen nanolithography® (abbreviated as DPN®), because of the analogy with the traditional dip pen writing method, becoming a registered trademark of NanoInk, Inc. (Chicago, IL). It applies to the process that is employed in NanoInk's products to create nanoscale patterns using a tip as a delivery system. However, the process itself of direct write molecules or nanostructures from a tip to a surface is not necessarily limited to products commercialized by NanoInk. This can be performed using a conventional AFM instrument and tips, as did in the first publications regarding this technique and widely demonstrated in several articles since then.[156, 169, 171, 172] For this reason, along this manuscript the most general term of direct-write AFM lithography is being used to define the general process of depositing molecules or nanostructures assisted by an AFM tip, being indicated in those cases where we have specifically used the instrumentation and tips from NanoInk.

Apart from this, notable efforts for the development and parallelization of the method have been made by NanoInk promoting important advances in this field of micro- and nanofabrication. Among the multifold contributions of NanoInk, the development and commercialization of dedicated instruments and specially designed tips, making it available to quite many research communities, have paved the way towards the development and standardization of this highly controllable writing technique. During the subsequent years after the invention of the term DPN®, the direct-write technique became increasingly popular[121, 124, 173] with a wide variety of materials being successfully structured, including small organic molecules,[140, 168, 169, 174-176] polymers,[177-180] NPs,[149, 172, 181] metal ions[182, 183] and sols[156, 184] (**Figure 1.13** a-d). Even more, this writing technique has emerged as a particularly attractive tool for the deposition of biomolecules onto surfaces while preserving their biological activity. For example, functional proteins,[185, 186] peptides[187-189], phospholipids[190] and DNA[191, 192] biomolecules have been positioned on surfaces in the context of large arrays made of structures that have been miniaturized down to 50 nm in diameter (Figure 1.13 e-f). The range of patterning substrates has also been expanded to include many insulating, semiconducting and metallic substrates as well as other functional monolayers adsorbed on a variety of surfaces.[124, 186, 193-195]

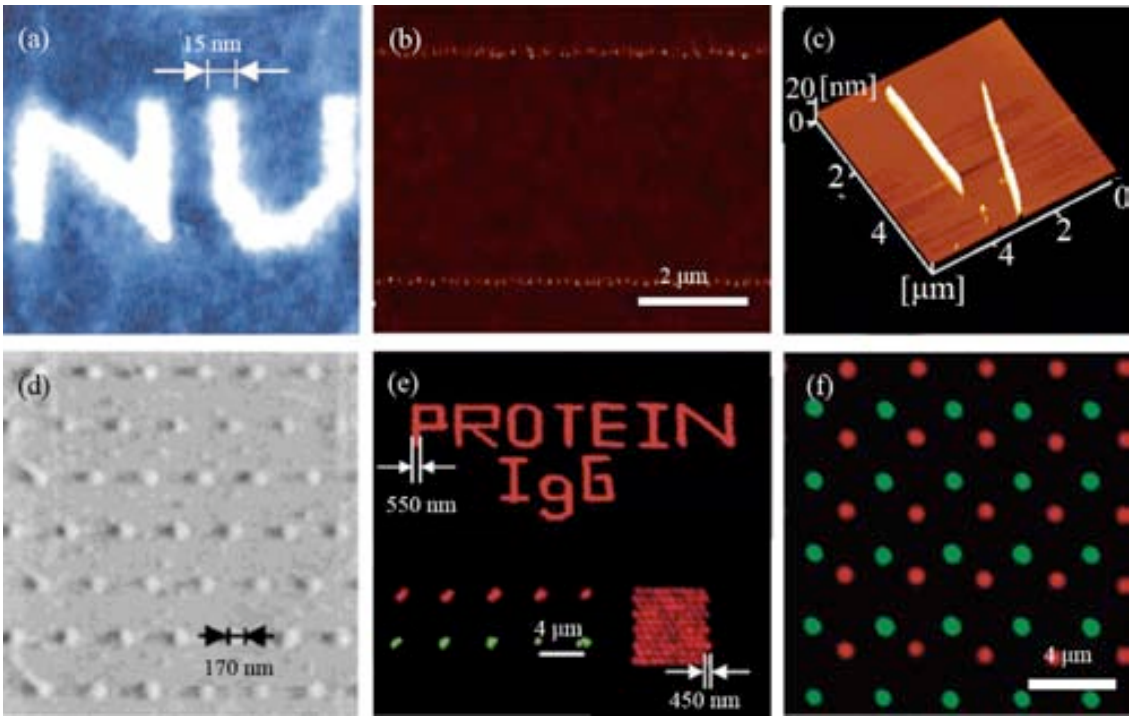

Figure 1.13 Examples of ink-substrate systems successfully deposited by DPN®: (a) LFM image of nanoscale letters written on an Au surface with 16-mercaptohexadecanoic acid (MHA) molecules, (b) AFM topography image of 5 nm Au NPs deposited as line-shaped features on SiO_2 surface, (c) 3-D AFM topography image of a semiconducting CdS pattern generated on mica by carefully controlling the reaction speed between the precursors contained in the ink (consisted of $(NH_4)_2S$ and CH_3CSNH_2), (d) LFM image of a dot array of Al_2O_3 deposited on SiO_2 by using as ink an inorganic solution precursor (sol) made of the inorganic salt ($AlCl_3$) and an amphiphilic block copolymer surfactant, (e) fluorescence images of fluorescently labeled immunoglobulin G (IgG) structures on a negatively charged SiO_2 surface and (f) combined red-green epifuorescence image of two different fluorophore-labeled DNA sequences simultaneously hybridized to a two-sequence array deposited on an SiO_2 substrate. Panels **a**, **b**, **c**, **d**, **e** and **f** reproduced from ref.[169], [181], [182], [156], [186] and [191], respectively.

In direct-write AFM lithography the structuration of materials is accomplished following two main strategies depicted in **Figure 1.14**: (i) the indirect deposition approach, where the tip is used for delivering molecules on surfaces (typically SAMs made of alkanethiols) that are used as a templates later on to guide the site-selective deposition of the material of interest in solution, and (ii) the direct deposition approach, where the tip is used for the direct deposition of the target material at specific positions of a substrate on a single-step simplifying enormously the structuration process itself. This second methodology is the one used in the present Thesis, since it eliminates the need for a previous functionalization of the substrate surface. This is an important advantage in view of its use for the integration of samples into sensors, as will be shown in the next chapters.

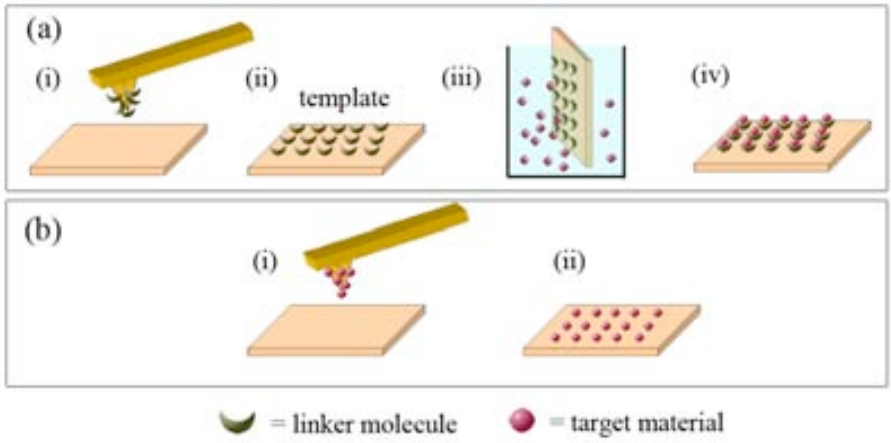

Figure 1.14 Schematic illustrations of the different strategies of patterning followed by direct write AFM lithography: (a) indirect deposition approach and (b) direct deposition approach.

The most widely studied ink-substrate system is 16-mercaptohexadecanoic acid (MHA) and 1-octadecanethiol (ODT) on Au. To date, the smallest structures made with this lithographic technique are MHA lines on Au with 14 nm line widths and dot-like features of 15 nm in diameter.[168, 169] Interestingly, the alkanethiol pattern has been used not only as template for the assembly of materials (indirect patterning approach), such as NPs[196] or biomolecules,[197] but also as a resist for creating 3-D multilayered solid-state structures by standard wet-etching techniques.[198] The structures are fabricated by patterning the etch resist of MHA on a Au/Ti/Sio_{ux}/Si substrate and then the exposed Au is removed by wet chemical etching treatment, giving rise to Au dot structures with sizes down to 25 nm. In addition, the tip can be used not only as a delivery system for the deposition of functional materials but also for inducing localized chemical reactions, such as Diels-Alder reactions.[199] Even more, by using the water meniscus as nanoscale electrochemical cell, it has been possible to directly fabricate metal and semiconductor nanostructures through an AFM tip coated with metals salts which are dissolved in the meniscus and reduced to metals onto a Si surface by means of a derived technique called electrochemical-DPN®.[171]

Whereas these examples prove the significant progress so far achieved in the structuration of a wide variety of functional materials by means of direct-write AFM lithography, fundamental

understanding of the detailed writing mechanism is still, at least partially, under debate.[128, 129, 166, 200] The precise mechanism of ink transportation is complicated and differs from one system to another. Over the past few years, several groups have reported a number of factors that have an influence on the deposition processes, including the composition of both the ink and the surface, the probe geometry, nature of the contact, the distribution and mobility of the ink on the tip, the water solubility of the ink, and the ambient environment (i.e. temperature and relative humidity) at which the experiment is carried out. These conclusions are mostly based on studies of ODT or MHA on Au. The writing mechanism of these small organic molecules through the water meniscus has been described, however the mechanism for more complex systems, such as is the case of NPs or the deposition of liquids, is still undisclosed.

In general terms, the process for small organic molecules, such as alkanethiols, can be split into three main steps.[121] The first step consists in the formation of a meniscus at the point-of-contact between the tip and the substrate, which will serve as bridge for the material transport. Theoretical simulations demonstrated that the size of the meniscus is strongly influenced by the relative humidity, the distance tip-substrate and the tip contact diameter (which varies with the geometry of the tip).[201, 202] The second step is the molecular transport of the ink from the tip to the substrate, which will determine the transport rate of the process. Three main parameters play an important role during this stage. First parameter is the solubility of the ink molecule in water, depending on whether the molecule is hydrophilic or hydrophobic, the tip-to-substrate molecular flow can be facilitated or resisted by the presence of the water meniscus. The second parameter is the temperature, which enhance the ink solubility into the water meniscus even in the case of hydrophobic molecules. And the last parameter is the wettability of the substrate since can increase the contact area of the meniscus through which the ink transport can occur and then enhance the ink transport rate.[166, 203] Additionally, the ink transport rate can also be influenced by other parameters even if the environmental conditions are maintained. It has been found that there is a dependence with the depletion of the ink after a given number of depositions with the same tip[200] as well as it has been observed that the time of contact of the tip with the surface and the scan speeds influence on the dimension of the structures when writing dot- and line-like features, respectively (**Figure 1.15**).[120, 204] The final step of the writing process is the diffusion of the ink molecules over the surface, which is strongly influenced by molecule-substrate bind strength.[205, 206] Thiol molecules on Au are a good example of a large number of strong binding sites. In this case, the first molecules delivered through the tip strongly bind with the surface and cannot rearrange. Then, the new molecules coming from the tip will diffuse over the first already immobilized layer and bind at the rim of the dot-like feature, giving rise to the radial growth of a circular monolayer. In contrast, when the binding is weaker, the diffusivity of the molecules is higher and the deposited molecules can easily move between the binding sites of the substrate, which can cause a loss in pattern fidelity.

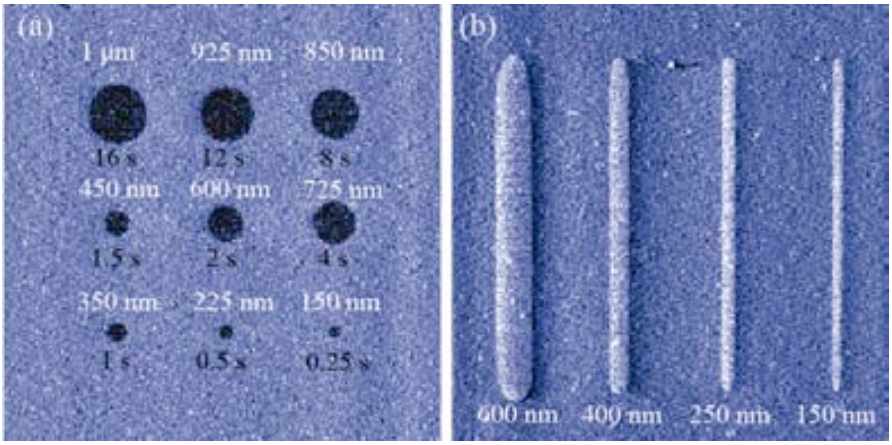

Figure 1.15. (a) LFM image of a Au surface after a tip, which was coated with alkanethiol molecules, had been brought into contact with the substrate for a set period of time, from 16 to 0.25 s (indicated in black letters). The diameter of the generated dot-like features clearly increase with tip contact time and is indicated in white letters above each nanostructure. (b) Similarly, feature size dependence is also observed by LFM for line-like features generated by scanning the coated tip and increasing the scan speed. Reproduced from ref.[120] and [204].

To conclude this section, it is also worth mentioning one essential aspect of any direct-write AFM lithography experiment, which is the process of bringing the ink onto the tip surface. This is usually achieved by either thermally evaporating the ink onto the tip or dip coating the tip into an ink solution. Although thermal evaporation results into highly homogeneous tip coatings for MHA and ODT inks, the great majority of inks do not seem suited to evaporation. An alternative is to directly dip coating the entire cantilever into an ink solution for a given time or drop casting the ink solution directly onto the cantilever and then allow the solvent to dry (e.g., under inert gas flow or heat treatment). The coating process has been used for the deposition of several inks, such as alkanethiols,[120] NPs[181] and biomolecules.[191, 207] In this case, in order to ensure a homogeneous coating of the tip, both the ability of the ink to wet the tip surface and how the ink solutes concentrate on the tip as it is dried are crucial aspects. Therefore is essential to ensure an optimal ink-tip affinity, which can be reached *via* pre-functionalization of the tip surface. For example, improved control over the DNA patterning was achieved through the modification of a silicon nitride probe with 3'-aminopropyltrimethoxysilane which promoted a reliable adhesion of the DNA ink to the tip surface.[191] The positively charged hydrophilic tip surface was readily wetted by the DNA ink solution, and the tip was used for several hours before it was needed to recoat the tip. A completely different tip coating approach, which is the one used in the present Thesis, is to dip coating the tip into an ink solution for a given time and immediately use it.[92] In this case, the transference of the ink on the substrate takes place through the delivery of less than a femtoliter droplet of the ink solution from the tip to the substrate surface. In order to ensure an efficient transfer from the tip to the surface, the ink should be maintained in its liquid state over the whole writing process. In this sense, the evaporation of the ink solution can be slowed down by using high boiling additives in the ink composition and controlling the environmental conditions (i.e. relative humidity and temperature). Herein, whereas a meniscus does exist at the point-of-contact between the tip and the substrate, it is composed of the actual ink liquid being deposited and not the water meniscus. In this sense, it is crucial to consider the affinity of the ink solution with the substrate surface (similarly as it

happens with the interaction of the water meniscus with the substrate mentioned above). As a general rule, the surface affinity of the ink is desired to be neither too weak nor too strong. In the case that the surface affinity is too weak the deposition will not occur, and when this is too strong the liquid will suddenly transfer from the tip to the surface and spread along in an uncontrolled manner.

1.3 Direct-write AFM lithography for the integration of magnetic molecules and nanoparticles into sensors

The work developed in this Thesis has been focused on demonstrating the viability of direct-write AFM lithography to directly integrate magnetic materials into the most sensitive areas of sensors without the need to previous functionalize neither the substrate nor the molecules or NPs. For this, and as a proof-of-concept, we have been working with three different families of materials, intended to be as much representative as possible: magnetic NPs, molecular magnetic materials and an intermediate situation such is the case of ferritins (**Figure 1.16**).

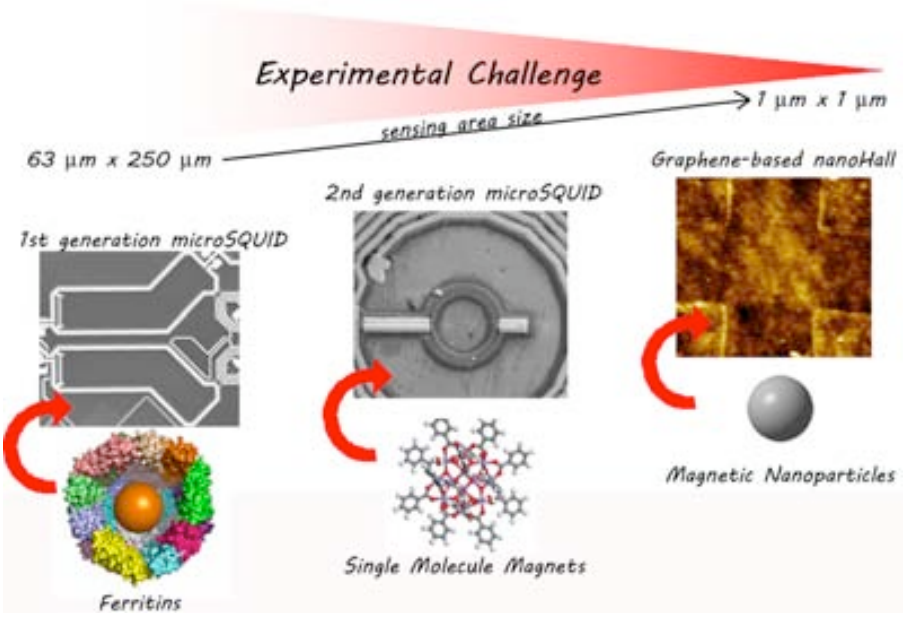

Figure 1.16 Schematic overview of the different families of magnetic materials and sensors considered in the present Thesis. The miniaturization of the sensing areas of the sensors down to 1 µm × 1 µm is indicated. (Images not drawn at scale).

Ferritin is the iron-storage protein of animals, plants and bacteria composed of a cage-shaped proteic shell about 12 nm in diameter that accommodates a NP inside of few nanometers in size. The advantage, as will be detailed later on, is that once the conditions for the structuration of the organic capsule (named apoferritin) are established, these can be used to any inorganic material that can be hold inside. Molecular materials is the second family of systems studied. In particular, we focused our attention to the most thoroughly studied family of SMMs, which is

that comprising a dodecamanganese core, the well known $[Mn_{12}O_{12}(O_2CR)_{16}(H_2O)_4]$ family (referred to from now on as Mn_{12}). Nevertheless, examples for the control on the structuration of these molecular systems on surfaces are given also for a POM of formula $[Er(W_5O_{18})_2]^{9-}$ (hereafter referred to as ErW_{10}). The last family of materials is that of magnetic NPs. In this sense, we have been working with cobalt NPs (Co-NPs) ~ 8 nm in diameter stabilized with a surfactant capping layer.

On the integration process we have also considered different families of sensors displaying sensing areas with different sizes, shapes and conformations, from hundred microns to less than one micron, SQUIDs and Halls sensors as well as with different requisites (Figure 1.16). First experiments were devoted to the integration of a ferritin derivative into a microSQUID with rectangular-shaped pickup coils of 63 μm × 250 μm in size made of SiO_2 and Nb, which corresponds to the sensing area of the sensor (Chapter 3). Afterwards, the structuration of Mn_{12} over a second generation of microSQUIDs has been attempted (Chapter 4). The sensing area of this sensor was reduced one order of magnitude in comparison with the first generation used for ferritin. In this case, the magnetic material must be positioned on a circular-shaped pickup coil of 30 μm in diameter. This represents a challenge to us on the continuous miniaturization of sensors. And finally, in the last case, we attempted the integration of Co-NPs into a graphene-based nanoHall sensor (Chapter 5). This represents the last step in the evolution of our methodology due to the highly-demanding requisite of this sensor. First, the dimensions of the sensing area have been reduced two orders of magnitude, with an effective Hall cross area of 1 μm × 1 μm. Moreover, due to the gradiometric configuration of the Hall sensor, the deposition must be strictly limited to this region, with a second cross that must be kept free of material and is separated only by a few micrometers. And last, but not at least, graphene requires a mild deposition that does not disturb their interesting electrical properties. Such high requirements forced us to a completely different integration methodology. In this way, three representative situations and their evolution on the demanding conditions in each case are reported.

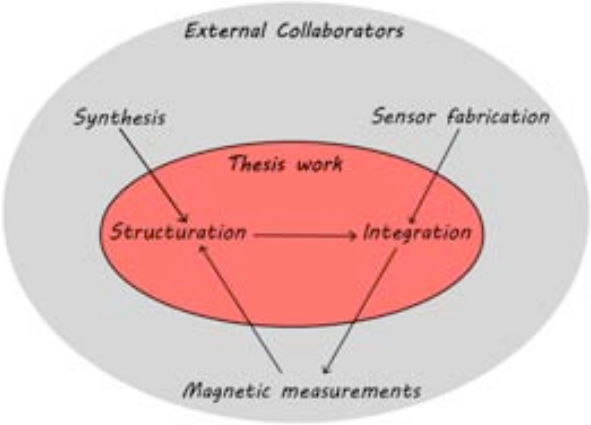

Figure 1.17 Schematic description of the methodology followed in the present Thesis work.

Finally it must be emphasized that the methodology followed in all the cases is the same. Initially, the experimental conditions for a proper structuration of the material are established,

preferably on a surface of the same nature than the one used for the sensors to ensure the feasibility of the posterior integration. In this second step challenges are focused mostly on the strong control needed for the deposition with (sub)micrometric control. It must be emphasized that due to the high pluridisciplinarity of the final objective pursued, this work has been in close contact with several collaborators, recognized experts in each one of their fields (**Figure 1.17**). For instance, the magnetic materials and the sensors have been provided to us by colleagues at Instituto Universitario de Nanociencia de Aragón (INA), Instituto de Ciencia de Materiales de Aragón (ICMA), Centre d'Investigació en Nanociència i Nanotecnologia (CIN2), Instituto de Ciencia Molecular (ICMol) and CNR-Institute of NanoSciences S3 (as stated in each one of the chapters). Afterwards, upon integration, the resulting hybrid materials are measured by our colleagues at ICMA and CNR-Institute of NanoSciences S3. The interpretation of the final magnetic measurements is used in a feedback process to add new insights into the structuration shapes, morphologies and dimensions that ensure a maximization of the sensitivity of the sensor.

Chapter 2

Objectives

The general objective of the present Thesis is to demonstrate the viability of direct-write AFM lithography as a feasible technique for the integration of magnetic NPs and molecular materials into the sensing areas of sensors. To achieve this, the following specific objectives have been planned:

Case 1: Ferritin

- Establish the experimental conditions for the structuration of natural ferritin on surfaces.
- Use of the same experimental conditions for the structuration of ferritin entities displaying different inorganic cores to demonstrate the use of the proteic shell (apoferritin) as a general carrier for the deposition of any inorganic NP that can be held inside.
- Establish the methodology for the integration of a ferritin displaying a CoO core (CoO@apoferritin) on the most sensitive areas of a microSQUID with a rectangular-shaped pickup coil of 63 μm × 250 μm in size.

Case 2: Molecular magnetic materials

- Establish the experimental conditions for the structuration of two different SMMs, Mn_{12} and the ErW_{10} POM.
- Establish the methodology for the deposition of molecular materials on the sensitive areas of a second generation of microSQUID which corresponds to a circular-shaped pickup coil of 30 μm in diameter. As a representative example, the family of Mn_{12} is selected.

Case 3: Magnetic NPs

- Establish the experimental conditions for the structuration of magnetic NPs on surfaces and especially on graphene without damaging it. As a representative example we structure Co-NPs showing a diameter of ~ 8 nm.
- Establish the methodology for the integration of Co-NPs into a graphene-based nanoHall sensor with a Hall cross sensing area of 1 μm × 1 μm.

Chapter 3

Ferritin structuration and integration into first generation of microSQUIDs

In this chapter we demonstrate the uniqueness of ferritin to act as a carrier for the deposition of NPs by direct-write AFM lithography. Initially a brief revision of the different strategies so far followed for the deposition of ferritins on surfaces is given. Afterwards, the experimental conditions and methodology for a controlled deposition by direct-write AFM lithography are given. Control over the deposition on different surfaces in the form of arrays and miniaturized structures that can go down to 100 nm with the presence of only one ferritin per dot can be achieved. The presence of the proteic shell allows the deposition of any inorganic NP held inside by using universal conditions and afterwards the proteic part can be removed upon thermal treatment.

Finally the conditions previously described are used for the controlled deposition of ferritin on the most sensitive areas of a microSQUID sensor. In any of the cases, a previous functionalization of neither the substrate nor the ferritin is required.

3.1 Introduction: Advances on structuring ferritin on surfaces

NPs are attracting researcher's interest as the key material of nanotechnology. NP are already used or expected to be used in many fields, such as magnetic recording materials, catalytic materials, fluorescent markers, drug delivery systems, among others. For this, it is required a high control on the NP size, composition and stability, among others. In this context, the use of biomimetic templates provides a new avenue for the controlled synthesis and assembly of NPs. Special attention has been paid to the use of protein cage supramolecular structures, such as ferritin and viral capsids.[208] Their specific size and highly reproducible biosynthesis make them ideal templates for accommodating a variety of inorganic NPs with controlled size, shape and crystal structure in their inner cavities, a process commonly known as biomineralization.[209-211] For example, tobacco mosaic virus (TMV) hollow cylinders have been used as biotemplates for the controlled formation and organization of Pt, Au, Ag, FePt, CoPt and $FePt_3$ NPs.[212-214] Among the great variety of cage-shaped protein molecules, the most extensively studied and used as a template is ferritin[210, 215] though other ferritin-like protein such as that of the bacteria *Listeria innocua* are also ideally suited for the synthesis of NPs, like γ-Fe_2O_3 and Co_3O_4 NPs.[216, 217]

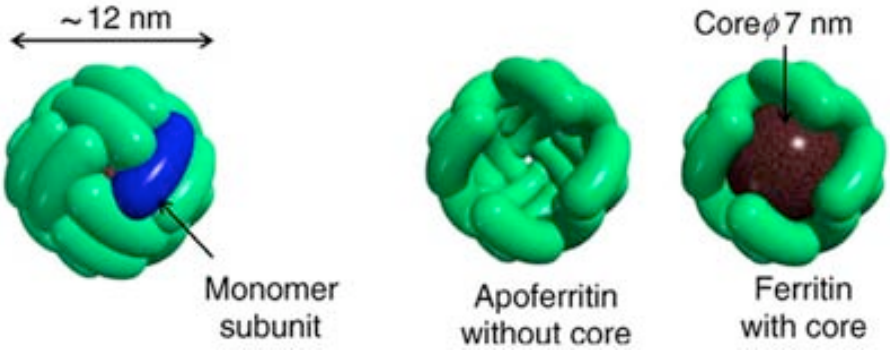

Figure 3.1 Schematic illustration of the structure of ferritin molecule. Reproduced from ref.[215].

Ferritin is a roughly spherical protein consisting of 24 polypeptide subunits that self-assemble into a cage-like architecture with a diameter of ~ 12 nm and an internal cavity of ~ 7 nm (**Figure 3.1**).[218] Ferritin stores iron that is not required for immediate metabolic needs and at the same time protects against the toxic effect of its excess.[218] There are narrow channels in the protein sphere connecting the cavity and outside formed at the intersection of three or four peptide subunits. Three-fold channels are hydrophilic where negative-charged residues are aligned and four-fold channels hydrophobic. The hydrophilic channels which penetrate the protein shell are considered to be the pathways of metal ions, e.g. Fe (II), and small molecules of appropriate size into the cavity of the protein.[219, 220] Natural apoferritin consists of two types of polypeptide subunits, heavy (H) and light (L) chains, the relative ratio of which varies with the type of biological species and organ. The H-subunit has a "ferroxidase" catalytic site at the interior surface where Fe (II) is oxidized to Fe (III), whereas the nucleation is aided by residues of glutamic acid in the interior surface of the protein.[221-223] In this way, the protein naturally

stores up to 4500 Fe atoms predominantly as an antiferromagnetic particle of ferrihydrite (Figure 3.1).[218, 224] By suitable chemical processes, it is possible to remove the internal inorganic core and use the empty protein shell, called apoferritin, as a confined environment in which different inorganic NPs possessing potential for magnetic, catalytic and biomedical applications can be artificially synthesized.[225] This approach has successfully been used in the synthesis of a wide variety of metal oxide NPs, such as Fe_3O_4/γ-Fe_2O_3 (known as magnetoferritin),[226, 227] Co_3O_4[228] as well as Co, Mn, Eu, Fe and Ti oxyhydroxide NPs.[229-231] Metallic and semiconductor NPs have also been synthesized, such as Cu,[232] Pd,[233] Ni,[234] Co,[234] CoPt,[235] CdSe[236] and ZnSe.[237]

Interestingly, the external protein shell can be modified to guide the assembly of ferritin on a given substrate while preserving all the inner characteristics. This property allows the use of ferritin as a vehicle (template) for guiding and positioning a large variety of internal inorganic NPs to desired positions on a surface by using in all the cases the same experimental conditions. Indeed, since proteins are more easily decomposed than inorganic materials, once structured on a surface the organic protein shell can be selectively eliminated by means of heat or UV/ozone treatment, while the inorganic material preserves its original integrity and location on the surface.[238, 239] In view of these unique properties, ferritin emerges as a fascinating scaffold for the structuration of NPs on a substrate. Representative complementary examples for the structuration of these materials already described in the literature are revised next.

3.1.1 Organizing ferritins on surfaces

To date, several strategies to assemble ferritin entities into well-ordered mono- and multilayers including the transference of a ferritin film from an air-liquid interface onto a solid support[238, 239] as well as the use of scratching[240] and spread coating[241] methods, have been described. The obtained ferritin assemblies were used in some cases for the fabrication of magnetic NP arrays by selectively eliminating the protein shell by subjecting the sample to either heat or UV/ozone treatment while preserving the order of the array.[238, 239]

The interaction of the ferritin with the substrate can be tailored through specific covalent or electrostatic bonds to induce the formation of more stable ferritin networks. Several strategies have been developed in this direction, such as modification of the substrate surface with SAMs bearing terminal functionalities (i.e. succinimidyl groups) suitable to covalently interact with the protein shell.[242-244] Alternatively, functional groups such as thiol can be introduced to the protein shell to facilitate the attachment of the protein on bare Au substrates,[242, 245] or even the shell can also be genetically modified with target-specific affinity peptides to induce a specific interaction of the modified ferritin with the target inorganic surface.[246, 247] A completely different strategy takes advantage of the electrostatic interaction between ferritin and a given substrate.[248-250] In this case, the charge of the protein shell is manipulated by either genetic modification of ferritin or changing the pH of the solution media. This can easily be performed since the isoelectric point of ferritin is ~ 4.5, by changing the pH to lower values it becomes positively charged, while at larger pH values ferritin is negatively charged. The genetic modification of ferritin to

modulate its charge at neutral pH has also been reported.[250]

Beyond the fabrication of mono- and multilayer assemblies of ferritin, several efforts have been devoted to control the arrangement of this protein on surfaces and organize them into well-defined patterns with control up to single particle level assisted by lithographic or other external techniques as is the case of AFM-based lithography. Next section is devoted to describe the advances reported so far in this direction.

3.1.1.1 *Deposition of ferritins on surfaces assisted by templates and/or lithographic techniques*

Several patterning techniques have been implemented, such as nanosphere lithography (NSL),[251] microlens array (MA) patterning,[252] block copolymer (BCP) micelle lithography,[253] electron beam lithography (EBL)[254] and biomimetic layer-by-layer assembly (BioLBL),[255] among others. The great majority of the developed methodologies are based on the indirect deposition approach, where pre-modified chemical patterns are first fabricated and used as templates in a second step to guide the site-selective immobilization of the protein onto pre-defined areas. Following this strategy, well-ordered ferritin arrays have been successfully fabricated bearing few or even a single ferritin immobilized on each feature of the array.

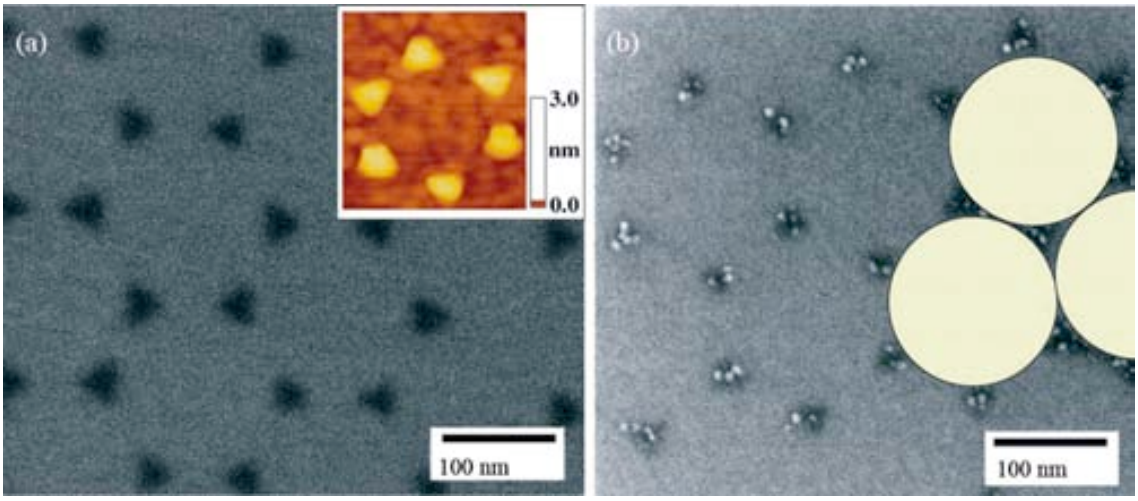

Figure 3.2 (a) SEM image of Ti pattern on SiO_2 fabricated by means of NSL and EBL technique. Inset shows an AFM topography image of the pattern. (b) SEM image after site-selective adsorption of ferritin (displaying Ti-binding peptides on their surface). The maximum number of adsorbed ferritins per Ti pattern was four. Three imaginary polystyrene particles used for the Ti patterning by NSL technique were drawn. Reproduced from ref.[256].

A genetically modified ferritin with target-specific affinity peptides was used to guide the immobilization of the modified protein selectively onto lithographically pre-patterned areas (i.e. Au[257] or Ti[255, 256, 258]). For example, Yamashita *et col.* made use of a modified ferritin displaying a peptide with high affinity for Ti, named TBP-1, which selectively adsorbed onto a hexagonal pattern made of triangular 40 nm Ti dots.[256, 258] The Ti template was fabricated on a SiO_2 surface using NSL and EBL techniques, where a 2D hexagonally closed-packed array of polystyrene (150 nm) particles was used as a mask for the deposition of the Ti film (**Figure 3.2**a).

Afterwards the Ti-based template was immersed in a ferritin solution for a given time at room temperature followed by intensive washing and drying (Figure 3.2b). After ferritin immobilization, the protein shell was selectively removed by UV/ozone treatment (at 110 ºC for 40 min) while preserving the hexagonal periodic array, leading to well-ordered NP arrays on the Ti pattern. The specific binding of the modified protein was not affected by the inner NPs, and therefore, the procedure was reproduced for ferritin displaying two different NPs synthesized inside its cavity, ferrihydrite and Co_3O_4 cores.

More recently, Sano *et col.* made use of the same peptide TBP-1 to genetically modify the ferritin molecules and fabricate multilayered structures selectively adsorbed on nanopatterned Ti stripes fabricated by EBL.[255] This method, called BioLBL, employed the target-specific affinity peptide not only as a binding molecule to immobilize the ferritins but also as a mediator for the biomineralization of a thin film of the target material (i.e. TiO_2) from a precursor reagent present in solution. Moreover, the TiO_2 film was used in turn as a target for the adsorption of a second ferritin layer. By repeating the process, multilayered structures with different NP-containing ferritins (filled with Fe and Co oxides) deposited between TiO_2 layers were selectively build on top of the original strip pattern and characterized by means of SEM and energy dispersive X-ray spectroscopy (EDX) mapping.

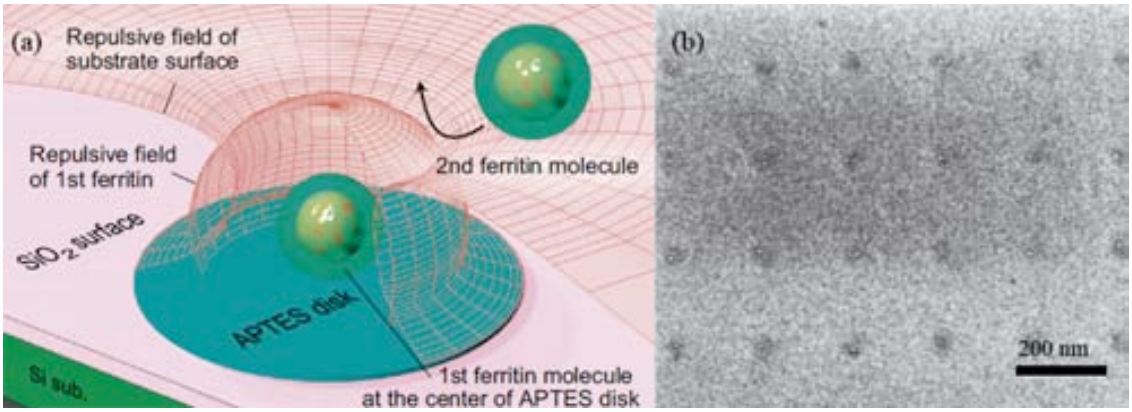

Figure 3.3 (a) Schematic illustration of the adsorption of a single ferritin molecule onto an APTES disk, where the repulsive fields between the substrate surface and the first adsorbed ferritin avoids the approaching of a second ferritin. (b) SEM image of an APTES array showing the adsorption of single ferritin molecules on each disk. Reproduced from ref.[259].

In further studies, Yamashita *et col.* used electrostatic interactions as driving force to made ferritins to selectively adsorb individually onto specific regions of a lithographically pre-patterned substrate.[259, 260] They fabricated a pattern made of circular 3-aminopropyltriethoxysilane (APTES) disks with two different sizes (~ 15 and ~ 45 nm) on a SiO_2 substrate by means of EBL, vapor-phase APTES deposition and lift-off processes. Ferritin was first genetically modified to increase its surface charge density and therefore enhance the electrostatic interaction with APTES disks while avoiding secondary ferritin adsorption (**Figure 3.3**a). The patterned substrate was then incubated into the ferritin solution for a given time at room temperature and studied by means of SEM. The suitable tailoring of the electrostatic interactions (supported by numerical calculation) allowed the placement of a single ferritin molecule on top of each APTES disk of the array, whose disk diameter (up to 45 nm) was much

larger than the size of a ferritin (~ 12 nm) (Figure 3.3b). Additionally, the obtained single ferritin array on 15 nm APTES disks was subjected to rapid thermal annealing under O_2 gas at 500 ºC for 10 min in order to selectively eliminate not only the protein shell but also the APTES pattern, thus leaving independent iron oxide NPs located on the designated positions of the array. Interestingly, the obtained periodic single NP array has recently been used as a catalyst for the position-controlled vertical growth of individual CNTs.[261]

3.1.1.2 *Deposition of ferritins on surfaces assisted by AFM-based lithographies*

The electrostatic interaction as driving force was also used with AFM-based lithography techniques, specifically with LON (already described in Section 1.2).[126] In this technique, a suitable bias voltage applied to a conductive tip is used to create oxide dots and stripes with a resolution of only few nanometers. These oxide patterns can be exploited as templates for the selective attachment of ferritin molecules.[155, 262, 263] Yoshinobu *et col.,* explored two different protein patterning routes based on the LON technique.[262] In the case of the negative patterning, a thin oxide layer was formed on the silicon surface by wet-chemical etching, and functionalized with positively charged APTES molecules ready to electrostatically interact with the negatively charged ferritins. Then, oxide patterns were formed on this surface by the AFM tip and subsequently ferritins were selectively immobilized outside the oxide patterns. In the case of the positive patterning, the Si substrate with the oxide layer on top was first protected with octadecyltrichlorosilane (OTS) to introduce unreactive long alkyl groups on the surface. Then, the tip was used to fabricate oxide patterns which in turn were modified with APTES to produce the region on which the immobilization of the ferritin was promoted.

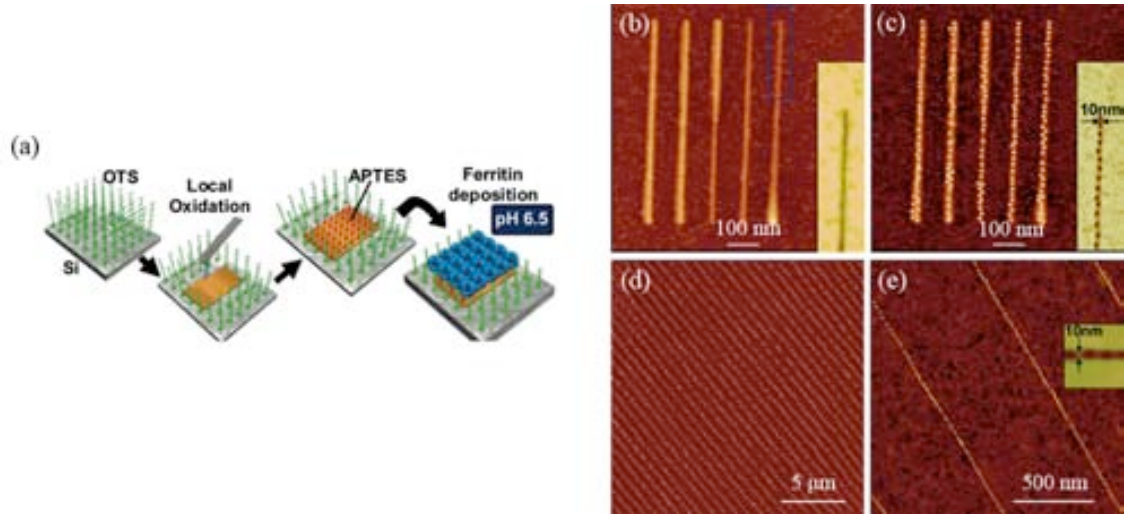

Figure 3.4 (a) Schematic illustration of the ferritin patterning by combining LON and surface functionalization with OTS and APTES. AFM topography images of the local oxide pattern made of parallel lines with widths of 10-15 nm (b) before and (c) after adsorption of ferritin proteins into single molecule chains. (d, e) AFM topography images of the parallel patterning of ferritin molecules by means of lithography controlled dewetting. Insets correspond to phase images. Reproduced from ref.[155].

Interestingly, the use of electrostatic interactions presents additional advantages such as controlling the attachment/removal of this protein on the surface by changing the pH of the

solution (**Figure 3.4**).[155, 263] The deposition at the single particle level was possible due to the high spatial resolution of LON, which allow to accurately match the size of the oxide pattern to the protein size (~ 12 nm).[155] Thus, individual ferritin entities were positioned into chain-like structures over sub-micrometer areas (Figure 3.4b,c). By means of print-based methods such as lithography-controlled dewetting instead of LON, this approach was successfully extended to pattern ferritin entities over macroscopic regions (1 cm^2) (Figure 3.4d,e).

3.1.2 Surface structuration strategies: Summary

The patterning strategies reviewed above are representative examples of the significant efforts that have been made so far to control the organization of ferritin proteins into well-defined patterns. As we have seen, the deposition of ferritin is typically achieved using an indirect deposition approach. In this sense, in a first step a template is fabricated on the surface to define the regions on which the ferritin is then site-selectively attached from solution. During the present Thesis, some excellent works in this direction have been reported by Yamashita *et col.*[259] and Coronado *et col*.[264] The authors reported the fabrication of ferritin arrays in which the number of protein entities deposited on each feature was controlled at the single particle level. Both strategies are based on the indirect deposition of ferritin and used the electrostatic interaction between ferritin and the template as driving force for the site-selective adsorption of the protein.

As far as we known, no previous examples exploiting the direct deposition approach for the patterning of ferritin into well-defined arrays with nanometric resolution have been reported so far. Herein, we demonstrate that this direct strategy is feasible by using direct-write AFM lithography.

3.2 Experimental conditions for the structuration of ferritin on surfaces by direct-write AFM lithography

In this section, the methodology for the direct deposition of ferritin on surfaces in the form of well-defined patterns by direct-write AFM lithography is established. The schematic overview of the different approaches followed with this aim is shown in **Figure 3.5**. The experimental conditions can be used for the structuration of ferritins displaying different inorganic cores inside its cavity, which is demonstrated by creating arrays using natural ferritin, apoferritin and magnetoferritin. These results demonstrate how the proteic capsule can be used as a general carrier in direct-write AFM lithography experiments for the deposition of any inorganic material that can be held inside. Once the structuration on surfaces is done, the protein pattern is subjected to heat treatment to eliminate the organic shell while preserving the order of the array. Finally, in this section we go one step further to demonstrate that the use of direct-write AFM lithography also allows controlling the amount of ferritin entities deposited on each one of the

dot-like features of the fabricated arrays. These experiments were performed in collaboration with Dr. D. Maspoch from the CIN2.

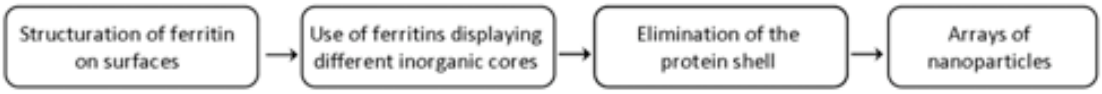

Figure 3.5 Schematic overview of the steps followed for the structuration of ferritin proteins that involve the use of apoferritin as a carrier for structuring ferritins displaying different inorganic cores and the fabrication of arrays of NPs made of the inorganic cores that rest on the surface after subjecting the ferritin arrays to heat treatment.

3.2.1 Ferritin arrays on surfaces

The first experiments with ferritin were to find the proper experimental conditions to achieve their controlled deposition on surfaces since there were no previous examples (even today) in the literature by direct-write AFM lithography, as previously described. Nevertheless, other types of biomolecules have already been directly deposited by using this technique and were used as a tentative guide for our experiments.[265] These works have faced several difficulties, such as the slow transportation of high-molecular-weight biomolecules from the tip to the surface, difficulties of preserving their biological functionalities and short operation time due to the fast evaporation of the ink as well as limited ink volume. In order to overcome these restrictions, two main approaches are commonly used, namely the chemical modification of the tip surfaces[185] and the use of additives in the ink solution, such as agarose, phospholipids or glycerol, in the biomolecular-based ink solutions.[265-268]

Herein, we made use of glycerol as an additive for the formulation of the ferritin ink solution. In this sense, the use of glycerol has several advantages over the direct deposition of a pure biomolecule sample for use in direct-write AFM lithography experiments. First, due to its high boiling point (b.p. 290 ºC), glycerol slows down the evaporation rate of the ink solution. Let us note that here the deposition strategy is accomplished by dispensing femtoliter droplets of the ink solution in the form of the desired pattern. Under these conditions, an efficient transfer from the tip to the surface requires maintaining the ink in its liquid state during the whole writing process.[269, 270] Second, glycerol protects proteins from drying and denaturing while on the tip. And third, the increasing viscosity compared to a buffered solution facilitates tip coating without the need of prior tip surface modification (viscosity of glycerol is 1.4 Pa·s at 20 ºC). Furthermore, the enhancement in molecular ink viscosity also favors the transference of the ink solution from the tip to the substrate surface.

For the initial experiments the ferritin of choice was a commercially available natural ferritin solution (horse spleen ferritin, 69 $mg \cdot mL^{-1}$ in saline solution, 150 mM NaCl, more information in Experimental Section 7.1). An ink solution consisted in a mixture of 80 % (v/v) natural ferritin solution and 20 % (v/v) glycerol (final ferritin concentration was 55.2 $mg \cdot mL^{-1}$, ~ $3.7 \cdot 10^{16}$ ferritin entities$\cdot mL^{-1}$) was prepared following a standard formulation for the deposition of biomolecules. The structuration procedure was performed using the fabrication instrument

Nscriptor™ from NanoInk (for more information see Experimental Section 7.2). For tip coating procedure we made use of a microfluidic ink delivery chip-based system (Inkwell, NanoInk) following standard inking routines (see Experimental Section 7.2). The coating procedure first involved the addition of few drops of the freshly prepared ink solution into an Inkwell reservoir, whereafter it flowed into the tip-sized microfluidic well. Let us note that in our observation, a drop of this ink remained in a "wet" state in the reservoir over few days due to the presence of glycerol in the ink solution. Then, a tip was coated with the ink solution by dipping it into the microwell for a given time. The coated tip was then brought into contact to the target surface to fabricate the structures by traversing the tip over the surface in the form of the desired pattern. It is important to notice the robust nature of ferritin since it is known to stay intact at temperatures as high as 80 ºC, which strongly facilitates the whole experimental procedure. In all experiments, ferritin patterning was performed under controlled environmental conditions (~ 35 % relative humidity and room temperature). In some experiments performed at lower relative humidity values we observed an increased drying rate of the ink solution, which significantly hampered the writing process.

By using the above mentioned experimental conditions, ferritin structuration was investigated onto a variety of surfaces of technological interest such as Au, Si/SiO_2, Nb/Nb_2O_5 and Al/Al_2O_3. To this aim, we made use of chips commercially available from NanoInk displaying a cantilever array made of 12 tips in parallel, called M-type pen tips and abbreviated from now on as MP tips (for more information see Experimental Section 7.2). This type of tips are specially designed for writing viscous liquids in addition to be modified with a recessed area surrounding the tip base that increases the loading of the ink material, providing extended printing times without recoating the tip. For patterning, MP tips were coated using Inkwell chips (Inkwell Arrays: M - 6MW from NanoInk), which are specially designed for dipping simultaneously six tips into six independent microwells (see **Figure 3.6**). In this experiment, the process of coating was repeated for the six remaining tips in order to coat all the twelve tips of the chip. If needed, the Inkwells can also be filled with different inks, thus increasing the flexibility of the process. However, this was not performed in these experiments and all the reservoirs were filled with the same ferritin-based solution.

A representative example of the deposition procedure is shown in Figure 3.6c,d. This process was monitored by using the camera integrated in the Nscriptor™ instrument, which has a resolution of ~ 3 μm. Initially, the excess of ferritin ink was reduced through cantilever and tip *bleeding* by bringing the coated tip into contact with the substrate surface. Between depositions, the MP tips were displaced to new regions of the surface in order to avoid undesirable contact of the tips with already deposited drops. After few *bleeding* spots, the tip started writing uniform (sub)micron sized dots. Then, we executed the writing process in constant height mode (more information about operation modes in Experimental Section 7.2) using patterns previously designed in InkCAD Nscriptor™ design software. In this context, twelve identical rectangular-shaped structures were created in one single step using the MP tips. In Figure 3.6c,d rectangular-shaped shadows on the surface can be distinguished which corresponds to the ferritin patterns. In this case, each array consists of 10 × 10 ink dots separated by 2 μm, in which each dot was fabricated by keeping the tip in contact with the substrate surface during 0.3 s.

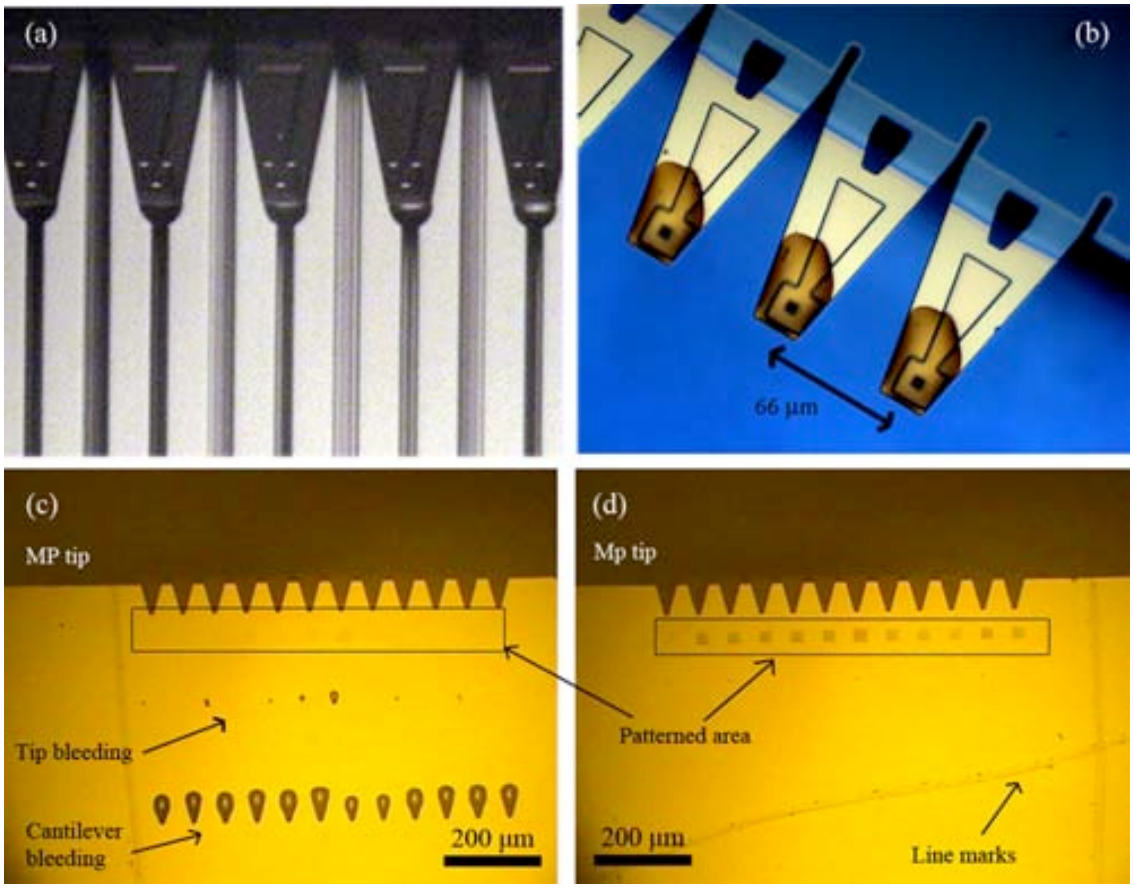

Figure 3.6 (a) Image captured with the integrated camera to the Nscriptor™ instrument during dipping the MP tips into the microwells filled with the ferritin-based ink solution. (b) Optical image of three tips right after coating step. (c,d) Optical images captured during direct-write AFM lithography experiments on a Si/SiO_2 substrate. *Bleeding* spots delivered to eliminate the excess of ink coating the tip are indicated on the image. After the elimination of this excess, MP tips fabricate well-defined arrays which can be distinguished on the image by the presence of rectangular-shaped shadows (the patterned area is indicated on the image). Before patterning process was performed, we made line marks on the surface with a diamond scribe in order to help localizing the arrays over the surface during subsequent characterization.

Figure 3.7 shows optical microscope images captured right after patterning process that illustrate the successful fabrication of ferritin arrays on each one of the investigated substrates (i.e. Au, Si/SiO_2, Nb/Nb_2O_5 and Al/Al_2O_3) prepared as described in Experimental Section 7.2. These results demonstrate the generality of this fabrication approach. Let us note that even though patterning by an individual tip was quite uniform inside each array, slights variations in writing between tips were observed (see Figure 3.7a). Ideally, patterns fabricated by the twelve MP tips should be uniform in size across the entire patterned area. However, several different factors may affect the resolution of the writing and the patterned dot size for each particular tip, which include the individual conditions and shape of each tip of the chip, the loading of the ink material onto the tips and surface features or contaminants. In addition, it is crucial to ensure that the twelve tips are precisely aligned with the Inkwell surface (during coating step) and substrate surface (during deposition step). For this, leveling was optically determined and corrected by viewing the relative deflection between cantilevers and performing leveling operations using a three z-axis motor leveling system in the Nscriptor™ instrument. In Figure 3.7a, we also observe a gradual decrease of the size of the features printed by a single tip

between sequential arrays. This effect is explained due to the depletion of the ink solution. In any case, this reflects the control of the technique needed to obtain reproducible results.

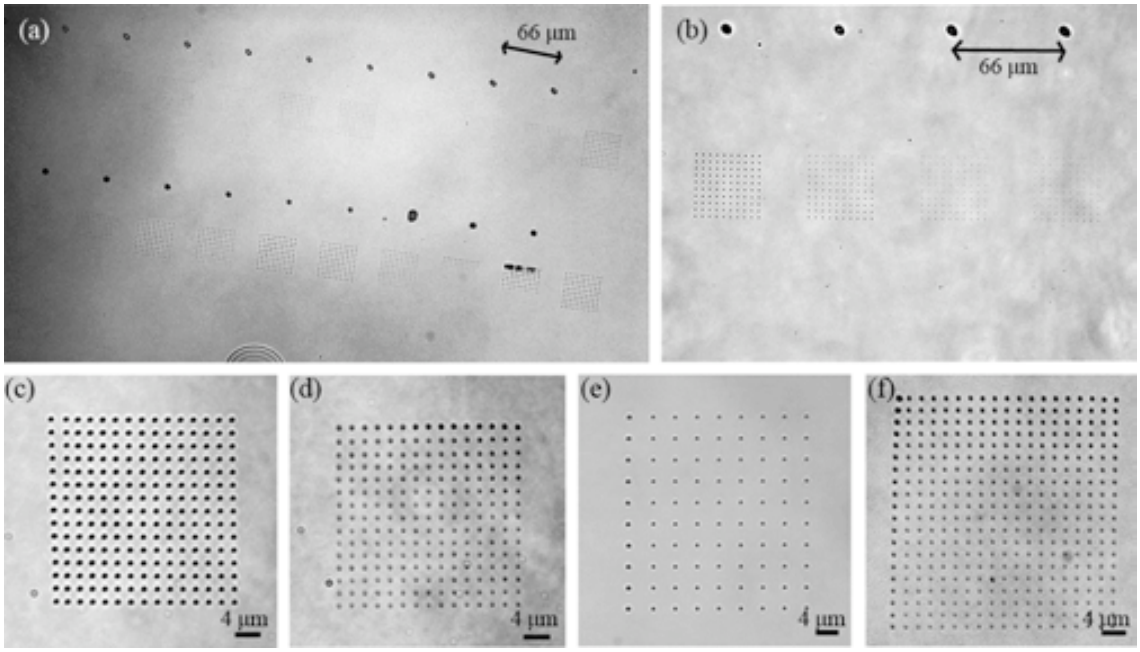

Figure 3.7 Optical microscope images of ferritin arrays generated by direct-write AFM lithography on (a-c) Au, (d) Si/SiO_2, (e) Al/Al_2O_3 and (f) Nb/Nb_2O_5 substrates. Panels **a** and **b** show several arrays separated a distance of 66 µm, which corresponds to the distance between MP tips. *Bleeding* spots on top of the arrays can be observed.

The morphology of the structures was investigated in detail by means of AFM. Characterization of the structures of the array was performed by randomly selecting almost 25 different dots of the array and measuring their diameter and height. For each array, we obtained the mean diameter and height and the 95 % confidence interval for the mean value. **Figure 3.8**a-c shows an AFM image of a ferritin array fabricated on Au consisting of very uniform dots with a diameter of 539 ± 33 nm separated by 1 µm. Height profile analysis of one of the rows of the array is shown in Figure 3.8c. The average height of the structures was 13 ± 3 nm, in good agreement with the size of a single ferritin particle (ca. 12 nm) indicating a distribution of the ferritin entities on each generated dot-like structure in the form of a (sub)monolayer. In some cases, the presence of peaks with heights up to 50 nm inside the dot features was distinguished (see Figure 3.8b). It is important to note that the topographical features not only came from ferritin entities but also it is expected that other components present in the ink solution (e.g. salts and glycerol) should also contribute to the final dot height (*vide infra*).

An important feature of direct-write AFM lithography is the ability to generate structures with control over feature size by adjusting tip-substrate contact time. As commonly observed for alkanethiol or protein features generated by direct-write AFM lithography,[166, 185, 186] the size of the ferritin spots were controlled by regulating the time the tip is in contact with the substrate surface and taking into account the depletion of the ink solution on the tip. In this way, the size of the features was miniaturized down to 100 nm in diameter by diminishing the tip-substrate contact time down to 0.1 s per each spot. As an example, AFM topography image of a high-density array of ferritin spots with average diameters of 150 ± 21 nm is shown in Figure 3.8d.

We have also investigated the possibility of organizing such proteins into well-defined lines on surfaces in order to create more complex patterns. In contrast to the case of dot generation where the tip is held stationary for the deposition time, during the fabrication of lines the tip continuously moves along the surface (dynamic writing). In a typical experiment, after *bleeding* step a coated tip was brought in contact to the substrate and subsequently traversed over the surface at a fixing tip scan speed in the form of the desired pattern. For example, lines were generated on Au by simply moving the ferritin-coated tip at a fixing rate (1 $\mu m \cdot s^{-1}$) on the surface creating microscale molecular letters forming the word *ferritin* (Figure 3.8e).

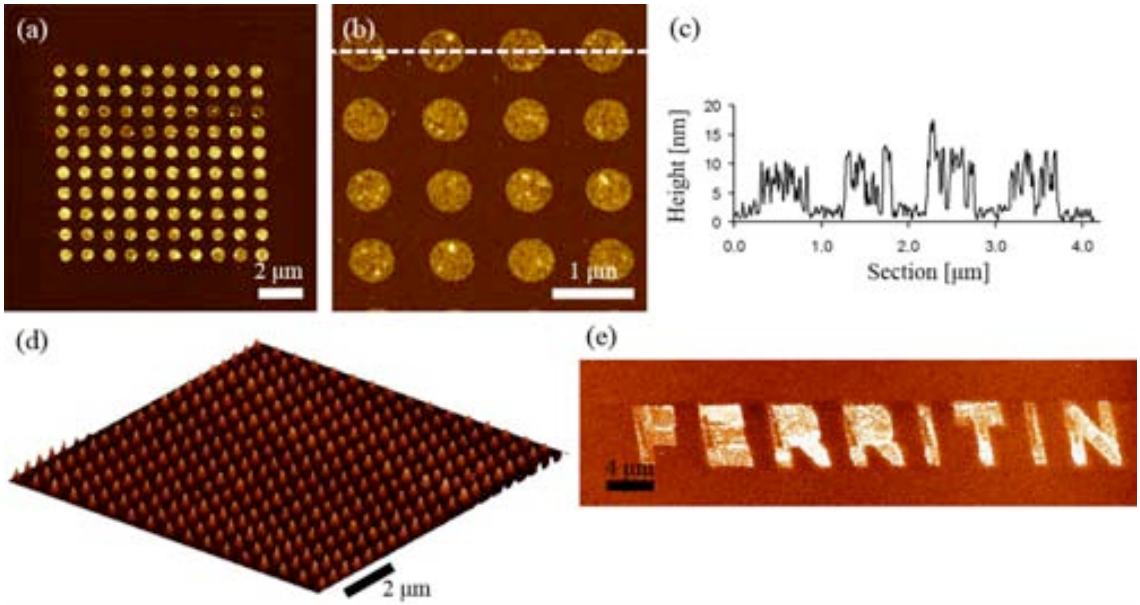

Figure 3.8 Ferritin arrays fabricated by direct-write AFM lithography onto Au substrates. (a) AFM topography image of a ferritin array made of repeated dots 539 ± 33 nm in diameter spaced a distance of 1 µm. (b) Magnification view of image **a**. (c) Height profile of one of the rows of array shown in panel **a**. (d) 3-D AFM topography image of a ferritin array with spacing between features of 500 nm and dot diameter of 150 ± 21 nm. (e) AFM topography image of microscale molecular letters forming the word *ferritin*.

To have more evidences that ferritin proteins were placed on each spot of the patterned areas, a fluorescent dye was used to label the ferritins, and the deposition process was investigated by fluorescence microscopy. For this purpose, a widely used amine-reactive fluorophore, Atto 488 *N*-hydroxisuccinimide (NHS) ester, was covalently attached to the ferritin surface by Dr. A. Lostao and R. de Miguel at INA (see Experimental Section 7.1) (**Figure 3.9**a). Labeled ferritins were then deposited on Au substrates using the same mixture 80 % (v/v) of labeled ferritin in phosphate buffered saline (PBS) solution (16.6 $mg \cdot mL^{-1}$) with 20% (v/v) glycerol while reproducing the above experimental conditions. In the first experiment, no fluorescence was detected from the arrays, which could be due to a low labeling of the ferritin with the fluorophore molecule and/or due to fluorescence was quenched by the underlying Au substrate. In a second experiment, they introduced a variation to the labeling protocol in order to increase the protein labeling degree (see Experimental Section 7.1). By using this labeled ferritin sample, ferritin arrays were fabricated as described above on Au and fluorescence signal was detected

on each dot-like feature which clearly confirmed the presence of ferritin particles on each spot of the array (Figure 3.9b).

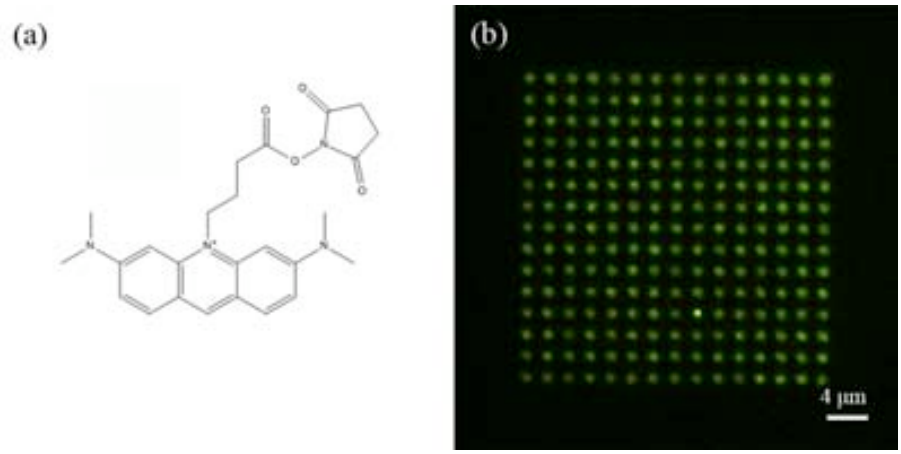

Figure 3.9 (a) Atto 488 NHS ester fluorophore has an excitation peak at 498 nm and an emission peak at 520 nm in 0.1 M PBS pH 7.0. The succinimidyl ester group of the dye enables an effective reaction with primary amino groups of the protein. (b) Fluorescence image of a fluorophore-labeled ferritin array.

3.2.2 Structuration of ferritin displaying different inorganic cores

So far, we have demonstrated the controlled deposition of ferritin entities by means of direct-write AFM lithography on a wide variety of surfaces. The objective of the work developed in this section was to shown that the deposition process works not only with natural ferritin but with other ferritins by exploiting the capability of the proteic shell (apoferritin) to act as vehicle for any kind of NP synthesized inside.

With this aim, two ferritin derivatives were investigated: (i) the empty protein shell, named apoferritin, and (ii) ferritin with an internalized ferrimagnetic maghemite γ-Fe_2O_3 NP of ~ 5.9 nm in diameter containing an average number of 1000 Fe atoms/protein, named magnetoferritin, synthesized by Dr. A. Lostao and R. de Miguel at INA (ferritin synthesis and characterization information is given in Experimental Section 7.1). The apoferritin ink solution consisted in a 27 $mg \cdot mL^{-1}$ solution in PBS and 20 % (v/v) of glycerol (~ $3.7 \cdot 10^{16}$ apoferritin entities$\cdot mL^{-1}$). In the case of the magnetoferritin, the concentration was intentionally decreased since it was experimentally observed the tendency of these ferritins to aggregate in solution. This observation suggests that the organic shell could be partially disrupted after the synthesis of the inorganic core resulting in increased aggregation of the proteins. In addition, the iron-based particles exhibited a broad size distribution with large particles showing a magnetic moment high enough to induce the aggregation mainly by dipolar interactions. Therefore, in order to guarantee a good dispersion of ferritin entities in solution, we worked with a diluted solution containing 20 $mg \cdot mL^{-1}$ of magnetoferritin in PBS and 20 % (v/v) glycerol in the presence of 0.4 M of glycine, which is a protein stabilizer (~ $2.1 \cdot 10^{16}$ magnetoferritin entities$\cdot mL^{-1}$).

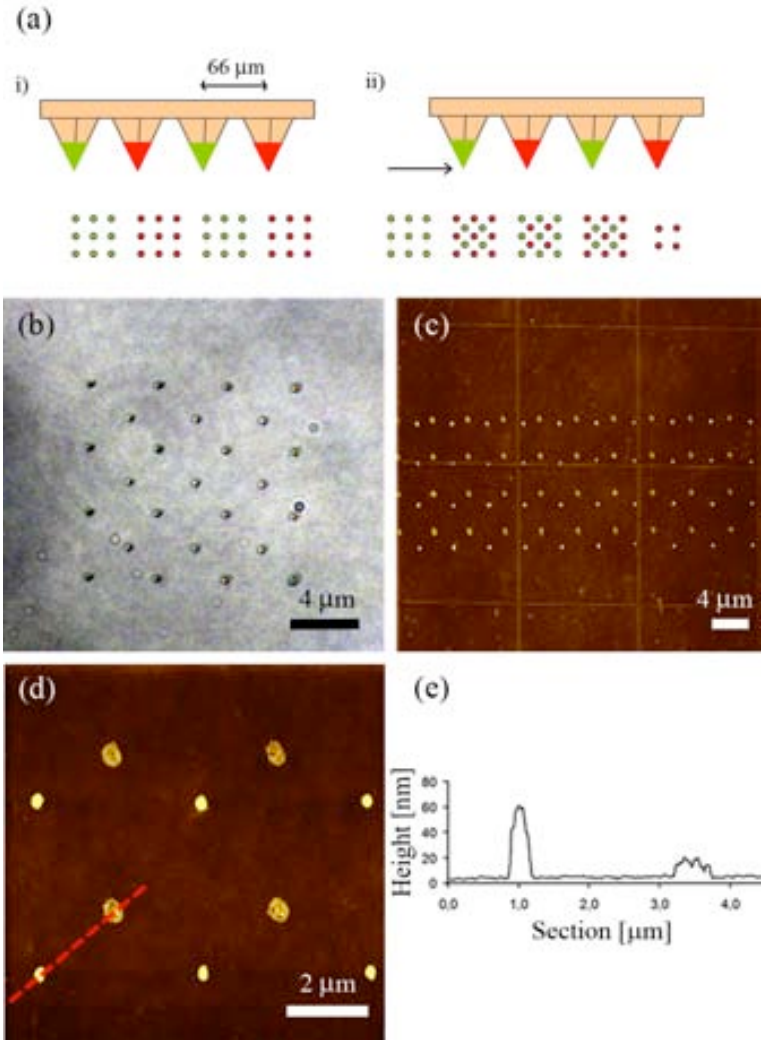

Figure 3.10 (a) Schematic illustration of the deposition procedure followed to obtain two-component arrays by direct-write AFM lithography using MP tips. (b) Optical image of a two-component array made of apoferritin and natural ferritin on Si/SiO_2. (c) AFM topography image of a two-component array made of apoferritin and magnetoferritin on Si/SiO_2 and (d) magnification view of the same array. (e) Height profile along the red dashed line in panel **d**.

We decided to perform the deposition of both types of ferritins simultaneously in a single pattern and create two-component arrays. For this purpose, six MP tips were alternately functionalized with the two different ferritin ink solutions by using the Inkwell delivery system. Since the microfluidic channels of the Inkwell are designed to match the MP tips geometry, each tip can be loaded with a different ink while preventing cross-contamination between tips. Three alternately reservoirs of the Inkwell chip were filled with one type of ink solution whereas the other three were filled with a different ink solution. Then, the MP tips were coated with the desired ink following standard routines. The strategy for the fabrication of the combined arrays consists of two steps as shown in **Figure 3.10**a. In the first deposition, one-component arrays of the two different ferritin types were created with a separation determined by the distance between MP tips (66 µm). In the second step the tips were translated horizontally 66 µm. A pattern was design that starts few µm shifted in X and Y positions. In this way the fabrication of the second set of arrays was ensured to take place right in the middle of the former arrays leading to the formation of combinatorial structures (except in the first and

last of the arrays). Using this strategy, several combinations writing with natural ferritin, apoferritin and magnetoferritin were performed (Figure 3.10b,c). Even though, natural ferritin as well as apoferritin were structured in the form of (sub)monolayers, in the case of magnetoferritin we observed multilayered structures with heights up to 60 nm under the same experimental conditions (Figure 3.10d,e). These height values could be explained due to the tendency of this type of ferritin to aggregate, as already mentioned above, and to the presence of additional components in the ink solution (i.e. glycine).

3.2.3 Protein shell removal

As already described in Section 3.1, the protein shell of ferritin is vulnerable enough to be selectively eliminated by heat or UV/ozone treatment, while preserving the original pattern on which the inorganic NP rest. For that purpose, arrays of natural ferritin were fabricated on Si/SiO_2 surfaces and subsequently subjected to controlled elimination of the organic protein shell. Based on procedures already described in literature,[239, 271] the ferritin arrays were exposed to heat treatment under inert atmosphere to avoid excessive oxidation of the surface and the inorganic cores. This treatment was performed with the help of Dr. M. J. Esplandiu at the CIN2 using a Lindberg Blue furnace. The patterned substrate was placed in the centre of a quartz tube in the electronic oven and argon gas was flown through the system at the rate of 500 $ml \cdot min^{-1}$. The quartz tube was heated to 450 ºC for 1 h before allowing the quartz tube and sample to cool naturally back to room temperature.

Field emission SEM (FE-SEM) images of one of these heated arrays are shown in **Figure 3.11**, which consists in an array of 10 x 10 dots separated by 4 μm with a diameter of 1.2 ± 0.1 μm. FE-SEM characterization confirms that the order and spacing of the dot structures in the array was maintained after heat treatment. Furthermore, the presence of material exactly on the original dot features together with its absence over the unpatterned surface suggests that the inorganic cores remain at the same location after heat treatment. EDX was used to determine the presence of iron inside each dot of the array. In this sense, EDX is a chemical microanalysis technique that detects X-rays emitted from the sample during bombardment by an electron beam to characterize the elemental composition of the analyzed volume. However, this technique was unable to detect the signal corresponding to iron species on these locations and just signals coming from the Si/SiO_2 substrate were detected (Figure 3.11c). Therefore, we cannot confirm the complete elimination of the protein shell and the presence of the inorganic cores by FE-SEM, so some other means of observation was necessary to determine whether or not the protein was completely removed and confirm the presence of the inorganic cores inside the structures.

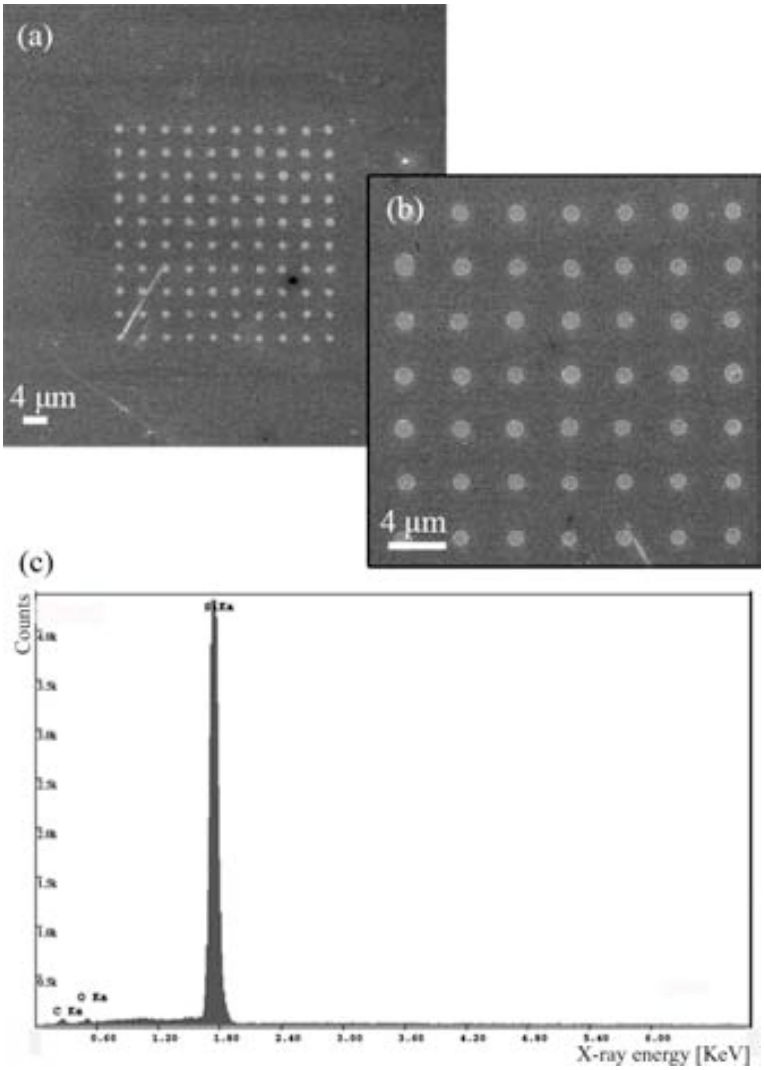

Figure 3.11 (a) FE-SEM image of a ferritin array fabricated on Si/SiO_2 after heat-treatment and (b) a magnification view of the same array. (c) EDX spectrum of one of the dots of the array showing the Si peak from the substrate surface and the absence of Fe peaks.

The presence of the inorganic NPs on these dot-like features and the complete elimination of the protein portion were verified by time-of-flight secondary ion mass spectrometry (ToF-SIMS) analysis. In ToF-SIMS a focused ion beam (primary ions) is used to bombard the surface. Atomic collisions transfer the primary ion energy to the target atoms thereby setting up a "collision cascade". Part of the energy is transferred back to surface allowing surface atoms and molecular fragments to overcome surface binding energy. While most secondary particles come off neutrally charged, a small proportion comes off either as positive or negative ions which can be mass analyzed. This technique is a very powerful method applicable to many types of systems, such as for the detection and characterization of proteins and SMM on surfaces.[39, 272, 273] This arises from its excellent mass resolution, surface sensitivity and high spatial resolution, providing both chemical and distributional (laterally and depth) information for a wide variety of materials and applications.[274-276]

These experiments were performed in collaboration with Dr. R. Pérez-Rodríguez of the Plataforma de Nanotecnologia at the Parc Científic de Barcelona (the experimental conditions are described in Experimental Section 7.3). The initial ferritin arrays (before heat treatment)

showed a negative secondary ion spectrum with two main peaks at 26 and 42 *m/z*, which correspond to the peptide bond fragments CN^- and CNO^-, characteristic of proteins.[277] ToF-SIMS ion images of CN^- and CNO^- showed good contrast between the spots and the remaining surface (see **Figure 3.12**a-c), that is, ferritin particles were written and well-structured on surfaces. It is also interesting to note that no iron-based fragments were detected (Figure 3.12d). This is consistent with the extremely shallow information of ToF-SIMS, whose sampling depth is typically in the range of 1 – 2 nm, which is close to the dimensions of the protein shell that involves the inorganic NP (ca. 2 nm). Importantly, this result clearly suggests that the protein shell surrounding the inorganic core was preserved upon the deposition process. After subjecting the ferritin arrays to heat treatment, ToF-SIMS analysis showed a negative secondary ion spectrum that did not show the two characteristic protein peaks at 26 *m/z* (CN^-) and 42 *m/z* (CNO^-) (Figure 3.12 e,f). However, ToF-SIMS ion images of iron-based fragments showed good contrast between the spots and the remaining surface (Figure 3.12g). These results demonstrate the location of the inorganic cores on each one of the dot-like features generated by direct-write AFM lithography. In addition, due to the extremely superficial nature of ToF-SIMS sampling depth, the only detection of iron-based compounds after heat-treatment also evidenced the selective elimination of the protein shell that typically surrounds the inorganic core.

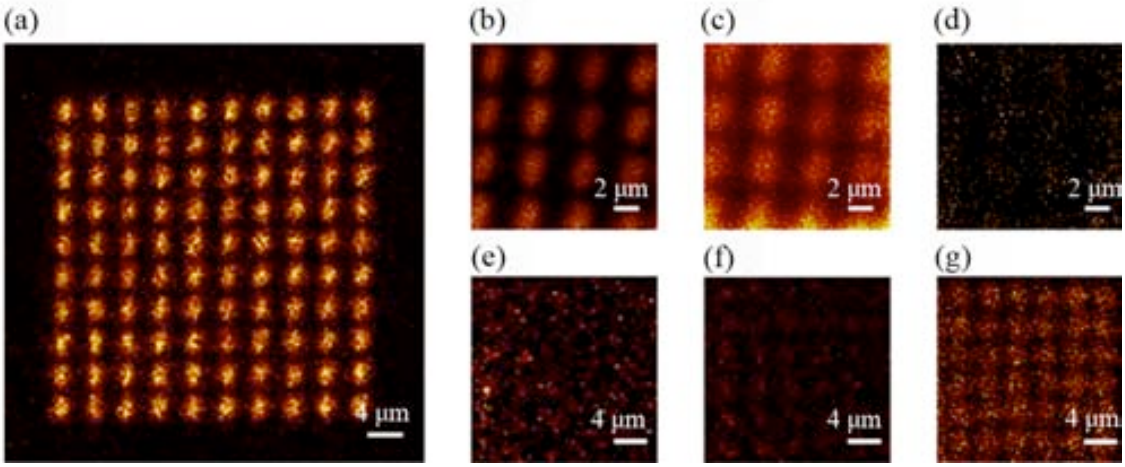

Figure 3.12 ToF-SIMS analysis of the array of ferritin before heat treatment: (a) complete nanoarray detected by negative ion CNO^- and magnification view of the same nanoarray of (b) negative ion CNO^-, (c) negative ion CN^-, and (d) positive ion Fe^+. ToF-SIMS analysis after heat-treatment: (e) negative ion CNO^-, (f) negative ion CN^-, and (g) score image of the first principal negative Fe-based fragments detected on the arrayed areas.

3.2.4 Controlling the number of ferritins deposited

Up to now we have shown the capability of direct-write AFM lithography for the controlled deposition of ferritin proteins on surfaces as a universal carrier for any kind of inorganic NP encapsulated inside its internal cavity. Control on the morphology of the arrays, dot size or structural dimensions have been achieved. In addition, the arrangement into arrays is retained even upon burning the proteic shell. The last question that remains to be answered is: Do we have control on the number of ferritins deposited, if feasible down to the controlled deposition

of a single ferritin? Such advances can fuel the detailed understanding of their individual and collective properties by having the possibility to study them at the individual (or few of them) level. Previous works have already demonstrated this control on structuring ferritin down to single particle level, as already described in Section 3.1. These examples are chemically-assisted methods (i.e. indirect deposition approach) based on the chemical modification of the ferritin surface and/or the use of templates to constrain the amount of ferritin entities attached. However, as far as we know, there are no previous works demonstrating the ability to control the amount of deposited ferritins or even NPs by using a direct deposition approach.

For this purpose, we combined both techniques: direct-write AFM lithography and transmission electron microscopy (TEM). The central electron-dense core of ferritin allows its visualization by TEM, and therefore, the identification of individual ferritin particles on surfaces (**Figure 3.13**). So, the fabrication of arrays on TEM grids would allow visualizing and studying the number of ferritin entities deposited on each one of the generated structures.

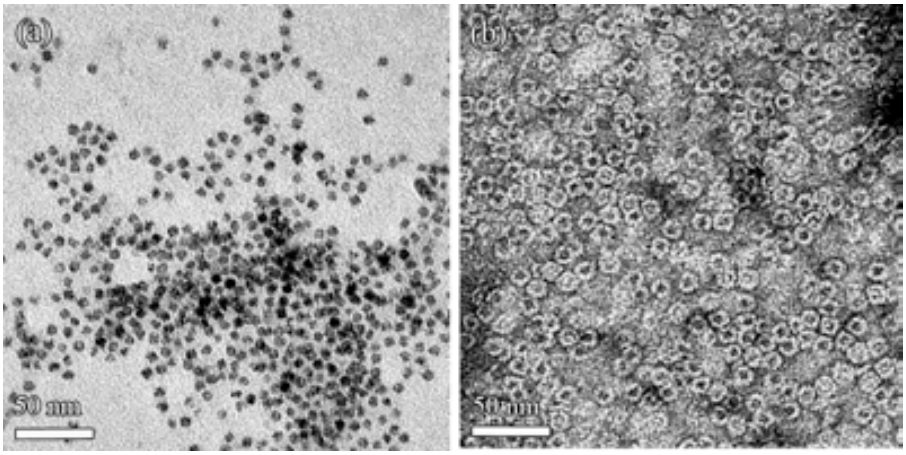

Figure 3.13 (a) TEM image of ferritin proteins deposited onto a carbon-coated TEM grid by drop casting. (b) TEM image of ferritin molecules negatively stained with 3 % (w/w) aurothioglucose on a carbon-coated TEM grid. The negative stain forms a thin layer on the surface that surrounds each molecule as a ring and then allows visualizing the protein shell around the central core.

The structuration process on carbon-coated TEM grids is a challenging issue due to the non-rigid nature of its surface (**Figure 3.14**a). It consists of a fined mesh grid on which is deposited a film made of a membrane of amorphous carbon (15 to 25 nm thick) supported by a polymer layer (30 to 60 nm thick). Its delicate constitution implies and additional effect to avoid; the rupture of the membrane with the tip along the writing process. Figure 3.14b shows a representative example of a carbon-coated TEM grid which was damaged during the patterning process. To avoid damaging, a qualitative optical control of the deflection of the tip as approaches the surface is used. The position at which the tip is considered to be in contact with the surface is then determined in this way by the user (i.e. constant height mode, described in Experimental Section 7.2). However, if needed, this control can also be achieved under feedback conditions by monitoring the tip deflection by the displacement of a laser beam from the back of the cantilever into a position-sensitive photodiode detector (i.e. constant force mode, described in Experimental Section 7.2). Let us note that the first mode was a faster process since it eliminates the need to align the laser spot on the cantilever. Moreover, tip deflection

monitoring gives an excellent control to preserve the membrane intact as shown in Figure 3.14c,d, so it was used for the great majority of the experiments.

A crucial issue is to ensure an optimal alignment of the twelve MP tips with respect the surface. In this sense, TEM grids are quite difficult to manipulate with tweezers to fix them on a support stage (before patterning) while preventing them from bending. In addition, the carbon-based surface is not flat at all, instead it shows a well-like shape. For all these reason, ensure the proper alignment of the tip with the surface typically results in a quite tricky task.

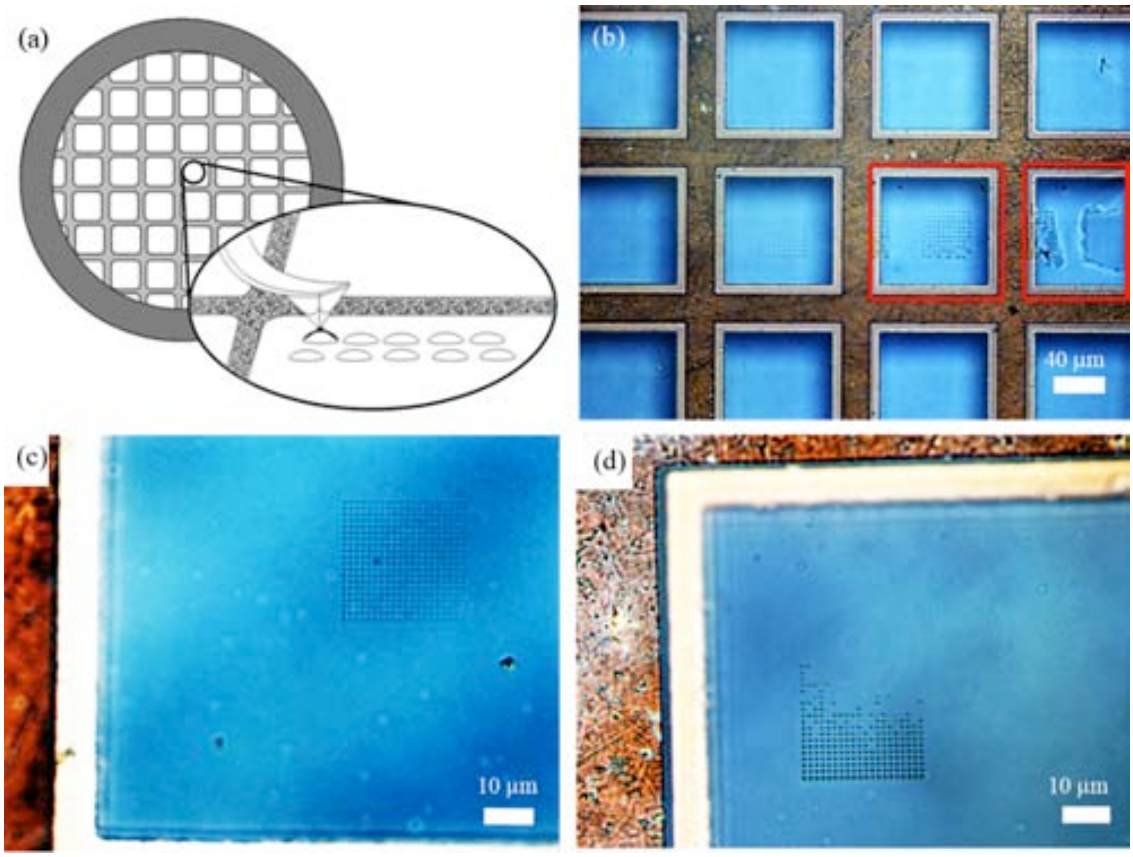

Figure 3.14 (a) Schematic illustration of the fabrication of arrays on a carbon-coated TEM grid. (d) Optical image of a carbon membrane which was damaged during writing, indicated with red marks, and (b,c) ferritin arrays successfully fabricated by controlling the deflection of the tip.

All patterning experiments were performed following the same experimental conditions described in previous sections. For this, MP tips were coated with an ink solution of 55.2 $mg \cdot mL^{-1}$ of natural ferritin containing 20 % (v/v) of glycerol. **Figure 3.15** shows a representative array directly fabricated on a carbon-coated TEM grid and characterized by TEM. The array consists of 40 x 40 dots separated by 500 nm and very uniform in size, with a diameter of 150 ± 4 nm. Focusing on a dot, the high resolution of TEM technique as well as the good contrast of the ferritin cores, allows visualizing the ferritin entities, that is, their central cores on each dot (Figure 3.15 c). In addition, ink solvent components give to a slight shadow on the surface that permits to perfectly distinguish the size of the dot-like structure and then determine its diameter. Therefore, the characterization of the structures by TEM allows the determination of both the number of ferritins and the dot diameter of each one of the dots of an array.

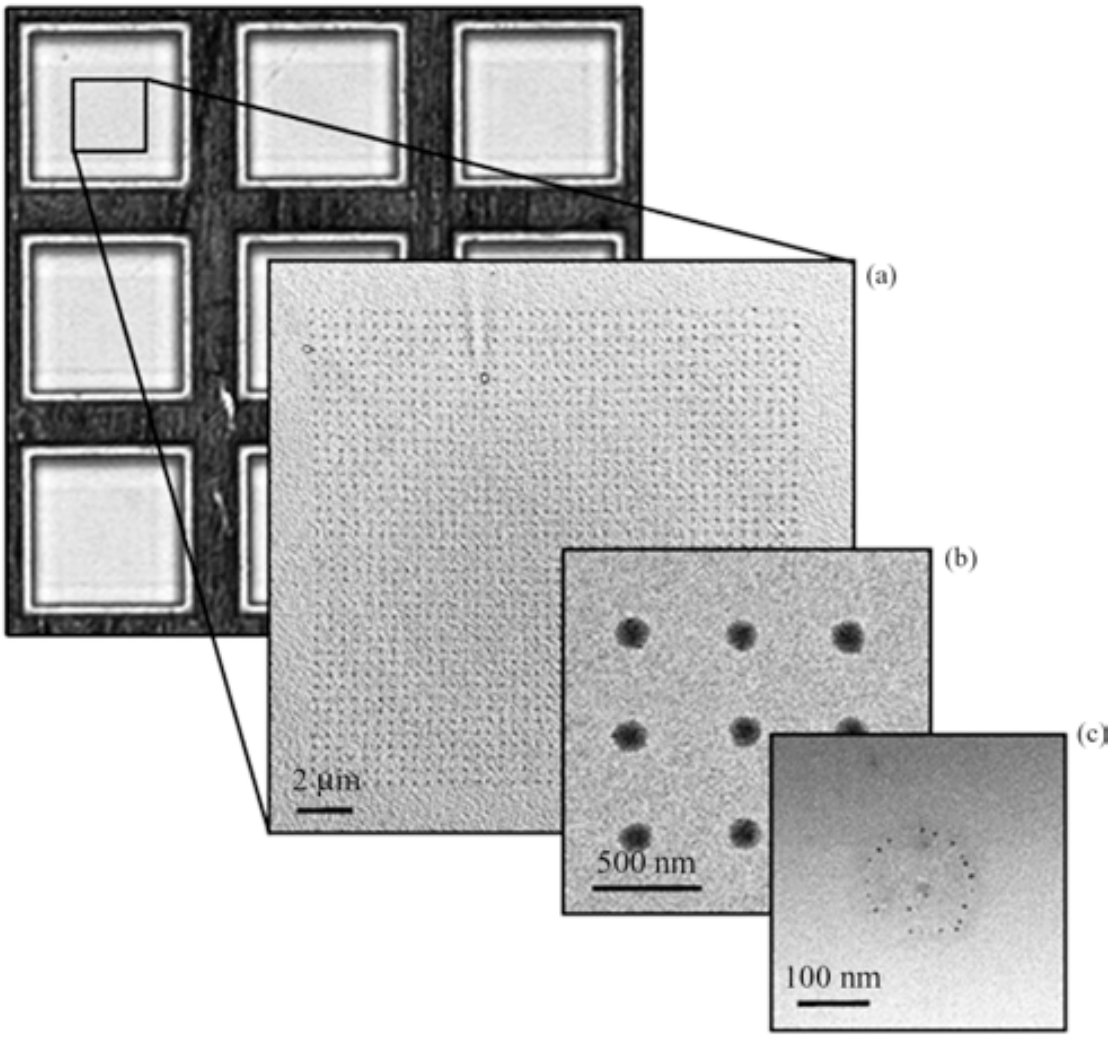

Figure 3.15 TEM images of representative ferritin array fabricated on a carbon-coated TEM grid. The array consists in 40 × 40 uniform dots separated a distance of 500 nm and with a dot average size of 150 ± 4 nm. Different magnification views of the same array are given.

Transferral of the ferritin entities takes place through the tip that dispenses less than a femtoliter droplet of the protein solution onto the surface. Then, the number of ferritin entities (n) located in the droplet, which will be the final amount of particles placed on the resulting dot-like feature after solvent evaporation, is given by

$$n = \frac{V \cdot C \cdot N_A}{M_W} \qquad (3.1)$$

where V is the volume of the delivered droplet in liters, C is the concentration of the initial ferritin solution used to coat the tips in $g \cdot L^{-1}$, N_A is the Avogadro number and Mw is the molecular weight (900000 $g \cdot mol^{-1}$ for a complete ferritin).[278] Then, assuming that a nanosized

droplet delivered on a surface can be considered as a sessile droplet with a spherical cap geometry,[279] the droplet volume is expressed as

$$V = \frac{\pi \cdot \left(r_b \cdot 10^{-8}\right)^3}{3} \cdot \left(\frac{2 - 3\cos\theta + \cos^3\theta}{\sin^3\theta} \right) \qquad (3.2)$$

where θ is the contact angle in º, and r_b is the contact radius in nm. Now, replacing all these values, including the ferritin concentration initially used to coat the tips (55.2 g·L^{-1}), allows for Equation (3.1) to be written as

$$n = 3.868 \cdot 10^{-5} \cdot r_b^{\,3} \cdot \left(\frac{2 - 3\cos\theta + \cos^3\theta}{\sin^3\theta} \right) \qquad (3.3)$$

Thus, the number of ferritin entities deposited on each dot-like feature generated by the coated tip for a given ferritin concentration depends on the contact radius and the contact angle. Even though the contact radius was easily determined by TEM, it was not the same situation for contact angle. Typically, this value is obtained using a goniometer instrument which routinely determines the contact angle for droplets of few microliters. The study of even smaller droplets with sizes at the (sub)micrometer range, which correspond to volumes of femtoliter or smaller, is experimentally difficult since it requires the use of instruments with nanometric resolution.[280, 281] In this sense, the use of these high resolution techniques evidenced that the measured contact angle remains the same for droplets with sizes down to few nanometers.[280] The main problem arises since the measurement of the contact angle using the goniometer requires substrate areas large enough to accommodate a microliter droplet on top. However, carbon-coated TEM grids have small accessible areas, which makes unfeasible to perform the measurement and significantly hampered the resolution of Equation (3.3).

In this context, we decided to design an alternative experiment in order to obtain the contact angle parameter. A series of arrays of 10 × 10 dots that varied in diameter were systematically created on carbon-coated TEM grids under the same experimental conditions described above by controlling tip-substrate contact time and ink depletion. From these arrays, eleven arrays with diameters ranging from 50 to 300 nm (in 25 nm increments) were studied. For each array, at least 35 different dots were then randomly selected and individually imaged by TEM, and the number of ferritin entities placed on each one of these dots was counted (see **Figure 3.16** to **Figure 3.20**).

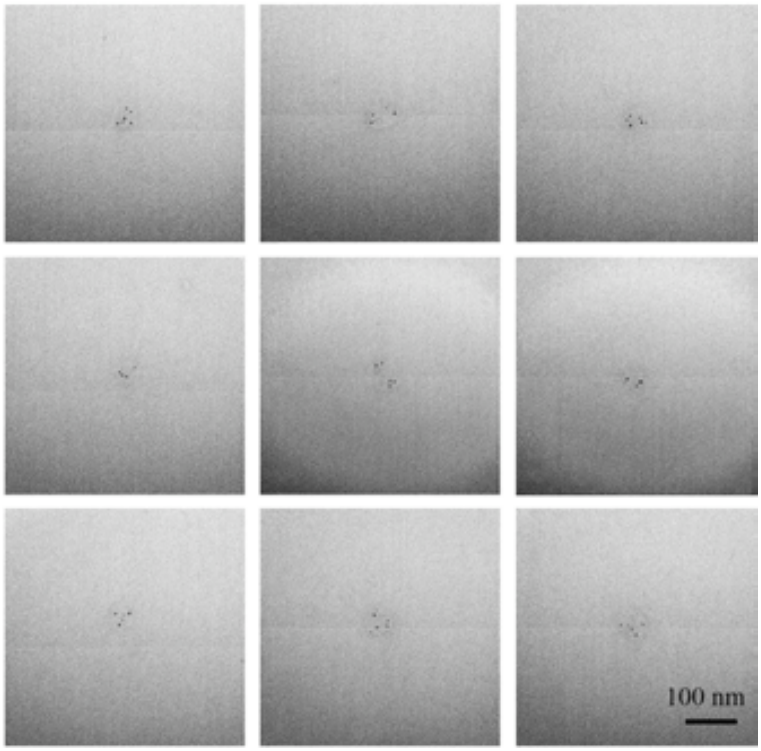

Figure 3.16 TEM images of representative 50 nm in diameter dots fabricated on a carbon-coated TEM grid.

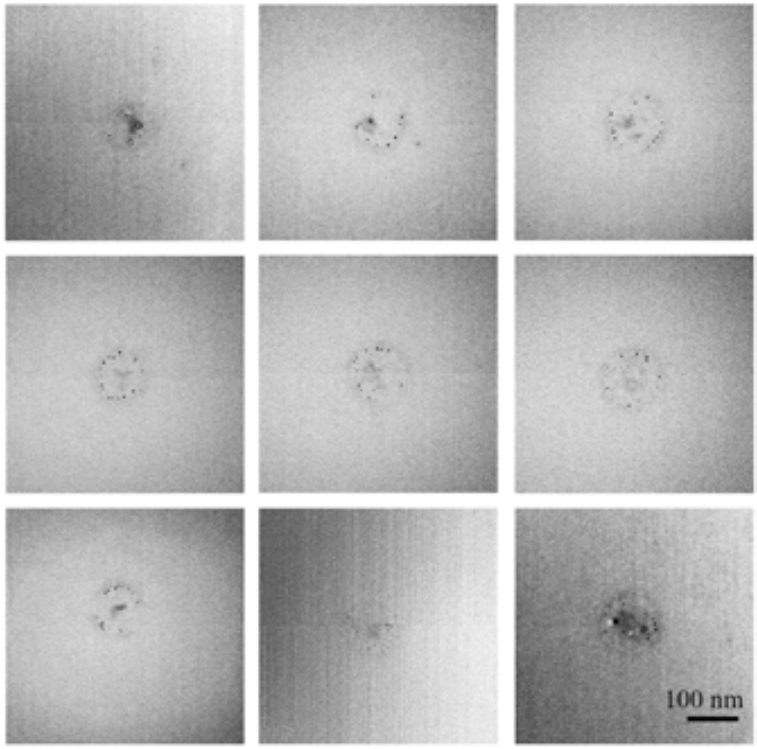

Figure 3.17 TEM images of representative 100 nm in diameter dots fabricated on a carbon-coated TEM grid.

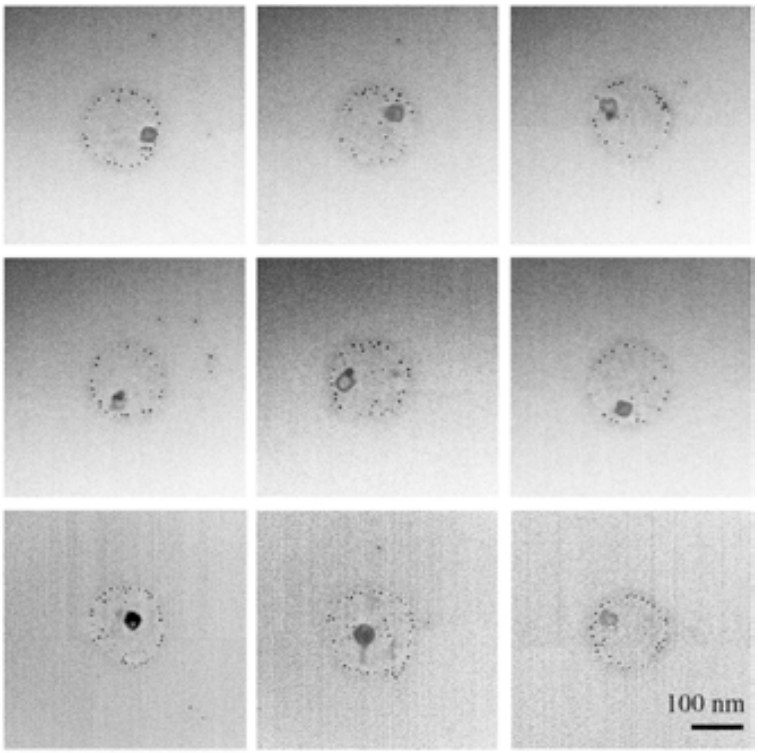

Figure 3.18 TEM images of representative 150 nm in diameter dots fabricated on a carbon-coated TEM grid.

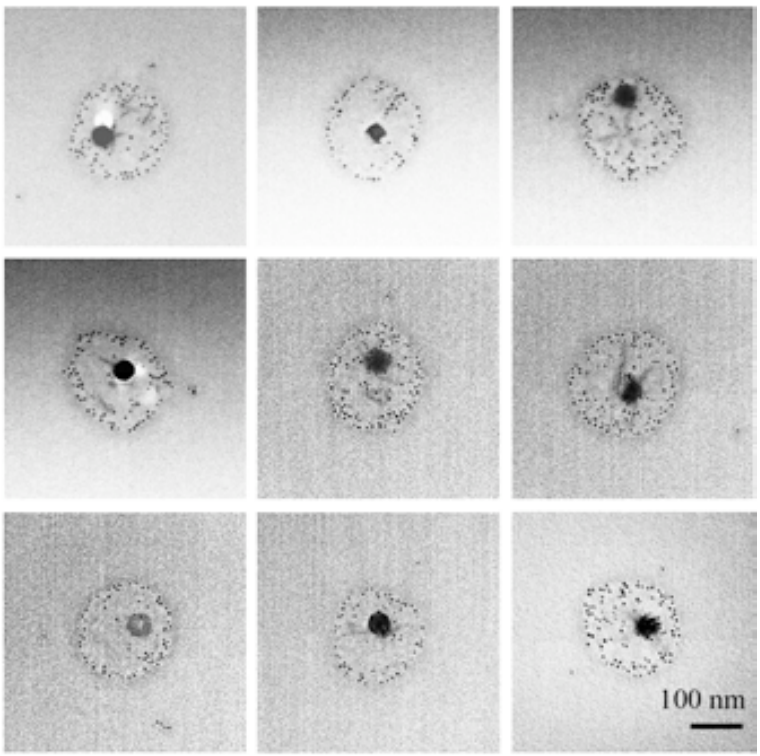

Figure 3.19 TEM images of representative 200 nm in diameter dots fabricated on a carbon-coated TEM grid.

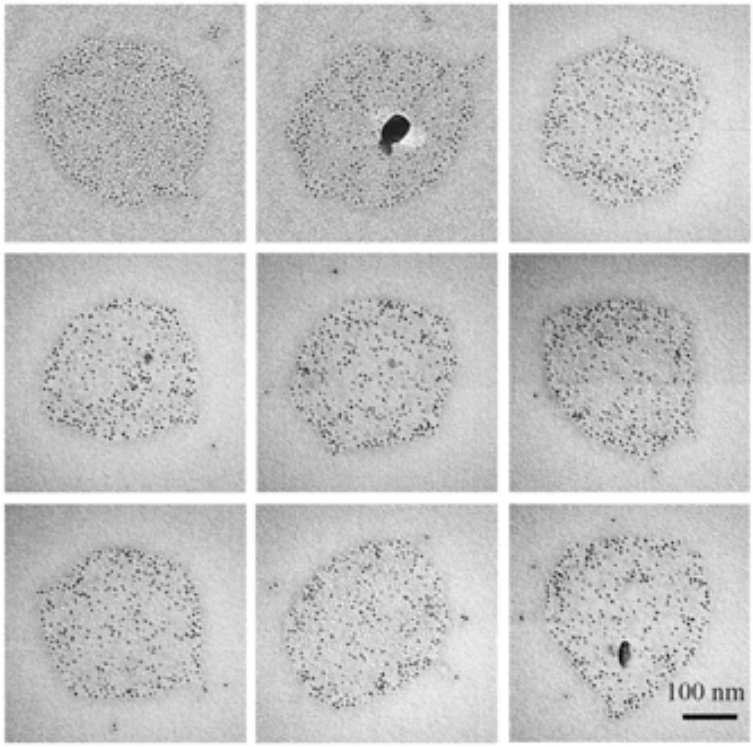

Figure 3.20 TEM images of representative 300 nm in diameter dots fabricated on a carbon-coated TEM grid.

From Figure 3.16 to Figure 3.20 the presence ferritin proteins in all the dot-like structures are clearly observed and the diameter of the dots is distinguished. In addition, the tendency of ferritin to organize as (sub)monolayer on each dot is evidenced, in good agreement with previous results obtained by AFM characterization studies (see Section 3.2.1). Also, ferritins present a non-uniform distribution over the dot area and preferentially arrange at the circular edge of the dot. The reason is that of coffee-stain phenomena.[282] Due to the surface to volume ratio is larger near the edge of the droplet, the evaporation leads to a flow of liquid which transports material from the center towards the edge, where it accumulates. This occurs because the contact line remains pinned during the drying process and induces that the liquid evaporation from the edge is replenished by liquid from the interior. Let us note that even ferritin become concentrated at the edges of the dot, they still maintaining a (sub)monolayer distribution and no multilayered assemblies were observed in any case.

In these experiments, a black spot inside the dot structures was observed in some cases by TEM (see Figure 3.18 to Figure 3.20). In order to identify the nature of these black spots, we investigated them by EDX (**Figure 3.21**). The presence of Na and Cl elements in combination with the pattern observed by selected-area electron diffraction (SAED) (Figure 3.21c,d) confirmed that the black spots consisted in NaCl crystals formed from the salts present into the original saline solution in which ferritin particles were dispersed into.

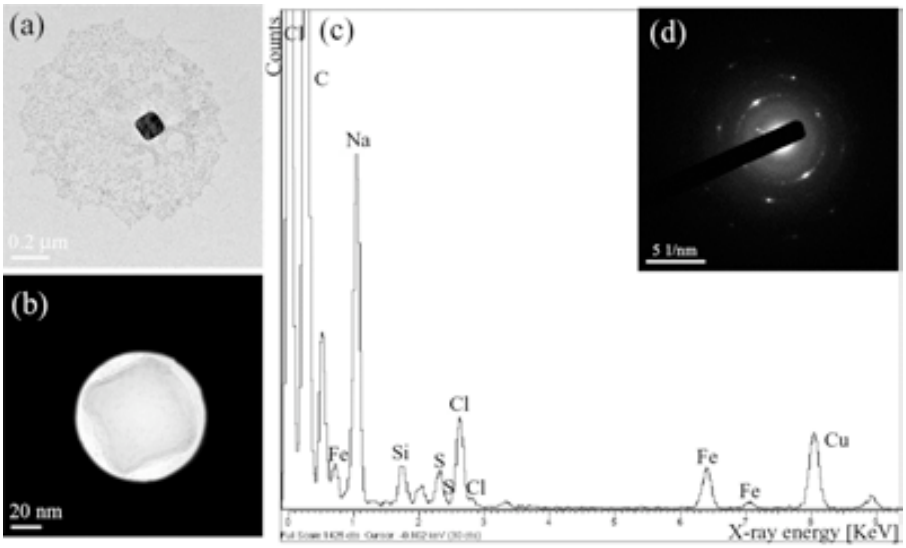

Figure 3.21 (a) TEM image of a representative ferritin-based structure fabricated on a carbon-coated TEM grid. (b) Reduced area focused on the black spot shown in panel **a** on which electron diffraction was performed. (c) EDX spectrum showing the Na and Cl peaks of the black spot in the dot structure shown in panel **a** and **b**. (d) Electron diffraction pattern obtained from the black spot in panel **a**.

From this study, we plot the average number of ferritin particles as a function of the dot radius, as shown in **Figure 3.22**. The average number of ferritin particles found in the 50, 75, 100, 125, 150, 175, 200, 225, 250, 275, and 300 nm diameter dots was 4.9 ± 0.3, 8.4 ± 1.1, 13.2 ± 1.1, 18.6 ± 1.6, 31.7 ± 3.1, 54.2 ± 6.3, 91.6 ± 7.6, 130.2 ± 7.3, 196.0 ± 8.4, 251.9 ± 10.0, and 300.1 ± 9.5, respectively. As expected, with larger dot diameters, the number of ferritin entities increased. Moreover, since this increase follows a third-order growth, we can fit our experimental data to Equation (3.3) *via* iterative fitting process. On the basis of the fitting results, we found a contact angle value of 89.8 º for the ink solution on carbon-coated TEM grids. Let us note that beyond the use of contact angle for developing Equation (3.3), this parameter also gives information about the ink solution-substrate affinity.

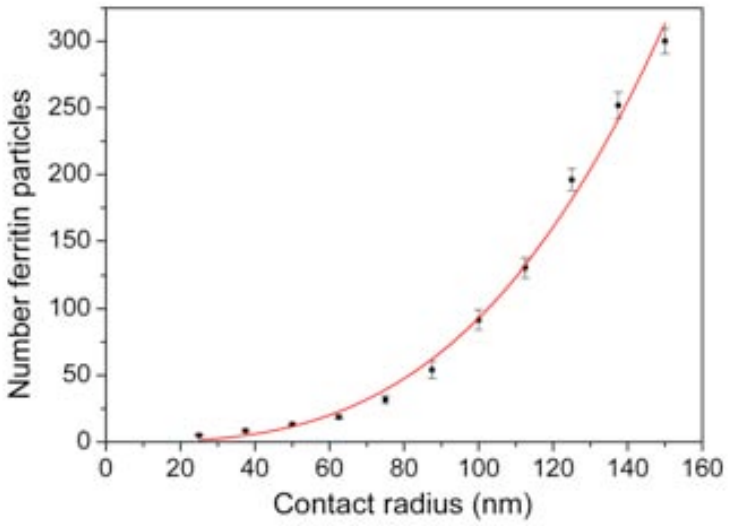

Figure 3.22 Average number of ferritin particles (n) as a function of the contact radius parameter (r_b). The line corresponds to the best fit of the data to Equation (3.3).

By introducing the constant values of the molecular weight, the Avogadro number, and the contact angle to Equation (3.1), we can determine that the number of ferritin particles finally depends on two experimental factors: the concentration of the ferritin solution used to initially coat the tips and the dimensions of the dot-like features generated by direct-write AFM lithography.

$$n = 1.389 \cdot 10^{-6} \cdot C \cdot r_b^{\,3} \qquad (3.4)$$

One of the major advantages of direct-write AFM lithography is its ability to control the dimensions of the dot-like features by adjusting the tip–substrate contact time and ink depletion, as already commented in Section 3.2.1. Fixing these dimensions, one can then start to conceive controlling the number of ferritin entities by simply varying the ferritin concentration of the initial ink solution.

This hypothesis was accurately confirmed by the experiments shown in **Figure 3.23**. By considering the dot-like features with a diameter of 150 nm, we fabricated arrays in which the average number of ferritin particles placed on each dot-like feature was very close to 10 and 5 units. Under these conditions, the theoretical ferritin concentrations needed to immobilize these particular amounts of protein entities can be easily obtained from Equation (3.4). The calculated values for immobilizing 10 and 5 ferritin entities on each dot-like feature are 17.1 $mg \cdot mL^{-1}$ and 8.5 $mg \cdot mL^{-1}$, respectively. In order to minimize the influence of other parameters, both solutions containing such ferritin concentrations were prepared by diluting the initial ferritin solution (69.0 $mg \cdot mL^{-1}$) with PBS solution and 20 % (v/v) of glycerol. Ferritin arrays of 150 nm in diameter dots were then prepared by using the same methodology and only changing the initial ferritin concentration used to coat the tips. Again, at least 35 different dots for both arrays were randomly selected and individually imaged by TEM, and the number of ferritin entities placed on each one of these dots was counted. Interestingly, the average number of ferritin entities found for both ferritin concentrations, 17.1 $mg \cdot mL^{-1}$ and 8.5 $mg \cdot mL^{-1}$, was 10.5 ± 1.5 and 4.9 ± 1.4, respectively.

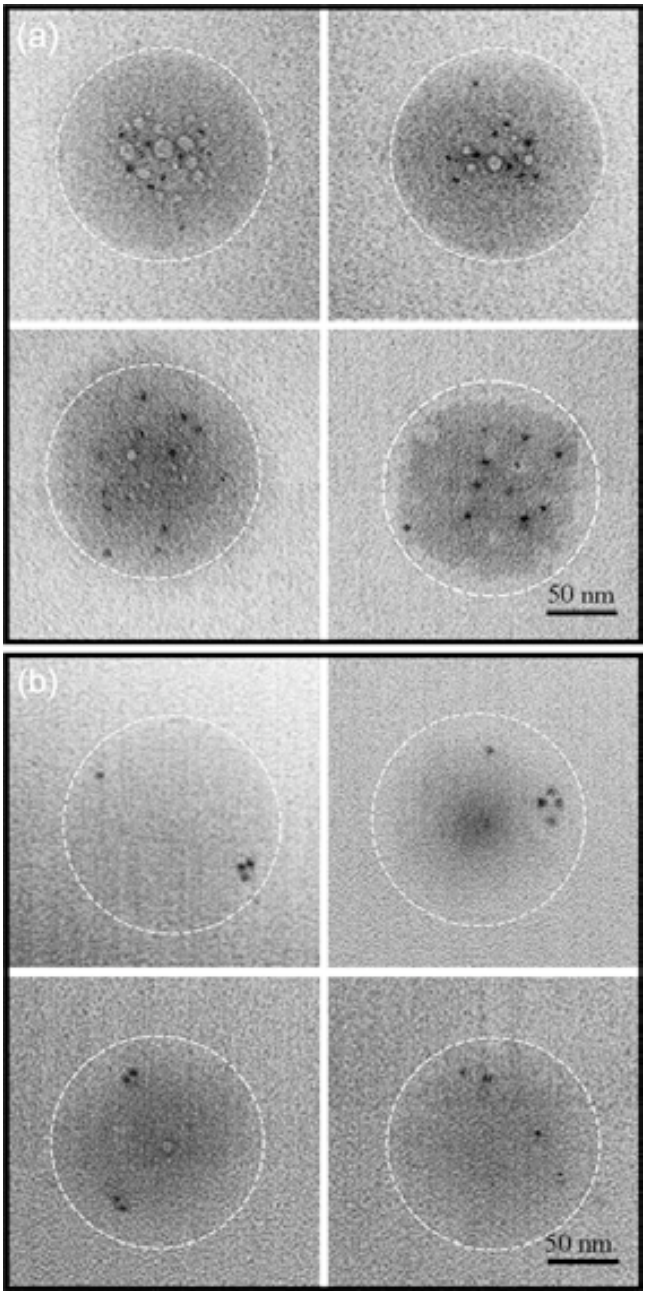

Figure 3.23 TEM images of dot-like features 150 nm in diameter generated on a carbon coated TEM grid using a ferritin concentration as ink solution to coat the tips of (a) 17.1 mg·mL^{-1} and (b) 8.5 mg·mL^{-1}. The dot area is indicated with a dashed white line.

All of the data presented thus far point to the ability to modulate the number of ferritin entities deposited on surfaces by direct-write AFM lithography, a capability that becomes crucial if one wants to control the deposition of nanoparticles on surfaces at the single particle level. To evaluate such ultimate capability, we fabricated arrays of 10 × 10 dots with an average diameter of 150 nm, with the aim of depositing an individual ferritin particle on each one of these dots. From Equation (3.4), the theoretical value of the ferritin concentration needed to deposit a single ferritin particle is 1.7 mg·mL^{-1}. Similar to the above-mentioned experiments, a solution of 1.7 mg·mL^{-1} of ferritin, which was prepared by diluting the initial ferritin solution with PBS solution and 20 % (v/v) glycerol, was used as the ink solution to fabricate the arrays made of

dots with diameter of 150 nm. One of these arrays was then randomly selected, and all dot-like features were individually imaged by TEM (**Figure 3.24**).

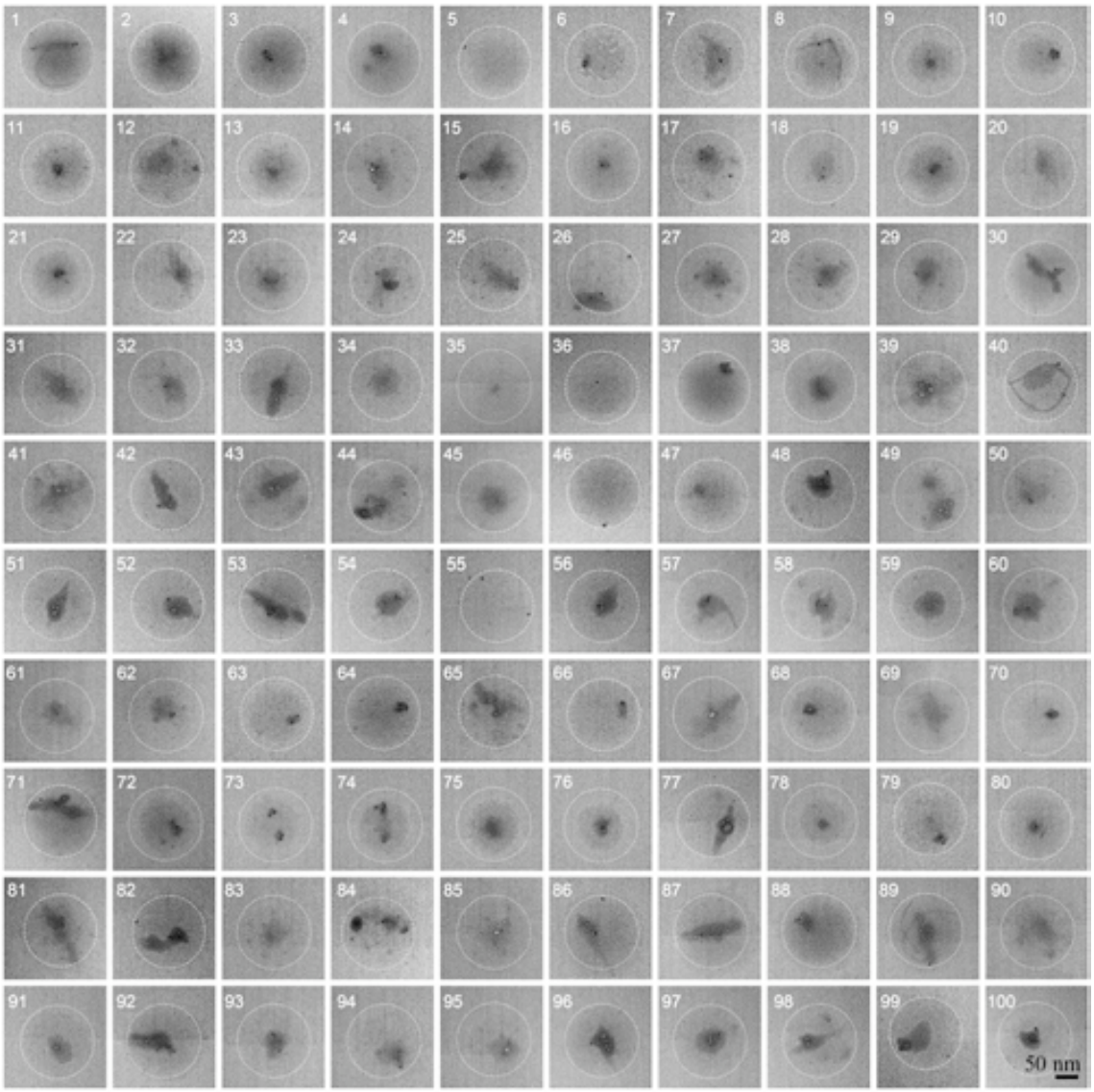

Figure 3.24 TEM images of individual 150-nm in diameter dots from a 10 × 10 array fabricated on a carbon-coated TEM grid using a ferritin concentration of 1.7 mg·mL^{-1} in order to deliver an average of one single ferritin particle inside each one of the dots.

From these one hundred images, it is possible to determine that the average number of ferritin particles placed on each dot-like feature, considering the whole array, is 1.4 ± 1.2, and that the number of dot-like features that contain a single ferritin particle is 36, whereas 25, 22, 11, and 6 of these dot-like features contain zero, two, three, and four ferritin particles, respectively (**Figure 3.26**). Interestingly, none of these dot-like features show more than four ferritin particles.

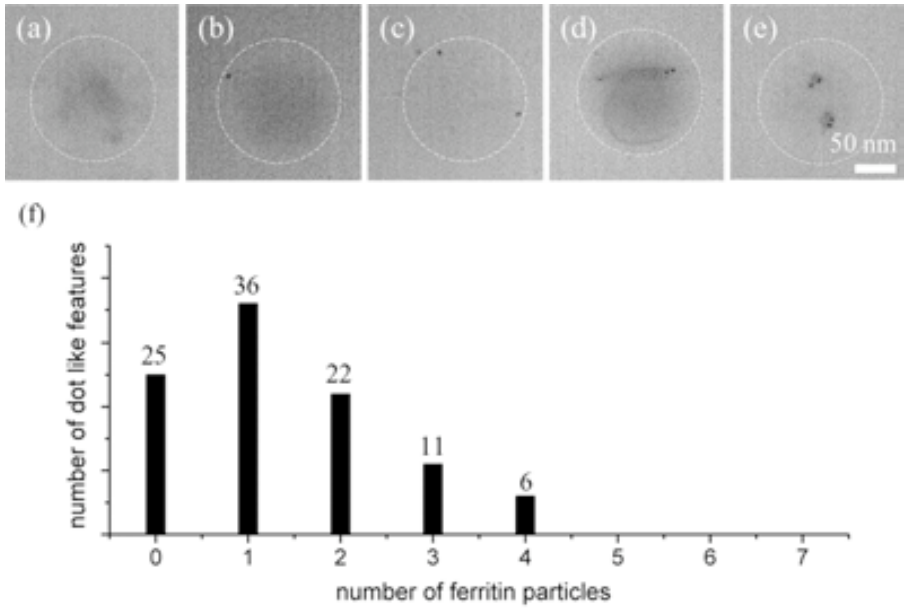

Figure 3.26 TEM images of representative 150 nm dots from the 10 x 10 array shown in Figure 3.25 fabricated on carbon-coated TEM grid and using a ferritin concentration of 1.7 mg·mL^{-1} that contain: (a) zero ferritins, (b) one ferritin, (c) two ferritins, (d) three ferritins and (e) four ferritins per dot. (f) Number of dot-like features from the array considered in the study as a function of the number of ferritin entities present in each dot.

In summary, we have demonstrated that direct-write AFM lithography can be used to control the number of ferritin entities immobilized on surfaces. We have shown that if one knows the contact angle between the ink protein solution and the substrate, and by selecting the initial protein concentration and the dot size, the number of ferritin entities deposited on a dot-like feature can be controlled. Such novel capability opens new opportunities to control the number as well as the organization of ferritin particles on sensors and devices.

3.3 Integration of ferritins into sensors by direct-write AFM lithography

In the previous sections we have demonstrated the controlled deposition of ferritin entities onto a wide variety of surfaces. In addition, the ability to modulate the average number of ferritin entities deposited on each structure fabricated on carbon-coated TEM grids has been demonstrated. All these results provide an excellent background in order to develop a novel strategy for the controlled integration of such entities into well-defined locations of hundreds of micrometers of sensors, such as microSQUIDs, *via* direct-write AFM lithography technique.

The sensor used for these studies forms part of a generation of microSQUID susceptometers recently developed by Dr. J. Sesé, Dr. F. Luis and Dr. M. J. Martínez-Pérez at INA and ICMA, in collaboration with Dr. D. Drung and T. Schurig from the Physikalisch-Technische Bundesanstalt (PTB). The sensor consists of four primary coils connected in series that create the exciting magnetic field and four pickup (sensing) coils connected in parallel in a

gradiometric design that couple the sample response directly to the front-end dc SQUID. These Nb coils are rectangular shaped with approximate dimensions of 63 μm × 250 μm. The pickup coils are covered with a 250 nm-thick layer of layer of SiO_2, and finally the primary Nb coil lies on top exactly matching the pickup coil geometry. The pickup coils couple no net flux to the SQUID due to their gradiometric design, unless a magnetic sample is placed onto one of them (as shown in **Figure 3.27**a). The susceptometer provides a signal proportional to the susceptibility of a magnetic sample located within the pickup coils, that is, to the magnetic moment induced in the sample by the field created by the primary coil (a more detailed description of the sensor used in this study is given in Experimental Section 7.4).

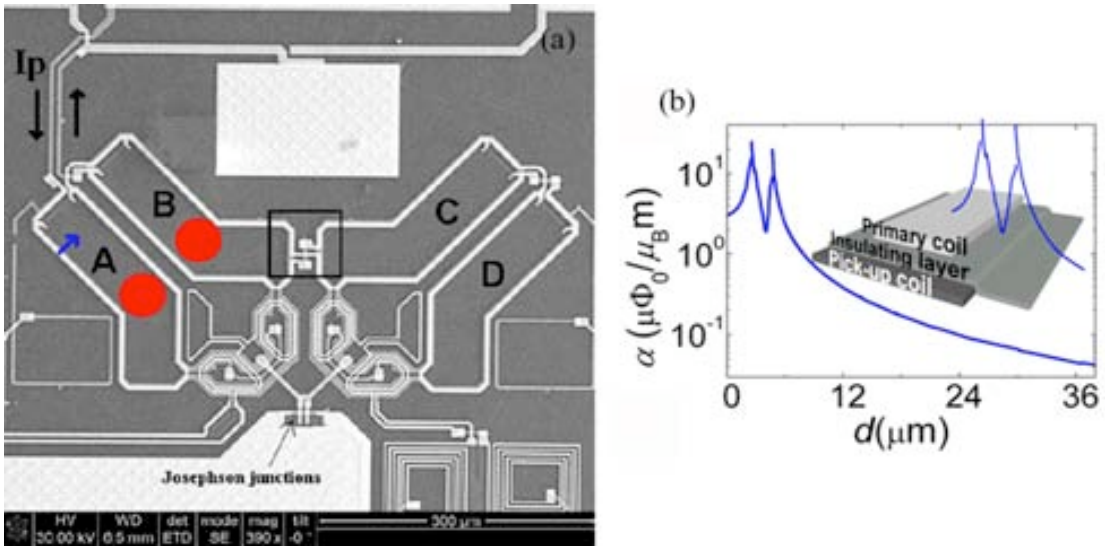

Figure 3.27 (a) SEM image of the microSQUID showing the four rectangular shaped pickup coils A, B, C and D which correspond to the sensitive areas of the sensor. The sample to be measured can be located on either the left side (A and B areas), wherein as an example a sample is placed indicated with a red circle, or the right side (C and D). (b) Numerical calculations of magnetic flux coupling factor α as a function of the distance from the center of the pickup coil wire towards the center of the coil (indicated in panel **a** with a blue arrow). The inset shows a 3-D cross section of the pickup and primary coil wires, where the profile has been superimposed. Reproduced from ref.[283].

Dr. M. J. Martínez-Pérez and co-workers identified the most sensitive areas of the pickup coils by calculating the magnetic flux $\phi_{coupled}$ generated by a sample located at a particular position (for more information about this calculations see Experimental Section 7.4). They found that the most sensitive ("active") areas of the sensor corresponded to the coil wire edges of the pickup coil (Figure 3.27b). Therefore the integration must take place preferably in these areas of the sensor.

3.3.1 Controlled integration of ferritins into the active areas of a microSQUID sensor

For this, a ferritin derivative synthesized and characterized by Dr. A. Lostao and R. de Miguel at INA was chosen. The sample consisted of ferritin displaying a CoO core ~ 2 nm in diameter (referred to as CoO@apoferritin), shown in **Figure 3.28**. (A detailed description of the synthesis

as well as characterization of the sample can be found in Experimental Section 7.1). The CoO NPs that presents a magnetic moment ~ 12 μ_B, close to that of a typical single molecule magnet (SMM),[18] do not exhibit blocking of the magnetic susceptibility down to 1.8 K (the minimum temperature reached in preliminary experiments with the bulk sample using a commercial SQUID magnetometer, see Experimental Section 7.1).[283]

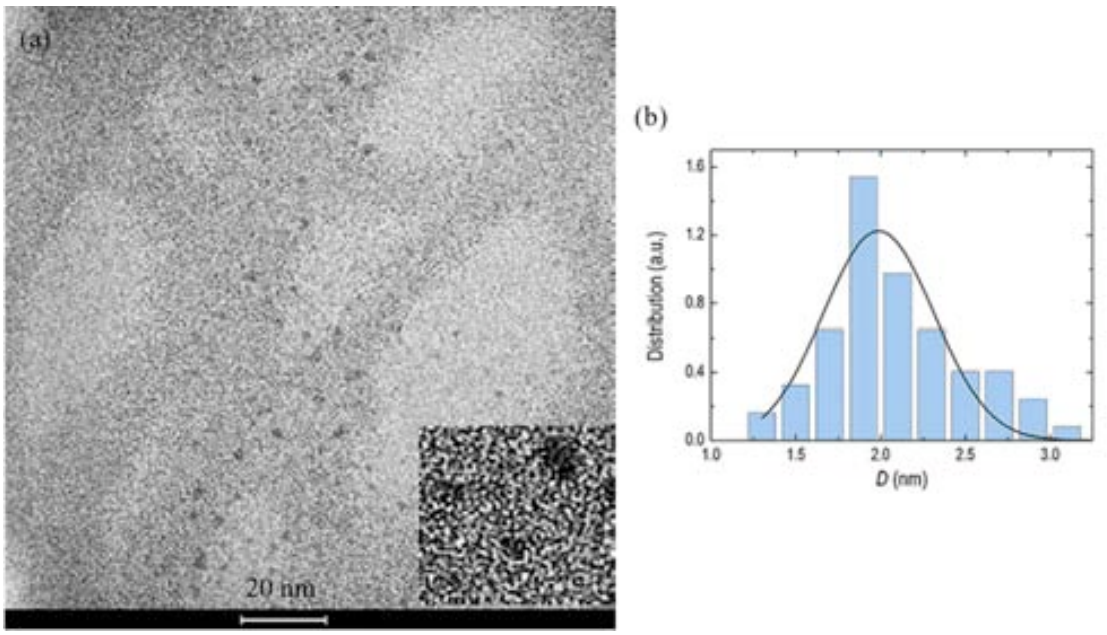

Figure 3.28 (a) TEM image of a CoO@apoferritin sample used in this work. Black spots correspond to the CoO core. The inset (10 × 21 nm) is a magnification view. (b) Particle size distribution of the CoO@apoferritin sample obtained from the analysis of the TEM images. The solid line is the Gaussian fit showing an average diameter of D = 2.0 nm and variance σ = 0.32. Images obtained by R. de Miguel.

The magnetic ink solution used for this study was prepared by dissolving the lyophilized CoO@apoferritin in PBS solution containing a 20 % (v/v) of glycerol (55.2 mg·mL^{-1} corresponding to ~ 6.9·10^{16} ferritin entities·mL^{-1}). First of all, the microSQUID surface was cleaned by carefully washing it with ethanol and acetone, and dried by blowing nitrogen gas before ferritin deposition. It is important to notice that this was an extremely crucial step in the process, since the presence of contaminants on the surface significantly affected the writing process. This contamination was mainly due to the previous manipulation of the sensor in order to measure with the same microSQUID the bulk sample.

All the deposition procedure was carried out under the same experimental conditions described in previous sections for the deposition of ferritin proteins by direct-write AFM lithography. The main difference is that in this case a single MP tip of the cantilever array was used. The ferritin deposition took place by dispensing femtoliter droplets of the protein solution onto the specific regions of the pickup coils. For this, we pre-designed a pattern in order to ensure that the deposition took place onto the active areas of the sensor. The pattern consisted of three rows of dots separated by 4 μm on the pickup coils labeled 3 and 4 in **Figure 3.29**a. The other two pickup coils labeled 1 and 2 must remain unmodified for a proper background signal. The first row was deposited on the primary coil, and the other two were deposited on the SiO_2 layer by

traversing the soaked tip over the surface in the form of the designed pattern towards the center of the coil, as depicted in Figure 3.29b-d.

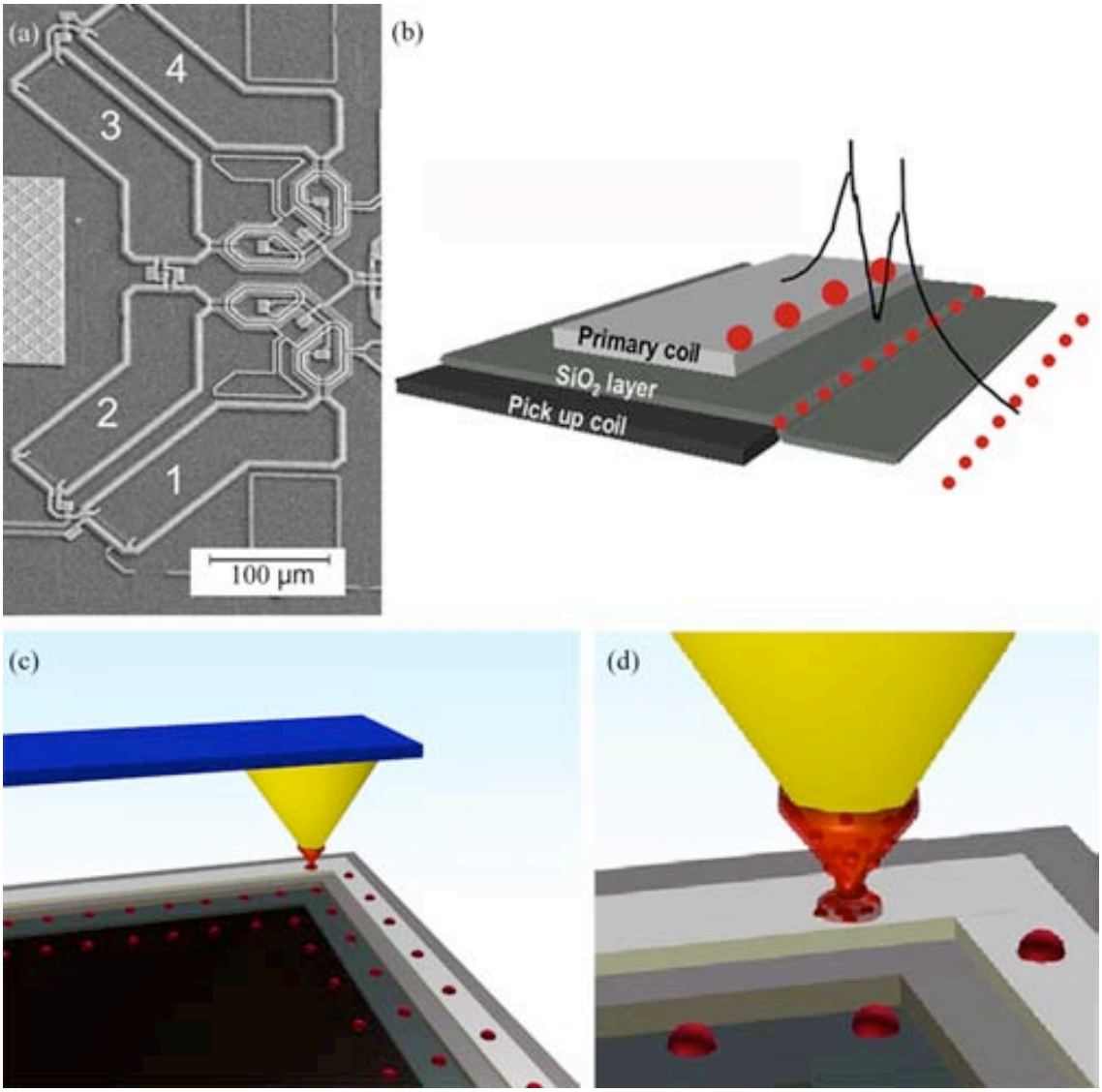

Figure 3.34 (a) SEM image of the SQUID showing the four rectangular-shaped pickup coils with effective areas of 63 µm × 250 µm. (b) 3-D cross section of the pickup and primary coil wires, a profile of the most sensitive areas has been superimposed. The red circles correspond to the pattern pre-designed for the deposition of ferritin. (c, d) Schematic illustration of the deposition of ferritin following the pre-designed pattern on the most sensitive areas of the sensor by direct-write AFM lithography.

Note that the dimensions of the rectangular-shaped coils were 63 µm × 250 µm. Such dimensions are larger than those of the piezo scanner that controls the relative movement of the tip with respect to the sample (90 µm × 90 µm) in Nscriptor™. Therefore, to overcome these limitations and cover the full perimeter of both coils, it was necessary to induce, after each patterning step, an X-Y stage translation that relocates the tip over different coil areas separated by more than 90 µm × 90 µm. Such translation was controlled by the software and optically controlled with the coupled camera, as can be seen in **Figure 3.35**.

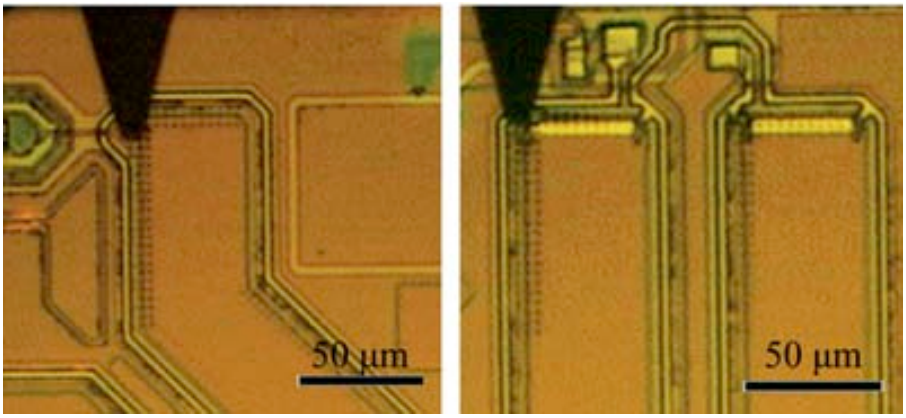

Figure 3.35 Optical images captured during the CoO@apoferritin writing by direct-write AFM lithography along the perimeter of the pickup loop.

The excellent results obtained with the deposition process are shown in **Figure 3.36**. FE-SEM characterization revealed the high precision achieved in positioning the dots exactly at those positions for which a maximum sensitivity was theoretically predicted while maintaining the rest of the SQUID sensor area unmodified. AFM characterization of the sensor allowed to confirm the (sub)monolayer distribution of ferritin inside each one of the dot of the array, however the visualization of the dots was quite difficult due to the topography of the coil wires (Figure 3.36d).

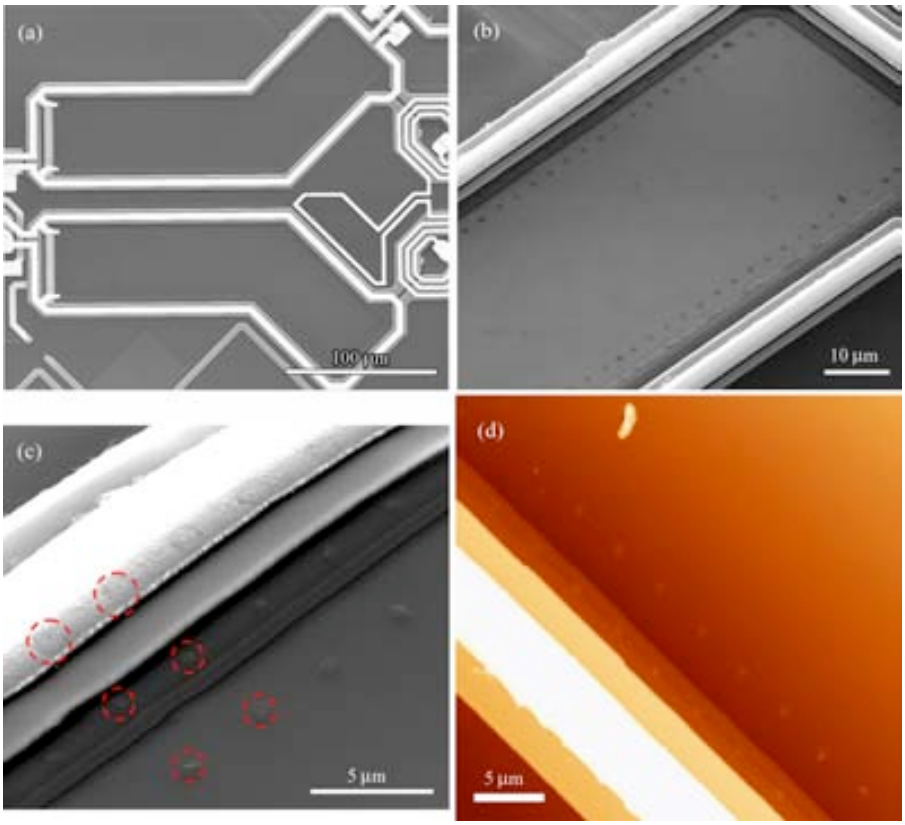

Figure 3.36 (a-b) FE-SEM image of the microSQUID sensor right after the deposition of CoO@apoferritin as three arrows of dots along the pickup coil. (c) Magnification view of the same sensor on which some of the dots are highlighted with red dashed circles. Image **b** and **c** are viewed at a 45 º tilt angle. (d) AFM topography image of the array of dots integrated into the microSQUID sensor.

The dots dimensions were measured by AFM on the microSQUID as well as on arrays deposited on bare Si/SiO_2 and Nb/Nb_2O_5 substrates fabricated under identical conditions (**Figure 3.37 a,b**). Average diameters of 1.3 ± 0.1 μm and 1.8 ± 0.1 μm for Si/SiO_2 and Nb/Nb_2O_5 substrates respectively, were found. The height profile of the arrays shows average dot height of 11 ± 1 nm in both cases (Figure 3.37 c,d), which is close to the size of a single protein (ca. 12 nm), thus showing that ferritin organized as (sub)monolayers on each dot.

The number of the ferritin entities located on the droplets deposited with the tip was estimated based on geometrical considerations. The average dot area for the dots generated on Si/SiO_2 and Nb/Nb_2O_5 was estimated from the average dot diameter measured by AFM to be 1.3 μm^2 and 2.5 μm^2, respectively. Considering that the area occupied by a ferritin is 113 nm^2 and considering a densest packing of identical spheres organized in a plane (hexagonal packing arrangement), with a packing density of 0.9069, the maximum number of ferritins that can be organized as monolayer on a 1.3 μm and 1.8 μm in diameter dot is around 10^4 and $2 \cdot 10^4$, respectively. Therefore, taking into account that the estimated number of ferritin entities deposited on the dots generated on the SiO_2 and Nb/Nb_2O_5 of the sensor is ~ 10^4 and ~ $2 \cdot 10^4$ respectively, and considering the number of dots deposited on the sensor, the estimated total number of CoO@apoferritin units over the pickup coils was about ~ 10^7.

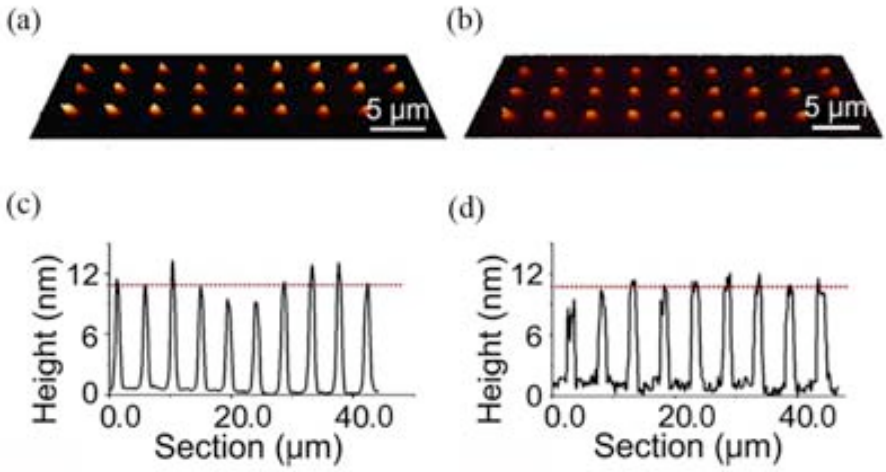

Figure 3.37 Arrays of CoO@apoferritin fabricated by direct-write AFM lithography on (a) Si/SiO_2 and (b) Nb/Nb_2O_5 substrates. (c, d) Height profile of one of the dot lines of the arrays shown in panel **a** and **b**, respectively.

Once the controlled integration of CoO@apoferritin onto the most sensitive areas of the microSQUID sensor was achieved with a high success, Dr. M. J. Martínez-Pérez and Dr. F. Luis from the ICMA performed the magnetic measurements.[283, 284] The large coupling between the CoO@apoferritin dots and the microSQUID enabled the measurement of the ac magnetic susceptibility of the structured sample down to T = 13 mK (see Experimental Section 7.4), as shown in **Figure 3.38**. Below 400 mK, a temperature dependent in-phase component signal (χ') shows up above the background signal of the bare sensor (previously measured and already subtracted in Figure 3.38).

Above approximately 100 mK the particles remain on a superparamagnetic state arising from antiferromagnetic interactions between the cobalt ions, with a T_N around 122 K. Below 100 mK

the in-phase susceptibility of the array presents a maximum which depends on frequency, showing the existence of a thermally activated spin reversal. This process is associated to the blocking of the relaxation on a similar manner as later on described for the Mn_{12} sample (*vide infra*). Curiously enough, the magnetic measurements performed on the array differ from the bulk sample in the sense that the latter show no clear maxima above 13 mK and seem to be "shifted" to lower temperatures below ~ 100 mK. The thermal shift was ascribed to a different thermalization of both samples with the He bath. In the array, with its larger contact area to volume ratio, the molecules can properly thermalize with the surrounding He bath. In contrast, the actual temperature of the bulk sample could stay above that of the He bath (and thermometer), therefore not reaching the blocking temperature. In this sense, Dr. M. J. Martínez-Pérez and co-workers realized that the data of the bulk sample can be made equal to those of the array by shifting them along the temperature axis. This interpretation is supported by the fact that the bulk susceptibility is shifted with respect to that of the array already at 200 mK, when susceptibility is nearly independent of frequency and therefore relaxation mechanisms should not influence its temperature dependence. This analysis suggests that patterning molecular samples, with low thermal conductivities, can provide a good method to investigate their magnetic properties down to the neighborhood of the absolute zero, when thermalization effects become a crucial issue.

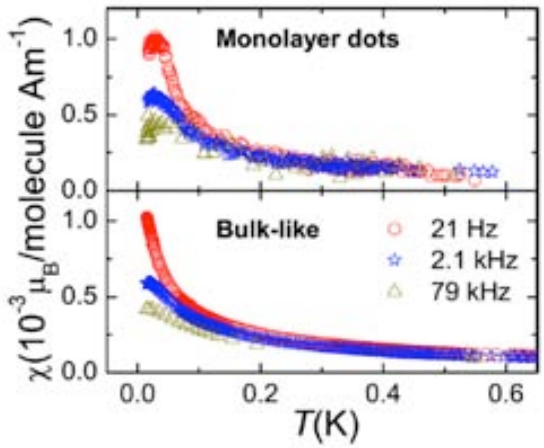

Figure 3.38 Top panel: in-phase ac magnetic susceptibility of ~ 10^7 CoO@apoferritins arranged as a (sub)monolayer. The out-of-phase component lies below the sensitivity limits of detection and it is therefore not shown. Bottom panel: in-phase susceptibility of ~ 10^{-3} mg of CoO@apoferritin (corresponding to ~10^{12} units). Data obtained by Dr. M. J. Martínez-Pérez and co-workers.

3.4 Summary

In this work we have demonstrated the unique capabilities of direct-write AFM lithography for the controlled structuration and integration of ferritin proteins on surfaces and sensors. The deposition strategy implies no chemical functionalization neither of the ferritin entities nor the substrate surface. First, the structuration of ferritin on a wide variety of surfaces of

technological interest, such as Si/SiO_2, Nb/Nb_2O_5 and Au, has been demonstrated. Even more interesting is the fact that ferritins deposited on each dot are organized as (sub)monolayers. The deposition method is not affected by the internal core, and therefore, the strategy can be applied to ferritins displaying different types of NPs inside its cavity. Complex patterns (i.e. array of dots separated at different distances, lines, combinatorial arrays, etc) as well as miniaturized structures down to 100 nm can be fabricated. Further heat treatment allows to selectively remove the protein shell, leaving the inorganic core on the surface while maintaining the original pattern. Experimentally demanding combined TEM and direct-write AFM lithographic techniques have also enabled us to develop a strategy to modulate the number of protein entities deposited on each dot of an array deposited on a carbon-coated TEM grid. This represents a novel approach that utilizes for first time the ability of this lithographic technique to fabricate controlled structures on carbon-coated TEM grids. In these experiments, we have demonstrated that this represents a versatile way to quantify the number of ferritin entities deposited on a dot-like feature and that this number can be controlled by knowing the contact angle between the ink protein solution and the substrate, and by selecting the initial protein concentration and the dot-like feature diameter.

Finally, we have developed a novel integration strategy for the accurate integration of ferritin proteins onto the most sensitive areas of a microSQUID, with sensing areas of 63 μm × 250 μm in size. As we had a very pretty good estimation of the number of ferritin entities deposited on the sensor, Dr. M. J. Martínez-Pérez and co-workers obtained an experimental estimation of the coupling factor and the sensitivity of the sensor.[283] Interestingly, they found that this controlled integration enhanced the experimental sensitivity by a factor of 10^2 compared with the one obtained for bulk samples, taking advantage of the maximum potentiality of these sensors. This enhanced sensitivity enabled them to directly measure the susceptibility of an array of ferritins distributed as (sub)monolayers, which shows that each ferritin entity preserves its magnetic properties after deposition.

Chapter 4

Single molecule magnet structuration and integration into second generation of microSQUIDs

In view of the interesting results obtained in the integration of ferritin proteins on the active areas of sensors by direct-write AFM lithography, we have explored in a further step the use of this lithographic technique to integrate SMMs. In particular, in this chapter we demonstrate that the integration strategy developed in the previous chapter is also suitable for controlling the deposition of SMMs into a novel generation of microSQUID sensors, whose sensing area has been reduced one order of magnitude.

In the first section we will introduce the more relevant advances towards the structuration of SMMs on surfaces. This step is necessary to know the existence of any previous example done with this technique to get knowledge out of it. Then, we will demonstrate how direct-write AFM lithography is a potential technique for the deposition of molecular materials onto well-defined locations of a given surface without the need of any previous functionalization of neither the molecule nor the substrate surface. For this, two types of molecules that exhibit SMM behavior have been studied: Mn_{12} and the ErW_{10} POM. The experimental conditions for their controlled structuration on surfaces are obtained. As an ultimate goal, we apply such acknowledge for the integration of such entities on pre-selected areas of few tens of micrometers in size. The dimensions of the sensing area of the sensor have been considerably reduced to improve its sensitivity, which in turn represents a new challenge for the idoneity of direct-write AFM lithography as an appropriate tool to integrate magnetic structures into sensors.

4.1 Introduction: Advances on structuring single molecule magnets on surfaces from solution

SMM is the family of magnetic molecules most widely studied on surfaces**.** Since their discovery in the early 1990s,[23] SMMs have been the focus of many investigations, motivated by the fact that these molecular exchange-coupled transition metal clusters show slow relaxation of the magnetization and magnetic hysteresis of purely molecular origin,[285,24] thanks to the combination of large-spin ground states and high axial magnetic anisotropy, resulting in a barrier for spin reversal.[23,25] The most thoroughly studied single molecule magnets are that comprising a dodecamanganese core, the well-known Mn_{12} family.[23, 286, 287] The first approach to deposit SMMs on surfaces was attempted by Coronado *et col*.[288,289] By making use of the Langmuir–Blodgett technique, the authors created a surfactant molecular film at the air–water interface where Mn_{12} arranged both in the form of isolated molecules or well-defined monolayers, which exhibited magnetic anisotropy depending on the orientation of the film with respect to the applied magnetic field. This fact was attributed to the preferential orientation of the complexes with their easy magnetization axis normal to the film surface. After this pioneering work, numerous experimental studies for the deposition and structuration of SMMs on different surfaces have been reported, mainly devoted to the archetypal SMM, the dodecamanganese derivatives (*vide infra*), though other promising SMM families have recently raised attention. Next a detailed revision of the main representative approaches followed is given.

4.1.1 Organizing single molecule magnets on surfaces from solution

The easiest way to assemble SMMs on a surface is by the direct deposition of a solution droplet of the target molecule and the posterior solvent evaporation (i.e., drop casting)[290, 291] or by dipping the native surface on the solution (i.e., *dip and dry*),[292, 293] whereupon pristine molecules are physisorbed *via* weak non-covalent interactions such as hydrogen bonds, ionic interactions, van der Waals forces, and hydrophobic interactions (**Figure 4.1**a).

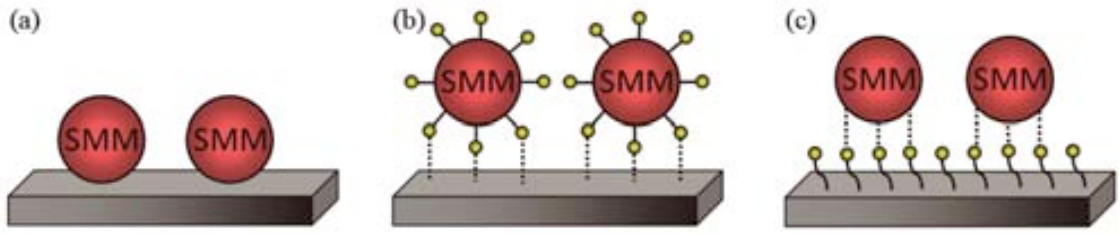

Figure 4.1 Representation of different strategies for the structuration of SMMs on surfaces: (a) SMM direct deposition on a bare surface to immobilize the SMM *via* weak non-covalent interactions, (b) pre-functionalization of SMMs with functional groups able to interact chemically with the bare surface, (c) pre-functionalization of the surface with suitable functional groups able to interact with the SMM.

To improve the absorption stability of molecular systems on surfaces and gain control on the orientation of the molecules with respect the surface,[44, 294] both SMMs and/or surfaces can be functionalized (Figure 4.1b,c). The first approach consists in the development of strategies to introduce specific functionalities (e.g. thiol and thioether groups) around the magnetic core of the molecule that favor the binding of the clusters on native surfaces (e.g. Au) without altering the SMM behavior.[32, 295-297] Another experimental approach is based on the pre-functionalization of the surface allowing for the deposition of the SMM through strong covalent ligand-exchange reactions.[290,298, 299107] Finally, a variant that combines both, the chemical modification of the surface and of the SMMs through electrostatic interactions as the driving force has also been described.[300]

4.1.1.1 *Deposition of single molecule magnets on surfaces assisted by templates and/or lithographic techniques.*

In addition to the stabilization of the interaction between the SMMs and the substrate, there is the quest to find new methodologies to organize the SMMs into small and discrete arrays of controlled dimensions and geometries. For this, different templates or lithography assisted techniques can be used to pattern the deposited molecular materials on surfaces, among which we can find (i) breath-figure templates, (ii) stamp-assisted soft lithographic techniques, (iii) focused ion beam (FIB) and (iv) EBL.

Ruiz-Molina *et col.* reported a procedure for obtaining self-assembled molecular magnetic rings taking advantage of the breath figures phenomenon (**Figure 4.2**a,b).[301] Specifically, water droplets formed upon cooling evaporation of the solvent were used as templates to arrange Mn_{12} bearing aromatic biphenyl groups by non-covalent interaction with the surface. The same breath figures phenomenon made possible the fabrication of highly ordered honeycomb structures by drop casting a solution of a Mn_{12} modified with stearic acid on glass and mica substrates at high relative humidity.[302] By changing the concentration of the Mn_{12} cluster solution, 2-D and 3-D honeycomb structures were successfully obtained.

The methods based on stamp-assisted techniques (soft lithographies) consist in grafting the SMMs by applying direct and indirect variations of the microcontact printing (μCP) technique in which an elastomeric stamp is inked with a dilute solution of the adsorbate (e.g. sulphur-functionalized SMMs or thiols) and brought in direct contact with a substrate (e.g. Au). Transfer of ink occurs only in the contact areas between the stamp and the surface. This strategy has afforded ordered Mn_{12} sulphur-derivative monolayer stripes with widths of 5 μm onto Au.[273] The chemical composition of the surface structured with the Mn_{12} derivative was verified by ToF-SIMS. The organization of such molecules into ordered structures down to the nanometer scale has been achieved using unconventional lithographic techniques.[303, 304, 305] For instance, Veciana *et col.* used a stamp-assisted deposition approach for the nanostructuration of Mn_{12} molecules bearing biphenyl groups by the confinement of a solution containing the molecules to the protruding regions of a stamp placed on top of the solution layer (Figure 4.2c,d).[303]

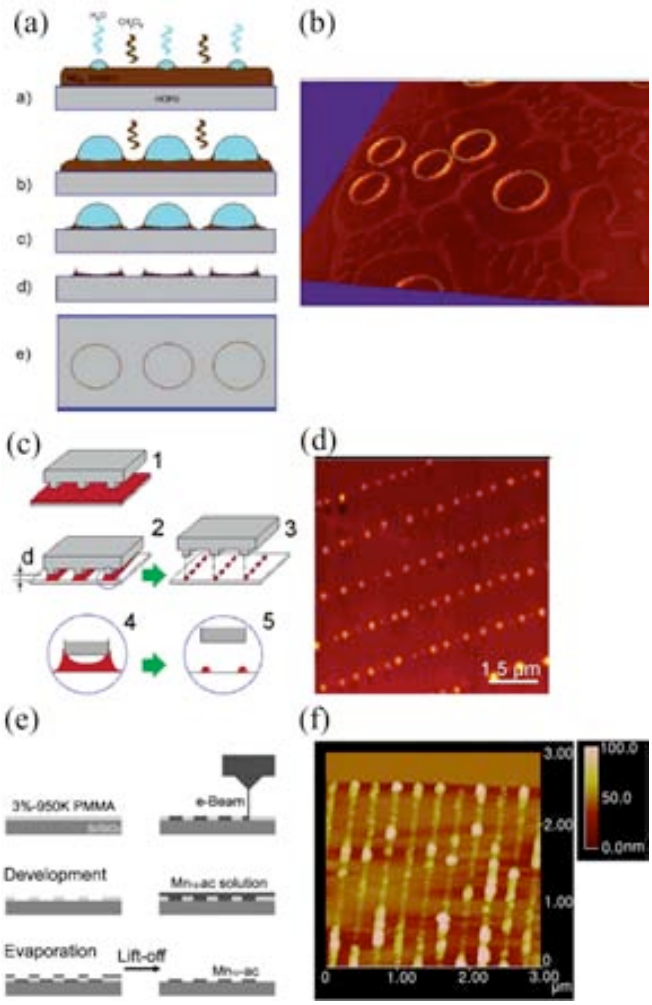

Figure 4.2 Structuration strategies used for the fabrication of SMM-based arrays on surface. (a) Schematic illustration of the method based on the breath-figures phenomenon and (b) 3-D AFM topography image of the ring-shaped structures fabricated on highly ordered pyrolytic graphite (HOPG) with an averaged diameters ranging from 4.2 µm to 4.6 µm. (c) Schematic illustration of the stamp-assisted deposition and (d) AFM topography image of the printed features. (e) Schematic illustration of the deposition process based on EBL and (d) AFM topography image of a line pattern. Panels **a** and **b** are reproduced from ref.[301]. Panels **c** and **d** are reproduced from ref.[303]. Panels **e** and **f** are reproduced from ref.[306].

The standard photolithographic approach is a straightforward way to fabricate micronsized patterned Mn_{12} films into arbitrary shapes through the fabrication of patterned photoresist layer on which the molecules are deposited on the exposed areas of the surface by drop casting.[307] XPS and magnetic measurements using a SQUID magnetometer were performed on larger patterns and thicker films respectively, showing that the chemical integrity and magnetic properties of the molecule were preserved after deposition. More recently, other methods have been implemented, which are also mainly indirect deposition procedures where pre-patterned surfaces are firstly fabricated to confine the SMMs deposition onto pre-determined nanoscale regions of the surface. The techniques used include (i) FIB lithography and (ii) EBL. High-resolution FIB milling was used to pattern matrices made of 100 x 100 nm^2 Au dots, on which sulphur-functionalized Mn_{12} derivatives were adsorbed in the (sub)monolayer coverage range.[308] They verified that the magnetic properties of the SMM were preserved on a thicker film directly deposited on a microHall magnetometer using the same deposition procedure. Teizer *et col.*

demonstrated the capabilities of EBL for the formation of high-resolution nanopatterns of Mn_{12}-acetate, of formula $[Mn_{12}O_{12}(O_2CCH_3)_{16}(H_2O)_4]$ (abbreviated as Mn_{12}ac), with arbitrary shapes, such as lines with a reduced width of only ~50 nm,[306] after confirming that the lithographic chemicals used in this study do not interfere with the core properties of Mn_{12} (Figure 4.2e,f). XPS was performed on larger patterns to verify the chemical composition of the film patterns. Magnetic characterization of the intactness of the Mn_{12} molecules was performed using a SQUID magnetometer. In order to ensure sufficient material in the film a concentrated SMM solution was drop casted on a bare surface repeating the process several times and then scratched off from the surface in order to obtain the powder sample.

4.1.1.2 *Deposition of single molecule magnets on surfaces assisted by AFM-based lithographies*

As already mentioned above, LON technique exhibits excellent resolutions allowing the fabrication of dots and stripes of only few nanometers, which in turn can be used as templates for the selective deposition of other components, such as Mn_{12} molecules. Coronado *et col.* took advantage of the combination of this lithography technique with electrostatic interactions for the SMM patterning.[300] They fabricated silicon oxide templates on a Si surface by means of LON to induce a preferential interaction between positively charged Mn_{12} molecules and the local oxide nanopatterns (Figure 4.3).[309] Prior to the local oxidation, the silicon surface was modified with an amino-terminated monolayer made of APTES to induce a repulsive interaction between the positively charged SMM and the rest of the non oxidized surface. To ensure that the integrity of the molecules was preserved after deposition, bare and APTES-functionalized silicon wafers were exposed to SMM solution. The resulting surfaces were then studied by using XPS and ToF-SIMS.

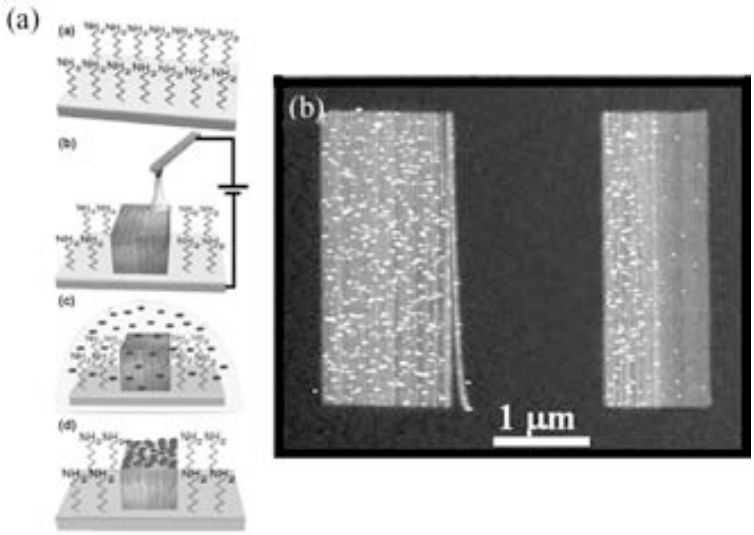

Figure 4.3 (a) Schematic illustration of the deposition process by LON. (b) AFM topography image after the deposition of the polycationic Mn_{12}. The SMM particles appear as white dots in the image. Reproduced from ref.[309].

4.1.1.3 *Deposition of single molecule magnets on carbon nanotubes*

Recently, the decoration of CNTs with SMMs has raised much interest due to their expected contribution to molecular spintronics in fields such as CNT-based FETs or CNT-based SQUIDs.[79] To date, several entities have been successfully grafted on the CNT walls, as magnetic NPs, biomolecules or quantum dots.[83-85, 310] However, the vast majority of strategies to decorate the walls make use of the introduction of defects on the CNT walls to graft the molecules. These alterations on the CNT walls will likely constitute scattering sites that will severely limit the performance of the electronic device. Alternative strategies to keep the presence of the scattering sites to a minimum include non-covalent binding. Bogani *et col.* used non-covalent π -stacking interactions to graft pyrene-functionalized tetrairon (III) SMM $[Fe_4(L)_2(dpm)_6]$ onto the walls of CNTs, under conditions compatible with the creation of electronic devices.[311] Another example of magnetic molecule with SMM like behavior, the double-decker $TbPc_2$, bearing a pyrenyl group, was successfully attached onto a CNT by immersing the CNT in a solution containing the SMM.[312] The assembly was obtained via π-stacking interactions between the pyrenyl groups and the CNT walls. The persistence of the SMM behavior of the conjugate upon deposition was proved by magnetic measurements on a SQUID magnetometer. Other examples of assembly of SMMs on CNTs are reported by Mallah *et col.*,[87,313] who shown the direct assembly of a SMM polyoxometalate of formula $[Fe_4(H_2O)_2(FeW_9O_{34})_2]^{10-}$ (Fe_6-POM) on a CNT though non-covalent grafting, with the preservation of the chemical integrity and SMM behavior upon assembly. The authors extended the grafting of the paramagnetic POM of formula $[As_2W_{20}O_{68}Co(H_2O)]^{8-}$ (CoPOM) together with its isostructural diamagnetic analogue $[As_2W_{20}O_{68}Zn(H_2O)]^{8-}$ (ZnPOM). The functionalization in all cases was done by simply stirring of CNTs in presence of POM molecules.

4.1.2 Surface structuration strategies: Summary

To date, several strategies for the structuration of SMMs on surfaces have been developed. The above reviewed works are good examples of such efforts. As we already observed for ferritin, complementary to self-assembly, patterning methodologies have been shown to be successful on fabricating SMM-based patterns with excellent resolution. This high control is typically achieved by the fabrication of templates on the surface on which the molecules are site-selectively deposited from solution. Alternatively, the use of stamps is an excellent approach to either indirectly or directly deliver SMM on bare surfaces in the form of the protrusions of the stamp.

To date, the excellent resolution of AFM-based lithographies has been exploited for the indirect deposition of SMM on surfaces, as demonstrated using LON. However, the direct deposition of SMM on unfunctionalized surfaces assisted by AFM-based techniques has not been demonstrated, not only at the moment of starting the present Thesis but even nowadays.

4.2 Experimental conditions for the structuration of single molecule magnets on surfaces by direct-write AFM lithography

The aim of the work described in this first experimental section was to provide a strategy and the experimental conditions to organize SMMs on surfaces in a very controllable manner before the integration into sensors is addressed. For this purpose, we have selected and studied two different types of SMMs on surfaces: the well-known Mn_{12} and the ErW_{10} POM. As far as we known, no previous works regarding the structuration of these materials using a direct deposition approach by direct-write AFM lithography have been reported. Therefore, special efforts were devoted to find and optimize the experimental conditions to achieve this goal, as is described next.

4.2.1 Structuration of Mn_{12} molecules on surfaces

The most thoroughly studied single-molecule magnets are those comprising a dodecamanganese core, the well-known Mn_{12} family, whose prototype is $[Mn_{12}O_{12}(CH_3CO_2)_{16}(H_2O)_4]$ denoted as Mn_{12}ac.[23, 286, 287] The Mn_{12} core consists of four Mn^{4+} S=3/2 ions surrounded by an antiferromagnetically coupled ring of eight Mn^{3+} S=2 ions, resulting in a ground state spin S=10 (see **Figure 4.4**). The high spin ground state, combined with large uniaxial magnetic anisotropy, results in a relatively high energy barrier for reversing the direction of magnetization.[314] As a consequence, they exhibit a slow relaxation of the magnetization at low temperatures whose origin is albeit based on individual molecules. Advantages of this family of clusters are multifold, including a relatively high blocking temperature (ca. 4-6 K) as well as a rich synthetic behavior that allows a straightforward modification of the peripheral organic ligands surrounding the magnetically active core in order to meet requirements of specific experiments or applications.[315-319]

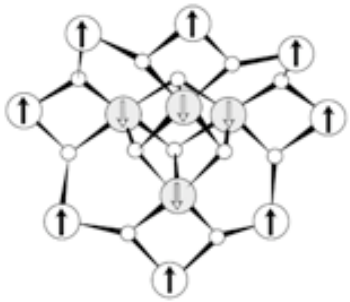

Figure 4.4 Schematic illustration of the $Mn_{12}O_{12}$ core. The spins of the four inner Mn^{4+} ions (in grey) are coupled antiparallel to those of the outer ring of eight Mn^{3+} ions (in white). The coordination sphere is provided by an outer shell of sixteen peripheral carboxylate groups (not drawn). Reprinted from ref. [287].

For the structuration on surfaces we selected the derivative $[Mn_{12}O_{12}(O_2CC_6H_5)_{16}(H_2O)_4]$, abbreviated from now on as Mn_{12}bz, synthesized by Dr. D. Ruiz-Molina at the CIN2 (see Experimental Section 7.1). **Figure 4.5** shows the molecular structure of the complex, which exhibits a coin-shaped Mn_{12} core surrounded by an outer shell of 16 benzoate ligands.[25] This molecule also exhibits a considerable thermal and chemical stability for the experimental conditions of the present work.[320, 321] The compound Mn_{12}bz exhibits the characteristic SMM relaxation of Mn_{12} molecules with out-of-phase ac magnetic susceptibility signals and hysteresis loops (see Experimental Section 7.1). Regarding the nature of the substrate surfaces selected in this study, we have mainly focused our attention on the adsorption on Si/SiO_2 since the final goal of the present study is the integration of the magnetic clusters into sensors which are made of this type of material.

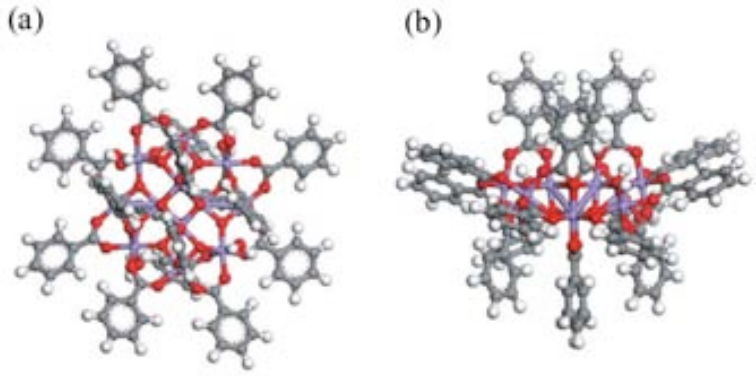

Figure 4.5 Two different views of the chemical structure of Mn_{12}bz. Reproduced from ref.[322].

As already evidenced in the previous chapter, the evaporation rate of the ink solution is a key parameter in direct-write AFM lithography experiments. It must be low enough to maintain its liquid-like behavior along the whole experiment to guarantee an efficient transfer of the ink from the tip to the surface. In addition, it is also important to identify a suitable solvent with appropriate Mn_{12} solubility and stability. All of the above requirements are met by dimethylformamide (abbreviated as DMF), which is a well-known solvent used for this family of molecules.[323] This solvent presents a high boiling point (b.p. 153 ºC) and ensures good solubility of the Mn_{12}bz clusters giving ideal conditions for its patterning. Ink viscosity as well as boiling point was further enhanced by the addition of glycerol in the final ink solution.

Contrary to the previous Chapter 3, where the use of ink solutions made of a mixture of aqueous solution and glycerol was previously reported, here we need first of all to optimize the ink composition since no previous works have reported on the use of the mixture DMF/glycerol as ink solution for performing direct-write AFM lithography. For this, a series of potential ink solutions were formulated with different glycerol concentrations from 0 to 20 % (v/v) and systematically studied to determine the optimum conditions for Mn_{12}bz deposition on Si/SiO_2 substrate. In order to investigate the ink-substrate affinity, which is relevant to determine the ink flow and spreading on the surface, we measured the contact angle for the different solutions under study (see Experimental Section 7.3). Contact angle measurements using a 3 µl drop on a Si/SiO_2 substrate showed a value of ~ 10º, ~ 18º, ~ 20º and ~ 24º for DMF, DMF + 5 % (v/v)

glycerol, DMF + 15 % (v/v) glycerol and DMF + 20 % (v/v) glycerol solutions, respectively (see **Figure 4.6**a-c). These values indicate that the deposited droplets made of DMF alone tended to spread out almost completely forming a quasi-thin film due to the high wettability of DMF on the surface. By contrast, the addition of a small amount of glycerol to the DMF solution made the droplet to spread partially but not completely on the Si/SiO_2 surface, and then stay in a beaded drop on the substrate.

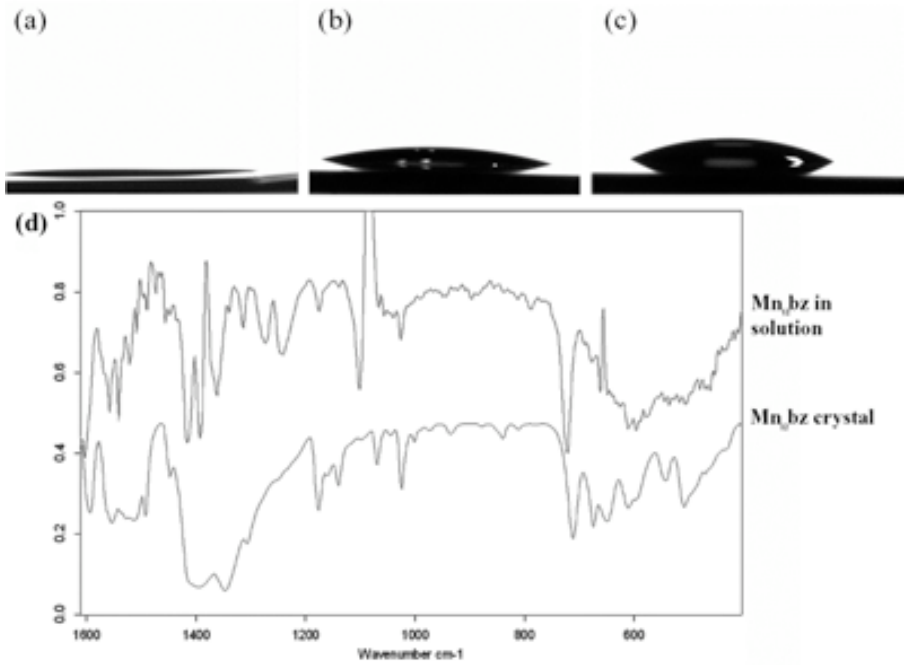

Figure 4.6 (a-c) Optical images of 3 µl droplets deposited on Si/SiO_2 obtained during contact angle measurements for mixtures of solvents made of (a) DMF; (b) DMF + 10 % (v/v) glycerol and (c) DMF + 20 % (v/v). (d) IR spectrum of the Mn_{12}bz crystal (bottom) and the Mn_{12}bz in a mixture of DMF and 5 % (v/v) of glycerol after subtracting background signal coming from the mixture of solvents (top).

Once the surface affinity of DMF/glycerol mixture was determined, a variety of Mn_{12}-containing ink solutions were prepared. In a typical experiment, the as-synthesized Mn_{12}bz crystals were dissolved into DMF, through vigorous stirring during 5 min to give diluted solutions of Mn_{12}bz. The studied concentration of the solution was in the range of 1 $mg{\cdot}mL^{-1}$ to 20 $mg{\cdot}mL^{-1}$ (higher concentrations resulted into some undissolved Mn_{12}bz). Then, 0 to 20 % (v/v) of glycerol was added to the solution and further stirred to finally obtain a homogeneous dark brown-colored solution. Immediately after its preparation, few drops of the freshly prepared ink solution were placed into a reservoir of the Inkwell chip. Then, MP tips were coated with the ink solution by dipping it into the microwells for a given time. The coated tips were then brought into contact to the Si/SiO_2 surface in the form of the desired pattern. All the patterning experiments were performed under controlled environmental conditions (~ 40 % relative humidity and room temperature) and using Ncriptor™ instrument.

In the simplest case, ink solvent is exclusively DMF. First attempts using this glycerol-free ink solution on Si/SiO_2 resulted into non-consistent patterns. Due to the affinity of DMF on Si/SiO_2, there was an excess of ink loading the tip as well as ink flow problems from the tip to the surface. Under these conditions, the tip delivered large amounts of ink (i.e. *bleeding*) on the

surface in the firsts deposit shots and in a non-controlled manner which typically resulted into a fast depletion of the ink. Furthermore, we also observed a relative fast drying of the ink solution for high Mn_{12}bz concentrations (~ 20 mg·mL^{-1}) which resulted into Mn_{12} solid precipitates on the tip and Inkwell. This observation could be explained due to two main reasons. First and foremost, the absence of high boiling glycerol component mixed in the solution. And second, the high ink-substrate affinity which is expected to make the solution to form a thin film also on the tip surface and lead to a faster drying on the tip.

The properties of the ink solution were varied by using mixtures of DMF and glycerol to adjust viscosity, evaporation rate and ink-substrate affinity, giving control over the writing process. In this sense, a gradual increase of glycerol concentration in the ink solution significantly improved the quality of the generated patterns. Several ink compositions were tested in this study. After multiple trials, best results were achieved by adding 5-10 % (v/v) of glycerol to the ink solution. Once the ration of the binary mixture was fixed, the next step was to show the stability of the compound in such mixture. For this, attenuated total reflectance-Fourier transform infrared (ATR-FTIR) experiments of a solution of the Mn_{12}bz 20 mg·mL^{-1} in DMF containing a 5 % (v/v) of glycerol were performed with the help of Dr. F. Novio from CIN2 (see Experimental Section 7.3). The background signal of the solvents was subtracted from the IR spectrum since the bands coming from the mixture of solvents almost completely hindered the peaks of the compound. In this way, the main characteristic peaks of the Mn_{12}bz were slightly distinguished in the resulting spectrum (Figure 4.6d).[25]

Under these conditions, reproducible and uniform in size patterns were obtained. Firstly, after tip coating (**Figure 4.7**a) the excess of ink was reduced through cantilever and tip *bleeding* (similarly to the ferritin proteins deposition process described in Chapter 3), until the tip started writing uniform dots. By controlling tip movement over the surface, tip-substrate contact time and ink depletion during the writing process, arbitrary shapes were generated made of repeated dots showing sizes ranging from few micrometers to 500 nm and heights from tens of nanometers to 5 nm (Figure 4.7b). In addition, the slow down on the ink drying provided extended printing times which allow fabricating several arrays until complete depletion of the ink (Figure 4.7c). Finally, surface morphology of the obtained patterns was examined using AFM (Figure 4.7d-f).

As an example, Figure 4.7d shows a well-defined array of Mn_{12}bz made of 20 x 20 dots spaced 2 μm apart on a Si/SiO_2 substrate using as ink a solution of 10 mg·mL^{-1} and 5 % (v/v) of glycerol. AFM topography of a single dot reveals the existence of a round-shaped dot with a halo of material that most likely is in agreement with the original droplet size (Figure 4.7e). Such halo of less than 0.5 nm in height could be explained due to residues (i.e. components present in the solution) coming from the ink solution and deposited during the evaporation process and that remains on the surface. Height profile analysis of each dot of the same array shows high uniformity in size, with diameters of 555 ± 39 nm and heights of 6 ± 1 nm (Figure 4.7f). Considering the size of a single molecule, the average height of the structures is in agreement with a multilayer distribution (up to 2-4 layers) of the molecules inside each dot-like feature. Though, we can not discard other effects that can contribute as well to the observation

of heights larger than those expected for a molecular monolayer, such as the background residues or remaining glycerol that is difficult to completely remove.

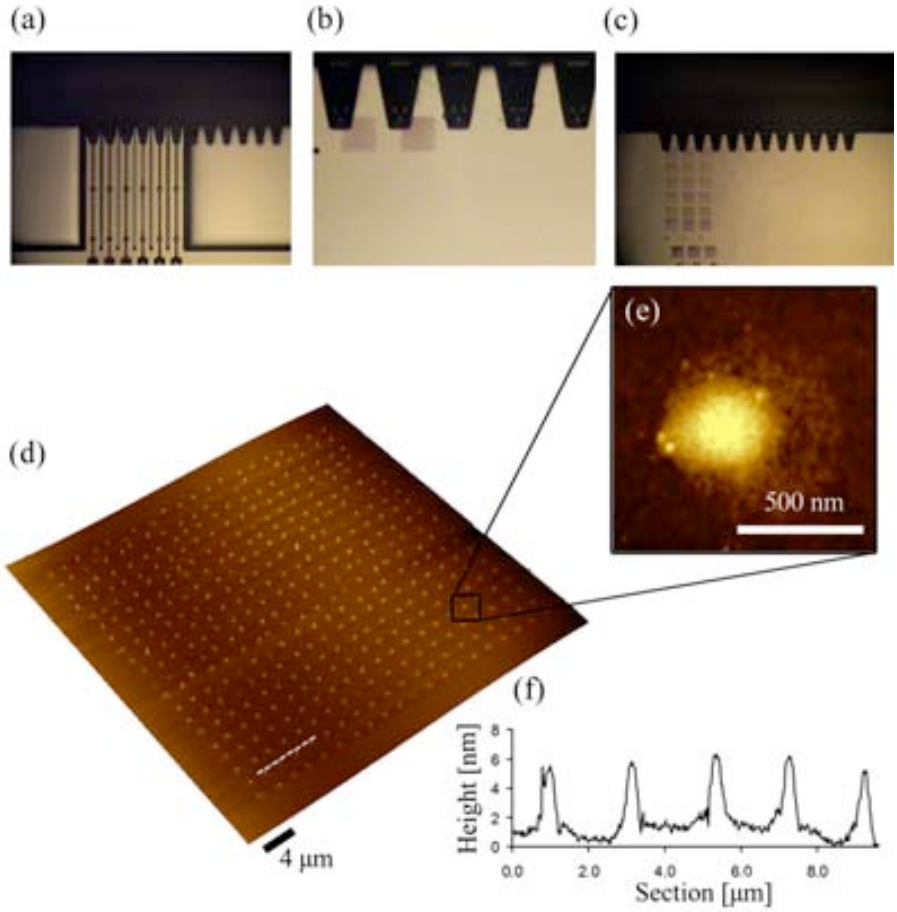

Figure 4.7 (a-c) Optical images captured during coating and writing processes to create different arrays made of Mn_{12}bz on Si/SiO_2. (d) 3-D AFM topography image of an array made of 20 × 20 dots separated by 2 µm. (e) Magnification view of one of the dots of the array in panel **d**. (f) Height profile along the white dashed line in panel **d**.

For this reason, in a control experiment, arrays using as ink a DMF with 5 % (v/v) of glycerol of high purity lacking the Mn_{12} molecule were also generated on a Si/SiO_2 surface under the same experimental conditions. These experiments were performed in collaboration with P. González-Monje from CIN2. During the deposition process, square shaped shadows were distinguishable by the optical camera, indicating the successful deposition of dots in the form of arrays (**Figure 4.8**a). Once deposited, the arrays were studied by AFM. In some cases, dots with a topographic profile up to 1 nm were observed (Figure 4.8b-c). Whereas in the case of the ferritin described in the previous chapter this situation was not crucial since it exhibits a roughly spherical shape of 12 nm in diameter that can clearly be differentiated from the background, this is not the case for the Mn_{12}. Due to its restricted molecular dimensions similar to those exhibited by the background, special care was taken in all the experiments described in this section. First, high purity solvents minimizing the quantity of solid residues must be used. Even so, a background with a blank solvent must be done before each experiment to know if all the topographic elements come from the molecules instead of the residual background. In this case, the height

profile observed for the background of 1 nm was considerably smaller than the 6 nm observed for the multilayer deposition previously described.

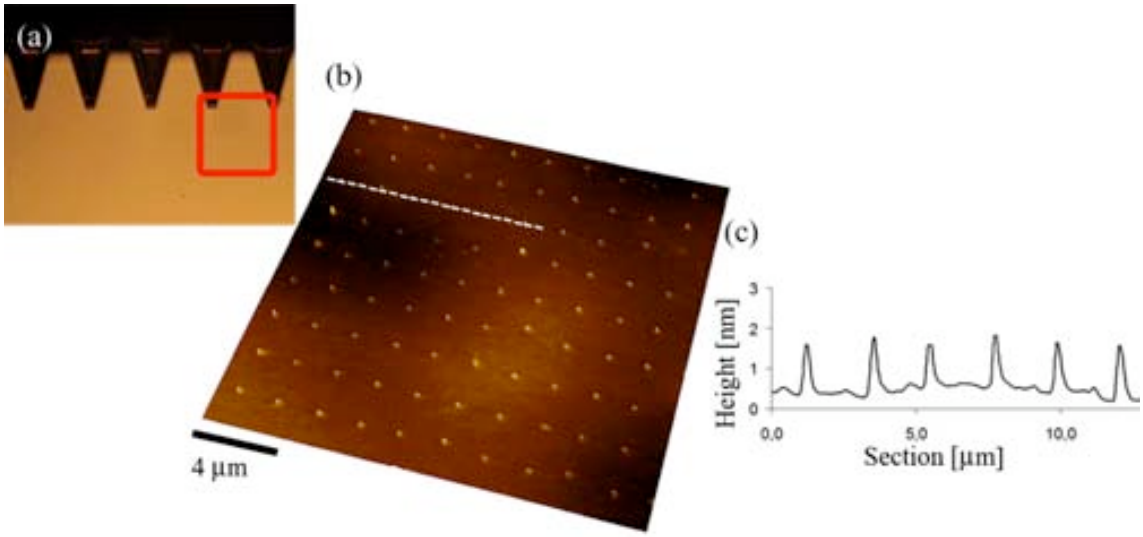

Figure 4.8 Characterization of an array fabricated on Si/SiO_2 using as ink solution a Mn_{12}-free solution containing DMF/glycerol mixture (95:5). (a) Optical image obtained right after the deposition process where a very slight shadow indicates the position of the array (for the sake of clarity the array is indicated with a red square on the image). (b) 3-D AFM topography image of the same array consisted of repeated 653 ± 48 nm dots separated by 2 µm. (c) Height profile along the white dashed line in panel **b**.

One of the main advantages of this direct-write strategy based on the direct deposition of pristine molecules on bare surfaces is that the process itself is not specific for a particular molecule-substrate system. In order to demonstrate the generality of our approach, we decided to examine the deposition process by varying both the peripheral organic ligands of the Mn_{12} cluster and the surface. For this, we focused on structuring on Mn_{12} derivative bearing aromatic biphenyl moieties, the full structure of which is $[Mn_{12}O_{12}(O_2CC_6H_4C_6H_5)_{16}(H_2O)_4]$ (abbreviated as Mn_{12}biph) on Au substrates. The complex was synthesized by Dr. D. Ruiz-Molina at the CIN2 (see Experimental Section 7.1). Special interest has been devoted to this specific molecule-substrate system because of the 16 biphenyl groups are expected to enhance adsorbate-substrate interactions[293, 324] as well as favor the molecular self-assembly through π-π interactions between the phenyl groups.[301] **Figure 4.9**a shows a schematic representation of the molecule in two orthogonal views, including the molecular dimensions.

A solution of Mn_{12}biph at 2 $mg{\cdot}mL^{-1}$ with 5 % (v/v) of glycerol was used as ink to coat the tip following the procedure already described. Then, different pattern designs were created on Au and further characterized by means of AFM. Figure 4.9b shows a 15 × 15 array made of repeated 273 ± 38 nm in diameter dots spaced by 2 µm. Height profile of one section of the array is given in Figure 4.9c. The average height of the pattern was 10 ± 1 nm, which suggests a multilayer distribution of the clusters on the surface. Higher density arrays were further created as shown in Figure 4.9e-g consisting in a 20 × 20 array where features are spaced apart at a distance of 1 µm. The average diameter and height of the generated dots is 227 ± 44 nm and 4 ± 1 nm, respectively.

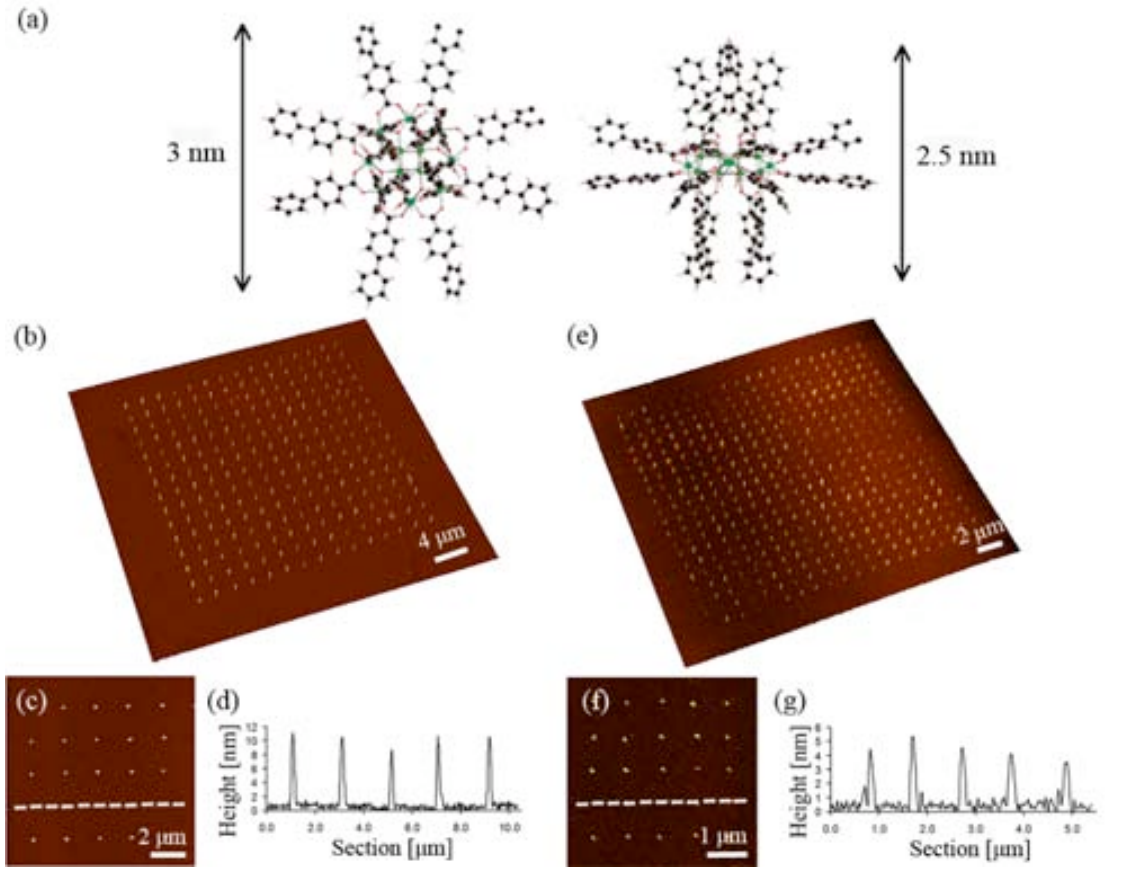

Figure 4.9 (a) Top (left) and side (right) views of the molecular structure of Mn_{12}biph molecule. (b) 3-D AFM topography image of an array fabricated on Au made of repeated dots spaced a distance of 2 µm showing a dot diameter of 273 ± 38 nm and height 9.6 ± 0.8 nm. (c) Magnification view of the same array in panel **b**. (d) Height profile along the white dashed line drawn on image **c**. (e) 3-D AFM topography image of an array fabricated on Au made of repeated dots separated 1 µm showing a dot diameter of 227 ± 44 nm and height 4.0 ± 0.4 nm. (f) Magnification view of the same array in panel **e**. (g) Height profile along the white dashed line drawn on image **f**. Panel **a** is reproduced from ref.[293].

In addition, controlling the tip movement over the surface during the writing process (dynamic writing), arbitrary shapes were originated obtaining more complex patterns. For example, we were able to create patterns consisted of parallel lines and microscale molecular letters forming the word "*Mn 12"*. In this last case, the tip was coated with an ink solution containing a Mn_{12}bz concentration of 10 mg·mL^{-1} and 5 % (v/v) of glycerol under the same experimental conditions described above. Then, the tip was positioned onto pre-designed positions of the surface before start moving at a tip scan speed of 1 µm·s^{-1} and creating each one of the letters of the word "*Mn 12"*. From **Figure 4.10**, we can clearly distinguish the presence of dots at one of the edges of each letter of the word. These dots correspond to the initial and final position of the tip and showed diameters of 651 ± 100 nm and heights of 6 ± 2 nm clearly higher than the rest of the pattern. In contrast, very uniform lines with widths of 573 ± 56 nm and heights of 2 ± 1 nm were obtained for the rest of the structure. This height is smaller than those previously reported for the fabrication of arrays. This can be due to a different topographic profile obtained with the dynamic writing mode. However, since this height is very similar to that previously described for the background, special care must be taken.

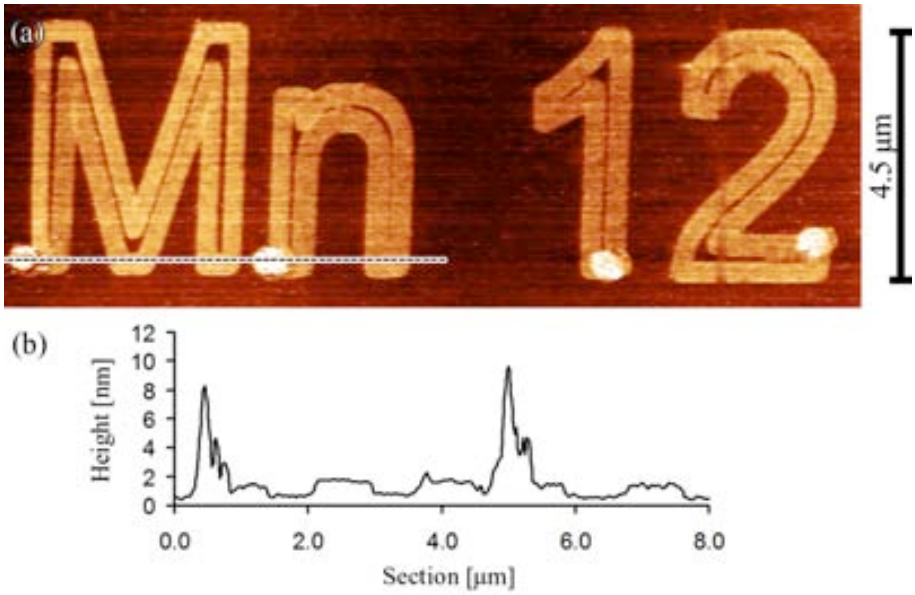

Figure 4.10 (a) AFM topography image of the deposition of Mn_{12}bz molecules on Si/SiO_2 in order to fabricate microscale molecular letters in the form of the word "*Mn 12"* and (b) height profile along the black dashed line on panel **a**.

Once Mn_{12} molecules were successfully structured and characterized by means of AFM, we went one step further and demonstrated our ability to structure such molecules into large arrays over extended areas. To this aim, we made use of the twelve MP tips of the chip, which once coated, allows creating 12 identical structures in one single step on Si/SiO_2. The pattern chosen for these experiments was an array of 50 × 50 μm^2. The process was repeated several times until complete depletion of the ink (**Figure 4.11**a). From the optical image, we observed slight variations in writing between different tips that have already been observed in Section 3.2 for the fabrication of ferritin arrays using MP tips (Figure 4.11b). In order to create patterns over even larger areas of the substrate, the cantilever tips was repeatedly dipped into the Inkwells, allowing patterning of large arrays over a span of hours. As an example, by loading the tip 3-4 times we created a pattern of Mn_{12}bz molecules on Si/SiO_2 over areas up to 0.7 × 1.8 mm^2 in size (Figure 4.11c).

The fabrication of such large patterns on surfaces is important if real applications of these systems are envisioned in the future in addition to facilitate its study by other techniques that require larger printed areas. This is the case of grazing incidence X-ray diffraction (XRD). This technique is widely used to characterize thin films and can give valuable information about the degree of crystalline order of our sample after drying under ambient conditions. To this aim, diverse patterns, as the one shown in Figure 4.11c, were characterized by grazing incidence XRD by Dr. J. Santiso at the CIN2 (see Experimental Section 7.3). The characteristic diffraction pattern obtained on crystalline bulk Mn_{12}bz samples was described by Luis *et col.* in ref.[325]. Figure 4.11d shows the grazing incidence X-ray diffraction of two different samples of Mn_{12}bz. The absence of any clear diffraction peak at low 2θ angle may indicate (i) either the overall sample volume was too small to detect any diffraction signal from the crystallites (the sample consisted of discrete dots so the volume was just a small fraction of the illuminated area) or (ii)

the sample was not crystalline or the degree of crystallinity was too small to be detected by the present XRD setup.

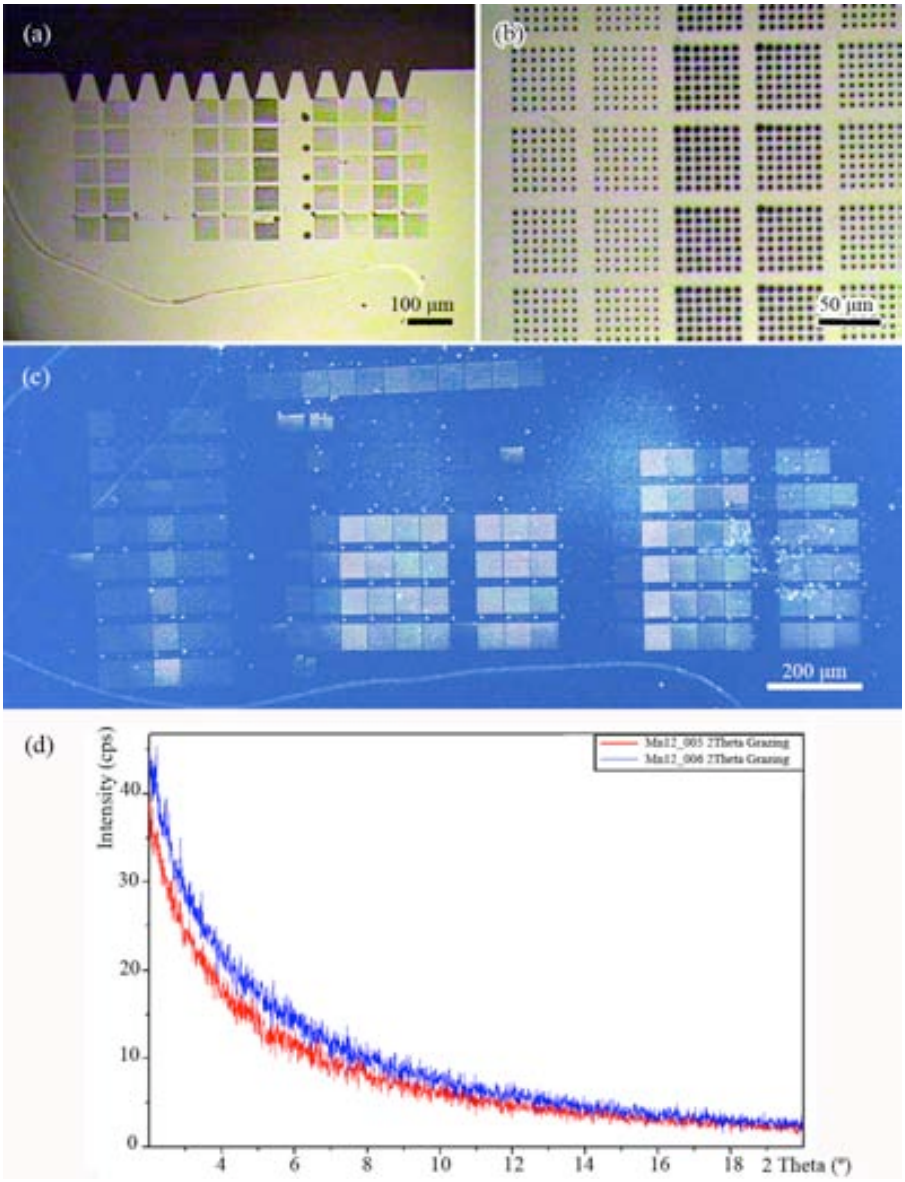

Figure 4.11 Optical microscopy images of (a) simultaneous patterning of Mn_{12}bz on Si/SiO_2 by using the twelve MP tips of the cantilever array, (b) magnification view of a section of the pattern were differences between arrays fabricated with different tips can be observed and (c) large pattern fabricated by repeating 3-4 times coating and writing steps. Variation in bright between arrays indicate different degrees of drying of the arrays as well as differences in dot size. The line mark used as reference for localize the array can be observed. (d) The graph shows the grazing incidence XRD scan of two Mn_{12}bz patterns similar to the one shown in panel **c**.

In view of such inconclusive results obtained by XRD, we decided to perform complementary experiments to also investigate the degree of crystallinity of the Mn_{12}-based dots upon deposition by high-resolution transmission electron microscopy (HR-TEM). This characterization technique was already used for determining the degree of crystallinity of bulk samples by Luis *et col.*[325] In our case, it was necessary to fabricate the arrays of Mn_{12}bz on carbon-coated TEM grids. The process of writing on such type of non-rigid surfaces has been

already described in Chapter 3. Therefore, the same experimental conditions described above were reproduced and a variety of arrays were fabricated on TEM grids (**Figure 4.12**). Let us note that in order to avoid beam damage of the sample, TEM experiments were performed while minimizing the electron dose.[325] Typical HR-TEM image of a dot of an array and a high magnification view of a region inside the dot is shown in Figure 4.12c and inset, respectively. Even though several dots were investigated along the sample, no crystalline fringes were identified inside any of them, as shown in Figure 4.12c (inset). This observation is in agreement with Luis *et col.*, and suggested the amorphous nature of the deposited sample. In addition, electron diffraction (SAED) pattern from regions inside the dots showing a diffuse halo further confirmed that the Mn_{12}bz based droplets consisted in an amorphous material after drying under ambient conditions.

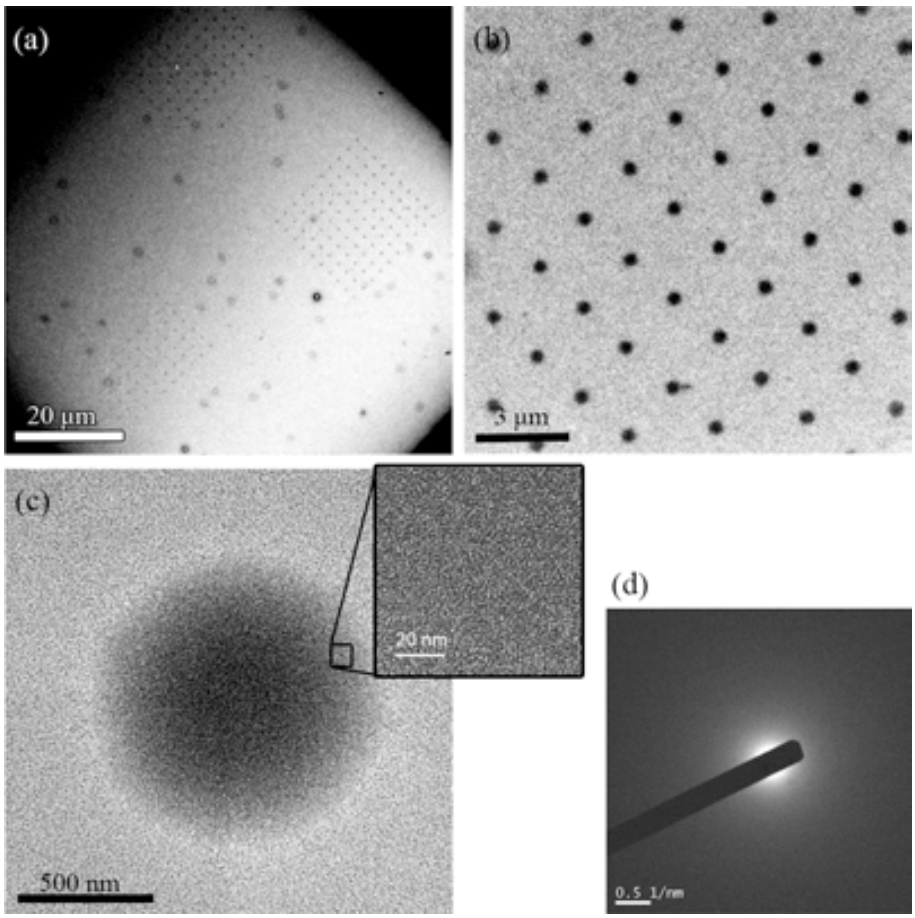

Figure 4.12 HR-TEM images of (a) three different arrays of Mn_{12}bz fabricated on a carbon-coated TEM grid and (b) magnification view of one of the arrays. (c) Detail of one of the dots of the array. (Inset is a magnification view of a region inside de dot). (d) Electron diffraction pattern obtained from a region inside the dot.

Along with the HR-TEM study, additional information regarding to the elemental composition of the arrays was obtained by inspecting the sample using EDX microanalysis. In these experiments, different X-ray spectra were collected by focusing the electron beam of the EDX-equipped TEM on different dots of the arrays (**Figure 4.13**). In the spectra pattern, the presence of Mn element inside each one of the dots was clearly confirmed by the presence of the

corresponding peak. Interestingly, these results emerge as the first evidence for the presence of Mn_{12} inside the structures generated by means of direct-write AFM lithography.

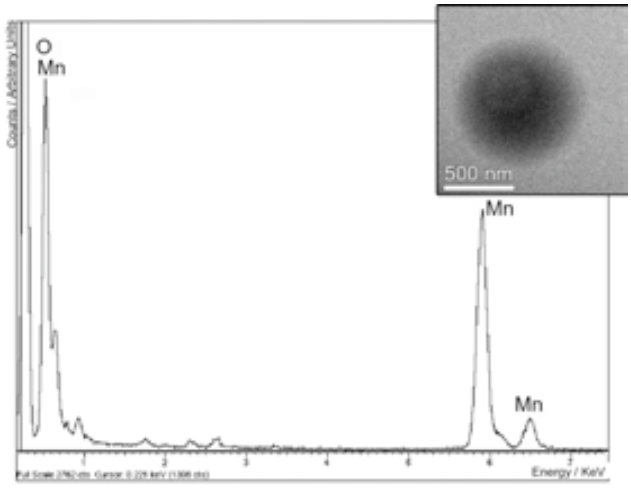

Figure 4.13 EDX spectrum showing the Mn peaks of an area of the dot nanostructure shown in inset image.

4.2.2 Structuration of polyoxometalates on surfaces

In the previous section we have show the possibility to structure Mn_{12} molecules on surfaces. However, the deposition takes place as an amorphous material as confirmed by different complementary techniques. This will be the sample to be deposited on the microSQUID sensor. However, at this stage, further experiments were planned with another SMM. In this case the molecule of choice was the POM of formula $[Er(W_5O_{18})_2]^{9-}$, referred as ErW_{10}. The objective was to show the validity of this technique not only to deposit but to have control on the crystalline state or the formation of supramolecular structures of the resulting material.

4.2.2.1 *Introduction*

POMs represent a large group of early transition metal-oxygen clusters with enormously diverse chemical structures, physical properties and promising applications as catalytic, magnetic, electrical and optical materials.[326-330] POMs are formed by covalently connecting multiple transition metal (Mo, W, V, Cr, Fe, etc) oxide polyhedrals (used as building blocks) and arranging them geometrically into diverse molecular structures that can bridge several length scales. Some of these molecular clusters are hydrophilic in nature and are very soluble in polar solvents, carrying a moderate amount of charges in solution balanced by small counterions such as Na^+ or NH_4^+. It is widely expected that soluble inorganic ions distribute homogeneously in dilute solutions, with the anions attracting cations and repelling other anions. However, POM molecules had totally different solution behaviors and usually do not exist as single ions in dilute solutions. Instead, such highly soluble, fully hydrophilic macroanions exist as discrete

ions in dilute solution when first dissolving in polar solvents, but tend to spontaneously self-assemble into a more stable single layer, spherical hollow-capsule structures by non-covalent interactions (**Figure 4.14**).[331-334] Interestingly, this unusual behavior shows similarities to the self-assembly of virus capsid proteins (which are also soluble macroions) into spherical capsid shells.[335]

The POM hollow capsules, so-called by Liu *et col.* as "blackberries structures",[333] typically present sizes ranging from tens to hundreds of nanometers and have a narrow size distribution. Their size is tunable with changing solvent content, charge density of macroions, additional salts and sometimes the pH of the solution.[333, 336-341] The supramolecular structure has been described in solutions of a wide variety of POM macroanions, such as $\{Mo_{154}\}$,[332] $\{Mo_{132}\}$,[339] $\{Mo_{72}Fe_{30}\}$,[342, 343] $\{Mo_{72}V_{30}\}$[340] as well as $\{P_8W_{48}Cu_{20}\}$[334] in various polar solvents (e.g. water, ethanol, acetone and their mixed solvents) in bulk. This suggests that this type of self-assembly is quite universal phenomenon for hydrophilic macroions with different shapes and sizes. Interestingly, the shape of the POMs does not significantly affect the final morphology of the assemblies (spherical). This is likely due to the fact that the clusters are not in direct contact on the capsule surface (because of electrostatic repulsion), but are separated by counterions.

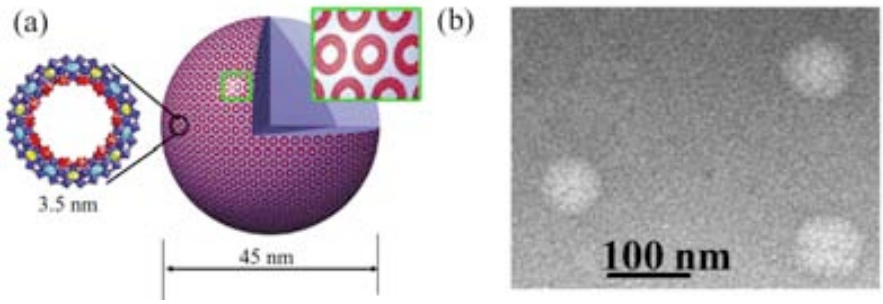

Figure 4.14 (a) Schematic illustration showing the capsule-like structure formed by $\{Mo_{154}\}$ macroions in aqueous solution and (b) TEM image of a dilute aqueous solution of $\{Mo_{154}\}$ macroions negatively stained with uranyl acetate showing the existence of spherical, ~ 45 nm radius assemblies. Reproduced from ref.[332].

Many important issues regarding the spontaneous association of POM clusters into hollow supramolecular structures in polar solvents still remain unclear and huge efforts are directed towards further elucidate the unique solution POM behavior.[333-336, 343] The POM self-assembly differs from the formation of surfactant vesicles because there are no obvious hydrophobic parts in POM macroanions. Even more, the macroions still keep certain distance with each other inside the hollow capsules, while the hydrophobic interaction is effective only in a very short range. For this self-assembly process, certain driving forces must be present to overcome the electrostatic repulsion among macroanions and attract them together during the hollow capsule formation. Liu *et col.* evidenced the presence of another attractive force different than van der Waals force (responsible for the aggregation of colloids), which performs as the major driving force for the supramolecular structure formation.[343] The same authors found that the presence of charges on POM macroanions is necessary for the self-assembly, and therefore, the small counterions play a decisive role.[336, 341, 344] The disparity in size and charge density between cations and anions in such solutions leads to the partial association of counterions around the

macroanions, called counterion association, which in turn may provide an attractive force contributing to the hollow capsule formation. Therefore, the negative charges on macroanions have a dual effect: they contribute to both short-range repulsion and large-range like-charge attraction, possibly via the counterion association which provides an attractive force between two adjacent macroanions (so-called like-charge attraction). Hence, the driving forces behind the self-assembly of these structures are believed to be a delicate balance between like-charge attraction effects, along with hydrogen bonding between adjacent macroanions and weak van der Waals force.

In this Thesis, we dealt with the capsule-like assembly of ErW_{10}, synthesized and characterized by Prof. E. Coronado and S. Cardona-Serra at the Instituto de Ciencia Molecular (ICMol) (see Experimental section 1.7). This molecular cluster belongs to the POM family containing individual lanthanide atoms namely $[Ln(W_5O_{18})_2]^{9-}$. As illustrated in **Figure 4.15**, the POM complex consists of a single Er^{3+} ion sandwiched between two $[W_5O_{18}]^{6-}$ POM moieties twisted an angle of 44.2 ° with respect to the other, generating a coordination site described as slightly distorted square-antiprismatic. The magnetic properties of this POM reveal the typical features associated with the SMM behavior, both in-phase and out-of-phase ac magnetic susceptibility signals show strong frequency dependencies, which indicate the presence of a slow relaxation process involving an energy barrier for the reversal of magnetization.[345-347]

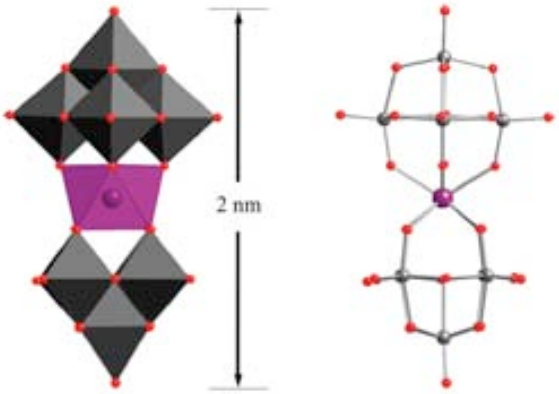

Figure 4.15 Structure of the ErW_{10} POM: polyhedral (left) and ball-and-stick (right) representation (oxygen, red; tungsten, gray; erbium, purple). Reproduced from ref.[346].

4.2.2.2 *Self-assembly of ErW_{10} in bulk and deposited on surfaces*

Even though the investigation of the magnetic properties of this POM compound showing SMM behavior have raised great attention,[346, 347] as far as we known no previous works regarding the self-assembly of ErW_{10} into capsule-like supramolecular structures have been reported so far. For this reason, our first experiments were devoted to study the spontaneous self-assembly of this particular POM into supramolecular structures in bulk. To this aim, pale-pink crystals of the sodium salt of the ErW_{10}, of formula $Na_9[Er(W_5O_{18})_2]\cdot xH_2O$, were carefully weighed and dissolved in Milli-Q water at ~ 50 ºC with stirring to give diluted solutions at different concentration (0.5 - 30 $mg\cdot mL^{-1}$). The homogeneous solution was filtered and then sealed and placed at room temperature. Under these experimental conditions the self-assembly of POM

molecular clusters is favored, giving rise in some cases to the formation of capsule-like structures in solution.[333, 337] It is important to note that POM self-assembly is slow process that typically takes a few days before observation of the formation of the spherical structures and up to several weeks to reach thermodynamic equilibrium at room temperature.[331, 337] During the whole period, an increased amount of hollow capsules forms, while the average size of the hollow capsules remains almost unchanged with time. In addition, the POM self-assembly is an endothermic process and hence it can be accelerated at elevated temperature.[348] The slow formation of the supramolecular structure has been attributed to the high energy barrier that POMs need to overcome for the transition from single macroions to hollow capsules.[334, 335, 348]
In this regard, first characterization was performed on freshly prepared ErW_{10} solutions of 0.5 – 30 $mg{\cdot}mL^{-1}$ deposited on carbon-coated TEM grids by drop casting and left to dry under air. **Figure 4.16** shows a very inhomogeneous sample mainly formed by a mixture of needle-like structures combined with an amorphous material and without the evidence of capsule-like structures formation along the TEM grid surface.

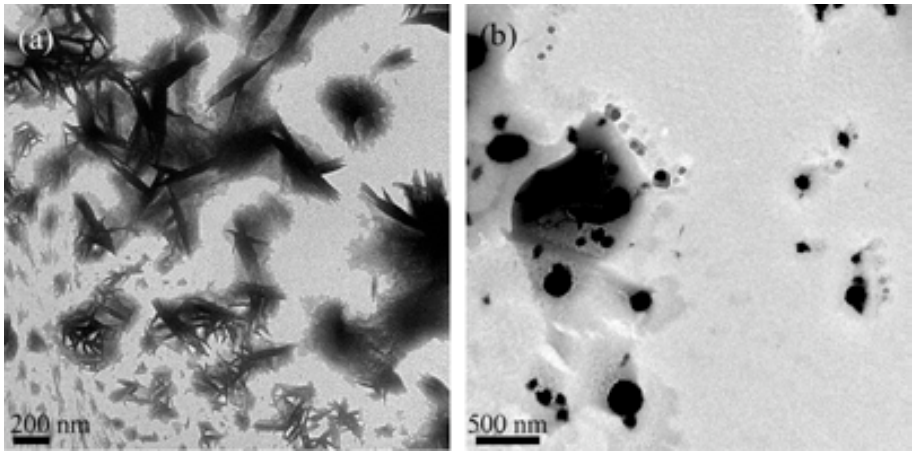

Figure 4.16 TEM characterization of a freshly prepared 30 $mg{\cdot}mL^{-1}$ ErW_{10} solution deposited by drop casting on a carbon-coated TEM grid. Sample consisted of a very inhomogeneous material presenting (a) needle-like structures combined with (b) aggregates with a thin film of amorphous or polycrystalline material.

Afterwards, in another sample the diluted ErW_{10} solution without was maintained for five days without any disturbance before its characterization. After such period, a droplet of the incubated solution was drop casted on a carbon-coated TEM grid for its study. Under these conditions, TEM images revealed the presence of spherical structures with an average diameter of 19 ± 6 nm (**Figure 4.17**). In some cases, larger spherical structures with diameters up to 500 nm were also observed. In all the cases, a large tendency of the capsules to aggregate as well as the simultaneous precipitation of a thin-film material is observed. It is interesting to emphasize that the structures are stable even upon vacuum treatment in the electron microscopes and with time (i.e. the spherical structures deposited on the TEM grid were observed after a few months). A close look reveals that each structure consists of a sphere of nearly uniform intensity surrounded by a darker ring, consistent with a shell of POM clusters surrounding an empty core (Figure 4.17d). Such contrast is in agreement with the formation of hollow capsules as the supramolecular structures obtained for other POM molecules described in the previous section.

Interestingly, the measured sizes for the ErW_{10} nanostructures did not show any obvious concentration dependence under the studied range, from 0.5 $mg{\cdot}mL^{-1}$ to 30 $mg{\cdot}mL^{-1}$. This fact is in good agreement with previous investigations on the self-assembly of POMs where the size of the formed structures does not change with increasing POM concentration.[337, 343]

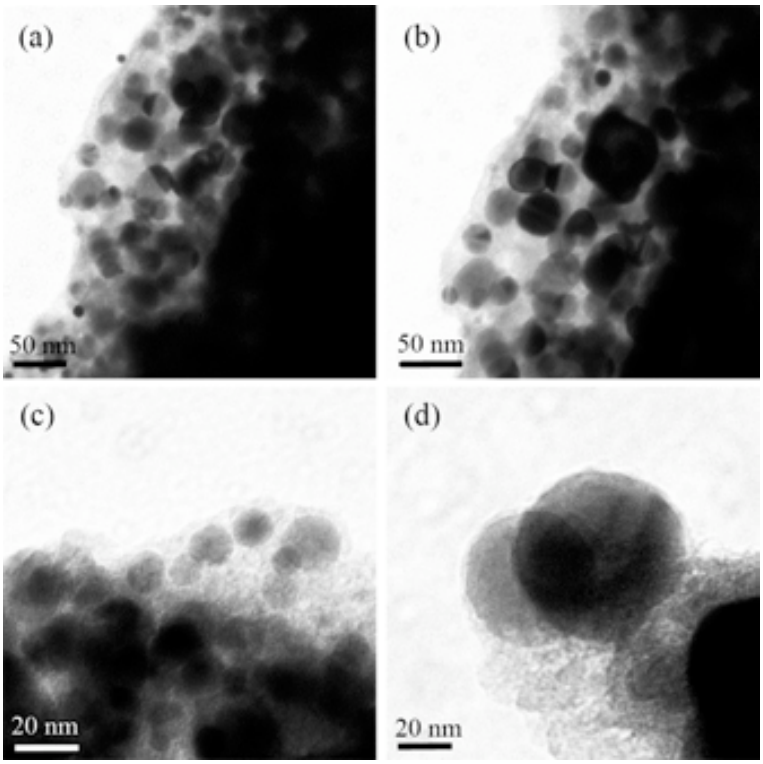

Figure 4.17 (a-c) TEM images of spherical capsules obtained from bulk solution of ErW_{10} after five days. (d) TEM magnification view showing in detail two of these spherical structures where the darker ring suggesting the hollow nature of the structures can be clearly visualized.

Once the formation of these nanostructures was shown to take place in bulk, the next step was to investigate their formation on surfaces. The formation of such capsules structures on surfaces remains so far elusive not only for the ErW_{10} but for any other POM. Two different methodologies were used with this aim: drop casting and spraying. For this purpose, we prepared ErW_{10} solutions at different concentrations (0.5 - 30 $mg{\cdot}mL^{-1}$) following the same experimental procedure described above. Then, the freshly prepared solution was deposited on a Si/SiO_2 surface by any of both techniques and left to evaporate under ambient conditions. SEM characterization of the samples show similar structures as the once obtained on the TEM grid shown in Figure 4.15 but also allowed to observe thicker aggregates made of an amorphous solid or a dispersed polycrystalline material over the whole surface without any evidence of hollow capsule formation (**Figure 4.18**a). The formation of such dispersed structures can be attributed to a fast evaporation process where the solution lacks the required time to favor the formation of the hollow capsules.

Different treatments of the deposited sample were explored varying diverse parameters, such as POM concentration, relative humidity, temperature and time of incubation, giving rise to highly heterogeneous samples with a long range of diverse structures, as represented in Figure 4.18. In all the cases the same experimental conditions for its deposition were used. To slow down the

evaporation rate of the solution, the deposited substrate was placed in an air-tight chamber saturated with water. After incubation without any disturbance for a given time, the substrate was removed from the chamber and dried in air.

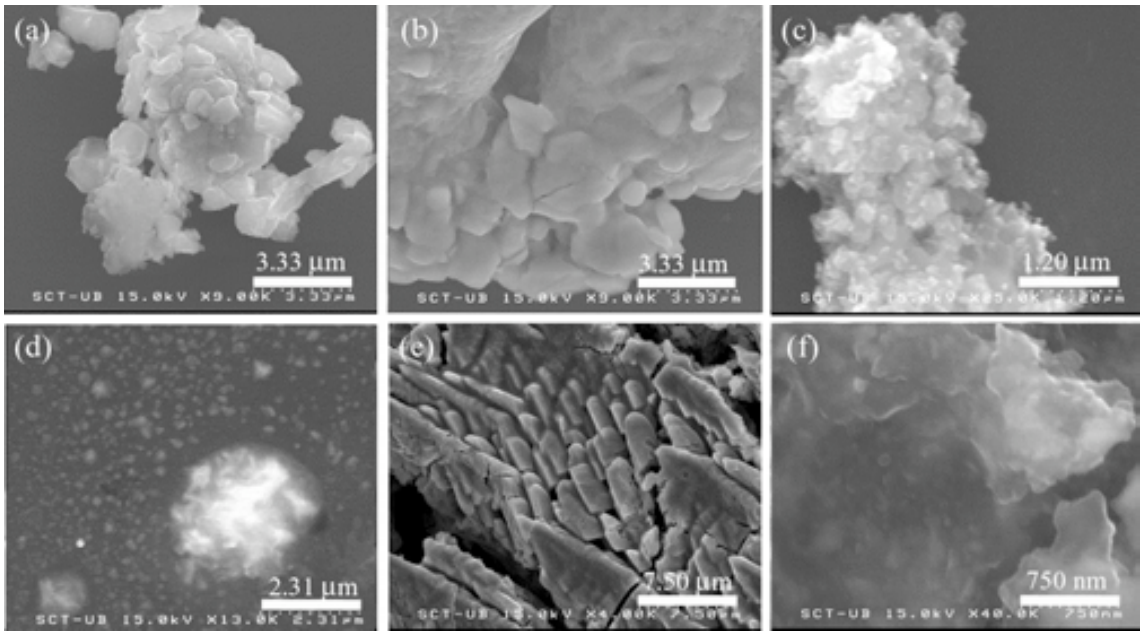

Figure 4.18 FE-SEM images of the structures formed on a Si/SiO_2 after deposition of the POM solution under different treatments. Deposition of 30 $mg{\cdot}mL^{-1}$ ErW_{10} solution (a) dried in air at room temperature, (b) under water vapors at low temperature during two days, (c) under water vapors at 50 ºC during two days and (d) under water vapors at room temperature during two days. Deposition of 100 $mg{\cdot}mL^{-1}$ ErW_{10} solution (e) dried in air at room temperature and (f) under water vapors at room temperature during two days.

In view of these results, we decided to further increase the incubation time up to five days in order to promote similar conditions as the ones in bulk solutions that favor the capsule-like structure formation. For this, diluted solutions (0.5 – 30 $mg{\cdot}mL^{-1}$) were deposited by drop casting or spray on a Si/SiO_2 and incubated for five days in the air-tight chamber saturated with water vapors at room temperature and without any disturbance. After five days the substrate was removed from the chamber and dried in air. **Figures 4.19** show FE-SEM images of a drop casted sample after incubation and drying. Well-defined spherical structures with sizes varying from 700 nm to 1 µm were observed along the majority of the surface. Similar spherical structures were also observed for the sprayed sample, showing sizes ranging from 600 nm to 8.5 µm. Similarly to the study in solution, the formed spherical structures did not show any clear dependence with POM concentration for the range under study. Though it is important to evidence the significant increase in size of these spherical structures when deposited by drop casting or spraying compared to the ones obtained in solution (described above). The evaporation of the solvent as well as the spatial confinement appears to enormously influence on the self-assembly process. Hence, the method of deposition emerges as a key parameter in determining the final structure size obtained from the spontaneous assembly of POM molecules.

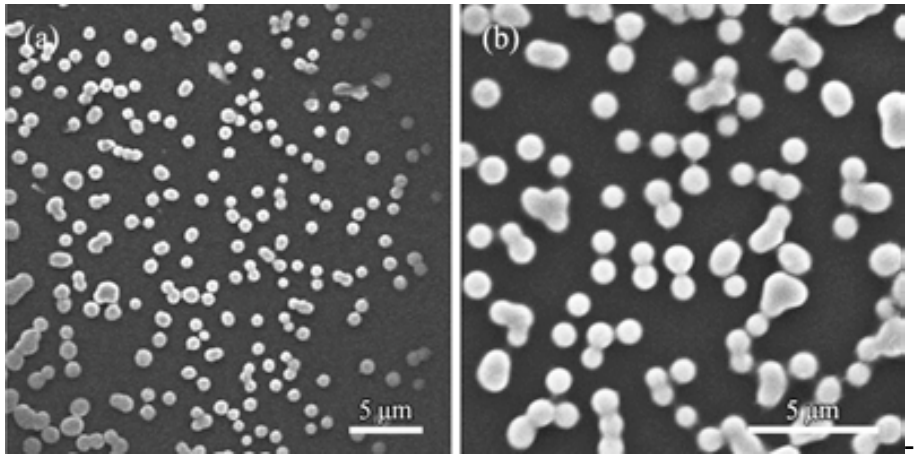

Figure 4.19 FE-SEM images of a 0.5 mg·mL^{-1} ErW_{10} solution drop casted onto a Si/SiO_2 surface and incubated for five days under high humidity conditions.

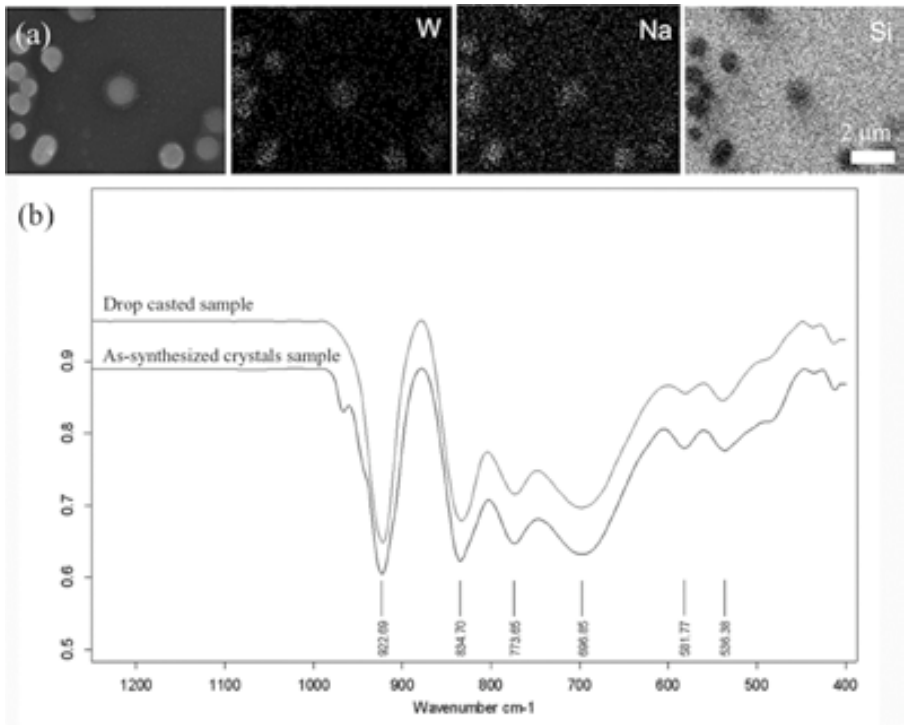

Figure 4.20 (a) EDX elemental mapping obtained for a 30 mg·mL^{-1} ErW_{10} drop casted sample onto a Si/SiO_2 surface and incubated for five days under high humidity conditions. (b) IR spectrum bottom: as-synthesized ErW_{10} crystals where the characteristic bands of the compound are indicated with marks. IR spectrum top: drop casted 30 mg·mL^{-1} ErW_{10} sample after incubation for five days under high humidity conditions.

In order to demonstrate that these structures consisted of ErW_{10} molecules arranged into spherical assemblies we further characterized them by EDX elemental mapping. **Figure 4.20**a shows maps of some of the key elements of a section area of the drop casted sample. A bright area of the map indicates a high concentration of the element, while a dark area of the map indicates a low concentration of the element. Tungsten as well as sodium elements were dominant at the regions corresponding to the presence of the spherical structures, which suggests the presence of ErW_{10} molecules on these structures. The stability of POM molecules

after the whole experimental procedure (i.e. deposition, incubation and drying) was characterized by ATR-FTIR experiments of a drop casted sample after incubation process and dried in air with the help of Dr. F. Novio (see Experimental Section 7.3). Then, the acquired spectrum was compared with the obtained for the as-synthesized ErW_{10} crystals. As shown in Figure 4.20b, the spectrum of a drop casted sample after incubation process still exhibit the characteristic bands of the ErW_{10} POM described by S. Cardona-Serra *et col.*,[346] and demonstrates the stability of the material along the whole experimental procedure.

4.2.2.3 *Self-assembly of ErW_{10} into droplets deposited by direct-write AFM lithography*

Once the formation of capsule-like structures made of ErW_{10} molecules was shown to take place on surfaces, the objective was to confine its formation on localized femtoliter droplets dispensed by means of direct-write AFM lithography. For this purpose, we first prepared the solution used as ink to coat the tip. In particular, the solution consisted in a 30 $mg{\cdot}mL^{-1}$ solution of ErW_{10} filtered right before its use. In a typical experiment, few drops of the recently filtered POM solution were placed into the reservoirs of an Inkwell and then a MP tip was dipped into the microwells for a given time. Then, the coated tip was brought into contact with a Si/SiO_2 surface in order to deliver droplets of the POM solution in the form of arrays of dots. The deposition process was performed using Nscriptor™ instrument. Note that, since the ink was an aqueous solution, we observed a fast drying of the ink on the Inkwell chip which significantly difficulted the coating process. In addition, the solution was also fast dried on the tip resulting into the deposition of solid pieces on the surface during writing. Therefore, in order to slow down the evaporation rate of the ink and hence ensure a controllable deposition of the ink material from the tip to the surface, the whole patterning process was performed under controlled environmental conditions at high humidity (~ 75 % relative humidity and room temperature). On the contrary to the work developed with ferritin proteins and Mn_{12} molecules, the addition of other co-solvents to slow down the evaporation rate and increase viscosity is not feasible in this case since it could modify the formation of the supramolecular structures.

After the patterning process, the substrate was immediately placed in an air-tight chamber saturated with water vapors at room temperature and incubated during five days. The generated arrays were first studied before the incubation process by FE-SEM. Nice arrays were already obtained demonstrating our ability to place POM based droplets on well-defined positions on a surface. However, the fast evaporation limited the process and only few small arrays were fabricated in a single process before tip stops writing due to the progressive ink drying on the tip surface. As an example, **Figure 4.21**a and b shows an array consisting of uniform dots with a diameter of 826 ± 45 nm separated by 8 μm. At this point, no presence of spherical structures was detected on any feature of the array. This was further demonstrated by reproducing the same experiment on a carbon-coated TEM grid (Figure 4.21c). In some cases, the formation of polycrystalline or amorphous structures inside a dot of the array was also observed (Figure 4.21d).

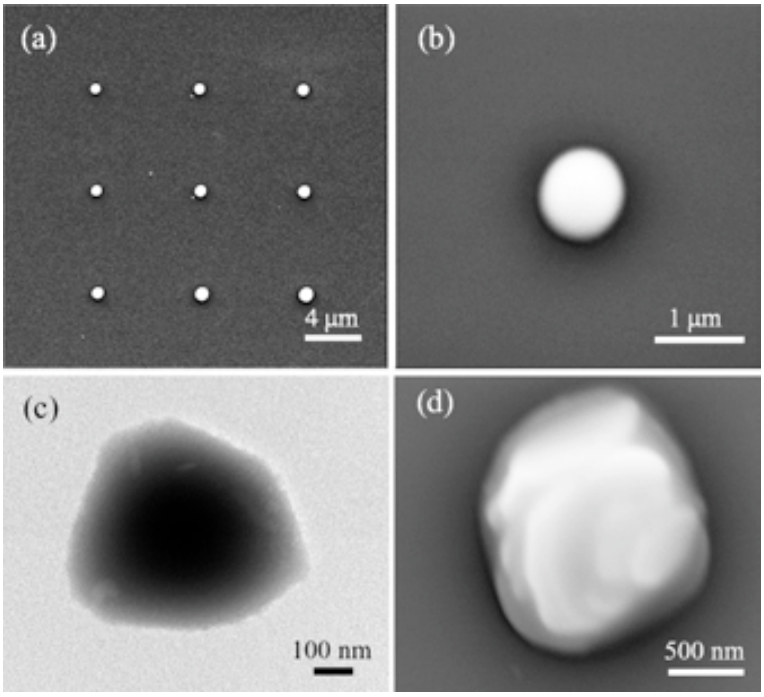

Figure 4.21 POM-based arrays fabricated by means of direct-write AFM lithography characterized before the incubation process. (a) 3 x 3 array of dots on a Si/SiO_2 surface and (b) detail of one single dot of the array. (c) TEM magnification view of a single dot of an array fabricated under the same experimental conditions on a carbon-coated TEM grid. (d) FE-SEM image of a dot on Si/SiO_2 where the presence of a polycrystalline or amorphous material inside the structure is distinguished.

Exposure of the as-prepared droplet array to ambient conditions seems to induce a fast evaporation of the ink solvent, preventing the self-assembly of POM molecules into supramolecular structures. In contrast, a slow evaporation turned out to be ideal to induce the growth of capsule structures on each deposited droplet, as we can clearly see in **Figure 4.22**. Magnification of these dots showed the growth of such structures more clearly with diameters of 440 ± 60 nm. Herein, the size of the spherical structures differed from the obtained by drop casting and spraying, which further evidences the importance of the deposition method on the final size of these structures. It must be emphasized that in addition to capsules, it was also possible to observe the formation of some needle-like structures. Even though several experiments have been reproduced, we must emphasize that in most of the cases there was a coexistence of both type of structures. Further experiments are required to achieve full control over the kinetic and thermodynamic parameters that guide their formation.

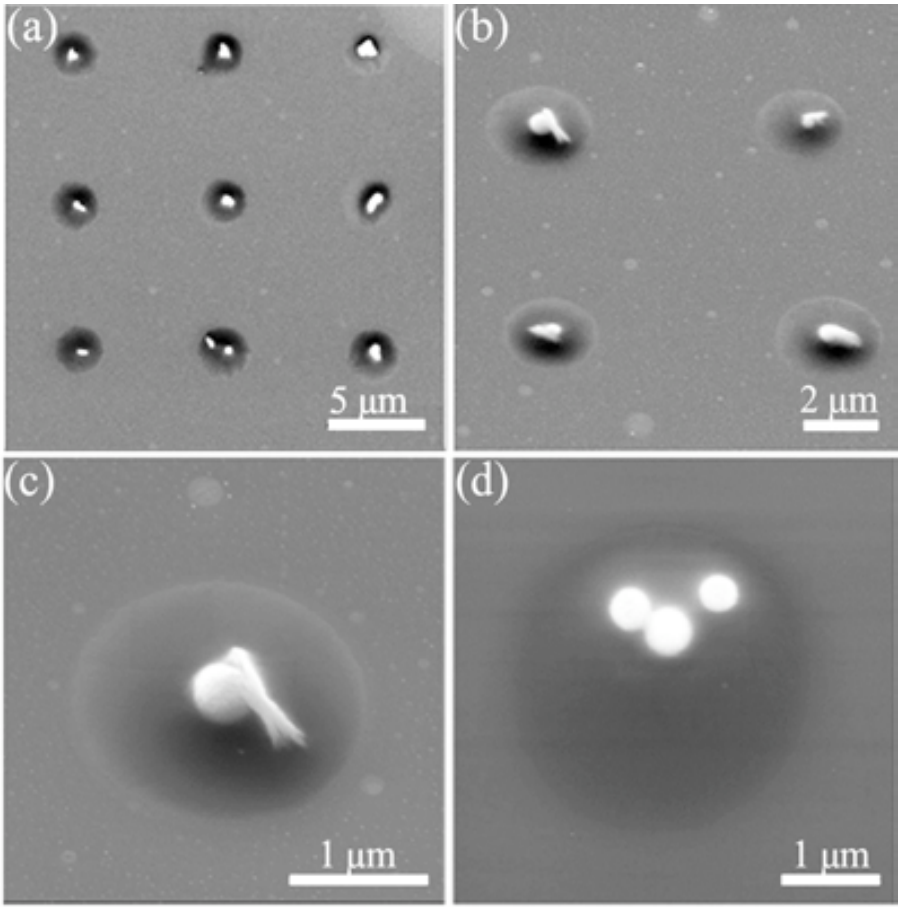

Figure 4.22 FE-SEM images of POM-based arrays onto a Si/SiO_2 after incubation for five days under high humidity conditions. (a,b) Well-defined POM capsules can be observed in each dot of the arrays, viewed (a) from above and (b) at a 45º tilt angle. (c,d) Details of the obtained spherical structures grown inside each dot, viewed (c) at a 45º tilt angle and (d) from above.

4.3 Integration of Mn_{12} single molecule magnets into sensors by direct-write AFM lithography

The last step was the integration of the molecular systems into a microSQUID susceptometer to be measured. For this, Mn_{12} was the family of choice since it can be deposited as a few layers in relatively control manner in comparison with POM molecules that is deposited either in the form of supramolecular structures or amorphous layers. The sensor used with this aim consists of a second generation of microSQUIDs with a sensing area of smaller dimensions and different pattern than the one used for the ferritin proteins, specially designed to ensure a maximum response. However, this improvement of the sensitivity implies a considerably larger experimental challenge on our side, due to its circular shape and reduced dimensions.

This second generation of microSQUIDs was provided by Dr. J. Sesé from the INA. It consists of two pickup coils connected in parallel, which correspond to the sensitive areas of the sensor, and form part of the SQUID loop itself (see **Figure 4.23**). These Nb coils are circular-shaped with external and internal diameter of 35 µm and 27 µm, respectively (a more detailed description of the sensor used in this study is given in Experimental Section 7.4). In this way,

the sample to be measured needs to be placed on one of the two pickup coils while maintaining the other one completely unfunctionalized.

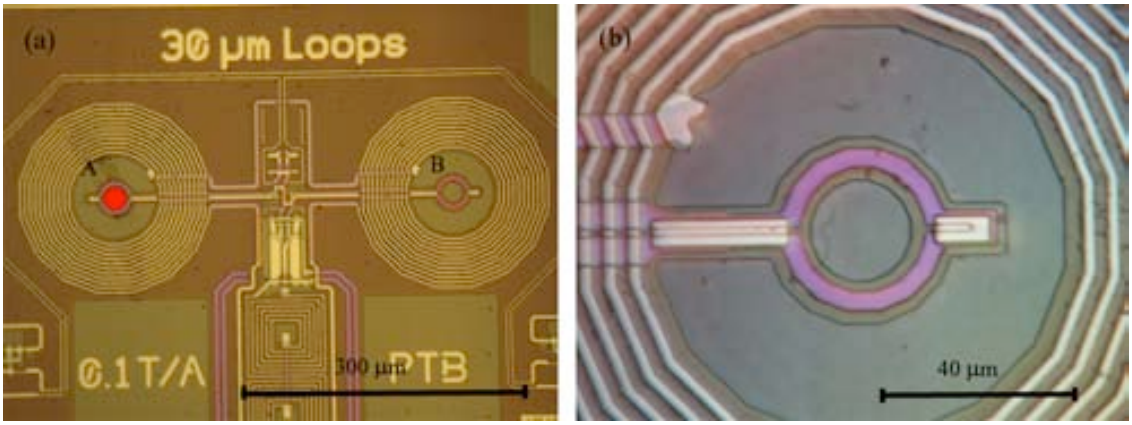

Figure 4.23 (a) Optical image of the two pickup coils of the second generation of microSQUIDs which corresponds to the sensitive areas of the sensor. The sample to be measured can be located either on the left side (A), wherein as an example a sample is indicated with a red circle, or on the right side (B). (b) Magnification view of one of the coils. Images obtained by Dr. J. Sesé.

The experimental parameters used for the structuration of Mn_{12}bz molecules onto bare Si/SiO_2 substrates in Section 4.2, were implemented for the integration of such molecules on the sensing areas of the sensor. First experiment was devoted to site-selectively functionalize one of the coils with the Mn_{12} molecules by completely filling the entire sensing area of the coil with dots made of the magnetic material. These experiments were performed by P. González-Monje from CIN2 and M. Jenkins from ICMA and Universidad de Zaragoza.

Before tackling this issue, patterns consisted in concentric circles made of repeated dots were fabricated on a Si/SiO_2 surface using a Mn_{12}bz solution at 10 mg·mL^{-1} with 5 % (v/v) of glycerol as ink (**Figure 4.24**). AFM image shown in Figure 4.24c consists of an array with a diameter of 30 µm. In this case, the generated structures show an average diameter of 1.6 ± 0.2 µm and height of 46 ± 10 nm.

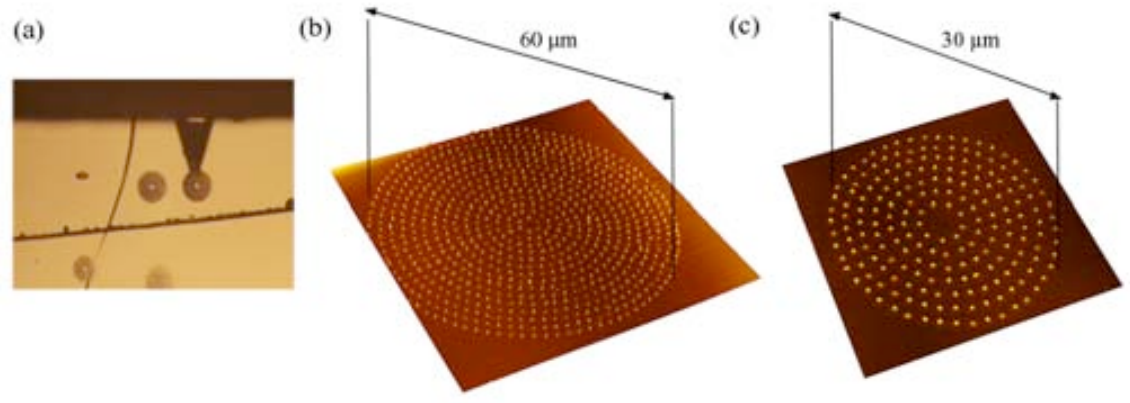

Figure 4.24 Structuration of Mn_{12}bz into circle-shaped patterns fabricated on Si/SiO_2 surfaces. The ink solution used for the fabrication of the arrays consisted of 10 mg·mL^{-1} Mn_{12}bz in DMF and 5 % (v/v) of glycerol. (a) Optical image captured during the fabrication of the arrays. (b) Round-shaped array of 60 µm in diameter. (c) Round-shaped array of 30 µm in diameter with an interdistance between concentric circles of 2.5 µm.

Afterwards, for the sensor integration a MP tip was coated with a solution containing 10 $mg \cdot mL^{-1}$ of $Mn_{12}bz$ with 5 % (v/v) of glycerol. Then the coated tip was positioned on the wire of one of the pickup coils assisted by optical control, and traversed over the surface in the form of the desired pattern. The integration process was performed using Nscriptor™ instrument. The pattern design consisted in the circular-shaped array of 30 μm in diameter shown in Figure 4.24c. In this way, the more externals circles of the pattern matched with the coil wire and the sensing area was completely filled with dots. Optical images captured before and right after the integration process are shown in **Figure 4.25.** During the integration process, a circular-shaped shadow was distinguished by the optical camera, indicating the successful deposition of dots inside the coil. The resolution of the optical camera allowed us to localize the circular sensing area and position the tip on top of the coil wire with a good control, as observed in Figure 4.25.

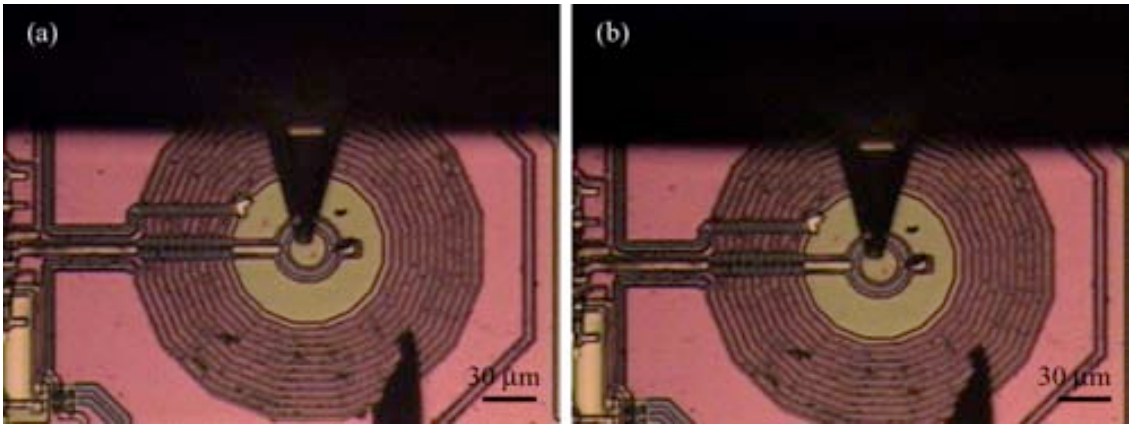

Figure 4.25 Optical images captured (a) before and (b) after the integration of Mn_{12} clusters into the most sensitive areas of the sensor. A very slight shadow corresponding to the patterned area was optically distinguished during the integration process.

Let us note that these superconducting microcircuits were very sensitive sensors that were easily damaged by electrostatic discharges when they were manipulated. For this reason, special attention was paid during integration experiments, which can be listed as: (i) wear antistatic bracelet and shoes when manipulating the sensor, (ii) avoid touching the electrical contacts on the sensor whenever possible, (iii) earth the sample stage using a wire connected directly to the earth on a wall plug, (iv) carefully move the sensor to the sample stage, (v) use copper tape to cover active contacts (those that are wire bonded to the chip) and connect the tape to the stage (earth), (vi) move the stage onto the Nscriptor™ system, (vii) after deposition, take the stage out and reconnect to earth and (viii) remove copper tape and place sensor (carefully) back into its antistatic box.

The morphological characterization of the sensor upon the $Mn_{12}bz$ integration process was done in the last step, right after the measurement of the magnetic properties. In this way we avoided any sample damage of the sensor due to their delicate handling even in the presence of small residual electrostatic currents. Even though the optical camera during writing as well as magnetic measurements already confirmed the presence of deposits on the sensor, the AFM topography of the surface confirmed this fact. As can be seen in **Figure 4.26** the topographical image is not very significative for the presence of the $Mn_{12}bz$ deposits mainly due to the

presence of residues on the surface of the sensor that, even though do not alter the magnetic properties, interfere on the localization of the sample specially considering their small height. Similar difficulties were obtained by characterizing the sensor by FE-SEM. More evident results were obtained in the AFM phase image where the presence of periodical dot arrays was clearly differentiated (Figure 4.26c).

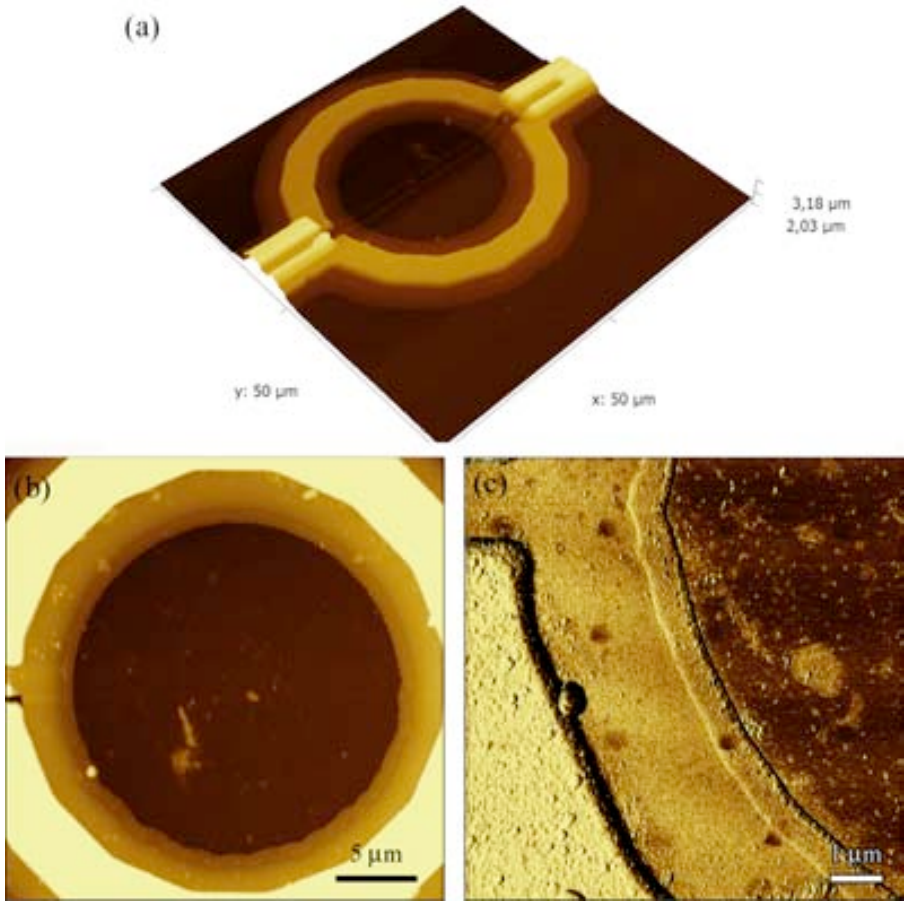

Figure 4.26 AFM characterization of the second generation of microSQUID after site-selective deposition of Mn_{12}bz molecules onto the sensing areas of the sensor corresponding to the pickup coils. (a) 3-D AFM topography image of the sensor. (b) AFM topography image where the amount of residues along the surface is clearly observed. (c) AFM phase image showing the deposited dots along the pickup coil.

At the moment of writing the present manuscript, preliminary ac susceptibility measurements at low temperatures (T = 4.2 K) had already been done with the integrated sensor by Dr. F. Luis and co-workers at ICMA. The in-phase contribution of the Mn_{12} samples once corrected the background signal from the sensor is shown in **Figure 4.27**a. The magnetic behavior of single crystals of the well-known Mn_{12}ac and Mn_{12}bz sample measured exactly with the same sensors are shown in Figure 4.27b for comparison purposes. As can be seen there the Mn_{12}bz crystal exhibits the response of the two relaxing species present in the sample whereas the Mn_{12}-acetate only exhibits that assigned to the slow relaxing species. In the case of the Mn_{12}bz deposited by direct-write AFM lithography the experimental data was fitted to the Debye law to describe the relaxation process of the sample and is written as

$$\chi' = \chi_S + \frac{\chi_T - \chi_S}{1 + (\omega\tau)^2} \qquad (4.1)$$

where χ' is the in-phase ac susceptibility component, χ_T and χ_S stand for the equilibrium and high-frequency (or adiabatic) limits respectively, ω is the frequency and τ the relaxation time. Best fitting yields a relaxation time of the patterned sample around 1.3 ms at 4.2 K. The magnetic behavior in the patterned sample is similar to that expected for Mn_{12} species confirming that most of the Mn_{12}bz species retain their SMM behavior upon structuration. The high χ_S/χ_T value obtained from the fit would indicate a large contribution of a fast relaxing species though measurements were not completed to the whole frequency range as previously done for the single crystals mainly due to experimental limitations of the sensor that added a very high noise specially, at high frequencies. For this reason these magnetic measurements are too preliminary to extract any conclusion at this point, being strictly necessary to reproduce these measurements with improved results that can fully confirm and asses this approach. Nevertheless, they represent a first confirmation of the validity of our approach to deposit Mn_{12} on the selected areas of these sensors.

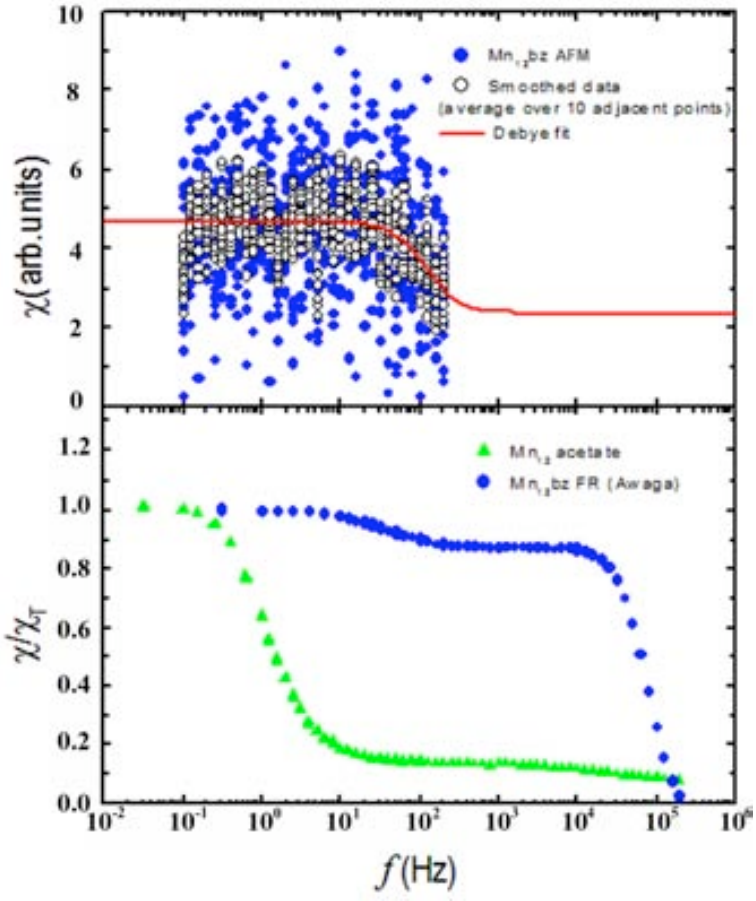

Figure 4.27 (a) In-phase ac susceptibility of the Mn_{12}bz sample deposited by direct-write AFM lithography measured at T = 4.2 K. Solid line represents the best fitting of the experimental data to the Debye function, Equation (4.1). (b) In-phase ac susceptibility of Mn_{12}-acetate and Mn_{12}bz single crystals measured with the same microSQUID sensor at T = 4.2 K. Measurements within the whole bandwidth of the system enable to observe the magnetic relaxation of the two molecular species present in this sample (the slow and fast relaxing species). Data obtained by Dr. F. Luis and co-workers.

4.4 Summary

Overall, this study demonstrates the feasibility of direct-write AFM lithography to structure molecular systems on surfaces. Both families of molecular materials showing SMM behavior, the well-known Mn_{12} and ErW_{10} POM, were used for this study. Mn_{12} molecules were organized into few layered structures in the form of dots and lines with sizes down to 200 nm. In addition, large areas in the range of millimeters were covered with arrays by repeating the process of writing with the tip. XRD as well as HR-TEM experiments revealed that the deposited Mn_{12} molecules arranged into an amorphous material rather than in a crystalline phase once the droplet was evaporated under air. In the case of ErW_{10} POM molecules, the supramolecular self-assembly of this molecule into capsule-like structures was investigated. For this, first experiments were devoted to the investigation of this self-assembly process in solution as well as on surfaces by depositing the material by drop casting or spraying it on a surface. The evaporation rate of the deposited solution appeared as a key parameter in order to induce the formation of such spherical structures. Once the conditions for the formation of such structures on surfaces were identified, we moved to the study of their formation into droplets deposited by direct-write AFM lithography. By slowing down the evaporation rate of the droplets, the formation of spherical structures was observed inside the dots of the fabricated arrays. However, in addition to the capsules, the formation of some needle-like structures was also observed. Having control to strictly obtain capsules and then avoid the presence of other structures requires further experiments in order to control the kinetic and thermodynamic parameters that guide their formation. These results show that direct-write AFM lithography can be used to induce the assembly of molecules on surface into well-organized supramolecular structures.
In the last section of this chapter, the integration of molecular materials into a second generation of microSQUIDs with sensing areas that have been reduced down to 30 μm was described. For these experiments, we decided to work with the Mn_{12} molecules since their magnetic properties are well-characterized and we had a better control on its structuration rather than with POM. If confirmed upon additional Mn_{12} decorated sensors are measured, these results would confirm:

- The feasibility of direct-write AFM lithography to decorate the sensing areas of sensors with sizes down to a few tens of microns without any previous functionalization, just at the frontier of the detection limit of the sensor.

- Mn_{12} molecules still conserve their characteristic SMM behavior upon deposition on surfaces even though some previous works of other authors seem to evidence the contrary. For instance, Sessoli *et col.* reported that Mn_{12} molecules organized as single layers on Au surfaces lose their SMM behavior by XMCD.[43] Such divergence of results may arise from the presence of more than one layer on the deposits fabricated. While the first monolayer is clearly influenced by the substrate even up to the point of losing their SMM behavior (either due to molecular deformations or redox reactions), further layers deposited on top of the first one are not. This would result on the observation of the SMM behavior. This selective alteration of the molecules upon the

number of deposited layers has already been pointed out by Ruiz-Molina *et col.* on previous studies by AFM.[293] Nevertheless further experiments are required to confirm this theory.

Chapter 5

Magnetic nanoparticle structuration and integration into graphene-based nanoHall sensors

In the previous chapters we have already demonstrated the potential of direct-write AFM lithography to successfully integrate magnetic samples onto the sensing areas of microSQUID susceptometers. At this point, it is important to notice that the sensing region of the sensors was rectangular-shaped area of 63 μm × 250 μm in the first case and circular-shaped area of 30 μm in diameter in the second case. Therefore, the integration into these regions required a micrometric control that can be achieved by monitoring the tip movement over the sensor surface by optical control. However, this approach becomes inadequate when we need to accurately integrate such entities into sensors whose sensing areas are significantly miniaturized down to 1 μm × 1 μm in size. Herein, we develop a strategy based on one of the major advantages of AFM lithography, that is, this technique offers not only writing but also imaging capabilities. A three step protocol has been specifically designed for this purpose, where a single tip acts not only as a delivery system but also as imaging tool. First the target area is located by scanning the tip over the predetermined positions. Second, the tip is functionalized *in situ* by scanning over a droplet containing the NPs deposited within the X-Y range of the scanner. And finally, the tip is placed back on the sensor to deposit the desired material. The main advantage of this approach is that it is easy to implement with any AFM platform since the same tip is used both, to visualize the target area and subsequently to deposit the material with (sub)micrometric resolution over the same region. As a proof-of-concept to validate this approach cobalt NPs (Co-NPs) have been successfully positioned into a 1 μm × 1 μm sensing area of a graphene-based nanoHall sensor. As in previous chapters, first a brief overview of the experimental approaches followed for the structuration of magnetic NPs on surfaces is given, followed by the experiments done to establish the deposition conditions.

5.1 Introduction: Advances on structuring magnetic nanoparticles on surfaces from solution

NPs are of intense current interest for a variety of applications, not only for the general miniaturization of devices, but because their physical properties vary dramatically from their bulk counterparts. Magnetic NPs show remarkable new phenomena that arise from finite size and surface effects that dominate the magnetic behavior of individual NPs, such as superparamagnetism and enhancement of the magnetic anisotropy.[12] In recent years, the synthesis of diverse NPs with control on distribution particle size, shape and chemical composition has made substantial progress.[12, 13] Beyond the efforts devoted to the development of synthetic routes, one of the most important challenging parts is their organization at the nanoscale, which is crucial for their characterization and realizing their novel applications. In the first part of this section a review of the different experimental approaches so far followed for the structuration of magnetic NPs on surfaces is given.

5.1.1 Organizing magnetic nanoparticles on surfaces from solution

Self-assembly is the autonomous organization of pre-existing entities through non-covalent interactions leading to spontaneously formed hierarchical and complex architectures.[349, 350] While being already common on nature for the creation of multi-dimensional and complex biological structures such as cells,[350] the concept of self-assembly has been more recently used as a powerful strategy for controlling the structure and properties of man-made nanostructures. Magnetic NPs have not been indifferent to this approach. Self-assembly has been undoubtedly one of the most fruitful approaches for their organization on surfaces influenced by three main factors: (i) deposition process, (ii) category of interactions and (iii) geometry and environmental parameters. Several examples of self-assembled magnetic NPs have been described in the literature.[351-354]

Chemical assistance is an attractive approach to fabricate highly stable and well-ordered monolayer films of magnetic NPs over large substrate areas. With this approach the stability of the films is strongly improved by introducing appropriate linkers with suitable terminal functionalities that anchor the magnetic NPs to the surface. Beyond the stability gain, this approach clearly favors the monolayer distribution of the magnetic NPs over the substrate instead of the formation of multilayers and provides control on the surface coverage.[355, 356] The use of the linkers can be done in three different ways: (i) functionalization of the NPs with linkers bearing terminal groups able to react with the surface,[355, 357] (ii) functionalization of the surface with linkers bearing terminal groups able to react with the NPs[356, 358, 359] and (iii) a combination of both[360] (**Figure 5.1**). Alternatively, the presence of an applied external magnetic field either perpendicular or parallel to the substrate was exploited to induce the organization of NPs in a specific directional manner.[361-363] It is not our aim to make a complete review of all such examples but to concentrate in those examples where an external technique is used to template their organization, such is the case of direct-write AFM lithography.

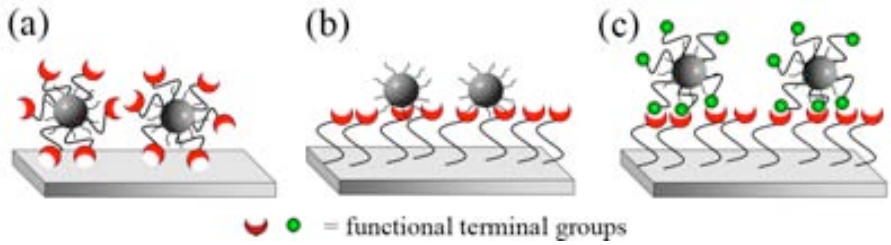

Figure 5.1 Schematic illustration of the three main approaches used on the chemically-assisted assembly of magnetic NPs on a substrate: (a) functionalization of the NPs with linkers bearing terminal groups able to react with the surface, (b) functionalization of the surface with linkers bearing terminal groups able to react with the NPs and (c) a combination of both.

5.1.1.1 *Deposition of magnetic nanoparticles on surfaces assisted by templates and/or lithographic techniques.*

Magnetic NPs can be organized into structured motives down to the nanoscale level on a substrate with lithographic techniques following two main techniques, stamp-based (soft lithography) and other lithographic techniques. Moreover, each one of them can be used following two different approaches: (i) direct deposition approach and (ii) the indirect deposition approach, where templates are used to first pattern a chemically modified substrate that subsequently guides the site-selective assembly of the NPs.

Stamp-assisted structuration. The technique most widely used for the stamp-assisted structuration of magnetic NPs on surfaces is that of μCP. This technique can be used for the direct patterning of NPs on surfaces though most of the examples so far reported rely on the indirect deposition approach. In general, in the indirect deposition approach the elastomeric stamp fabricates SAM patterns on which the magnetic NPs are attached upon dipping the structured surfaces (**Figure 5.2**a).[364-366] For instance, Whitesides *et col.* applied this process to the selective deposition of positively or negatively charged Fe_3O_4 NPs (5-12 nm in size) on Au substrates, which were previously patterned with both hydrophobic and hydrophilic SAMs with features sizes of microns and thickness between 50 and 100 nm by μCP.[364] Further organization of magnetic NPs into ring-like structures of approximately 10 μm in diameter and 450 nm in high was also feasible by the fabrication of patterned hydrophobic and hydrophilic SAMs using μCP (Figure 5.2b).[365]

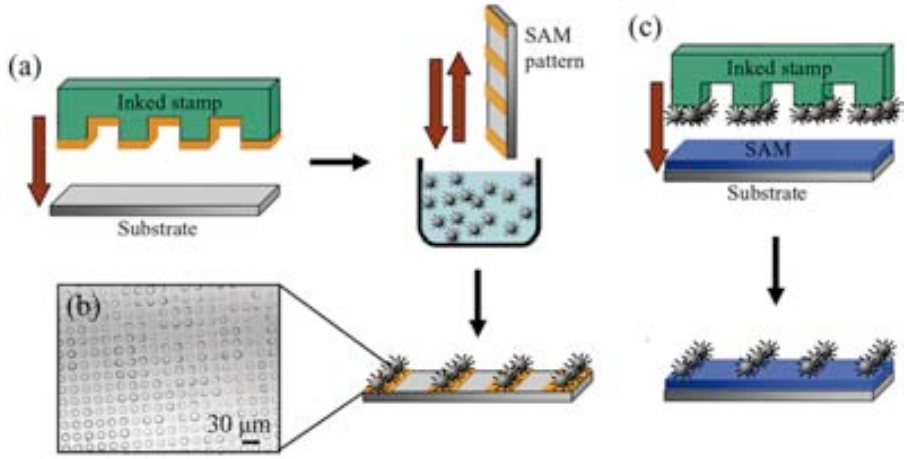

Figure 5.2 (a) Schematic illustration of the indirect deposition approach by means of µCP. (b) Optical image of a polystyrene-coated ~ 10 nm Fe_3O_4 NPs into ring-shaped structures. (c) Schematic illustration of the direct approach by means of µCP. Panel **b** reproduced from ref.[365].

By combining both µCP and click chemistry, Kinge *et col.* directly generated patterns of highly packed ~ 5 nm FePt NPs monolayers with an elastomeric stamp that was directly immersed into a solution containing the NPs.[360] The stamp can also been functionalized with a LB film, technique known as patterned Langmuir-Blodgett (pLB) (**Figure 5.3**a).[367-369] Following this approach Guo *et col.* prepared LB films on top of a stamp of γ-Fe_2O_3 NPs (~ 13 nm)[367] or core-shell ~ 4 nm Pt@Fe_2O_3 NPs patterns[368] that later on were transferred to silicon or other substrates (Figure 5.12b-d). Uniform NP patterns with different shapes were printed including micrometer size lines, squares and meshes, with heights of 40 ± 3 nm corresponding to six NPs.

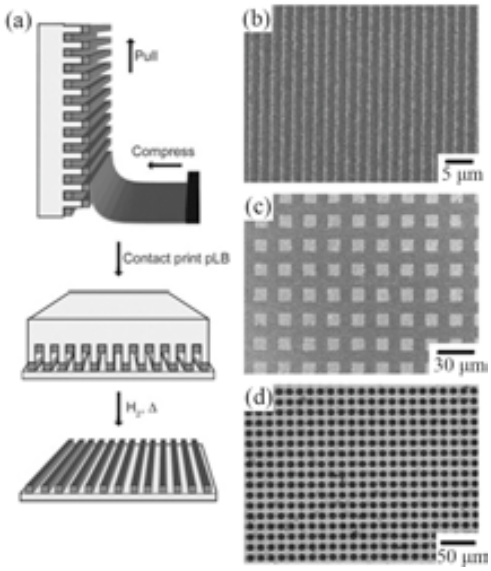

Figure 5.3 (a) Schematic illustration of pLB procedure followed by additional thermal treatment. SEM images of the obtained FePt microstructures after thermal annealing: (b) lines (1 µm wide), (c) squares (2 µm wide) and (d) meshes (10 µm dot diameter). Reproduced from ref.[368].

Finally, a variation of the stamp-assisted methodology called micro-injection molding in capillaries (MIMIC) was used by Cavallini *et col.* to pattern ~ 13 nm Fe_3O_4 NPs in micrometric stripes and dots on mica.[370] First, an elastomeric stamp was placed in contact with a solid

surface forming a sub-micrometric channel network at the interface. Then, a solution containing the NPs was deposited at the open end of the stamp spontaneously filling the μ-channels by capillary forces. The MIMIC method allowed the formation of spatially well-organized microstripes whose thickness corresponded to a single layer of Fe_3O_4 NPs.

Lithography-assisted structuration. This approach involves mostly the use of electron EBL and photolithography for the fabrication of physical templates that can be used to structure the magnetic NPs. The topographically structured surfaces physically guide the assembly of the magnetic NPs to specific areas, such as porous on a substrate, without the need of specific chemistry.[371-373] For instance, Chen *et col.* have recently reported the use Si surfaces patterned with nanometric pits by EBL that act as templates for the site-selective positioning of ~ 18 nm core-shell FeO@$CoFe_2O_4$ NPs (**Figure 5.4**).[373] Interestingly, this method successfully controlled the number of NPs down to a single one per unit pit by accurately controlling the pit and the NP size, as well as the NP concentration.
An alternative approach is the use of masks that guide the self-assembly of the NPs exclusively onto the bare areas of the substrate, while the lift-off of the mask removes the rest of the NPs. The masks are prepared by spin coating a polymer on a surface and posterior pattern with the desired motive by means of photolithography.[374, 375] Using this strategy, 3-4 nm FePt NPs were covalently anchored on a H-terminated silicon surface and patterned into ordered arrays of 1 μm^2 dots with heights of 15-30 nm, which corresponded to 2-4 layers of NPs.[374]

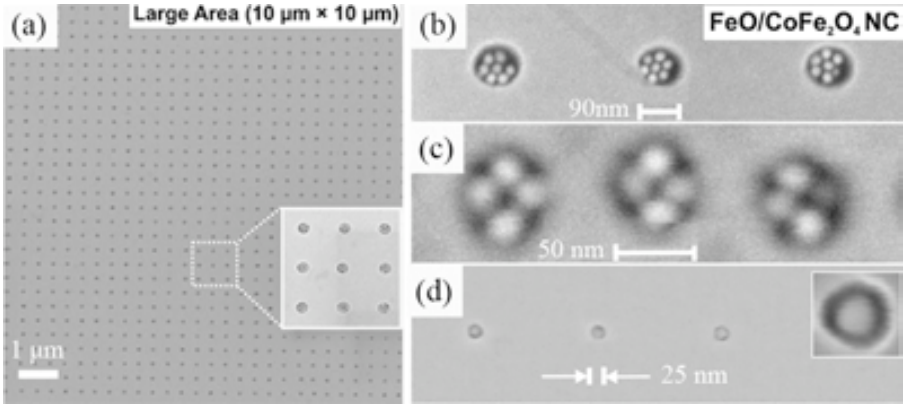

Figure 5.4 Patterns of ~ 18 nm FeO/$CoFe_2O_4$ core-shell and ~ 50 nm Fe_3O_4 NPs. (a) Large-area SEM image of an array with 110 nm pit diameter filled with NPs. (b-d) SEM images showing the control over the number of NPs per pit down to the single particle level, simply by adjusting the pit diameter from 90 to 25 nm. Reproduced from ref.[373].

5.1.1.2 *Deposition of magnetic nanoparticles on surfaces assisted by AFM-based lithographies*

AFM-based lithography techniques have attracted much interest because of their exceptional capabilities for patterning magnetic NPs onto a given substrate with nanometric resolution. Significant advances have been made in this direction including the use of LON, nanoembedding (n-EM) and direct-write AFM lithography. Representative examples of these approaches are revised next.

Local oxidation nanolithography (LON). LON has been applied for the local modification of the terminal groups of SAMs in order to create templates that afterwards are used to induce the assembly of magnetic NPs. For example, terminal CH_3-terminated SAMs on a Si substrate were first locally converted into -COOH terminal groups by applying a suitable voltage to the conductive tip to induce an electrochemical reaction exclusively at the terminal functionalities of the SAM while fully preserving the integrity of the whole layer. The SAM template was then used for the selective attachment of NPs such as γ-Fe_2O_3, Fe_3O_4 and FePt into stripes and arrays of dots with feature sizes down to sub-100 nm (**Figure 5.5**).[376-378]

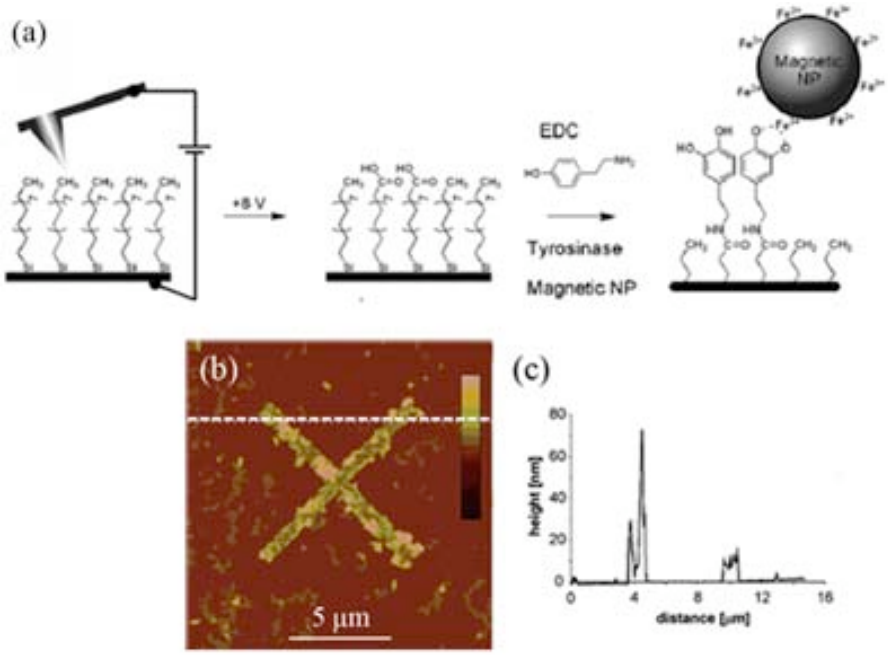

Figure 5.5 Pattern of ~ 9 nm γ-Fe_2O_3 fabricated by means of bias-assisted AFM nanolithography. (a) Schematic illustration of the procedure. (b) AFM image of the magnetic pattern, whose height scale is 100 nm, and (c) height profile along the white dashed line in panel **b**. Reproduced from ref.[376].

Nanoembedding (n-EM). The n-EM consists in a modification of the previously described bias-assisted nanolithography technique and was implemented by Cavallini *et col*. In a first step the deposition of the particles takes place by techniques such as spin coating or lithographically controlled wetting (LCW). Subsequently the magnetic NPs are embedded by a conductive tip that applies a bias voltage to the silicon surface, inducing the growth of a local oxide coating layer while preserving their morphological and magnetic properties. The use of this technique has been reported so far for the nanoembedding of $CoFe_2O_4$ NPs (~ 6 nm) on silicon substrates (**Figure 5.6**a).[379] Moreover, replacement of the tip by a conductive stamp permitted the structuration of NPs into parallel stripes or grids (width of 200 nm) applied along vast areas of 1 cm × 1 cm (Figure 5.6b). The number of embedded NPs depended on the NP concentration of the initial colloidal solution.

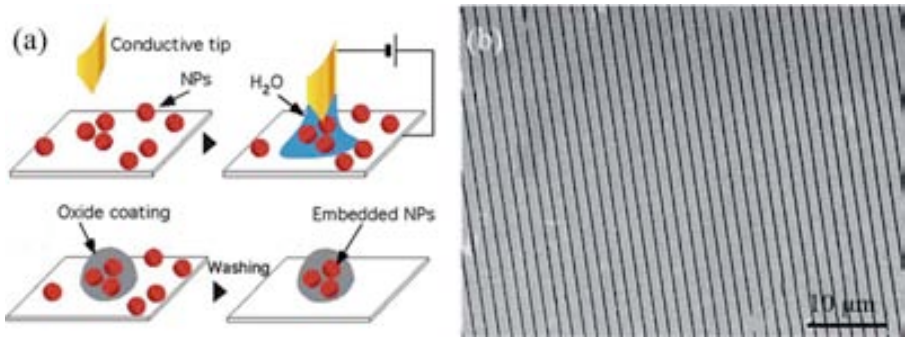

Figure 5.6 Patterns of ~ 6 nm $CoFe_2O_4$ NPs fabricated on Si substrate by means of nanoembedding (n-EM) technique. (a) Schematic illustration of the process. (b) SEM image NPs embedded into parallel stripes of SiO_2 patterns. Reproduced from ref.[379].

Direct-write AFM lithography. While for the ferritin and SMM cases there were no previous examples of the use of direct-write AFM lithography for their structuration on surfaces, this was not the case for magnetic NPs. For example, after coating a tip by immersion into a colloidal dispersion of citrate-capped ~ 11 nm γ -Fe_2O_3 NPs and posterior drying, Gundiah *et col.* fabricated magnetic nanostructures by scanning in contact mode a mica or Si substrates.[172] Although this method achieved single layer lines ranging from 140 to 200 nm and lengths extending to 10 μm, the major drawback was its extremely slow patterning process, which needed scan speeds of ~ 1 $\mu m \cdot s^{-1}$ for a period of 30 min. By contrast, Zhang *et col.* reported a DPN® process for magnetic NP structuration over large areas on a Si/SiO_2 or quartz substrate at shorter time periods (e.g. dots of 381 nm in diameter were generated by holding the coated tip in contact with a surface for 0.8 s).[269] Co NPs (~ 5 nm) capped with oleic acid and trioctyl phosphine oxide (TOPO) were kept on the tip in a fluid-like state in order to ensure an efficient material transfer from the tip to a substrate through a meniscus composed of the ink material itself. By controlling the contact time of the tip over the substrate, lines of 880 nm in width and dots down to 68 nm in diameter composed of 2-3 layers of NPs were generated. Additionally, the patterned NPs served as catalysts to guide the site-selective growth of well-aligned single-walled CNT arrays on quartz substrates by chemical vapor deposition.

This technique has also been used to assist the assembly of magnetic NPs on surfaces by the indirect deposition approach.[149, 177, 196] One possibility reported by Mirkin *et col.* is to fabricate templates/motives made of SAMs bearing COOH-terminal groups on a Au surface while the rest of the surfaces is passivated with an unreactive layer of CH_3-terminated SAM.[149] For this, alkanethiol molecules were first coated and dried onto the tip and then brought in contact with the Au substrate by DPN®. The resulting template was then dip coated into a basic solution containing either Fe_3O_4 or $MnFe_2O_4$ NPs (both of ~ 10 nm) coated with positively charged tetramethylammonium ligands in order to favor the electrostatic interaction with the negatively charged COO^--pattern. Single-layer NP structures of dots and stripes with high control on the feature size (from few micrometers to 45 nm) and homogeneous arrays of 21 × 22 dots with a fixed dot diameter (85 ± 5 nm) were achieved. Further studies by Mirkin *et col.* were directed towards accommodating single NPs per each feature of a nanoarray by DPN®.[196] This was accomplished by using a solvent that selectively wets the carboxylic pattern but not the methyl passivating regions. The effect of the template feature size to the MNP assembly was studied with dots of sizes in the range between 50 and 120 nm, and it was found that feature sizes of 60

nm were optimal to generate single Fe@C NP (~ 5 nm) per feature, what demonstrates the high control on the deposition at a single particle level (**Figure 5.7**).

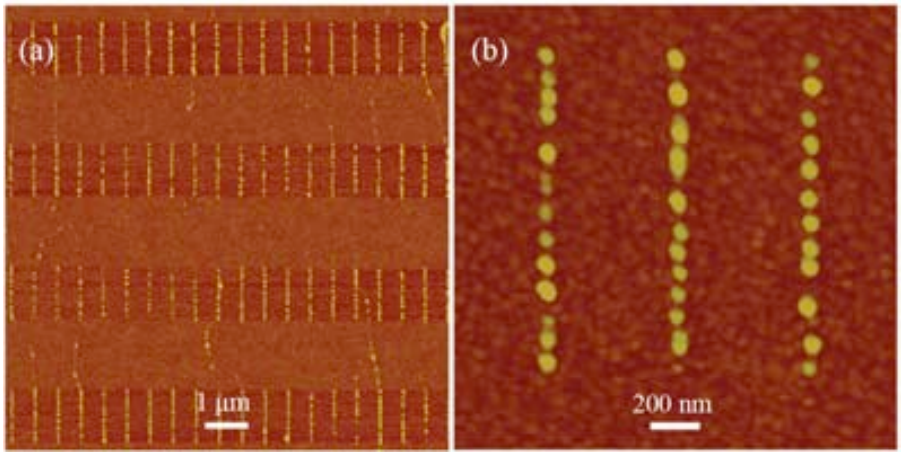

Figure 5.7 (a) AFM image of an array made of lines accommodating individual Fe@C NPs and (b) a higher magnification of the same array fabricated by DPN®. Reproduced from ref.[196].

Finally, a variation of the AFM-based lithography technique, referred to as thermal DPN®, makes use of a cantilever with integrated resistive heaters. Initially the ink deposited on the tip is solid at room temperature but upon heating, the melted ink flows from the tip to the surface.[380] Depending on the scan speed and the tip temperature, the deposition can be switched on and off and the feature sizes controlled to sub-100 nm resolution. Interestingly, this technique allows both the deposition of nanocomposites composed by a wide range of polymers containing either NPs or molecules as well as non-specific substrate deposition. In particular, Lee *et col.* reported the use of this technique for the structuration of magnetic NPs by coating a tip with a composite ink of ~ 7 nm Fe_3O_4 NPs and polymethylmethacrylate (PMMA).[151] In this way lines between 78 and 400 nm in width by controlling the tip temperature and scan speed were fabricated (**Figure 5.8**). Furthermore, the polymer matrix was successfully removed from the pattern upon exposure to oxygen plasma treatment, which drastically reduced the width of the lines down to just 10 nm well-defined single particle rows.

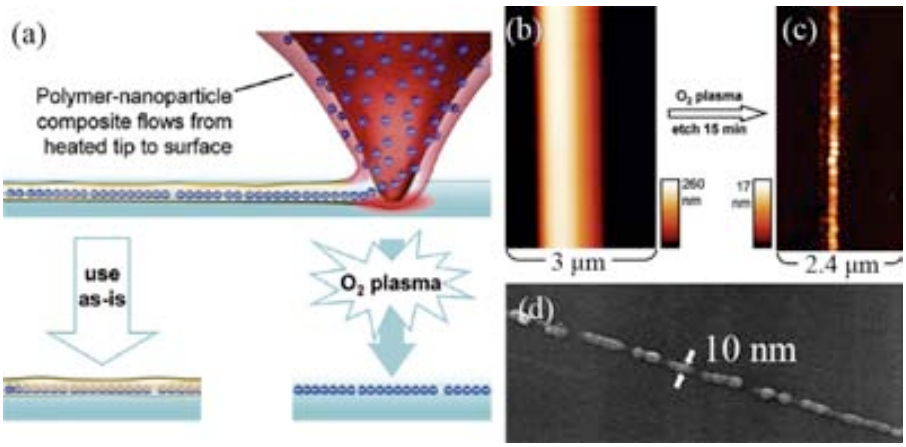

Figure 5.8 (a) Schematic illustration of the fabrication of the thermal DPN® process. After deposition of the composite ink the polymer was removed by oxygen plasma treatment. AFM and SEM images of the fabricated pattern (b) before and (c, d) after the elimination of the polymer. Reproduced from ref.[151].

5.1.2 Surface structuration strategies: Summary

Overall the reviewed works are representative examples of the great efforts made on organizing magnetic NP on surfaces into well-defined patterns with control down to single particle level. Lithographic techniques such as soft lithographies based on the use of stamps have been applied following the direct as well as the indirect deposition of these magnetic systems. We would like to focus our attention to the advances reported on using AFM-based lithographies. In this case, direct-write AFM lithography has already been used for the direct deposition of magnetic NPs without the need of any template before the present Thesis.[172] Even more, a continuous development of better inks for different surfaces appeared during the present Thesis for the structuration of magnetic and non-magnetic NPs. For example, in 2008 Zhang *et col.* reported excellent results on directly delivering Co NPs on Si/SiO_2 and quartz substrate.[269]

However, to the best of our knowledge, to date there are no previous works regarding the use of this technique for the structuration on graphene even at the moment of writing this manuscript though graphene has raised much attention due to their interesting electrical, optical, thermal and mechanical properties.[110-113] Graphene exhibits a high Young's modulus and fracture strength with potential applications in reinforced composites.[381] Its high thermal/chemical stability and large specific surface area are also of interest in catalysis and sensors,[382] whereas the interesting transport phenomena and high optical transmittance are of great relevance in photonics and optoelectronics,[383] as well as in electronics and spintronics.[116, 117, 384, 385]

Most of these applications require the development of graphene-based hybrids systems in order to enable versatile and tailor-made properties with performances far beyond those of the individual materials.[386] Though, the accurate incorporation of different families of organic and/or inorganic materials without modifying the graphene intrinsic structure and properties is a delicate step. To date, this challenge has been addressed in bulk by means of either *in-situ* syntheses[387-389] or self-assembly processes,[390, 391] which permitted the uniform functionalization of graphene with a wide variety of materials, such as organic compounds, polymers, inorganic NPs and other molecular-based materials.[116, 382] The structuration of materials into patterns on graphene surfaces have been less reported and mainly focused on the fabrication of arrays of Au deposits by thermal evaporation[392] or combined electron beam, metallic film deposition and lift-off processes.[393] Although these studies were successful on structuring materials into regular patterns on graphene with control on feature thickness and size down to nanometer scale, the ability to accurately control the positioning of these structures on pre-selected sites of a graphene surface still remains a challenge.

In this chapter we describe a novel methodology for direct deposition of magnetic NPs on graphene without modifying its interesting electrical properties, having control not only on the final morphology but especially on the positioning. This capability allowed us as an ultimate goal to integrate these magnetic materials into the sensing areas of a graphene-based nanoHall sensor. These experiments were performed in collaboration with Dr. N. Domingo from CIN2.

5.2 Experimental conditions for the structuration of magnetic nanoparticles on surfaces by direct-write AFM lithography

We first investigated the deposition of magnetic NPs on Si/SiO_2, since this surface was largely studied for the structuration of the other magnetic materials along this Thesis. The deposition of magnetic NPs on surfaces requires the use of particles uniform in size and shape while stable during the writing process. In this sense, cobalt NPs (abbreviated as Co-NPs) with an average size of 7.6 ± 1.0 nm, synthesized and characterized by Dr. I. Ojea-Jiménez at the CIN2, were selected (see **Figure 5.9**). The NPs were surrounded by oleic acid molecules, which create an excellent capping layer that sterically stabilize the NPs in the organic solution while protecting against oxidation. These NPs are superparamagnetic at room temperature with a blocking temperature of $T_B \approx 130$ K, and a magnetic moment of $\sim 10^4\ \mu_B$ (for more information about their synthesis and characterization see Experimental Section 7.1).

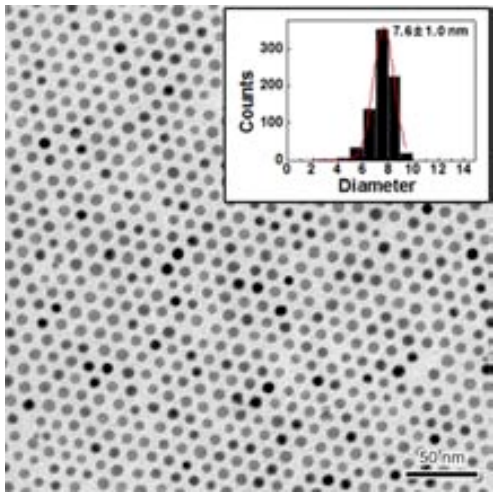

Figure 5.9 Morphological analysis (TEM) of a monolayer of oleic acid-coated Co-NPs with a hexagonal packing. The inset shows the mean size distribution of Co-NP measured from TEM images. Images obtained by Dr. I. Ojea-Jiménez.

Our model ink solution consisted in a dispersion of Co-NPs ($2 \cdot 10^{15}$ NPs·mL^{-1}) in *o*-DCB with an excess of oleic acid (0.08 % w/w), which was made by diluting (1:10) the as-synthesized Co-NP solution (described in the Experimental Section 7.1). However, different ink compositions were also tested by precipitating and redispersing the NPs into different solvents (1:10 dilution), of varying boiling points, and evaluating the effect in the final ink behavior. The use of hexane as solvent significantly hampered the structuration process due to its highly volatile character (b.p. 69 ºC), since it rapidly evaporated during the tip coating step. By contrast, the use of toluene as solvent (b.p. 110 ºC) partially reduced the evaporation rate of the ink solution, allowing the adequate coating of the tip and the deposition of the Co-NPs in the form of arrays on top of Si/SiO_2. However, after the fabrication of few arrays the ink solution unavoidably dried on the tip surface leading to the deposition of broken solid pieces on the surface during the writing process.

Overall, the use of *o*-DCB in the ink solution was the most convenient solvent since its high boiling point (b.p. 180 ºC) increased the total drying time of the ink, favoring the homogeneous transference of the NPs from the tip to the substrate. Additionally, the relatively large aliphatic chains of oleic acid are also capable of trapping solvent molecules, thus maintaining the ink in a liquid-state behavior for extended times, as already observed by Ondarçuhu *et col*.[270, 394]

Another important point related with ink transport is the high viscosity of oleic acid (whose value is 27.64 mPa·s at 25 ºC). As we have already mentioned with the use of glycerol in the final ink formulation (see Chapter 3 and 4), in direct-write AFM lithography experiments the use of high viscosity additives in the ink solution favors not only the controlled direct transfer of the material from the tip to the surface but also the coating of the ink on the tip.[266, 267] We noticed that the presence of oleic acid is pivotal to ensure an effective transfer of NPs on a surface when we tried to perform control experiments on Si/SiO_2 surfaces with oleic acid-free inks, such as *o*-DCB or toluene. Under these conditions, the writing process could not get any consistent patterning of the ink.

On the other hand, the non-polar character of the ink solution forced us to modify our tip coating procedure from that used in the previous chapters. Up to now we have used the Inkwell chips for a simple and easy transfer of the ink to the tip. However, this microfluidic system is specifically engineered to be filled with polar solvents such as aqueous ink solutions. For this reason, in order to bring a non-polar ink solution onto the tip is necessary to follow an alternative route called the *scanning coating* method.[269, 270] Based on this strategy, our experiments followed the steps depicted in **Figure 5.10**a. First, the ink solution was drop casted onto a Si/SiO_2 substrate and left to partially evaporate for a given time until it remained a very thin liquid film at the edge of the droplet. Then, a tip was approached to the surface until it touched the film in a very smooth manner. Once in contact, it was scanned twice in contact mode over a 5 x 5 μm^2 area at 1 line·s^{-1}, while keeping the tip dipped into the ink film. This coating procedure ensured a uniform coating of the tip with sufficient loading of ink, as verified by FE-SEM in Figure 5.10b,c. Finally, the freshly coated tip was used for the patterning of Co-NPs on a second Si/SiO_2 substrate by traversing the tip over the surface in the form of the desired pattern. Note that previous to the writing process, it was necessary to reduce the excess of ink loading the tip through cantilever and tip *bleeding*. For this study, we made use of commercially available single pen tips (A-Type single pen from NanoInk, described in Experimental Section 7.2 and abbreviated to as SP tips). Similar to the MP tips, this type of tips is optimized also for writing viscous liquids in addition to be modified with a recessed area surrounding the tip base that increases the loading of the ink material. Similar results were obtained using MP tips as well; however MP tips provided extended printing times due to their larger recessed area. All the experiments were performed using Nscriptor^{TM} instrument and under controlled environmental conditions (i.e. relative humidity at ~ 50% and room temperature).

By using these experimental conditions on Si/SiO_2 substrates, well-defined structures from few micrometers to down to 500 nm were fabricated in a controlled manner. As an example, a representative array consisting of repeated 981 ± 62 nm dot-like features spaced by 4 μm is shown in **Figure 5.11**a. The height profile analysis shows a high uniformity in size

demonstrating the ability to structure NPs on surfaces via this patterning strategy. The cross-section analysis of one row of the array is given in Figure 5.11b. The average height of the pattern was 12 ± 1 nm, which is close to what is expected for a single layer of Co-NPs.

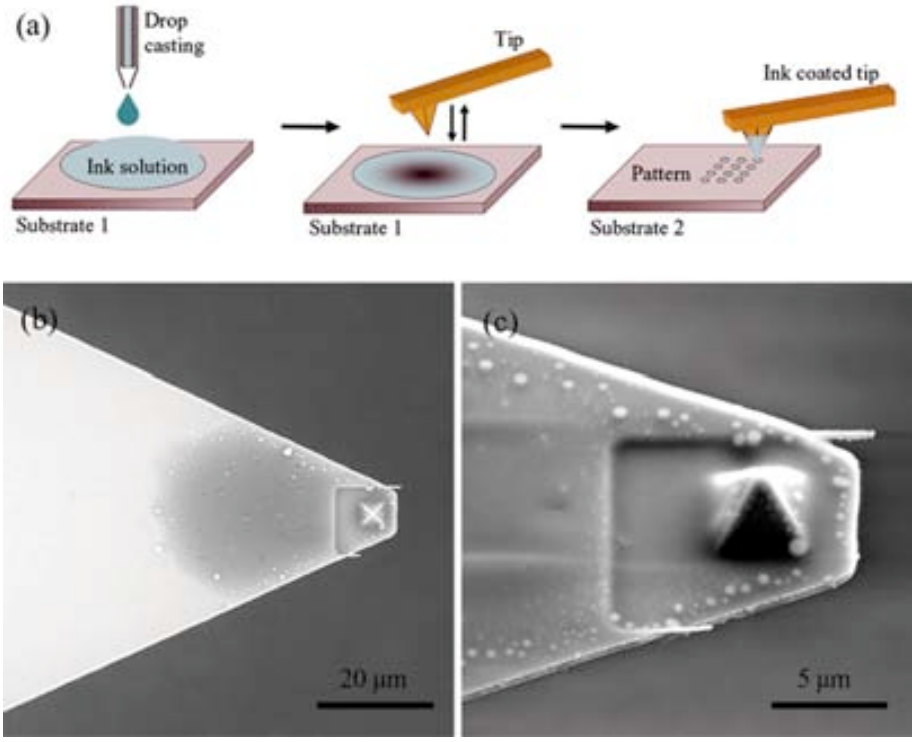

Figure 5.10 (a) Schematic illustration of the tip coating procedure by means of *scanning coating* method and subsequent deposition of the ink onto a surface in order to fabricate a given pattern. FE-SEM image of a SP tip loaded with the ink viewed (a) from above and (c) at 45º tilt angle.

In a control experiment, two different solutions, one of them containing Co-NPs and a NP-free solution composed of a mixture of *o*-DCB and 0.08 % (w/w) oleic acid were used to generate similar arrays on a Si/SiO_2 under the same experimental conditions. Whereas the AFM characterization of the arrays generated with the NP-based ink revealed a reproducible feature height of 10 ± 1 nm for a dot diameter of 559 ± 29 nm (Figure 5.11c,d), the array fabricated with the NP-free ink shown an average feature height of 3 ± 1 nm for a dot diameter of 473 ± 51 nm (Figure 5.11e,f). In this case, the observed heights might be due to remaining solid solvent residues. More importantly is to notice that these experiments were the first evidence of the presence of Co-NPs on the structures generated by using the NP-containing ink via this patterning strategy.

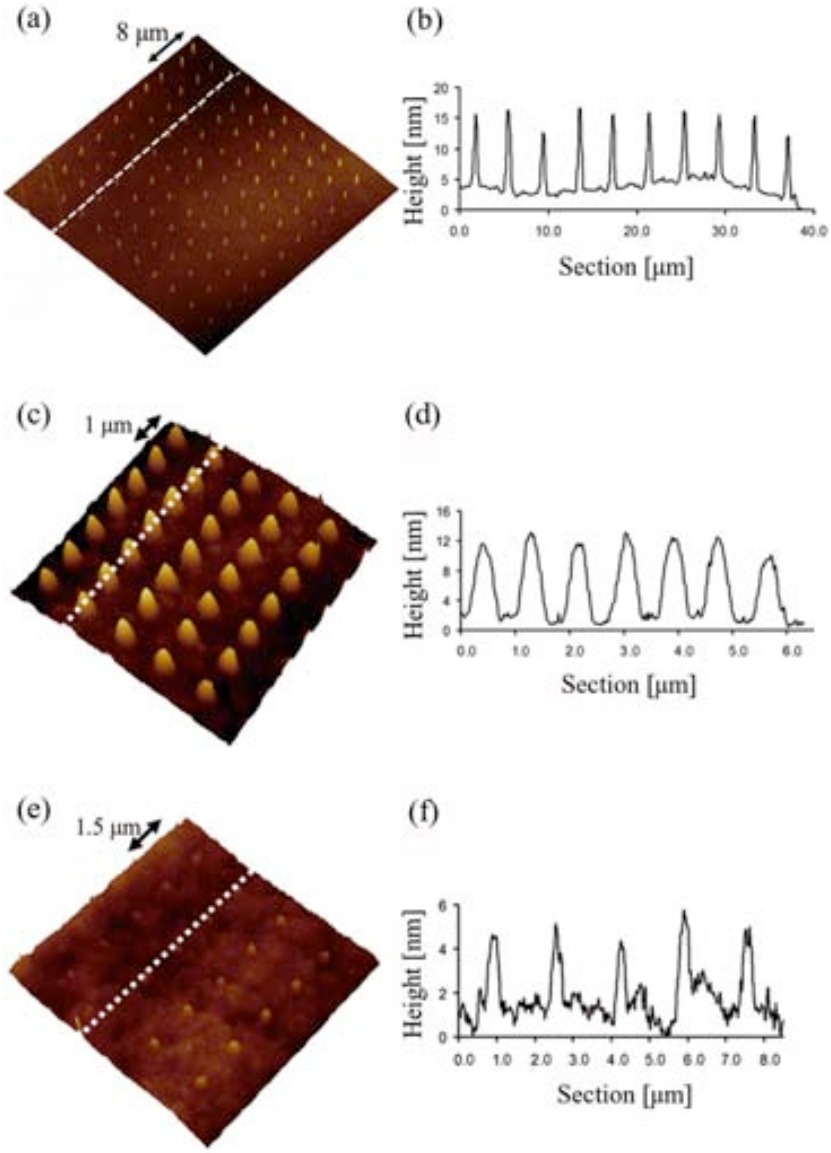

Figure 5.11 Array of repeated dots fabricated on Si/SiO_2 substrate. (a) 3-D AFM topography image of an array of Co-NPs whose spacing between features is ~ 4 µm and (b) height profile along the white dashed line in panel **a**. (c) 3-D AFM topography image of an array of Co-NPs whose spacing between features is ~ 1 µm and (d) height profile along the white dashed line in panel **c**. (e) 3-D AFM topography image of an array generated with a NP-free ink solution (*o*-DCB and 0.08 % w/w oleic acid) whose spacing between features is ~ 1.5 µm and (f) height profile along the white dashed line in panel **e**.

5.2.1 Structuration of cobalt nanoparticles on graphene

Graphene samples were prepared and characterized by Prof. M. Affronte and co-workers at CNR-Institute of NanoSciences S3. Graphene flakes were obtained by micro-mechanical exfoliation method and deposited onto a p-doped Si wafer with a 300 nm SiO_2 capping layer (see Experimental Section 7.2). The deposited flakes were optically located with respect to lithographically pre-patterned alignment marks. Interestingly, graphene becomes visible in the optical microscope when deposited on oxidized Si substrates with a finely tuned thickness of the oxide layer (typically 300 nm SiO_2) since it modifies the reflected light to slightly change the

interference color with respect the empty surface.[395] The number of graphene layers of the flakes was determined by Prof. M. Affronte and co-workers based on their optical contrast, and the exact number of layers was later on verified by micro-Raman spectroscopy.[396-398] In this sense, the electronic structure of graphene is captured in its Raman spectrum that clearly evolves with the number of layers. Raman fingerprints for single layers, bilayers, and few layers reflect changes in the electron bands and allowed the non-destructive identification of the number of layers.

Previous to the deposition of Co-NPs, we investigated the affinity of the ink solution on graphene. In this context, the interaction between the ink solution and graphene was studied by using a NP-free ink solution (*o*-DCB with 0.08 % w/w oleic acid) in order to keep the system as simple as possible. With this aim, micrometer size graphene flakes were first characterized in order to localize them as well as obtain a detailed topographical description of the sample as-received in our laboratories. As an example, **Figure 5.12**a shows an optical image of two single- and double-layer graphene flakes laying together on a SiO_2 surface were the number of flakes is indicated with white numbers (determined by AFM and micro-Raman spectroscopy at CNR-Institute of NanoSciences S3). Further analyses were done by AFM which determined a thickness of ~ 1.2 nm and ~1.8 nm for single- and double-layer graphene flakes respectively, which are much thicker of what is expected from the interlayer graphite spacing (ca. 3.35 Å) (Figure 5.12b). However, these values are consistent with previous AFM measurements which falls within 4 ~ 10 Å for single-layer graphene samples reported in the literature.[395, 399] This overestimation has been attributed to two main effects. First, the chemical contrast between graphene and SiO_2, which makes the tip to differently interact with both surfaces during AFM intermittent contact imaging (i.e. tips were found to attract much stronger to SiO_2). And second, the distance between the graphene layer and the SiO_2 surface, typically of several Å thick, that is attributed to the presence of ambient species (i.e. a layer of absorbed water) captured between both surfaces.[400]

The experiment was carried out following a pre-designed pattern which ensured the tip to simultaneously deliver the NP free-ink solution onto graphene and exposed SiO_2 areas. Figure 5.12c shows a section area where an array of 10 × 10 dots, with a dot-to-dot distance of 1.5 μm, was fabricated. The transference of the ink solution was successfully realized on both surfaces in a controlled manner and avoiding evident damaging of the graphene flakes. In addition, the ink behaves similarly when delivered either on single- or double-layer graphene flakes. A detailed study of three consecutive dots deposited two on the SiO_2 surface and the other one on the graphene evidences the surface effect on the deposited droplet. From Figure 5.12d, the dots on SiO_2 show a diameter of 528 nm and height of 4 nm (average from the two dots in the image). In contrast, the dot deposited on graphene shown a diameter of 676 nm and height of 3 nm. As the dots were generated in a consecutive manner, effects of depletion of the ink were neglected. These differences in dot size can be explained due to the non-polar character of *o*-DCB which resulted into a higher affinity of the ink for the graphene than for the SiO_2 surface. Even though several factors, such as the effect of the underneath SiO_2 surface and the presence of residues left from the adhesive tape during graphene preparation can modify it,[401, 402] graphene remains more hydrophobic than the surrounding SiO_2 surface. Therefore, the higher

wettability of the ink on graphene gave to a lower contact angle of the deposited droplets, and therefore, to higher dot diameters (Figure 5.12d). Interestingly, the differences in surface wettability were even more evident when the droplets were deposited on the near edges of the flakes, as shown in Figure 5.12e. An imaginary grid pattern on the AFM image of a section area of 6 μm × 6 μm of the flake near its edge show the expected positions for each dot of the array, as indicated by the intersection of two white-dotted lines. When the expected position falls in the edge of graphene, the dots appear clearly shifted up to 500 nm to the graphene surface due to the higher wettability of the graphene surface compared to the SiO_2.

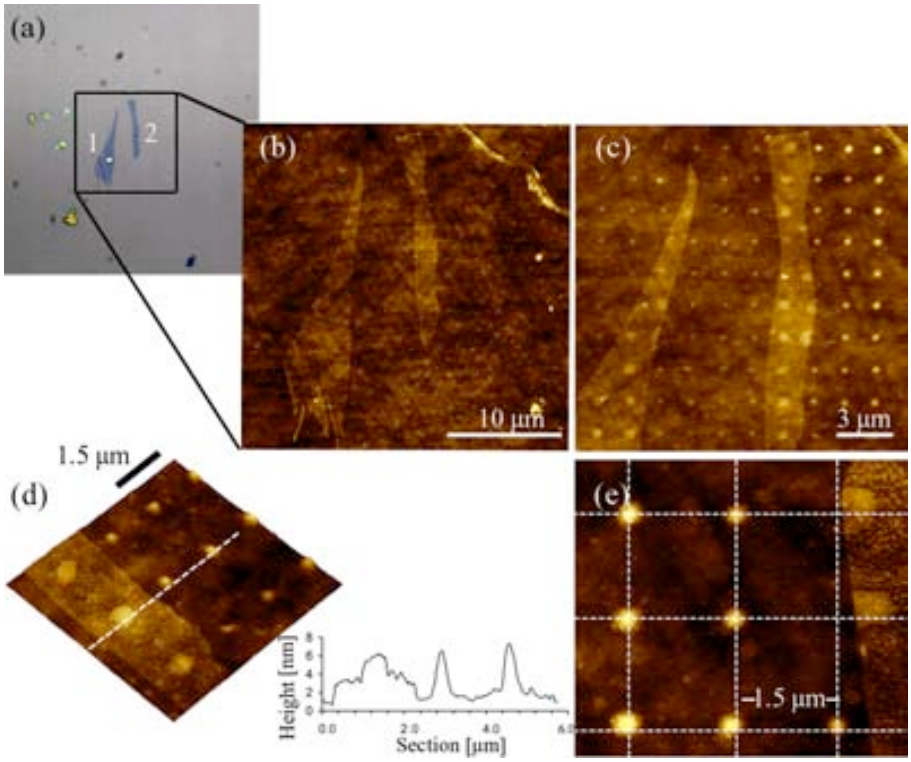

Figure 5.12 Array fabricated using a NP free-ink solution on graphene and SiO_2 surfaces. (a) Optical image of the graphene flakes before deposition where the number of graphene layers is indicated. AFM topography image of the two graphene flakes (b) before and (c) after the deposition of the NP free-ink solution in the form of an array of dots separated by 1.5 μm. (d) 3-D AFM image of a section of the array and height profile along the white-dashed line indicated on the AFM image. (e) AFM topography image 3 × 3 dots section of the array where an imaginary grid pattern indicates the expected positions for the dots.

The optimum experimental conditions found in these previous experiments were used afterwards for the successful deposition of Co-NPs as consistent arrays onto graphene flakes supported on a SiO_2 surface. In a representative example shown **Figure 5.13**, a 6 × 6 dot array of Co-NPs with a dot-to-dot distance of 4 μm was simultaneously fabricated on graphene and SiO_2. As can be seen there, dots of Co-NPs are nicely deposited on graphene though with a shape that considerably differs from those obtained on the SiO_2. As expected, effects of the differential wetting capabilities of the ink on both surfaces were clearly observed also in this experiment. Indeed, the average dot diameter on graphene was 1.2 ± 0.2 μm, considerably larger than the 747 ± 64 nm obtained on the SiO_2. The differences in the surface wettability were also evident when the droplets are at near edges of the flakes, where dots appear clearly shifted up to

800 nm towards the graphene surface. It is important to note that the presence of Co-NPs on the dot features was clearly evidenced due to the increase on the height of the structures compared to the obtained in NP-free experiment described above. For example, in Figure 5.13d the cross section of three aligned dots show a height of 8 nm (average from two dots) and 18 nm (from a single dot) on graphene and SiO_2, respectively. These values are in good agreement with the expected heights due to the presence of Co-NPs.

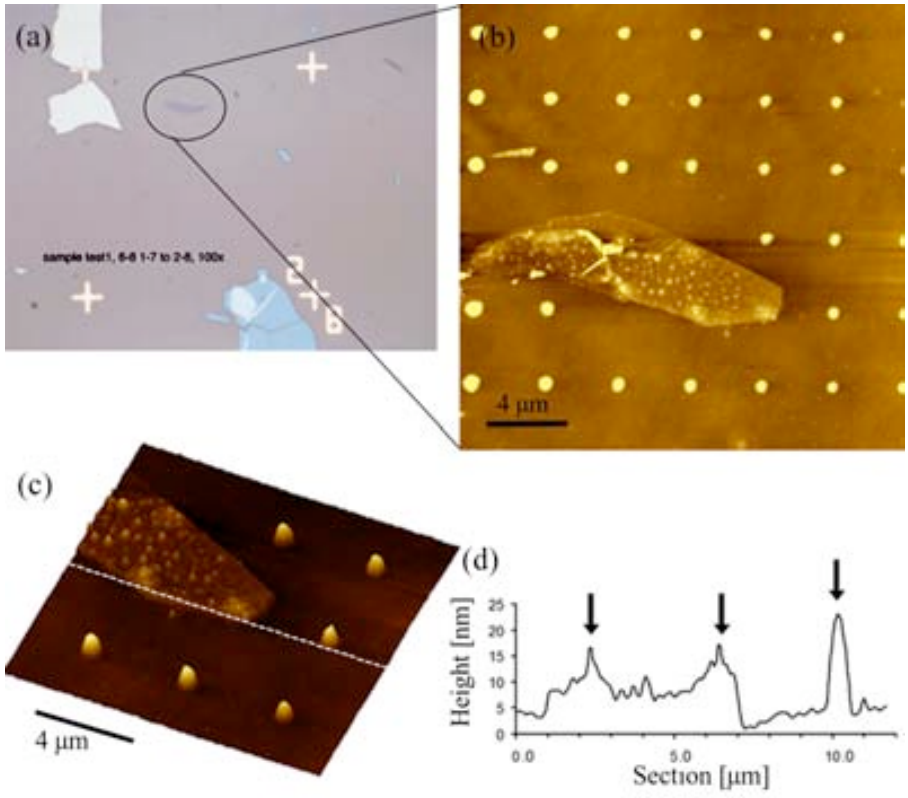

Figure 5.13 Array fabricated using a Co-NP ink solution on graphene and SiO_2 surfaces. (a) Optical image of the target graphene flakes before deposition. (b) AFM topography image of the graphene flake after the deposition of Co-NPs in the form of a 6 x 6 dots separated by 4 µm. (c) 3-D AFM topography image of a section of the array and (d) height profile along the white-dashed line in panel **c**.

The integrity of the graphene upon the deposition process was investigated by Raman spectroscopy by Prof. Marco Affronte and co-workers at the CNR-Institute of NanoSciences S3 (see Experimental Section 7.3). For this purpose, Raman spectra of the graphene flakes prior and after deposition of the Co-NPs were obtained. In this sense, Raman spectroscopy is as a powerful tool for the characterization of graphene, as it can identify the number of layers, the electronic structure, the type of doping and any defects in the graphene.[396, 397] For this experiment, dots of few micrometers in diameter were deposited in the form of arrays on a monolayer and multilayer graphene flake under the same experimental conditions described above. The results are shown in **Figure 5.14**. For both, graphene monolayers (a) and bilayers (b), the characteristic G and 2D bands at respectively ~1580 cm^{-1} and ~2700 cm^{-1} depend on the number of stacked layers and were well visible upon the deposition of the NPs. The absence of D band at 1340 cm^{-1}, which is usually associated to disorder, indicated that the integrity of

graphene was preserved after the deposition. The very slight shift of the G band was related to a small charge doping of graphene due to Co-NPs on top.

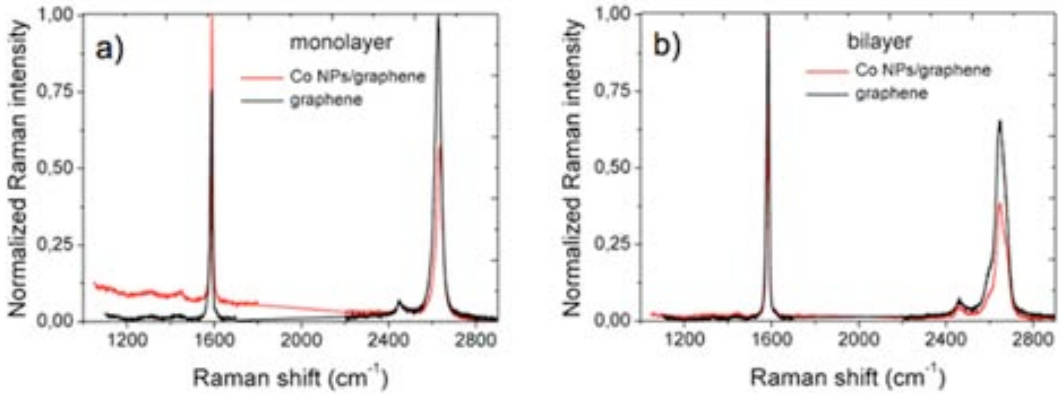

Figure 5.14 Raman spectra taken before and after deposition of Co-NPs arrays on graphene flakes. (a) Graphene monolayer. (b) Graphene bilayer. Data obtained by Prof. M. Affronte and co-workers.

Finally, the integrity of the graphene upon the deposition process was also checked by repeating the deposition process on a graphene flake contacted by electrodes. Prof. M. Affronte and co-workers performed electronic transport measurements in order to characterize the effective functionalities of graphene after the deposition process. **Figure 5.15** shows a resistance backgate voltage curve measured at T = 2 K in an elongated graphene flake decorated with a large number of Co-NPs and contacts in a longitudinal geometry (resistance mode). Reproducibility of the transport measurements before and after deposition step, showing a mobility of $\mu = 2000\ cm^2 \cdot V^{-1} \cdot s^{-1}$, evidenced that as expected from previous Raman experiments the graphene properties were not altered upon the NP deposition.

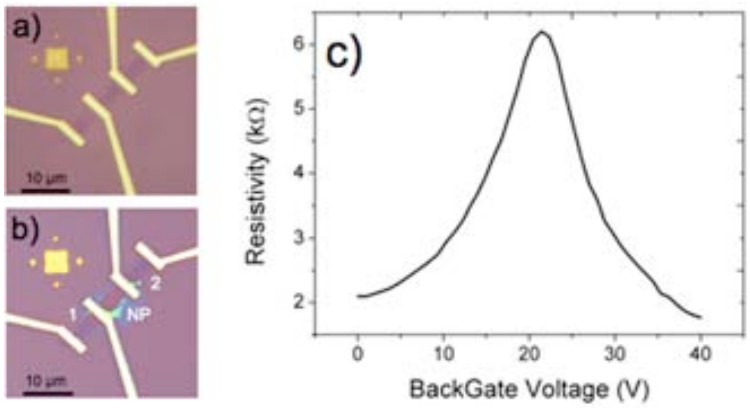

Figure 5.15 Graphene flake with four contacts in a row on which first tests of Co-NP deposition were performed. Optical image of the graphene flake contacted by electrodes (a) before and (b) after Co-NP deposition. (c) Resistivity vs back gate voltage of graphene flake taken after Co-NP deposition and showing characteristic resistance peak in graphene, corresponding to the Dirac point. The fact that this happens at a Vg ≠ 0 is most likely due to unintentional chemical doping during the fabrication and storage of the contacted graphene. The rapid decrease in resistivity on adding charge carriers indicates their high mobility. In this case, a carriers mobility of 2000 $m^2 \cdot V^{-1} \cdot s^{-1}$ was determined from the slope of the curve inverse. Images and data obtained by Prof. M. Affronte and co-workers.

5.2.2 Do we really deliver cobalt nanoparticles?: Deposition on carbon-coated TEM grids

To confirm the transfer of Co-NPs through the tip to the each feature of the arrays not only by AFM topography, the deposition process was repeated this time on a carbon-coated TEM grid, and further characterized by combined TEM and AFM experiments. As already demonstrated for the structuration of ferritin proteins described in Chapter 3, this is an excellent manner to visualize the NP delivered by direct-write AFM lithography and thus confirm their presence on the generated structures. TEM allows the identification of Co-NPs up to a single particle level due to the high contrast given by the metallic character of the NPs while correlated AFM topography can provide direct information about the topographical profile of the motives. Moreover, these are highly demanding experiments that require an excellent control over the tip force to avoid any damage of the TEM grid.

Thanks to our experience on this type of surface and the realization of several experiments that involved the controlled deposition of Co-NPs, we succeeded on fabricating the arrays. Following the same methodology used for the deposition on Si/SiO_2 and graphene surfaces, a series of arrays of dots with varied sizes (ranging from 675 nm to 3 μm) and lines with widths down to 670 nm were fabricated on carbon-coated TEM grids. The resulting arrays were characterized by TEM and AFM, and representative examples are shown in **Figure 5.16**.

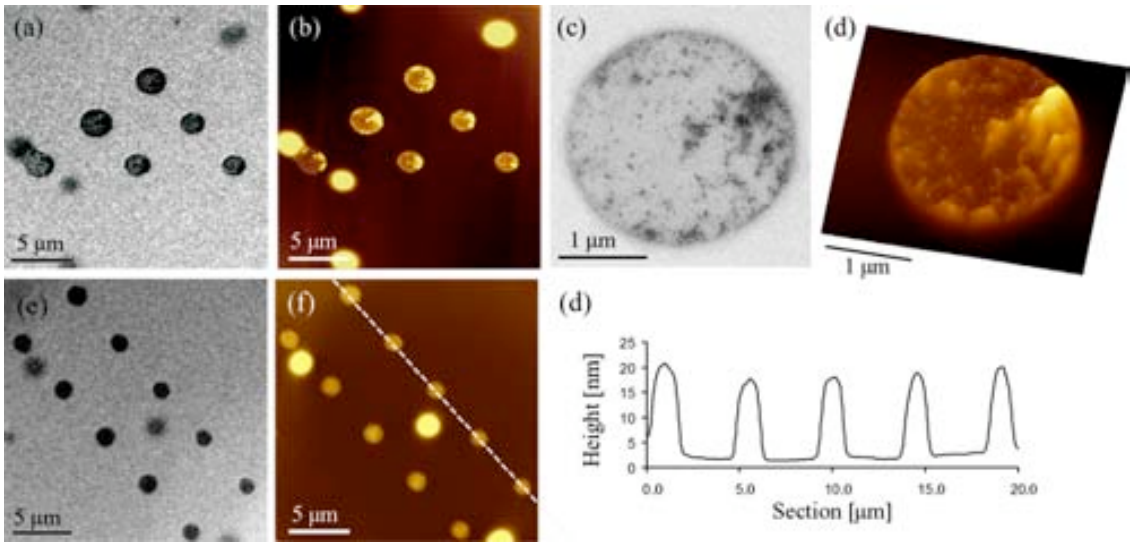

Figure 5.16 Co-NPs arrays generated on carbon-coated TEM grids (a, b) TEM and AFM topography images of an array. (c, d) Magnification of a single dot of the array viewed by TEM and 3-D AFM. (e, f) TEM and AFM topography images of an array. (g) Height profile along the white dashed line in panel **f**.

TEM experiments confirmed the effective transferring of Co-NPs from the tip to the graphene surface. In addition, TEM shows that the NPs were distributed on each dot as (sub)monolayers (Figure 5.26c). It is also important to notice the non-uniform distribution of the NPs over the dot feature, which differed from the typical 2D assembly obtained when the Co-NP solution was deposited by drop casting on a carbon-coated TEM grid (see Figure 5.9). This distribution can be explained due to the constrained evaporation of the NP solution to the specific volume of a droplet, which results into a preferential arrangement of the NPs, as local hexagonal ordered

assemblies (island-like assemblies) or isolated particles, at the perimeter of the drop following a ring-like pattern. This effect is based on the coffee-stain phenomenon, which was already observed and described in Chapter 3 for the distribution of ferritin molecules on each dot like feature.

To give more insights, each one of the dots of the arrays was individually imaged in detail by TEM and AFM (**Figure 5.17**). As mentioned above, two different types of motives were clearly differentiated: isolated particles and groups of several particles (island-like assemblies). The study of the AFM profiles of at least 20 selected motives associated to isolated NPs, such as those marked with red circles in Figure 5.17a, confirmed that whenever a single particle was present, a well-defined and narrow peak stood out above the solvent residue layer with typical heights of 9 ± 2 nm, in good agreement with the size of a single Co-NP. Brief mention should be made to the measured diameters since exhibit an average size of 40 ± 3 nm clearly greater than the real average diameter of a single NP. The widening of the topographical peak for single NPs was attributed to both: the tip convolution effect and the presence of solvent residues surrounding the particle.

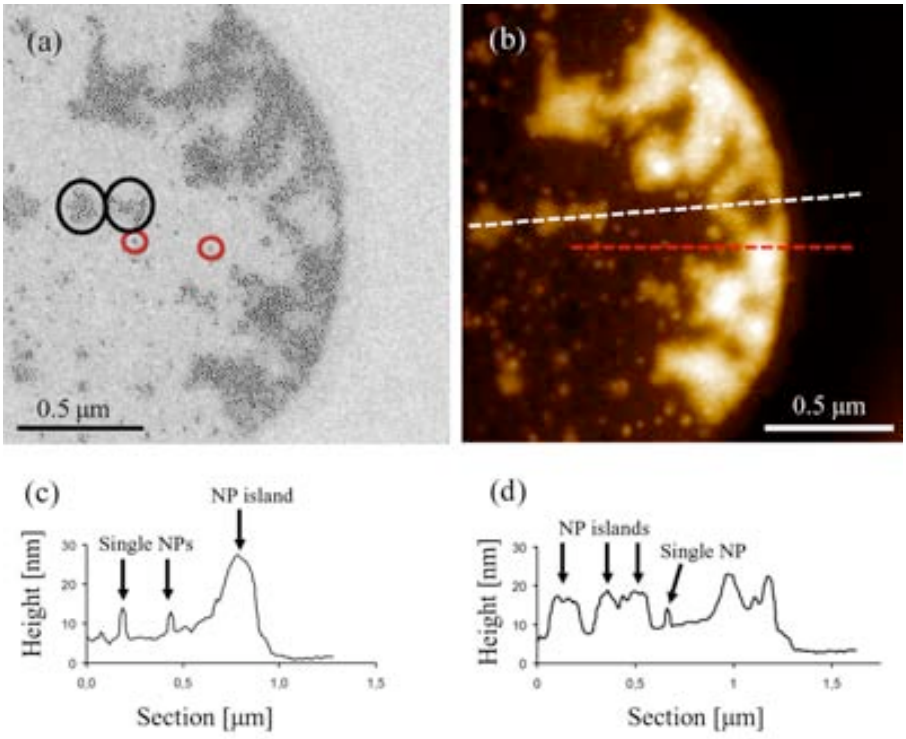

Figure 5.17 Co-NP arrays generated on carbon-coated TEM grids. (a, b) TEM and AFM topography image of a section of a dot-like feature from the array. Height profile along (c) the red dashed line in panel **b** and (d) the white dashed line in panel **b**. The presence of single NPs and NP islands are indicated with black arrows in panels **c** and **d** as well as some examples of these structures are indicated with red and black circles, respectively in panel **a**.

The effect of the solvent residues was especially more apparent when large groups of NPs were studied. The TEM images of such island-like assemblies, marked with a black circle in Figure 5.17a, reveal the formation of (sub)monolayers though their AFM profiles exhibited heights up to 30 nm. As an example, one of the assemblies indicated with a black circle in Figure 5.17a corresponds to 37 NPs with a topographical peak of 140 nm in diameter and 15 nm in height.

This suggests that during the last stages of the evaporation process of the droplet, the residual ink solvent was likely to accumulate onto the already formed NP (sub)monolayers giving to a higher and variable degree of solvent residues in the aggregation motives. A smooth topography with heights below 7 nm attributed to the presence of solvent residues was observed for regions inside the dot free of NPs. Since is possible to distinguish the topography obtained from a NP or an island of NPs from the one obtained from solvent alone, this study demonstrates the capabilities of AFM to detect the presence of NPs on the obtained structures. As we will show next, these measurements will also serve us to characterize the integration of such material into a graphene-based sensor.

5.3 Integration of cobalt nanoparticles into graphene-based sensors by direct-write AFM lithography

Once the capability of this technique for the structuration of Co-NPs on graphene flakes was demonstrated, with control on the size and morphology of the arrays, the next objective was to accurately control the positioning of these structures on pre-selected sites of a graphene surface. For instance, if the NPs are to be deposited on a 1 μm × 1 μm graphene area, the fabrication of ordered arrays will result in a serendipitous process requiring several experiments before a dot is deposited at the right position, especially considering that the optical camera lacks the required resolution to accurately visualize the target position. In this section, this challenge was overcome by developing a novel three step methodology that takes advantage of the combined positioning control and imaging capabilities of AFM.

As a proof-of-concept to validate this approach the Co-NPs were positioned into graphene-based nanoHall sensors developed by Prof. M. Affronte and co-workers at the CNR-Institute of NanoSciences S3 in collaboration with the Istituto Nazionale per la Fisica della Materia (CNR-INFM) (see Experimental Section 7.4). The sensing area of this sensor consists of two graphene Hall crosses 1 μm × 1 μm. Both crosses are separated a distance of 4 μm (**Figure 5.18**). Integration of the NPs on these sensors represents a real experimental challenge since it requires that the magnetic material is positioned exclusively on one of the Hall crosses while the other must be kept empty, due to the gradiometric design of the sensor.

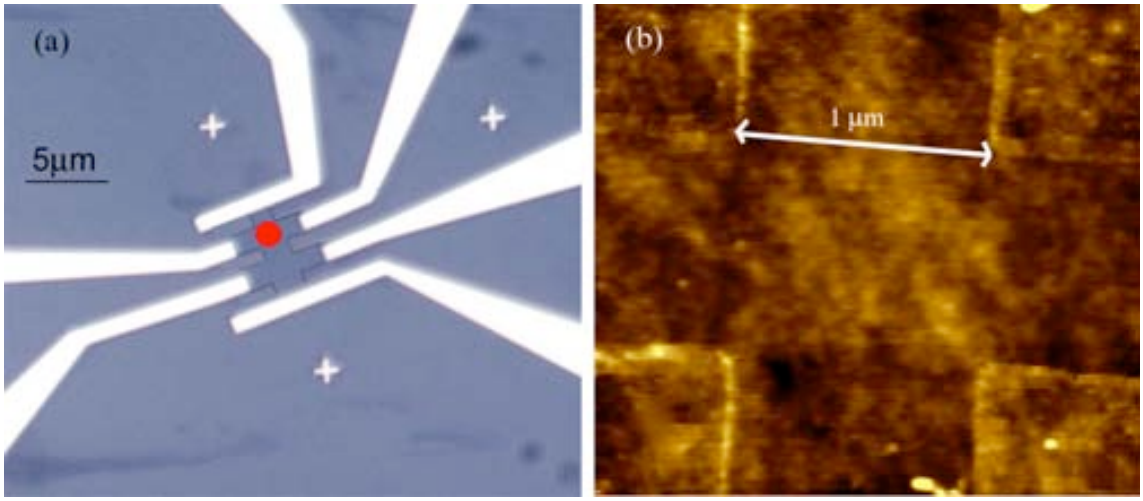

Figure 5.18 Optical image of the graphene-based nanoHall sensor showing the two Hall crosses which correspond to the sensitive areas of the sensor. The sample to be measured can be located either on the top cross (indicated with a red circle), or on the bottom cross. For the sake of clarity, the graphene edges have been highlighted with black lines. (b) AFM topography image of one of the Hall crosses 1 µm × 1 µm in size.

A suitable tip for these experiments should fulfill the following requirements: (i) must be appropriate to high resolution imaging experiments while preventing any damage of the graphene layer and (ii) allow sequential deposition, providing an optimal control of the quantity of material to be deposited on a single dot. The tip of choice for these experiments was non-contact high-resonance frequency tips, abbreviated as NCH tips (see Experimental Section 7.2). A comparison between the characteristics of these tips and those of SP tips used up to now along this chapter that justify its choice are explained next.

SP tips exhibit a tip radius of ~ 15 nm and a symmetric pyramidal shape of low aspect ratio. This geometry is specially designed with a recessed area surrounding the tip base, missing on the NCH tips, that provides a high degree of functionalization by increasing the loading of ink material, and therefore a long stable writing performance. Although this type of tip is suitable for imaging, the main disadvantage is that are optimized for contact mode imaging, which is likely to damage the Hall sensor and specifically the graphene sheet. It must be consider for this that the new three step methodology involves a previous topographic mapping of the sensor area. In contrast, NCH tips are designed for non-contact/intermittent contact mode imaging that enables the characterization of surfaces while greatly reducing surface damaging. NCH tips exhibit a sharper radius of ~ 7 nm and an asymmetric pyramidal shape of high aspect-ratio. In this sense, the increase on tip aspect-ratio has been already described to diminish the width of the solvent meniscus formed at the point-of-contact between the tip and the surface, and therefore it is expected to favor a low ink loading and creation of dots with smaller diameters.[201, 202] As a representative example of their comparative loading capacity, a FE-SEM image of both tips functionalized with the Co-NPs solution following the *scanning coating* method is shown in **Figure 5.19**a,b.

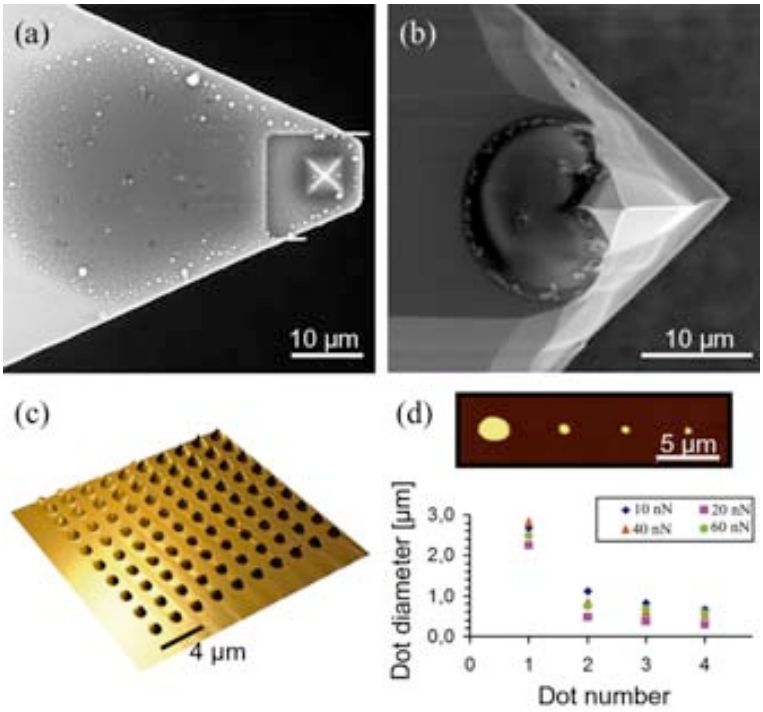

Figure 5.19 FE-SEM image of (a) a SP tip and (b) a NCH tip, both functionalized with Co-NP ink solution *via scanning coating* method. (c) 3-D AFM topography image of an array of Co-NPs generated with the coated SP tip on Si/SiO_2 substrate. The spacing between the dots of the array is 2 µm, dot diameter is 1.1 ± 0.1 µm and height is 21 ± 2 nm. (d) Evolution of the dot diameter according to the ink depletion of a coated NCH tip. The represented series of 4 dots on a Si/SiO_2 substrate were generated with the same tip but under different tip-substrate contact forces. Inset: AFM topography image of a series of 4 consecutive dots under at contact force of ~ 40 nN.

According with their different geometries and ink loading characteristics, both tips also exhibit different writing capabilities. As already observed in the previous sections, SP tips decorated with Co-NPs were able to create large arrays of repeated dots highly uniform in size thanks to its long stable writing performance. As an example, Figure 5.19c shows an array fabricated by a SP tip on a Si/SiO_2 substrate made of highly uniform in size dots of 1.1 ± 0.1 µm in diameter and height of 21 ± 2 nm. However, it must be emphasized that before SP tips starts writing uniform dots, the excess of ink which is typically loading the tip after tip coating step needs to be eliminated through cantilever and tip *bleeding* (as previously described in this chapter). On the contrary, this step is not necessary for NCH tips due to their low ink loading. AFM characterization of four consecutive dot arrays fabricated right after NCH tip coating step (i.e. no previous *bleeding* step) deposited on Si/SiO_2 evidenced a dramatic decay of the dot size upon the first deposition (Figure 5.19d). Moreover, such writing behavior was not dependent on the contact force applied during the deposition under the studied range,[170] though further control on the dot size was obtained by adjusting the contact time of the tip with surface as already described for SP and MP tips.[120, 185] Due to the imaging capabilities of NCH tips, we decided to perform the integration experiments using this type of tips, which would allow us to scanning the sensor area while preserving intact the graphene-based sensor characteristics. Moreover, since our aim in this study was to control the positioning of one single dot on the sensor, the weak writing capability of NCH tip was not a limiting factor in this particular case.

After selecting the tip, we envisaged a strategy to directly transferring the Co-NPs from the tip onto the sensing area of the sensor similar to that already described by Xiong *et col.*[109] (see Section 1.1 in Chapter 1) but without the need of pre-modifying the surface of the sensor with linker molecules such as alkanethiols. The designed strategy proceeds as depicted in **Figure 5.20** through three main steps. The first step involves the coating of a NCH tip with the NP-based ink solution by *scanning coating* method. Secondly; the freshly coated tip is positioned in the vicinity of the sensor and scanned in intermittent contact mode over an area in order to find a reference point on the sensor. Then, the coordinates of the sensing area of interest with respect this reference point are deduced from an AFM image of the sensor area previously obtained using an uncoated NCH tip. Finally, the coated tip is positioned at these coordinates and brought into contact to the surface in order to transfer the ink material on top of the target region. In order to avoid undesired depositions, the tip works in intermittent contact mode during the X-Y navigation and the amplitude set point is increased enough in order to lift the tip from the surface. During the deposition, both tip-substrate contact force and time of contact can be controlled in order to ensure the transference without damaging graphene layer and adjust the size of the dot. Let us note that the three steps of the process must be under feedback control to guarantee the positioning of the tip during the experiment. Therefore the X-Y navigation is restricted to the scan range of the instrument. These experiments were performed in an Agilent 5500 AFM/SPM instrument, equipped with a X-Y nanopositioning stage (scan range of 100 μm × 100 μm) to ensure an appropriate control of the positioning of the tip (see Experimental Section 7.2). The experiment was carried out under controlled environmental conditions (i.e. relative humidity at ~ 50% and room temperature).

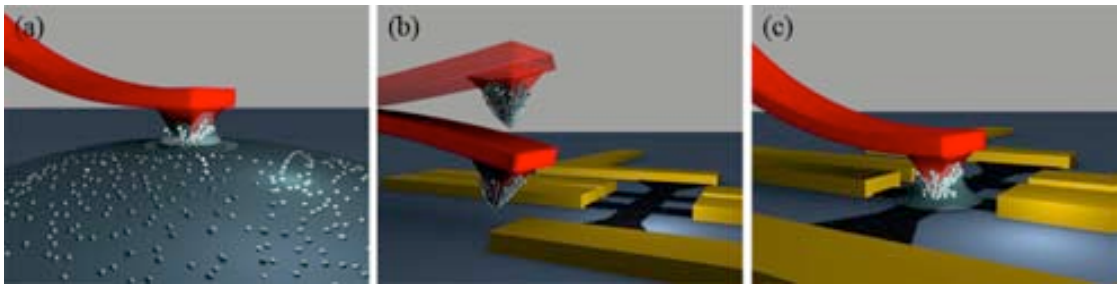

Figure 5.20 Schematic illustration of a methodology for the integration of NPs onto the sensing area of a graphene-based nanoHall sensor. (a) A NCH tip is coated by *scanning coating* method on a Si/SiO_2 substrate. (b) The coated NCH tip is situated in the vicinity of the sensor and scanned in intermittent contact mode to find a reference point. (c) The coated NCH tip is approached to the sensing area (whose coordinates are calculated from the reference point) and the Co-NPs ink is deposited.

To evaluate the feasibility of this strategy, the alignment procedure and deposition parameters were first investigated on labels lithographically created onto a p-doped Si wafer with a 300 nm SiO_2 capping layer fabricated by Prof. M. Affronte and co-workers at CNR-Institute of NanoSciences S3. As an example, **Figure 5.21**a shows a cross-shaped mark (16 μm × 16 μm in size) used as a reference to calculate 4 imaginary points on the surface indicated with red circles on the AFM image. The tip was coated and aligned on the desired regions as described above. Then, the depositions were performed in contact mode applying a tip-substrate contact force of ~ 10 nN during 10 s. Figure 5.21b,c show AFM images of two different crosses after the

deposition process where 4 dots made of Co-NP ink solution were generated on the desired positions surrounding the cross marks. The dots were irregular instead of round shaped, as usually obtained for the deposition of liquids on surfaces by direct-write AFM lithography, so we measured the shorter and longer axes of the structure to characterize them. The first dots in both examples shown sizes of 575 µm × 1.27 µm and 1.02 µm × 1.28 µm and heights of 47 nm and 35 nm, respectively. The heights of these depositions were consistent with the deposition of Co-NPs (see previous sections). However, second depositions sometimes gave to heights down to 6 nm (as observed in Figure 5.21c) which suggests that in reality we were transferring solvent alone instead of NPs. In addition, AFM demonstrates that the size of the structures varied between experiments, evidencing the poor reproducibility of the process. Interestingly, the imaging capabilities of the NCH tip were maintained after coating with the Co-NP ink solution (Figure 5.21c inset). However, the scanned area became contaminated by small amounts of the ink material and non-desired depositions were also observed along the surface due to the movement of the tip (see Figure 5.21b,c).

Even though the fabricated dots were successful localized on the desired positions of the surface, it is important to note the poor quality of the depositions, which typically were irregular shaped and not reproducible from experiment to experiment. Indeed, the intermittent contact of the coated tip with the surface during imaging step is likely to modify somehow the ink coating giving to an irregular transference of the ink from the tip to the substrate surface. From these results we can conclude that this strategy gives to well-localized but low quality and not reproducible depositions of the ink to the target zone. In view of these results, it was necessary to develop an alternative method that allow the use of a NCH tip for mapping before loading is performed to preserve the quality of the coating.

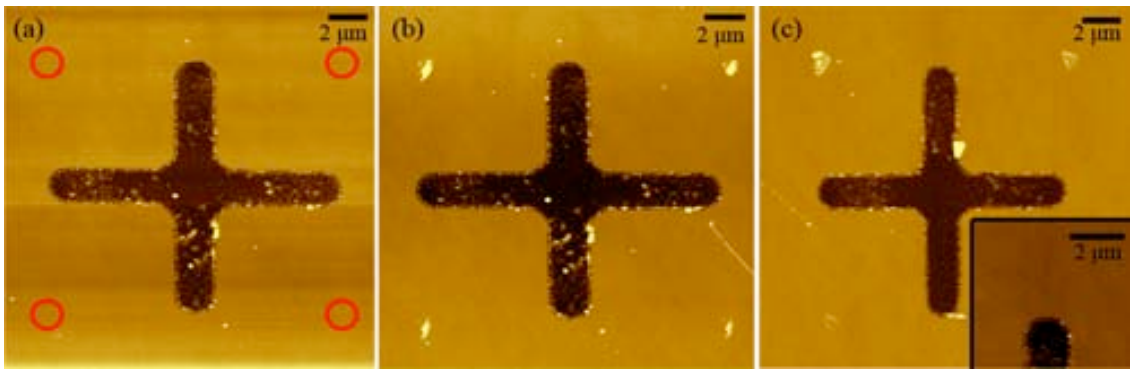

Figure 5.21 AFM topography images of deposition experiments following the strategy depicted in Figure 5.20. (a) Cross-shaped position labels lithographically generated on Si/SiO_2 surface where imaginary red circles indicates 4 regions chosen to selectively localize the deposition of NPs. (b) Same cross after the deposition of NPs onto the desired positions. (c) Second example of a cross after deposition. Inset: AFM topography image obtained using an ink-coated NCH tip to find a reference point that would allow to calculate the coordinates where carry out the deposition of the ink material.

This limitation was tackled by the development of a strategy that reverses the order of the followed steps, imaging was performed before coating of the tip as schematically depicted in **Figure 5.22**. As already described for the previous strategy, the three steps of the process must also be strictly developed under feedback control to guarantee the positioning of the tip with nanometric resolution, reason why the X-Y navigation is restricted to the 100 µm × 100 µm

scan range in the X-Y nanopositioning stage. To ensure this restriction, first a microdrop of the Co-NPs ink was deposited into the 100 μm x 100 μm scanning area nearby the target area (i.e., sensing area of the sensor) by optical control. This deposition was performed with a SP tip coated as described in previous sections. The deposited drop would serve as ink reservoir for the functionalization of NCH tip used for the final integration process without losing the feedback control. To this aim, the size of the droplet must be enough to ensure the optimal coating of the NCH tip while completely avoiding contacting and contaminating the rest of the substrate area. For instance, preliminary experiments using NCH tips functionalized on few micrometer droplets gave to quasi unfunctionalized tips which were unable to deliver droplets with enough quality. A second important issue that must be emphasized is the capacity of NCH tips to create dots right after tip coating without the need of previous *bleeding* steps (as already mentioned in this section), since it will be crucial for the development of the present integration strategy.

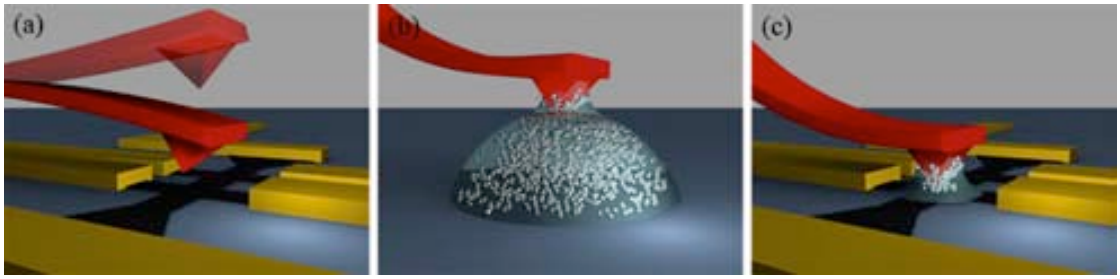

Figure 5.22 Schematic illustration of the steps followed in the second strategy to integrate NPs onto the sensing area of a graphene-based nanoHall sensor. (a) An uncoated NCH tip is used to obtain a map of the sensor in intermittent contact and register the coordinates of the sensing area. (b) The same tip is coated by *scanning coating* method onto a droplet situated in the vicinity of the sensor. (c) The coated NCH tip is positioned on the sensing area and the Co-NPs are deposited.

The three step protocol was applied for the functionalization of the 1 μm × 1 μm sensing area of a graphene-based nanoHall sensor as the one shown in Figure 5.18. For the sake of clarity, we recorded an entire integration experiment with the camera coupled to the AFM instrument and the image sequence of the process is shown in **Figure 5.23**. In the first step, an uncoated NCH tip was approached to the surface localizing its scan center between both the drop and the sensing area. From now on, all the tip movements were done with the scan feedback control. The uncoated NCH tip is used to imaging the target region in intermittent contact mode, registering the exact coordinates of the sensing area of the nanosensor. In a second step, the tip is moved to the drop (~ 20 μm in diameter), and gently coated by scanning in contact mode a 5 μm × 5 μm at 1 Hz while dipping the tip into the droplet. Finally, the tip was lifted and moved back exactly to the recorded coordinates corresponding to the sensing area avoiding undesirable depositions during the coated tip movement over the sensor. Once the coated tip was positioned exactly on the target area, the ink material was smoothly deposited by placing the tip in gentle contact with the surface simultaneously controlling the tip-substrate force and contact time, to prevent graphene damage and to adjust the final dot size. A contact force of ~ 10 nN during 10 s was shown to be enough to ensure the capillary transport of the ink from the tip to the surface without producing any evident damage to the graphene layer.

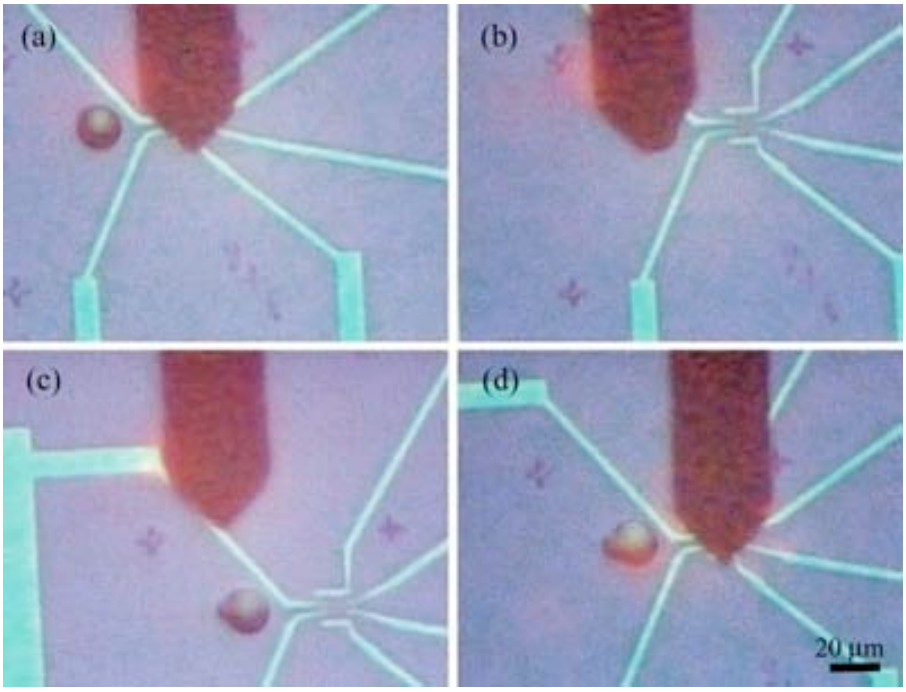

Figure 5.33 Optical image sequence captured during the integration of Co-NPs onto the sensing area of a graphene-based nanoHall sensor following the strategy depicted in Figure 5.22. (a) Imaging process in intermittent contact mode to register the coordinates of the Hall cross of interest. (b) Coating of the NCH tip on a droplet placed in the vicinity of the Hall sensor. (c) The coated NCH tip is lifted and moved towards the registered position (cross coordinates). (d) Deposition of the NP-based ink solution onto the target area.

The AFM characterization of the nanoHall sensor after the integration process confirmed the (sub)micrometric control achieved in the deposition of Co-NPs on the 1 µm × 1 µm sensing area (**Figure 5.24**). Differences in topography between both Hall cross areas are evident. While one of the Hall crosses was successfully functionalized, the other remained completely clean (Figure 5.24c,d), which is a limiting requirement to achieve differential Hall measurements. A more detailed AFM study revealed that the deposited dot exhibits a diameter of 835 nm with a basal background up to 6 nm or below that can be associated to solid residuals mainly coming from the oleic acid. In addition, two main peaks with heights of 11 nm and 15 nm and diameters of 133 to 114 nm were also observed and associated to the presence of Co-NPs assemblies (Figure 5.34 b,d). By comparison with the combined TEM and AFM characterization of the motives deposited on carbon-coated TEM grids (Section 5.2.2), the number of particles deposited on the sensing area of the sensor was estimated. According to the size (diameter and height) of the deposit, we selected two island-like assemblies measured in Section 5.2.2 by TEM and AFM whose dimensions where similar to the obtained on the sensor (i.e. indicated with black circles in Figure 5.17a). In this case, TEM image of both islands indicated the presence of a hundred of NPs assembled into a monolayer. Since in the sensor, the topographical features of both peaks are similar to the ones studied by TEM, we estimated that about one hundred Co-NPs were deposited on the 1 µm × 1 µm sensing area and organized into island-like assemblies as monolayers.

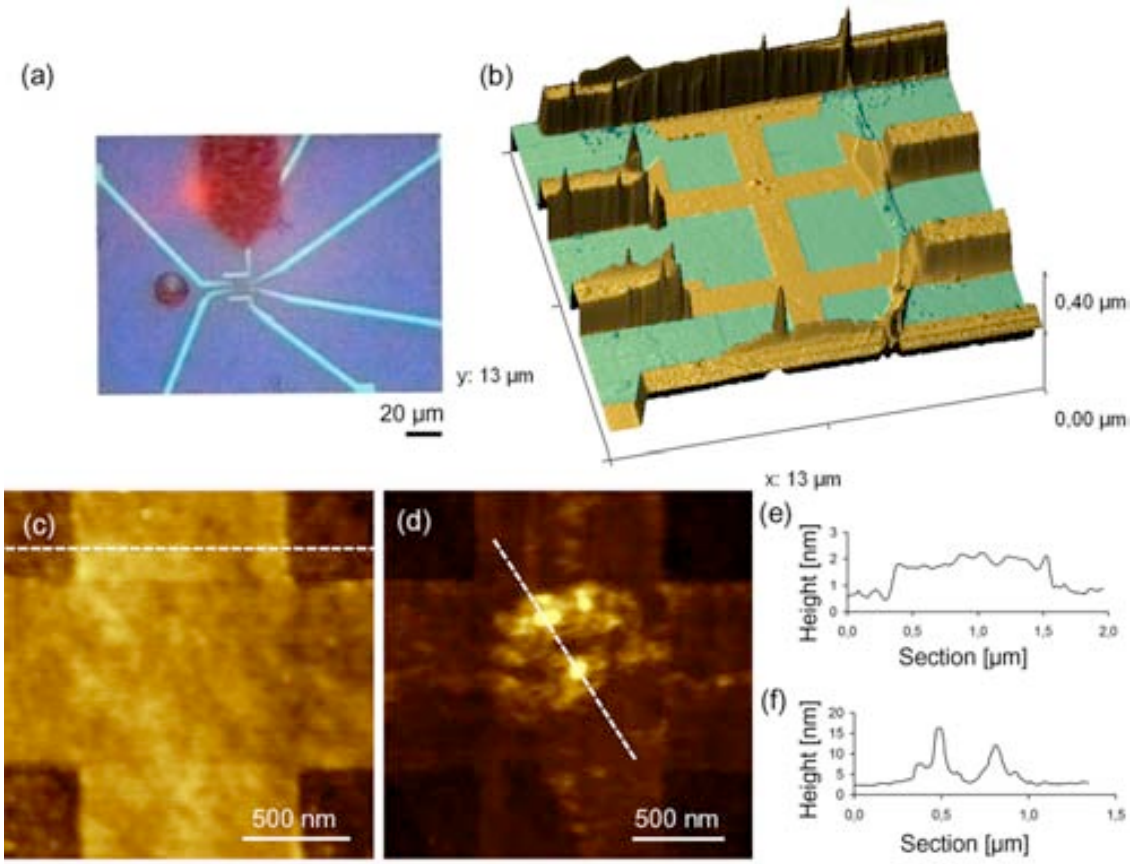

Figure 5.24 Deposition of Co-NPs onto the sensing area of a graphene-based nanoHall sensor following the integration strategy depicted in Figure 5.22. (a) Optical image of the sensor during integration process. (b) 3-D AFM topography image of the sensor after the deposition experiment. (c) AFM topography image of the Hall cross kept clean in the integration experiment. (d) AFM topography image of the Hall cross onto which a dot made of the Co-NP ink solution was accurately positioned. (e) Height profile corresponding to the white dashed line in panel **c**. (f) Height profile corresponding to the white dashed line in panel **d**.

5.4 Summary

Several factors identified along this Thesis have been shown to play an important role in the structuration process, such as the ink composition, the ink-substrate affinity and the environmental conditions. Once controlled all these experimental parameters, the writing approach was implemented for the structuration of Co-NPs on graphene. This approach was shown to be an excellent strategy to directly positioning Co-NPs on graphene substrates by capillary transport through the tip preventing its damage, without any previous functionalization neither of the NPs nor the graphene surface. We demonstrated the presence of NPs on the generated structures as well as studied their assembly after solvent evaporation by performing the patterning experiment onto carbon-coated TEM grids and characterizing the obtained structures by TEM. Interestingly, the NPs were organized as (sub)monolayer inside the deposited dots, as proved by complementary AFM and TEM experiments. On the other side, tips with different geometries, ink loading and depletion characteristics have been shown to exhibit different writing capabilities. SP tips are useful to fabricate NPs arrays with controlled

dimensions and morphologies thanks to their long stable writing performance while NCH tip exhibit a dramatic decay of the dot diameter upon the first deposition due to a low ink loading and very fast ink depletion process. Though the possibility to work under intermittent contact mode facilitate its use for a very precise deposition.

Finally, a three step methodology was designed to address the deposition to a specific position on a surface with (sub)micrometric control. The integration process involved three main steps: (i) localization of the target region by intermittent contact AFM imaging, (ii) functionalization of the tip in a nearby ink droplet and (iii) positioning of the tip on the target area to deposit the desired material, working always under feedback control. As a proof-of-concept to validate this approach Co-NPs were successfully positioned onto a 1 μm × 1 μm sensing area of a graphene-based nanoHall sensor. In this case, optimal control on both, the localization of the target area and the deposition of small quantities of material, was achieved with the use of NCH tips. This type of tips shows optimal imaging capabilities and a low degree of functionalization that favored the deposition of very narrow dots without the need of previous *bleeding* steps. This methodology opens new perspectives not only for magnetic sensors but for any kind of device where the direct integration of materials and molecules with (sub)micrometric resolution under mild conditions is required.

However, up to the moment of writing the present manuscript only preliminar measurements were done where it is rather difficult to discard background from sample signal. One of the main limitations in this sense is the cleaning of the graphene surface, which remains dirty upon the fabrication of the sensor. During the lithographic process for the fabrication of the sensors, the graphene flakes are exposed to photoresist masks; giving the possibility that effects of the photoresist residues may have an influence on the graphene characteristics (they observed that these impurities introduced unknown and uncontrollable perturbations to the graphene-based sensor). To date different cleaning methods have been used such as annealing, though this process can induce doping and disorder in the graphene flake. Prof. M. Affronte and co-workers are currently searching for cleaning methods to completely remove the photoresist residues, while preserving graphene characteristics, and then maximize the contact between the graphene and the sample. Further development of the sensors is needed before any conclusive measurement can be extracted.

Chapter 6

General conclusions

Main general conclusions:

- Direct-write AFM lithography has been shown to be an effective technique for the integration of any type of magnetic nanostructures, ranging from molecules to NPs, on a broad range of sensors with different dimensions and characteristics.
- The use of this technique does not require previous functionalization of the ink material neither of the substrate, being shown as a mild technique suitable even for delicate surfaces such as graphene.
- For sensors with sensing areas within the hundreds of microns range, it allows for the specific deposition on the most sensitive areas ensuring a maximum coupling factor with the magnetic sample.
- For sensors with sensing areas of a few microns or less, difficult to be localized by optical means, a new three step methodology involving the localization of the sensing area with the tip, its functionalization with the magnetic sample and the posterior deposition has been developed.

Specific conclusions:

- Controlled arrays of diverse ferritins have been achieved with control on the shape and dimension of the arrays, with dots as small as 100 nm.
- By controlling the initial concentration, we have achieved control on the number of ferritins deposited per dot, down to only one or a few of such entities.
- A (sub)monolayer of a Co@apoferritin involving only around 108 Co atoms per protein has been successfully measured with a microSQUID with sensing areas within the hundreds of microns range, thanks to their controlled deposition on the most sensitive areas of the sensor.
- Direct-write AFM lithography has been successfully used for the first time to deposit SMMs on surfaces with different supramolecular states, ranging from amorphous materials to well-ordered capsules-like supramolecular structures.
- Diverse systems of the well-known Mn_{12} family have been structured on surfaces in the form of a few layers with control on the morphology and size of the resulting deposits.
- First magnetization measurements of Mn_{12} arrays deposited on the sensing areas of a microSQUID sensor have been obtained. Though preliminary, characteristics signals of their SMM behavior can be distinguished.
- The methodology for the controlled deposition of Co-NPs as a (sub)monolayer has been established.
- Different works have been developed for the first time to establish the experimental conditions needed for a proper deposition of NPs on graphene without damaging it by direct-write AFM lithography.
- The three step methodology previously described has been used to deposit Co-NPs on a cross-shape graphene-based nanoHall sensor with a sensing area of only 1 μm × 1 μm .

Perspectives:

Everybody agrees that the development of magnetic molecular devices, though a breakthrough if successful, nowadays represents a real challenge due to the technological limitations as well as the lack of basic information about the behavior of molecules upon integration. This challenge is applicable as well to ferritin or other inorganic NPs. For this, there are three main areas that deserves special attention: (i) development of structuration techniques that allow for a proper organization of the materials on surfaces and devices, (ii) retrieval of basic information about the chemical stability but mainly about the conservation of their magnetic properties on the translation from the macroscopic to the nanoscopic world, and (iii) integration into sensors and feasibility of their functioning on real devices.

As expected, the first area involving the development of surface structuration techniques is where scientists started to develop their work, and consequently, where most examples have been described. However, and in spite of the already large number of techniques described, new examples continue to appear. In this sense, though still necessary, from our point of view the scientific community should rather concentrate on the advancement of those techniques more feasible to integrate the molecules or other magnetic nanostructures into devices rather than simply describe new examples. From all them, those that have been shown to have more potential up to now combine self-assembly assisted with lithographic techniques. Integration of molecules on CNTs is also a successful and promising approach to indirectly measure magnetic properties at the single molecule level through conductive measurements.

In this Thesis we have demonstrated that direct-write AFM lithography is a complementary very successful technique for this. The integration of magnetic nanostructures on the most sensitive areas of sensors has been achieved, allowing for the first direct measurement of ac susceptibility of a (sub)monolayer of ferritins as well as the integration of magnetic NPs into a sensor with sensing area of 1 μm × 1 μm . However, still a long road is ahead us for this technique before a real application becomes a reality due to two main limitations, reproducibility and scalability. Improving both limitations will require to have a full control over the self-assembly processes of the molecules and particles, which is not an easy task. Actually, it represents one of the main objectives that pursue molecular nanotechnology nowadays. A good solution to overcome these limitations could be the combination of self-assembly with AFM-assisted lithographies.

If the integration of magnetic nanostructures into the devices could represent itself a real challenge, the maintenance of the magnetic properties upon integration is a must, especially for molecules. Perturbations arising upon molecule–surface interactions can induce numerous changes, from deformations to chemical modifications (such as redox processes and/or chemical decomposition) that can completely alter the magnetic properties inducing modification of the magnetic exchange pathway or simply alter the easy-magnetization axes. This is the case of the well-known Mn_{12} family, where also special attention is required to not confuse losing the SMM behavior with favoring the fast relaxation processes upon surface deposition!

In summary, though moving on a challenging field that is just starting simply to envisage some real applications, direct-write AFM lithography has been shown in this Thesis to be an excellent technique to advance a step further on this long road. Though, some advances must also take

place in parallel with the development of deposition techniques that ensure a complete success, such as that of the limiting capabilities of the sensors. In other words, as important as having control on the deposition of one or a few particles at a given position of a sensor, is to have a proper sensor with sensitivity limits able to detect them.

Chapter 7

Experimental section

7.1 Magnetic materials

In this section we will describe the magnetic materials used in this Thesis in order of appearance. Though their synthesis as well as characterization was performed by our collaborators (details are given for each case) a brief description of these materials is given (further details can be found in the corresponding references).

7.1.1 Natural ferritin

Natural ferritin (horse spleen ferritin) in saline solution (150 mM NaCl) was purchased from Sigma–Aldrich. Ferritin concentration is 69 $mg \cdot mL^{-1}$ and the molecular weight of the ferritin is 900000 $g \cdot mol^{-1}$.

7.1.2 Fluorescent-labeled ferritin

The labeled ferritin was synthesized by Dr. A. Lostao and R. de Miguel at INA. For this, they used a fluorophore named Atto 488 NHS ester, which has an excitation peak at 498 nm and an emission peak at 520 nm in 0.1 M PBS pH 7.0. This fluorescent label shows high molar extinction coefficient (90000 $M^{-1} \cdot cm^{-1}$) and quantum yield (0.80, i.e. emitted photons/excited photons) being characterized by its high photostability. The succinimidyl ester group of the dye enables an effective reaction with primary amino groups of the protein. The labeling procedure was performed as described in Sigma–Aldrich protocol for Atto 488 Protein Labeling kit with a variation to increase the protein labeling degree. First, horse spleen ferritin solution (from Sigma-Aldrich) was dialyzed to give a 46.0 $mg \cdot mL^{-1}$ ferritin in sodium bicarbonate buffer solution (pH 8.4). 80µL of a diluted solution of the ferritin solution in sodium bicarbonate buffer solution was transferred to a vial containing 20 µL of 10 $mg \cdot mL^{-1}$ of the reactive dye in a sodium bicarbonate buffer solution to have 1 mg of ferritin in the final vial volume. Then, the reaction mixture was incubated for 2 h under gently stirring and protecting the vial from light. The separation of protein-dye conjugates from excess free dye was done using the purification set included in the Atto 488 Protein Labeling Kit using gel filtration columns, and following the procedure described in the protocol. The molar dye/protein ratio was calculated as described in the protocol based on measuring the absorbance of the conjugate at 280 nm and 480 nm. The calculated molar dye/protein ratio is 1.3. Finally, the resulting concentration of the labeled ferritin solution was calculated as defined in the protocol giving to 16.6 $mg \cdot mL^{-1}$ in PBS (pH 7.5). Labeled conjugates were stored at 4 °C and protected from light until their use for the patterning experiment.

7.1.3 Apoferritin

Apoferritin was purchased from Sigma-Aldrich (molecular weight 440000 $g \cdot mol^{-1}$) and directly lyophilized by Dr. A. Lostao and R. de Miguel at INA using a Telstar Cryodos instrument. Lyophilized samples were kept at 4 ºC.

In view of the integration of ferritin samples into sensors, the stability of apoferritin exposed to vacuum and low temperature circles was investigated by Dr. A. Lostao and R. de Miguel at INA by fluorescence spectroscopy. Proteins contain three aromatic amino acid residues (tryptophan, tyrosine, phenylalanine) which may contribute to their intrinsic fluorescence. The fluorescence of a protein is a mixture of the fluorescence from individual aromatic residues. Those residues can be used to follow protein folding because their fluorescence properties are sensitive to their environment which changes when protein folds/unfolds. In the native folded state, tyrosine and tryptophan are generally located within the core of the protein, whereas in a partially folded or unfolded state, they become exposed to solvent. A detailed description of the experiments as well as the materials and instruments used is given in ref.[284] and [403].

The authors performed the experiments using a Perkin Elmer LS55 spectrofluorometer at 20 ºC, using an excitation wavelength of 280 nm. Initially, spectra of the bulk apoferritin in three different folding states in solution (native, a semi-denaturated state where the subunits retain their tridimensional structure and a completely unfolded state) were separately recorded to be used as models. Apoferritin was unfolded to semi folded and unfolded states with 0.01 M glycine hydrochloride buffer at pH 2.0 and 6 M guanidine hydrochloride at pH 1.9, respectively. The final spectra of the three different folding states are shown in **Figure 7.1**. Afterwards, experiments were performed on apoferritin samples deposited on Si/SiO_2 and Nb substrates, both as a bulk powder fixed with Apiezon grease or deposited from solution by drop casting (the small amount of material deposited by direct-write AFM lithography is below the threshold detection of the fluorescence experimental set-up). Such substrates were exposed to the same temperature cycles and vacuum conditions as the samples used for the magnetic measurements. However, due to experimental limitations that avoid direct in-situ fluorescence studies, the samples were removed from the surface before their study by extraction with water and posterior dilution in 10 mM Tris-HCl buffer at pH 7.0 down to a final concentration of 0.25 $mg \cdot mL^{-1}$. In the case of the bulk sample the spectrum after removal showed emission maxima at 340 nm and smaller peaks at 323 nm and 360 nm. The drop casted sample exhibited maximum emission at 340 nm, a smaller peak at 323 nm and a shoulder at 360 nm. By comparison with the model spectra of the three folding states previously described, it was rather difficult to unequivocally assign the folding status of the complex quaternary protein structure in these samples. However, there was a clear tendency, according to their emission spectra, which indicated that both samples contained a mixture of states, where the protein was mostly folded or semi-folded.

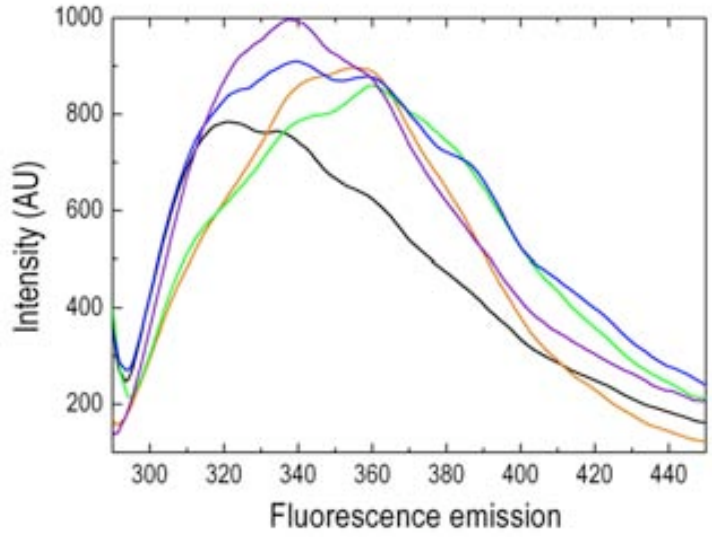

Figure 7.1 Fluorescence emission spectra of apoferritin. Excitation was at 280 nm. Black line: native apoferritin; orange line: apoferritin treated with 0.01 M glycine hydrochloride buffer at pH 2.0; green line: apoferritin treated with 6 M guanidine hydrochloride at pH 1.9; blue line: bulk powder protein mixed with vacuum grease sample after temperature and vacuum treatment; (purple line) drop casted protein sample after temperature and vacuum treatment. Images reproduced from ref.[284] and [403].

7.1.4 Magnetoferritin

Ferritin molecules displaying an internalized ferrimagnetic maghemite γ -Fe_2O_3 NP, named magnetoferritin, were synthesized and characterized by Dr. A. Lostao and R. de Miguel at INA following the protocol described in ref.[404]. Detailed information about the synthesis and materials used is given in ref.[403] and [405]. This synthetic procedure is based on the addition of increments of Fe(II) to anaerobic solutions of the apoferritin, at pH 8.6 and 65 °C, followed by stoichiometric amounts of the oxidant trimethylamine-N-oxide (Me_3NO). Controlling the number of stepwise cycles of the Fe(II)/oxidant additions they controlled the iron loading per protein. The final solutions were dialyzed against distilled water and then lyophilized. Lyophilized samples were kept at 4 ºC. Proteins with theoretical loadings from 50 to 3000 Fe atoms/protein molecule were synthesized, which shown inorganic cores with sizes ranging from 1.7 nm to 5.6 nm, respectively. For the experiments described in the present Thesis we used magnetoferritin displaying a maghemite core of 5.3 nm in diameter containing an average number of 1000 Fe atoms/protein and a molecular weight of 580000 $g \cdot mol^{-1}$ (estimated by theoretical calculations and experimentally by EDX).

Detailed structural and magnetic characterization of these samples is reported by M. J. Martínez-Pérez *et al.*[283, 405] In this study, TEM, electron diffraction and XRD, revealed that the crystalline disorder in magnetoferritin inorganic cores increased when its size became smaller than the inner size of the protein cavity. For large NPs 5.6 nm in diameter, the diffraction pattern showed a good degree of crystallinity, as checked by the excellent quality of the diffraction peaks. Similar results were obtained for the magnetoferritin used in this Thesis having a 5.3 nm in diameter core, however this sample showed a lower degree of crystallinity compared with the 5.6 nm NPs. The reflections observed agreed with the calculated patterns for

either maghemite or magnetite. Further chemical analysis indicated that the inorganic core was predominantly made of an iron oxide with composition close to maghemite.[405]

In addition, in the case of low iron contents they observed by TEM that particles were not spherical but with a "half-moon" or "horseshoe" shape, as observed for the NPs used in this Thesis (**Figure 7.2**). This was explained due to the special mechanism of crystal grown inside ferritin schematically depicted in Figure 7.2d. As it has been reported, there are multiple oxidation and nucleation centers located in the inner cavity of the protein,[406] this fact lead to different starting points for the inorganic crystal to start growing and the resultant particle evolves from the outside towards the center of the cavity and growth of multiple domains inside each protein. The processes that govern the oxidation, nucleation and growth steps leading to the formation of magnetoferritin inorganic cores are not well known yet. As is the case with natural ferritin, the oxidation of Fe(II) to Fe(III) is catalyzed at the ferroxidase centers located inside the apoferritin cavity, whereas the nucleation is aided by residues of glutamic acid in the interior surface of apoferritin.[407, 408] For high iron additions (more than 50 atoms per protein), as is the case with the synthetic method employed for the authors, the oxidation can also take place at the core's surface due to the catalytic activity of the surface of already nucleated iron oxide clusters for the oxidation of Fe(II).[404]

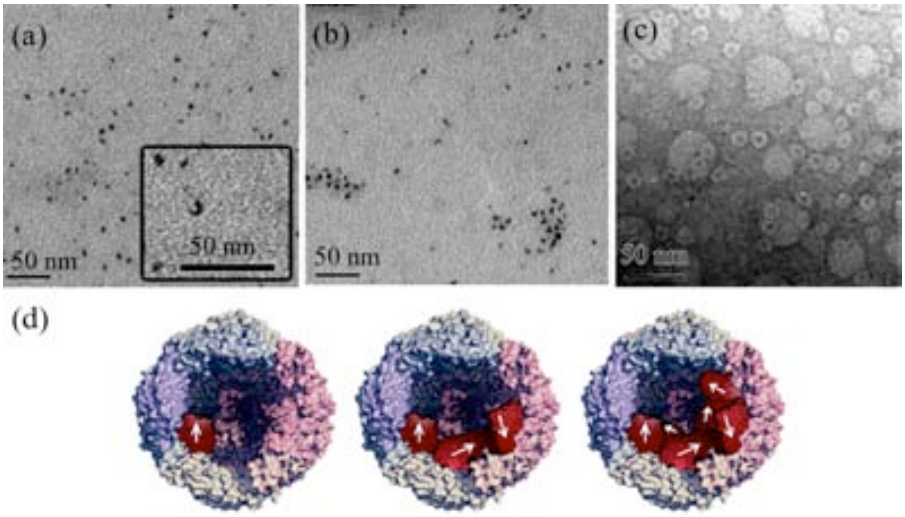

Figure 7.2 TEM images of magnetoferritin with an iron loading per protein of (a) 240 and (b) 1000 deposited on a carbon-coated TEM grid. The inset in panel **a** is an enlarged picture showing irregular NP shapes found in the sample. (c) TEM image of a negatively stained magnetoferritin sample (containing 1000 Fe atoms/protein) to show the contrast of the proteic shell (in white) around the inorganic core (in black). (e) Schematic illustration of the NP growth process. Crystallization begins at different points of the protein's internal surface leading to the formation of different crystalline domains. The white arrows represent the magnetization vectors of each of the crystalline domains that form the NP. Images reproduced from ref.[405] and [283].

7.1.5 CoO@apoferritin

Ferritin molecules displaying an internalized antiferromagnetic CoO NP were synthesized and structurally characterized by Dr. A. Lostao and R. de Miguel at INA. A detailed description of the followed protocol and materials used for their synthesis and characterization is described in

ref.[284]. However, the detailed mechanism of CoO growth inside ferritin cavity has not been described and remains unclear. A brief description of the synthetic procedure as well as further characterization is given.

The CoO NPs were synthesized inside apoferritin cavity following a previously reported method by introducing rational modifications that allowed them to achieve different results in cobalt loading and even composition of the NPs.[409] For their synthesis, 500 mL of 100 mM pH 8.3 HEPES buffer solution containing 0.5 $mg \cdot mL^{-1}$ apoferritin was prepared under argon atmosphere. The solution was stirred and ammonium cobalt(II) sulfate hexahydrate and sodium sulphate were added to final concentrations of 3.0 and 37.5 mM respectively, followed by the addition of hydrogen peroxide till a concentration of 1.5 mM. The solution was stirred for 20 minutes and then left at 50 ºC overnight. Under these optimum conditions, a pool of enriched CoO NPs encapsulated ferritin was obtained. The final solution was dialyzed against distilled water and then lyophilized. Lyophilized samples were stored at 4 ºC.

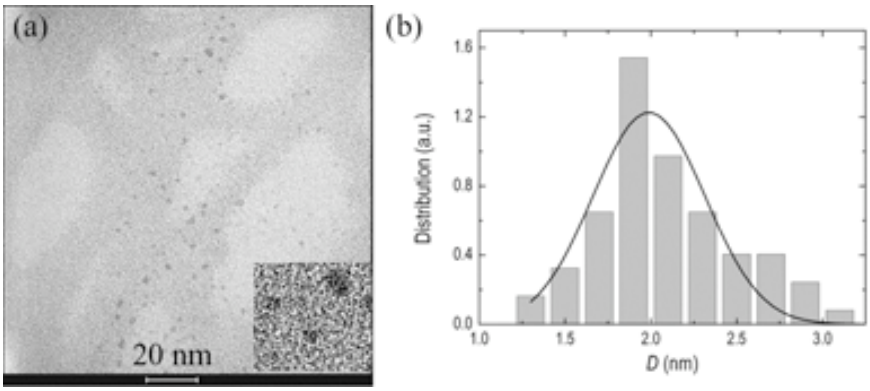

Figure 7.3 (a) TEM image of the CoO@apoferritin sample deposited on a carbon-coated TEM grid. The inset (10 x 21 nm) is a magnification view of the same sample. (b) Particle diameter distribution obtained from the analysis of TEM images. The solid line is a Gaussian fit that gives an average diameter of D = 2.0 nm and variance $\sigma = 0.3$. Images reproduced from ref.[284] and [403].

The size and shape of the internalized NPs were investigated by TEM (**Figure 7.3**). The average diameter of the NPs was near 2 nm. Moreover, most of NPs inside the cavity were spherical-shaped in the form of a unique particle. However, in few cases NPs with diameters over 3 nm (not shown in the figure) were observed, which presented a "bean-like" shape or several small cores inside a single cavity. This fact indicates that in the case of larger NPs the growth takes place from two or three different nucleation centers located in the inner cavity of the apoferritin. EDX together with theoretical calculations indicated an average of 108 Co atoms per protein and molecular weight of 481074 $g \cdot mol^{-1}$. The oxidation state of cobalt was determined by means of XPS analysis. From the experiments performed by R. de Miguel and co-workers it is evident that Co atoms in the ferritin-based NPs are clearly in the +2 formal oxidation state occupying octahedral sites suggesting the formation of CoO. For a more detailed description of the characterizations see ref.[284].

The bulk magnetic response of the CoO@apoferritin sample was characterized by Dr. M. J. Martínez-Pérez and co-workers at ICMA. A detailed description of the magnetic properties of the sample is described in ref.[283] and [284]. Experiments were performed with a commercial SQUID magnetometer (MPMS, Quantum Design) over a few milligrams of the sample fixed

with Apiezon-N grease on a typical holder. Magnetic measurements down to 1.8 K confirmed the antiferromagnetic character of the NPs with a T_N around 122 K. The measured net magnetic moment per particle is of ~ 12 μ_B for the CoO@apoferritin sample. Dc and ac susceptibility data measured at different frequencies are shown in **Figure 7.4**. There are no signs of a fully superparamagnetic blocking of the susceptibility down to 1.8 K, although a weak out-of-phase component (χ'') shows up below ~ 10 K.

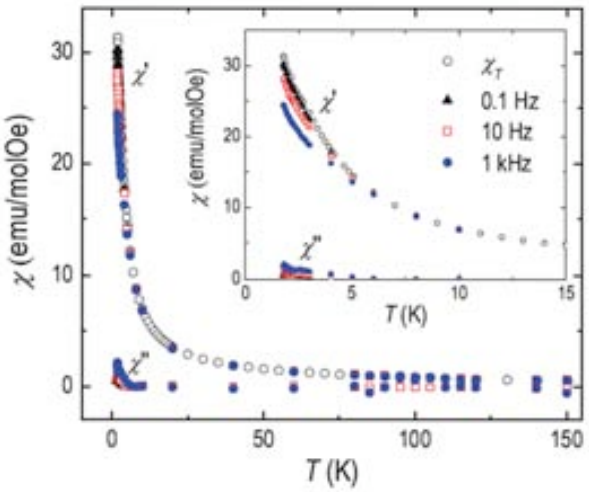

Figure 7.4 Initial susceptibility measurements as a function of temperature performed on a CoO@apoferritin bulk sample using a commercial SQUID magnetometer. In-phase (χ') and out-of-phase (χ'') ac susceptibility components and dc susceptibility (χ_T) as a function of temperature. Data obtained by Dr. M. J. Martínez-Pérez.

7.1.6 Mn_{12} molecules

In the present Thesis, two derivatives of the Mn_{12} family were structured on surfaces: the $[Mn_{12}O_{12}(O_2CC_6H_5)_{16}(H_2O)_4]$ (Mn_{12}bz) and the $[Mn_{12}O_{12}(O_2CC_6H_4C_6H_5)_{16}(H_2O)_4]$ (Mn_{12}biph). Both derivatives were synthesized by Dr. Daniel Ruiz-Molina at the CIN2.

Mn_{12}bz was synthesized following a previously described method reported by Sessoli *et col.*[25] The synthesis was based on the addition of C_6H_5COOH (1.0 g, 8.0 mmol) in a solution containing $[Mn_{12}O_{12}(O_2CCH_3)_{16}(H_2O)_4]\cdot CH_3COOH\cdot 3H_2O$ (0.50 g, 0.25 mmol) in CH_2C1_2 (50 mL). The mixture was stirred for 4 h and filtered to remove a small amount of undissolved solid. Then, hexanes (100 mL) were added to the filtrate, and the solution was stored overnight at room temperature. The resulting black microcrystals were collected by filtration, washed with hexanes and ethanol, and dried in air. The magnetic characterization of the bulk Mn_{12}bz sample down to 1.8 K was performed by Dr. F. Luis and M. Jenkins at ICMA with a commercial SQUID magnetometer (MPMS, Quantum Design). Ac susceptibility measurements of a few single crystals revealed the frequency-dependent out-of-phase peaks mostly coming from the slow relaxing species within the 3-5 K temperature range whereas there is also a small contribution of the fast relaxing species though in much less extent (**Figure 7.5**). These results confirm the integrity of the sample that retains the characteristic Mn_{12} SMM behavior though are not comparable to the final deposits on the sensors. Indeed, it is well-known that the presence of

one of the two relaxation mechanisms is highly dependent on the phonon bath, and therefore on the media.[325, 410] Therefore, upon solubilization of the sample, the finding of different magnetic behaviors with for instance an increase of the fast relaxing species would not be surprising at all.

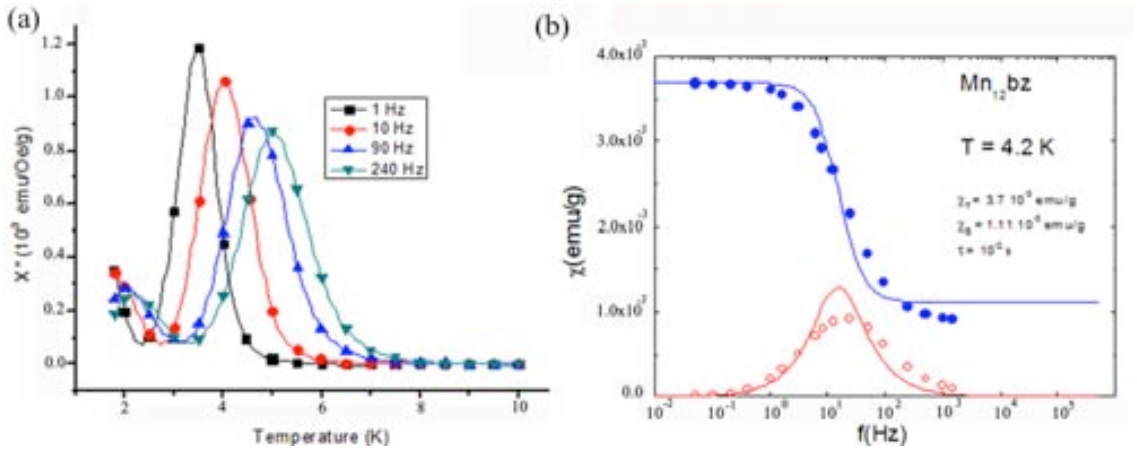

Figure 7.5 Magnetic measurements of a single crystal Mn_{12}bz performed with a commercial SQUID magnetometer. (a) Out-of-phase ac-susceptibility data as a function of temperature at different frequencies. (b) Ac susceptibility data as a function of frequency. Solid symbols in blue represent the in-phase susceptibility component and open symbols in red represent the out-of-phase component. Fitting of the data to Debye law provides the relaxation time of the slow relaxing species, $\tau \sim 10$ ms at 4.2 K. Data obtained by Dr. F. Luis and M. Jenkins.

Mn_{12}biph was synthesized following a previously described method reported by Ruiz-Molina *et al.*[319] The synthesis is based on the addition of $C_6H_5C_6H_4COOH$ (2.6 g, 13.3 mmol) to a solution of $[Mn_{12}O_{12}(O_2CCH_3)_{16}(H_2O)_4]\cdot CH_3COOH\cdot 3H_2O$ (1.0 g, 049 mmol) in 50 mL of toluene. The solution was allowed to stir overnight. Then, the mixture was concentrated to remove the acetic acid. The resulting solid and additional $C_6H_5C_6H_4COOH$ (1.3 g, 6.7 mmol) were dissolved in toluene (50 mL), stirred overnight and then concentrated to remove acetic acid. To fully substitute the acetate ligands, this procedure was repeated once more. The resulting brown powder was recrystallized by slow diffusion of hexanes into a CH_2Cl_2 solution of the complex. The resulting brown crystals of Mn_{12}biph were collected on a frit and washed with hexanes. The magnetic characterization of this sample shows a blocking of the in-phase ac susceptibility accompanied by the onset of a non-zero out-of-phase component in the 4-7 K region. Further magnetic characterization details of this molecule can be found elsewhere.[319]

7.1.7 ErW_{10} polyoxometalate

$Na_9[Er(W_5O_{18})_2] \cdot xH_2O$ (ErW_{10}) was synthesized by Prof. E. Coronado and S. Cardona-Serra at ICMol following a method previously described in ref.[411] and [412]. A detailed description of the synthesis, materials used as well as characterization is given in ref.[346] and [413]. In a first stage, $Er_2(CO_3)_2 \cdot xH_2O$ (2.180 g, 3.8 mmol) was dissolved in 30 mL of HCl (0.1 M) and heated at 80 °C for 30 min, giving rise to a colorless solution (A). Simultaneously, $Na_2WO_4 \cdot 2H_2O$ (50

g, 152 mmol) was dissolved in distilled water (100 mL) with continuous stirring; the pH was adjusted to 7.2 with acetic anhydride, and the resulting solution (B) was heated to 90 °C. Then, A was dropwise added to the hot stirred wolframate solution (B). After being vigorously stirred for 1 h, the mixture was filtered rapidly and left to evaporate at room temperature. A total of 3 weeks later needle-shaped pale-pink crystals of ErW_{10} were obtained.

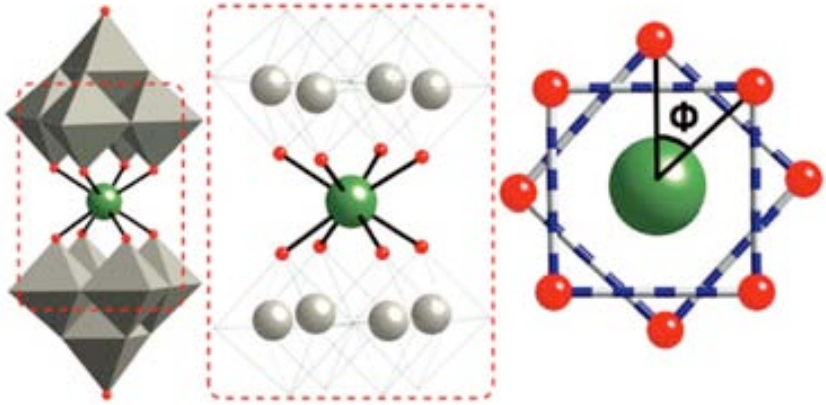

Figure 7.6 Structure of the ErW_{10} POM and projection showing the Er^{3+} ion square-antiprismatic coordination site. Reproduced from ref.[345].

S. Cardona and co-workers characterized the as-synthesized compound by FT-IR analysis and its characteristic bands in cm^{-1} are 935 (s), 845 (s), 798 (m), 706 (m), 586 (w), 545 (m), 490 (w). The band for W-O terminal stretching appears at approximately 935 cm^{-1}. There are bands for the W-O-W stretching at about 845 cm^{-1} and 798 cm^{-1}. The rest of the bands were not assigned by the authors. Single-crystal XRD was also used to determine the crystal structure of the Er complex and is given in ref.[346]. As illustrated in **Figure 7.6**, the POM complex consisted of two $[W_5O_{18}]^{6-}$ moieties encapsulating the central Er^{3+} ion. Each anionic moiety is twisted by an angle of 44.2 º with respect to the other which is very close to that expected for an ideal D_{4d} symmetry (45º). Therefore, the coordination site can be described as slightly distorted square-antiprismatic. The anionic cluster is surrounded by sodium cations, to balance the charge, which are octahedrally coordinated by water molecules. Consequently, a large amount of solvent molecules are present in the solid state. As a result, the Er^{3+} ions are quite well isolated giving a minimum Er-Er distance of ≈ 1 nm in the solid state. A detailed magnetic characterization of the compound exhibiting SMM behavior at low temperatures is described in ref.[345-347]. Both the in-phase and out-of-phase ac susceptibility show strong frequency dependencies, which indicate the presence of a slow relaxation process involving an energy barrier for the reversal of the magnetization. Depending on the frequency of the applied ac field, the in-phase signal presents a maximum between 5.5 and 7.5 K, while the out-of-phase component has also a maximum between 5 and 6 K for an ac field oscillating at frequencies 1000 and 10 000 Hz, respectively. Given the good insulation of Er^{3+} ions provided by the polyoxowolframate frame, the slow relaxation phenomena exhibited by ErW_{10} should be considered as a single-molecule property.

7.1.8 Cobalt nanoparticles

Spherical-shaped cobalt nanoparticles (Co-NPs) were synthesized and characterized by Dr. I. Ojea-Jiménez at CIN2 based on a thermal decomposition method already described in ref.[414]. Monodispersed oleic acid-stabilized Co-NPs ($2 \cdot 10^{16}$ NPs·mL^{-1}, aprox. 40 mg·mL^{-1}) of ~ 8 nm in diameter were prepared as follows. Briefly, trioctylphosphine oxide (0.1 g TOPO) and oleic acid (0.2 mL) were degassed in argon in a flask for 20 min. Then, 15 mL of *o*-DCB anhydrous was introduced into the flask under an argon atmosphere. The solution was heated to the reflux temperature of *o*-DCB (182 ºC) and 0.54 g of $Co_2(CO)_8$ (moistened with 5-10 % hexane) diluted in 3 mL of o-DCB was quickly injected into the mixture. The reaction continued for another 10 min and then the black colloidal solution was extracted using an airtight syringe and stored in a glass vial under argon. For the deposition experiments performed in this Thesis, the as-synthesized Co-NPs (2 mL) were washed by precipitation with anhydrous methanol (2 mL) followed by redispersion into a solution of *o*-DCB (20 mL) containing 0.08 % (w/w) oleic acid, giving to a final concentration of $2 \cdot 10^{15}$ NPs·mL^{-1}.

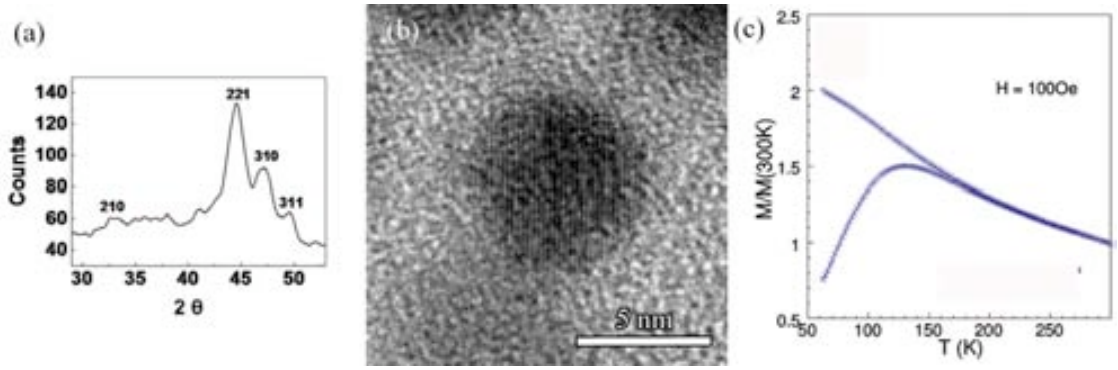

Figure 7.7 (a) XRD of Co-NPs showing its characteristic epsilon (cubic) crystal phase. (b) HR-TEM image of a single Co-NP deposited by drop casting on a carbon-coated TEM grid and characterized after 10 days of exposure to air. (c) Magnetization of Co-NPs after ZFC and FC in an external field of H = 100 Oe. Data shown in panel **a** and **b** was obtained by Dr. I. Ojea-Jiménez. Panel **c** is reproduced from ref.[415].

The typical epsilon (cubic) crystal anisotropy (ε-Co-NPs) was confirmed by XRD (**Figure 7.7**a). The uniformity in size and shape of the obtained NPs was verified by drop casting the NP solution onto a carbon-coated TEM grid and allowing the solvent to evaporate in air. Analysis of the TEM images determined a diameter of 7.6 ± 1.0 nm for the inorganic NPs (shown in Chapter 5 Figure 5.9). The NP stability against oxidation was verified by HR-TEM characterization 10 days after the drop casting of the NPs, which showed the formation of an approximately 1 nm thick CoO shell covering the Co as a result to the exposure of the NPs to air (Figure 7.7b). The creation of this oxide layer around the Co core is in agreement with previous reports that observed the formation of similar thicknesses, which has been shown to partially passivate the surface of the NP after the first weeks from the preparation of the sample.[416, 417] Magnetic characterization of the Co-NPs of 8 nm synthesized under the same reaction conditions is already described in ref.[415]. These NPs display a superparamagnetic behavior at room temperature, exhibiting hysteresis at low temperatures. Zero field cooling (ZFC)-field

cooling (FC) measurements in a magnetic field of 100 Oe revealed a blocking temperature of $T_B \approx 130$ K (Figure 7.7c). The measured magnetic moment per particle was ~ 10^4 μ_B.

7.2 Direct-write AFM lithography experiments

In this section we describe the materials used for the preparation of the ink solutions and the substrates used for the direct-write AFM lithography experiments described in this Thesis. Then, a description of the tips and instruments used as well as the standard routines followed for the deposition experiments is given.

7.2.1 Preparation of ink solutions and substrates

7.2.1.1 *Materials*

Glycerol (GC, ≥ 99 %), *N, N*-dimethylformamide (DMF, anhydrous, 99.8%), 1,2-dichlorobenzene (*o*-DCB, anhydrous, 99 %), toluene (anhydrous, 99.8%) and oleic acid (GC, ≥ 99 %) were purchased from Sigma-Aldrich. Acetone (Sps, ≥ 99.8 %), ethanol absolute (Sps, > 99.8 %) and acetonitrile (190 Sps, far UV/gradient quality, > 99.9 %) were purchased from Romil. All these materials are used as received. Phosphate buffered solution (PBS) (0.1 M sodium phosphate, 0.15 M NaCl, pH 7.2) was purchased from Pierce. The solution was filtered right before its use with a Nylon membrane filter of 0.20 μm pore size, purchased from Chmlab Group (Spain). The same type of filters has been used for POM-based ink solutions right before its deposition on surfaces.

7.2.1.2 *Substrate preparation*

Monocrystalline <100> Si wafers were obtained from Centro Nacional de Microelectrónica (CNM). Silicon with native oxide layer (Si/SiO_2) substrates were prepared by initially cutting Si wafers into 0.5 x 0.5 cm^2 pieces. Then, each Si/SiO_2 substrate was washed in an ultrasonic bath for 10 min in acetonitrile, ethanol and Milli-Q water, and dried by blowing nitrogen gas. Si/SiO_2 substrates prepared in the same way were also used to prepare the Au substrates at INA by thermal evaporation of a 10 nm-thick adhesion layer of Ti on the Si/SiO_2 substrate followed by a 40 nm layer of Au at a rate of 1 $Å \cdot s^{-1}$ and a base pressure of around $1 \cdot 10^{-7}$ Torr.
Niobium with a native oxide layer (Nb/Nb_2O_5) substrates were prepared by Dr. J. Sesé at the INA *via* a Si wafer with a 300 nm thermal silicon oxide, whereupon a 150 nm thick layer of Nb was deposited by using dc sputtering at room temperature. Nb substrates were also employed by Dr. J. Sesé to prepare aluminium with a native oxide layer (Al/Al_2O_3) substrates by depositing on it an Al layer of 5 nm thick using dc sputtering at room temperature.

Support films, carbon type-B, 200 mesh copper grids were purchased from Ted Pella, Inc (USA). Graphene samples were prepared and characterized by Prof. Marco Affronte and co-workers at the CNR-Institute of NanoSciences S3. Graphene flakes were obtained by the micromechanical exfoliation method[399] from natural graphite (NGS GmbH) onto a p-doped Si wafer with a 300 nm SiO_2 capping layer. Thin flakes were optically located with respect to lithographically pre-patterned alignment marks. The effective number of layers was checked by micro-Raman spectroscopy. Raman measurements were performed using a Jobin-Yvon LabRam spectrometer with a He-Ne laser at 632.8 nm wavelength.

7.2.2 Tips description

Direct-write AFM lithography experiments were carried out using three different types of tips, named: single pen (SP), M-type pen (MP) and non-contact high-resonance frequency (NCH) tips. The main characteristics of these tips are described.

7.2.2.1 *Single pen and M-type pen tips*

SP and MP tips are part of a full line of dedicated probes (commonly referred to as pens in DPN® technology) commercialized by NanoInk and specially optimized for patterning applications using NanoInk fabrication instruments (such as Nscriptor™ DPN System). These tips are also suitable for use with any commercial AFM instruments. NanoInk's probes display different geometries and force constants able to accommodate and deliver a wide variety of ink solutions and provide a greater versatility to the patterning process.
SP tips, also known as A-type Single Pens, are silicon nitride probes with a low force constant of ~ 0.1 $N \cdot m^{-1}$ specially designed for both contact mode imaging and patterning viscous liquids. This tip exhibits a tip radius of ~ 15 nm and a symmetric pyramidal shape of low aspect ratio (**Figure 7.8**a,b). This geometry is specially designed with a recessed area surrounding the tip that provides a high degree of functionalization by increasing the loading of ink material, and therefore a long stable writing performance (see Figure 5.19 in Chapter 5).
MP tips are part of a line of parallel-probe cantilever arrays (called passive pen arrays) developed to increase the throughput of direct-write AFM lithography thanks to an inherent serial fabrication process. MP tips consists of 12 parallel silicon nitride probes with a low force constant of 0.6 $N \cdot m^{-1}$, that duplicate 12 times the same pattern in a single deposition experiment (Figure 7.8c,d). The inter-ship separation between MP tips is ~ 66 μm. MP tips exhibit a tip radius of ~ 15 nm and a symmetric pyramidal shape of low aspect ratio like SP tips and are also optimized for patterning viscous liquids (Figure 7.8b). In addition, they are modified with a larger recessed area surrounding the tip to further increase loading of material and extend printing times (see Figure 7.8d and Figure 3.6 in Chapter 3). For the integration experiments, a single MP tip was used. For this, the rest of the MP tips in the cantilever array were removed with the help of tweezers and an optical microscope.

Tips were used as received for direct-write AFM lithography; however in some particular cases they were further cleaned by ozone cleaning treatment during 5 – 10 min for removal of molecular organic contamination using the PSD UV-ozone cleaning system from Novascan Technologies, available at the CIN2.

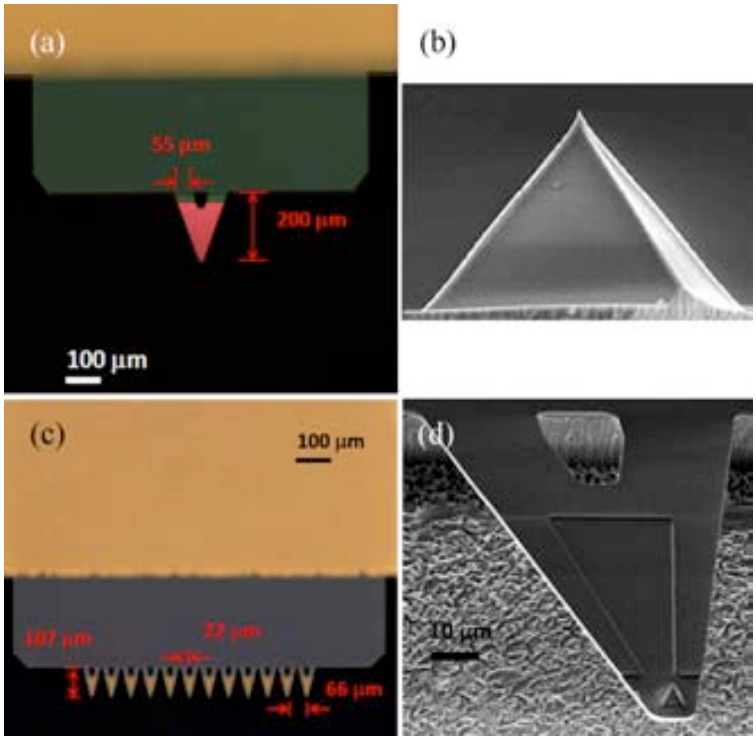

Figure 7.8 (a) Optical image of a SP tip and its measurements. (b) FE-SEM image of the tip (both SP and MP tips are the same). The tip has a pyramidal base and a tip radius of ~15 nm. (c) Optical microscope image of a MP tip and its measurements. (d) FE-SEM image illustrating the recessed area surrounding the MP tip. Reproduced from NanoInk's website: www.nanoink.net/.

7.2.2.2 *Non-contact high-resonance frequency tips*

NCH tips, also known as PointProbe® Plus (PPP) NCH silicon probes, are from Nanosensors™. NCH tips have a force constant of ~ 42 $N \cdot m^{-1}$ and exhibit a sharper radius of ~ 7 nm and an asymmetric pyramidal shape of high aspect ratio (**Figure 7.9**). This type of tips is designed for non-contact and intermittent contact mode imaging (resonant frequency ~ 330 kHz). These tips are suitable for AFM instruments.

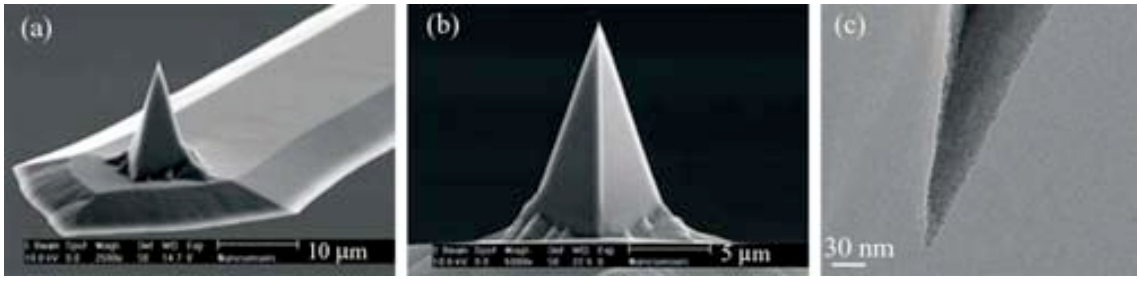

Figure 7.9 SEM images of NCH tip (a) 3-D view and (b) side view. (c) TEM image of a NCH tip apex. Reproduced from Nanosensors™'s website: www.nanosensors.com.

7.2.3 Instruments

The great majority of direct-write AFM lithography experiments were performed using a dedicated Nscriptor™ DPN System instrument from NanoInk. However, as we will see in the next section, we evidenced a better accuracy on tip positioning using a conventional AFM instrument (Agilent 5500 AFM/SPM microscope, formerly Molecular Imaging PicoPlus AFM, from Agilent Technologies). On the other side, one strong advantage of Nscriptor™ DPN System is that is a user-friendly instrument consisted of a specially modified AFM and optimized software for performing direct-write AFM lithographic experiments. In this Thesis, we chose the instrument more appropriate for each particular experiment depending on the level of tip positioning accuracy required. In this section we will describe both instruments as well as standard routines for the deposition experiments. Finally, the experiments performed in order to evaluate the tip positioning accuracy of both instruments are explained.

7.2.3.1 *Nscriptor™ DPN System*

DPN® is a patented and proprietary nanofabrication technology which is referred to the patterning process that makes use of NanoInk's products to structure functional materials on a given substrate surface by using a tip as a delivery system. NanoInk commercializes dedicated fabrication instruments specially designed for the development of DPN® processes which have significantly accelerated the direct-write AFM lithography experimentation process.
Nscriptor™ DPN system is the first member of the family of NanoInk nanofabrication instruments and consists of a modified AFM equipped and software system optimized for the DPN® process (**Figure 7.10**). Nscriptor™ closed-loop scanner has inductive position sensors that provide optimum control over the position of the tip for ensuring accurate and repeatable patterning (linearity error 1 % and precision of 10 nm). DPN® experimentation is assisted by an user-friendly interface NanoInk's InkCAD™ software, which provides a set of lithographic tools as well as imaging AFM modes (contact and intermittent contact modes) for tackling with patterning experiments as well as subsequently examining the generated patterns *in situ*, respectively. This fabrication system permits to easily designing complex patterns while also precisely controlling the tip movements during the writing process inside a scan range of 90 µm × 90 µm. In addition, an integrated environmental chamber as part of Nscriptor™ system allows monitoring and controlling the environmental conditions (i.e. temperature and relative

humidity) during the writing process in order to fulfill the requirements needed for each particular experiment. In addition, integrated optics provides the ability to monitor the position of the tip(s) relative to the sample surface. The resolution of the optics is ~ 3 μm. Double-back tape was used to mount the sample on the standard sample stage. The X-Y stage (2.5 cm × 2.5 cm travel) works with the optics to allow the user to position the sample area of interest beneath the tip(s). Nscriptor™ DPN System is situated on a solid granite support base on an air table to isolate the instrument from floor vibration.

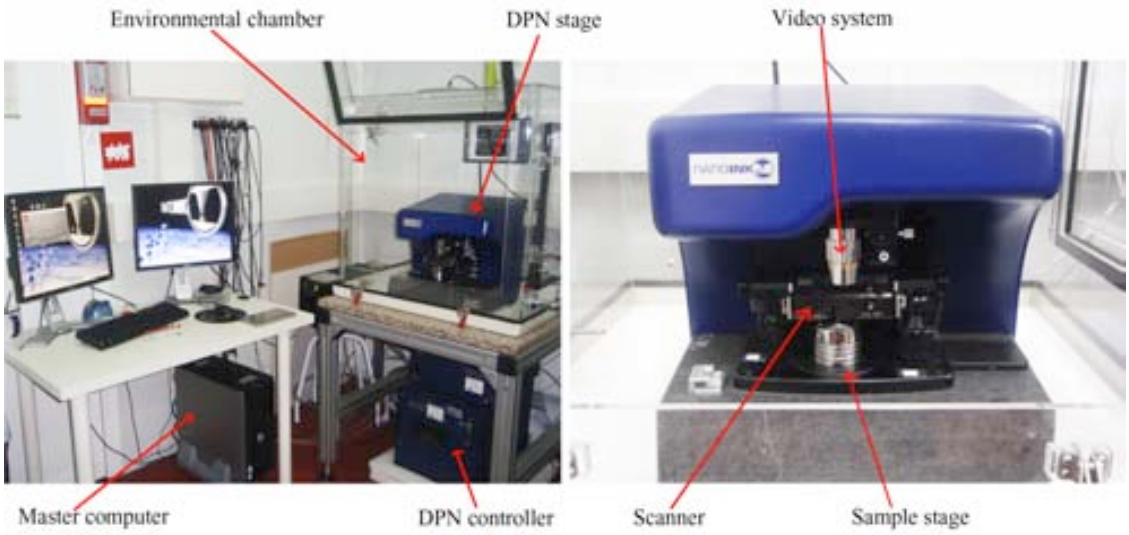

Figure 7.10 Components of the Nscriptor™ DPN System.

Standard NanoInk routines have been described in order to bring the material solution (referred to as ink solution) onto the tip and deliver it on the target surface. In this Thesis, we have followed a tip coating approach based on dip coating the tip into an ink solution for a given time and immediately use it in order to deliver a desired amount of the ink solution onto a surface in the form of droplets.

More precisely, the controlled coating of tips with polar ink solutions have been performed following standard NanoInk inking routines using a microfluidic ink delivery chip-based system, called Inkwell, developed and commercialized by NanoInk. This microfluidic system is specifically engineered to be filled with polar solvents such as aqueous ink solutions. A hydrophobic polymeric coating inhibits polar inks from spreading onto the chip substrate, while the channels, reservoirs and microwells remain uncoated and thus hydrophilic. In particular, we have use M‐6MW Inkwell chips specifically designed to be used with MP tips (**Figure 7.11**). The spacing between the microchannels is 66 μm, corresponding exactly to the spacing between the MP tips. The M‐6MW Inkwell features six 2 mm diameter reservoirs with a depth of 85 μm. The reservoirs are linked to the 20 μm diameter microwells *via* 40 μm wide channels that lead into 6 μm wide microchannels (Figure 7.11b). In a typical experiment, the reservoirs are filled with ink using a micropipette. Then, the ink solution is transferred by capillary action through the channels that connect the reservoirs with the microwells. The system was designed to keep the microwells full of ink, even as the ink supply slowly evaporates from the reservoir. In the final stage of the ink coating process, each tip is loaded with the desired ink by dipping

the tips into the microwells for a given time. The use of all the reservoirs allows to simultaneously loading six MP tip of the cantilever array with the same or different inks. An example of tips being dipped into microwells filled with a ferritin-based solution is shown in Figure 3.6 in Chapter 3.

In order to deliver the ink material on the surface in the form of well-defined droplets, the coated tips are carefully brought into contact with the substrate surface to fabricate the desired pattern by traversing the tip over the surface. Two different lithographic operation modes are available in Nscriptor™ DPN System: constant force and constant height. The first mode is the normal AFM feedback contact mode, where the system tries to keep the tip's downward force constant. On the other hand, constant height mode is a faster process that eliminates the need to align a laser spot on the cantilever. In this mode, the pen is not in feedback, and it remains at a user-controlled height optically determined by the cantilever deflection. During lithography the scanner lifts the tip up to 10 µm from the pre-defined height between elements in the pattern in order to reduce the amount of undesirable ink drawn between the elements. In this Thesis, the great majority of patterning experiments using Nscriptor™ DPN System were performed in constant height mode.

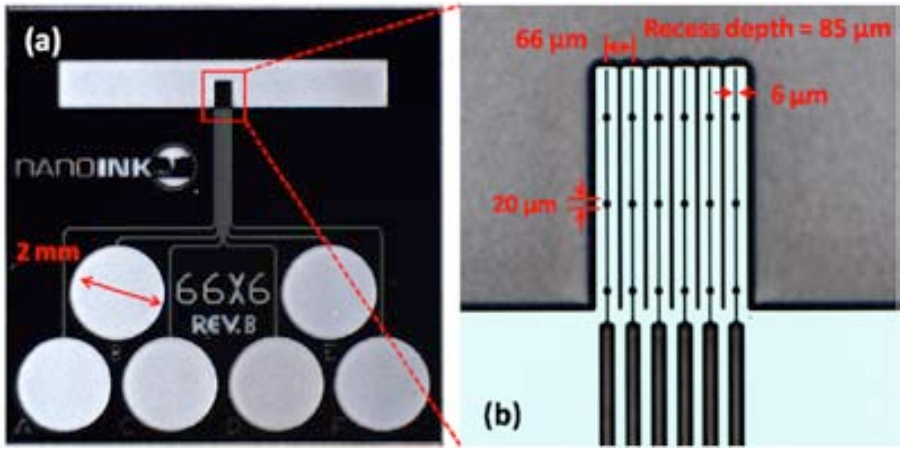

Figure 7.11 Optical microscope images showing (a) an overview of the M‑6MW Inkwell, which contains six reservoirs and (b) the dimensions of the microchannels and microwells. Reproduced from NanoInk's website: www.nanoink.net/.

7.2.3.2 *Agilent 5500 AFM/SPM microscope*

Agilent 5500 AFM/SPM microscope combined with PicoScan software from Agilent Technologies was used as an imaging and fabrication instrument. **Figure 7.12** shows the main components of Agilent 5500. The instrument is situated on a solid granite base and enclosed in a vibration isolation chamber that isolates the AFM from vibration, air turbulence and acoustic noise which would adversely affect imaging. Also, an environmental control chamber permits isolate samples for imaging in a controlled atmosphere. In addition, there is available a temperature control sample plate combined with Lakeshore 332 Temperature Controller. An integrated video system permits to locate regions of interest as well as align the laser on the probe tip.

Two different types of multi-purpose scanners have been used: (i) large scanner, which provides scans up to 90 μm × 90 μm for high resolution and speed for general use applications (z scan range 7.5 μm); and (i) small scanner, which provides scans up to 10 μm × 10 μm and it is capable of atomic-level resolution imaging (z scan range 1.6 μm). Additionally, Agilent 5500 is equipped with an X-Y nanopositioning stage designed to integrate with Agilent's 5500 microscope (NPXY100E from nPoint, USA) that utilizes closed-loop capacitive feedback to ensure scanning linearity and position accuracy within a scanning range of 100 μm × 100 μm (linearity error 0.03 % and precision of 0.5 nm). AFM imaging was performed using both scanners, whereas for AFM lithographic experiments the small scanner was used.

Agilent 5500 can be operated in a variety of imaging modes, including contact mode AFM, intermittent contact mode (AC mode) AFM, current sensing AFM (CSAFM), scanning tunneling microscope (STM), force modulation microscopy (FMM), magnetic force microscopy (MFM), electrostatic force microscopy (EFM) and kelvin force microscopy (KFM). In this Thesis, for imaging and direct-write AFM lithography we operated AFM in contact and intermittent contact mode.

Figure 7.12 Components of the Agilent 5500 AFM/STM Microscope.

Typically, the scanners used for moving the probe relative to the sample in an AFM are constructed from piezoelectric materials; such is the case of Nscriptor™ DPN System and Agilent 5500 AFM/STM Microscope. Ideally, the piezoelectric ceramics would expand and contract in direct proportion to the driving voltage. Correcting the non-ideal behaviors of piezoelectric materials, such as non-linearity, hysteresis and creep, which may cause the piezoes to drift from the expected positions, is essential for making accurate measurements with an AFM. As already mentioned, both instruments use position sensors in a closed-loop configuration, where the motion of the probe is corrected in real time with a feedback electronic circuit.

The tip positioning control of our Agilent instrument equipped with the X-Y nanopositioning stage was checked in an experiment performed by Dr. F. Rigato at CIN2 and the results are

shown in **Figure 7.13**. In these experiments, a fixed area of a patterned Si/SiO_2 substrate was imaged in intermittent contact mode using a NCH tip. Then, the tip was displaced by 40 μm and then placed back to the starting point. Then, a new scan was performed and a slight shift was found. This operation was repeated four times in different directions, indicated by the respective arrows in the Figure 7.11b. From this study, it was determined an X and Y shift of 30 nm and 60 nm from the ideal position, respectively. Similar experiments using Nscriptor™ DPN System gives shifts up to 450 nm. For this experiments, mounted close contact silicon probes from Agilent Technologies were used (force constant ~ 40 $N \cdot m^{-1}$, resonance frequency ~ 300 kHz). This behavior is extremely critical for precisely controlling the tip positioning during direct-write AFM lithography experiments. Therefore, highly-demanding experiments such as those described in Chapter 5, in which a small amount of NPs should be site-selectively integrated onto a well-defined of 1 μm x 1 μm, were performed using Agilent instrument instead of Nscriptor™ DPN System to ensure an adequate tip positioning control.

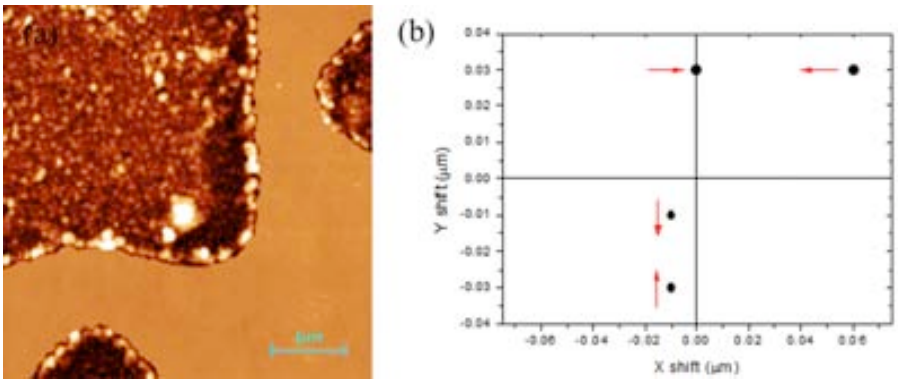

Figure 7.11 (a) AFM topography image of a patterned Si/SiO_2 surface. This selected region was imaged in intermittent contact mode and then the tip was displaced 40 μm in different directions (indicated in red arrows in panel **b**) and placed back to the starting position to scan the same region. The process was repeated 4 times. (b) Representation of the X and Y shift with respect to the ideal position after each one of the scannings. The direction of the 40 μm displacements is indicated with red arrows. Experiments performed by Dr. F. Rigato.

7.3 Characterization techniques

- *Contact Angle.* The affinity of the ink solutions and substrates was investigated by measuring the static contact angle based on the sessile drop method, i.e. drops of liquid are deposited on a solid surface (as smooth and horizontal as possible). The measurements were performed in our centre CIN2 using a drop shape analyzer Easy Drop combined with a user-friendly Drop Shape Analysis DSA1 from Kruss. In the experiment a 3 μl droplet of the ink solution was deposited on the target substrate surface using a micropipette. Contact angle was measured on five different regions of the substrate and an average value was obtained from all the measures.

▪ *Optical microscopy.* Optical and fluorescence images of the structures created by direct-write AFM lithography as well as of the tips right after ink coating step were obtained at the CIN2 with a Axio Observer Z1 inverted microscope with motorized X-Y stage combined with AxioVision imaging software from Carl Zeiss. The excitation sources available in this microscope for optical and fluorescent images are halogen and Hg lamp, respectively. 20×, 50×, and 100× air objectives from Zeiss were used in these studies.

▪ *Atomic Force Microscopy.* The topography of the created structures was investigated by AFM using an Agilent 5500 AFM/STM microscope combined with PicoScan software from Agilent Technologies. The main characteristics of this instrument have already been described in detail in Section 7.2. Large and small scanners with scan range up to 10 μm × 10 μm and 90 μm × 90 μm respectively, were used for imaging samples in intermittent contact mode under ambient conditions. Data acquisition time was significantly reduced using a X-Y nanopositioner stage (NPXY100E from nPoint, USA) with a scan range up to 100 μm × 100 μm integrated with Agilent's microscope, which allowed one-click zooming and repositioning capability. The AFM tips used for intermittent contact imaging were PointProbe® Plus (PPP) NCH silicon probes from Nanosensors™. This type of tips, named NCH tips, has already been described in detail in Section 7.2. Double-back tape was used to mount the sample on the standard sample plate.
AFM image processing and rendering was done using open source software, WSxM 5.0 software (version 5.0, Nanotec Electronica, Spain)[418] and Gwyddion data analysis software (version 2.25, http://gwyddion.net/). Characterization of the fabricated arrays by AFM was performed by randomly selecting almost 25 different dots in the array and measuring their diameter and height. For each array, we obtained the mean diameter or height and the 95 % confidence interval for the mean, which was calculated based on the sample mean and sample standard deviation. In some cases, dots with elongated shapes where observed instead of the ideal round shape. The radius of these dots was defined as $r = (a \cdot b)^{1/2}$ where a and b are one-half of the shorter and longer axes of the ellipse, respectively. This definition corresponds to setting r as the radius of a circle whose area matches that of an ellipse with one-half ellipse axes a and b.

▪ *Transmission Electron Microscopy:* All TEM characterization was performed at the Servei de Microscopia of the Universitat Autònoma de Barcelona, UAB. TEM images were taken with a JEM-1400 microscope combined with JENIE™ software from Jeol. This microscope is a high contrast TEM with an acceleration voltage of 40 to 120 kV and equipped with two cameras: CCD GATAN 794 MSC 600HP and CCD GATAN ES1000W Erlangshen™ from Gatan. Resolution of the TEM is 0.4 nm at 120 kV. In some cases, routine TEM characterizations were performed in a second more accessible TEM also available at the Servei de Microscopia (UAB), the Hitachi H-7000 instrument from Hitachi High Technologies Corporation. This microscope with an acceleration voltage of 25 to 125 kV is equipped with a CCD GATAN ES500W Erlangshen™ camera from Gatan. Resolution of the microscope is 0.4 nm at 120 kV. HR-TEM images, EDX analysis and SAED were carried out with a JEM-2100 microscope from Jeol with the technical support of Dr. E. Rossinyol (Servei de Microscopia,

UAB). This microscope is an advanced field emission electron microscope featuring ultrahigh resolution (0.18 nm at 200 kV) with an acceleration voltage of 80 to 200 kV. It is equipped with a CCD GATAN 895 USC 4000 camera from Gatan and an EDX detector combined with INCA software from Oxford Instruments with an energy resolution of 136eV for EDX analysis.
TEM sample preparation was performed by drop casting a solution on a carbon-coated TEM grid and allow the solvent evaporate under air. In addition, structured samples were created using direct-write AFM lithography on carbon-coated TEM grids. In all the samples, we used support films, carbon type-B, 200 mesh copper grids purchased from Ted Pella. Negative staining of ferritin sample was performed using aurothioglucose hydrate (≥ 97 %, Sigma-Aldrich), which is a well-known negative stain agent for ferritin.[228, 419] Carbon-coated TEM grids were glow discharged (Servei de Microscopia, UAB) in order to make the carbon film more hydrophilic and hence favor a more homogeneous distribution of ferritin proteins on the film. The ferritin solution (0.22 $mg \cdot mL^{-1}$ in PBS) was drop casted on the TEM grid and the excess was removed with a piece of filter paper. Then, the grid was dipped several times in Milli-Q water to further remove the excess of material on the film and left to dry under air. A solution of aurothioglucose (3 % w/w) was drop casted on the grid and after 2 minutes the excess was removed with a paper and left to dry under air.
Digital images were analyzed with the ImageJ software. The characterization of the arrays fabricated on the TEM grids (i.e. determination of the dot diameter) was performed in a similar manner as in the case of AFM topography images (see above).

- *Field-Emission Scanning Electron Microscopy.* FE-SEM characterization of tips and samples prepared by drop casting, spraying or structured by means of direct-write AFM lithography was carried out using a Quanta FEI 200 FEG-ESEM from FEI™ at the Institut de Ciència de Materials de Barcelona (ICMAB) with the technical support of Dr. J. Oró-Solé and A. E. Carrillo. It is equipped with a field emission gun (FEG) for optimal spatial resolution. The instrument can be used in high vacuum mode, low-vacuum mode and environmental SEM mode (ESEM) (the chamber pressure is monitored by water vapor injection). This makes it possible to study samples in pressures up to 10 to 2600 Pa in ESEM mode. The resolution is kept high at all conditions: 1.2 nm and 1.5 nm at 30 kV in the high and low vacuum modes, respectively. The capability to vary the chamber pressure is especially suited for the observation of uncoated non-conducting materials. In our case, FE-SEM characterization was mainly performed in high vacuum mode ($< 6 \cdot 10^{-4}$ Pa) and operating at an acceleration voltage of 5 – 10 kV. In some cases, routine FE-SEM characterizations were performed in a more accessible instrument, Hitachi H-4100FE from Hitachi High Technologies Corporation, at the Centres Científics i Tecnològics at the Universitat de Barcelona (CCiTUB). It is equipped with a FEG and it was operated an acceleration voltage of 10 – 15 kV. The resolution of the microscope is 1.5 nm. For the characterization of a drop casted ErW_{10} sample by EDX we used a MERLIN® FE-SEM from Carl Zeiss equipped with an EDX detector from Oxford Instruments, at the Servei de Microscopia (UAB) with the technical support of Dr. P. Castro-Hartmann. This tool enabled the chemical analysis of the sample with a high lateral resolution (elemental mapping).

▪ *Time-of-Flight Secondary Ion Mass Spectrometry*. ToF-SIMS data acquisition and treatment were performed by Dr. R. Pérez-Rodríguez using an ION-TOF IV instrument from ION-TOF at the Plataforma de Nanotecnologia located at the Parc Científic de Barcelona. The instrument was operated at a pressure of $5 \cdot 10^{-7}$ Pa. Samples were bombarded with a pulsed Bismuth liquid metal ion source (Bi^{3++}), at energy of 25 keV. For high image resolution the gun was operated with a 100 ns pulse width and 0.15 pA. Secondary ions were detected with a reflector time-of-flight analyzer, a multichannel plate (MCPs), and a time-to-digital converter (TDC). Images were acquired at 256 x 256 pixel image size and each ion image was normalized to the intensity in the brightest pixel. Charge neutralization was achieved with a low energy (20 eV) electron flood gun.

▪ *X-ray Diffraction.* Grazing angle XRD measurements were performed by Dr. J. Santiso at the CIN2 in a Panalytical X'Pert Pro X-ray diffractometer by using constant grazing incidence (0.5º) and parallel beam optics. Analysed area was about 5 x 20 mm^2. In this technique both incident and diffracted beams are nearly parallel to the sample surface and then it allows recording the diffraction pattern of thin films, with minimum contribution from substrate.

▪ *Attenuated Total Reflectance Fourier Transform Infrared Spectroscopy*. IR spectra were recorded in a TENSOR™ 27 FT-IR spectrometer from Bruker Optics with the help of Dr. F. Novio at the CIN2. An Attenuated Total Reflectance (ATR) accessory is mounted in the spectrometer's sample compartment. Mn_{12}bz characterization was performed as follows. First, a droplet of a DMF solution with a 5 % (v/v) of glycerol was directly deposited on the ATR crystal for obtaining the IR spectrum. Then, the IR spectrum of the Mn_{12}bz sample was obtained by characterizing a droplet of a Mn_{12}bz 20 $mg \cdot mL^{-1}$ in DMF containing a 5 % (v/v) of glycerol and then subtracting from the IR spectrum the background signal of the IR spectrum of the solvents alone. The ErW_{10} POM sample was prepared by drop casting a 30 $mg \cdot mL^{-1}$ ErW_{10} solution in a glass vial, immediately placed in an air-tight chamber saturated with water vapors at room temperature for 5 days and left the solvent evaporate under air. Then, a small amount of the resulting solid material was used for ATR-IR analysis without further preparation.

▪ *Raman spectroscopy.* Raman measurements were performed Prof. Marco Affronte and co-workers at the CNR-Institute of NanoSciences S3 using a Jobin-Yvon LabRam spectrometer with a He-Ne laser at 632.8 nm wavelength. The incident power was ~ 20 mW.

7.4 Sensors

In this section, we describe the main features of the three sensors used in this Thesis for the integration of magnetic materials onto their sensitive areas.

7.4.1 microSQUID sensors

First a brief introduction to SQUID principles is given. Then, we describe the main features of both SQUIDs.

7.4.1.1 *SQUID sensor principles*

SQUIDs are based on two phenomena in superconductivity, namely magnetic flux quantization and the Josephson effect, to measure extremely small variations in magnetic flux.[47, 420] Typically, a SQUID is a ring of superconductor interrupted by one or more Josephson junctions, called weak links. In a Josephson junction, two superconducting regions of a wire are interrupted by a resistive barrier (see **Figure 7.12**b). Until a critical current I_c is reached, a supercurrent can flow across the barrier; electron pairs can tunnel across the barrier and the superconducting current can penetrate the resistive barrier with no voltage drop. But when the critical current is exceeded, a non-zero voltage will develop across the junction.

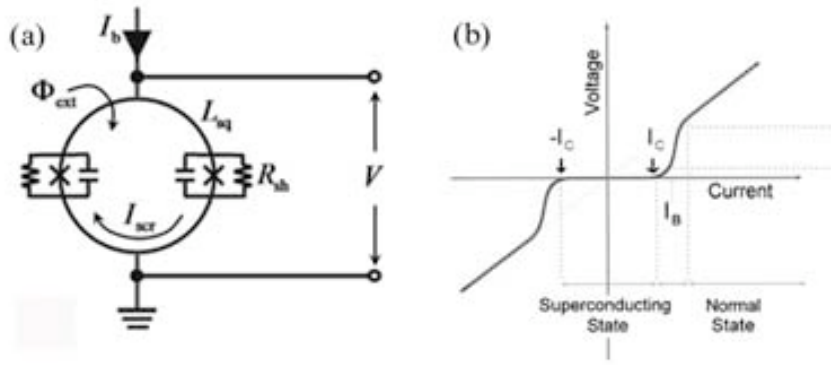

Figure 7.12 (a) SQUID loop scheme where the two Josephson junctions are marked with crosses. (b) Current vs voltage curve measured across a Josephson junction. I_c indicates the critical current and I_b a bias current. (c) Voltage vs externally applied flux Φ_{ext} at constant bias current I_b. The operation point W is chosen in the steepest part of the $V-\Phi_{ext}$ curve. Panel **a** reproduced from ref.[420]. Panels **b** and **c** reproduced from ref.[47].

The most widely used device based on these ideas receives the name of direct current or dc-SQUIDS. These systems consist of a superconducting loop interrupted by two junctions and is schematically depicted in Figure 7.12a. The SQUID loop is biased with an external current I_b with a slightly higher value than I_c, that, in absence of any external magnetic flux, distributes symmetrically over the two SQUID branches. When an external magnetic flux Φ_{ext} is coupled into the SQUID loop, a screening current (I_{scr}) will be generated in order to cancel this flux and the voltage drop across the Josephson junction will change. As the external flux increases or decreases, the voltage will change in a periodic manner with the period being that of the flux quantum. Monitoring the change in voltage allows the determination of the magnetic flux that has been coupled into the SQUID loop.

microSQUID susceptometry: SQUIDs behave effectively as very sensitive flux-to-voltage transducers. Therefore, they can be used to sense any physical quantity that can be converted

into magnetic flux, e.g. magnetic susceptibility. A susceptometer measures the magnetic susceptibility χ of a sample, i.e. the variation of the magnetization (M) with the external applied magnetic field (H), $\chi = \partial M / \partial H$. That is, the magnetic susceptibility χ is a measure of how sensitive the material is to an applied field H.

In the simplest configuration, that of a magnetometer, a pickup coil (L_p) is placed in the field to be measured, causing a current to flow on the input coil (Li), which in turn couples a flux that is detected by the SQUID. If the external field changes, the conservation of the overall magnetic flux induces a screening current in this superconducting circuit. The coil (L_i) generates then a magnetic flux which in turn is detected by the SQUID (see **Figure 7.13**a). One of the major disadvantages of such magnetometers is that they are extremely sensitive to the outside environment, that is, they sense not only the magnetic field coming from the sample, but also any other external magnetic field. This may be acceptable if one is measuring ambient fields. However, if what is to be measured is close to the detection coil and is weak, a gradiometric configuration may be preferred.

A gradiometer arrangement is essentially the same as a magnetometer except that the pickup coil is in fact made of two or more coils. A first-derivative order gradiometer consists of two identical and exactly parallel loops wound in opposite senses, as shown in Figure 7.13b). When an external uniform field (H_0) is applied, it will couple equally into both coils. A screening current should appear therefore in each one of the loops but, since they have opposite directions, no net flux is coupled to the SQUID. An object much closer to one coil than the other will couple better to the closer coil than to the more distant one. This magnetic field that is of different magnitude at the two sites of the coils will cause a non-zero total flux change, producing a net current flowing in the circuit. This device is therefore a measure of the field gradient.

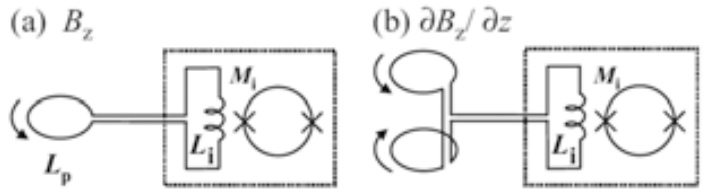

Figure 7.13 Schematic illustration of (a) magnetometer configuration and (b) first order gradiometric configuration. Images reproduced from ref.[421].

How does an ac susceptometer works:

A susceptometer consists of two circuits: (i) the primary circuit, that creates the ac exciting magnetic field, and (ii) the secondary circuit, that consists of two (or more) pickup coils designed in a gradiometric fashion. The latter circuit couples the magnetic signal coming from the sample (see **Figure 7.14**a). When an oscillatory magnetic field ($H_{ac} = H_0 \sin(\omega t)$, where H_{AC} is the amplitude of the driving field, ω is the driving frequency) is used as the excitation magnetic field, two components will be obtained. One, oscillating in-phase with H_{ac}, is proportional to the real part of the susceptibility χ', while the other, oscillating with a $\pi/2$ phase shift with respect to H_{ac}, is proportional to the imaginary part χ''. An example of the ac

susceptibility of a magnetic material as a function of frequency, performed at constant temperature, can be seen in Figure 7.14b. When the experimental frequency equals the inverse of the magnetic relaxation time (τ) of the sample, a peak appears in the imaginary component.

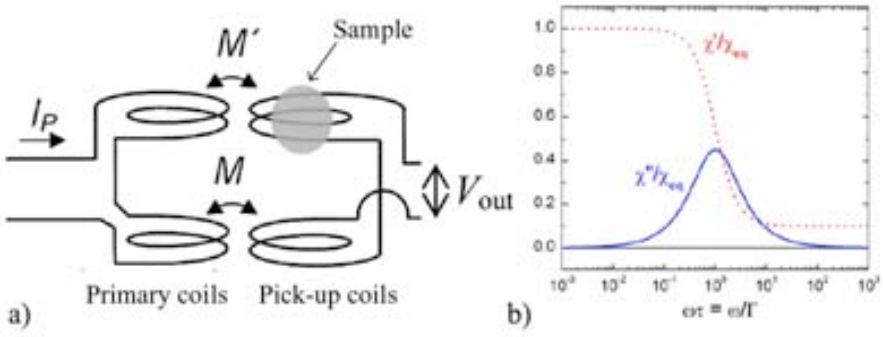

Figure 7.14 (a) Schematic illustration of a generic ac magnetic susceptometer. When a current I_P is injected to the primary, the output voltage (V_{out}) of the secondary is different from zero when a sample with susceptibility χ modifies one of the mutual inductances, M and M' (referred to the inductance in the pickup coils due to the magnetic field created by the primary coil). (b) Typical ac-susceptibility curve as a function of frequency. Reproduced from ref.[283].

In the present study, once the magnetic material was integrated into the microSQUID susceptometer, magnetic measurements were performed in order to obtain the ac magnetic susceptibility of the deposited sample and to determine the magnetic behavior of the system. The ac magnetic susceptibility of magnetic NPs and SMMs provides useful information on their spin and magnetic anisotropy,[422] as well as on the magnetic relaxation mechanisms.[18, 423, 424]

7.4.1.2 *1st generation microSQUIDs*

The sensor used in Chapter 3 forms part of a new generation of integrated microSQUID susceptometers developed during the doctoral research performed by Dr. M. J. Martínez-Pérez supervised by Dr. F. Luis and Dr. J. Sesé from the ICMA and INA, in collaboration with Dr. D. Drung and T. Schurig from the PTB. Their complete characterization and performance has already been reported and a brief description is given next.[283, 425, 426]

Their purpose was to develop a novel generation of ac magnetic susceptometers that combines high sensitivity and broad frequency bandwidth with operation down to very low temperatures and user friendliness. To measure very small magnetic signals, arising from e.g. molecular monolayers or a small number of NPs, they took advantage of a commercial easy-to-use two-stage SQUID sensor fabricated at the PTB (from Magnicon GbR). This sensor is well suited to operate at mK temperatures with a broad bandwidth and sensitivities close to the quantum limit.[427] They made use of such optimized sensor as starting point for the fabrication of the susceptometer. It turns out that, via a simple modification of superconducting circuits to reroute some of the SQUID input wires, a fully integrated microSQUID susceptometer was obtained. Modification of the chips was performed by FIB etching and *in situ* deposition. In this way, Dr. M. J. Martínez-Pérez and co-workers succeeded in fabricating a new generation of SQUIDs in

which one intermediate inductive coupling is avoided and the sample is directly placed on the SQUID loop, thereby improving the coupling between them (**Figure 7.15**).

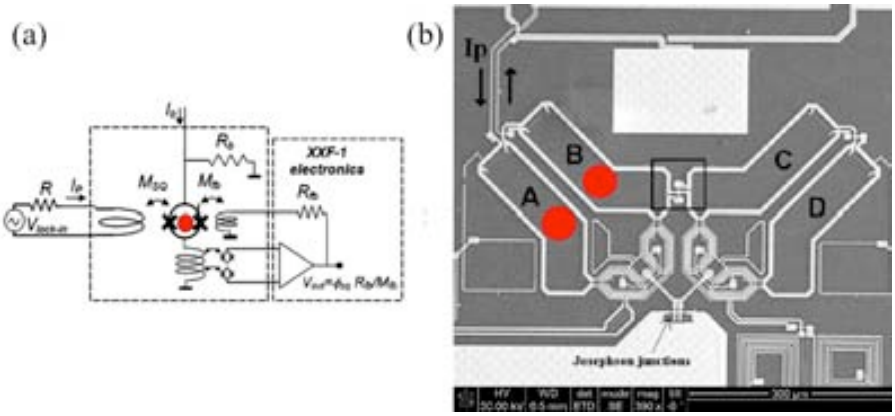

Figure 7.15 (a) Schematic diagram of the SQUID susceptometer chip (inside dashed line) after modification by FIB. (b) SEM picture of the front-end SQUID. The main contribution of the SQUID loop inductance comes from the four banana-shaped coils A, B, C and D that are connected in parallel. These are the sensitive areas. The sample to be measured can be located on either the left side (A and B areas) or the right side (C and D areas). The sample is indicated with a red circle in both images as an example. I_p is the primary current that creates the excitation magnetic field. The center square marks the modified region. Images reproduced from ref.[283].

This sensor consisted of four pickup coils connected in parallel with gradiometric design, made of Nb, rectangular-shaped and with approximate dimensions of 63 μm × 250 μm (shown in Figure 7.15b). The pickup coil wire (cross area of 9 μm × 300 nm) is covered with a 250 nm-thick layer of SiO_2. Finally, on top of these coils and exactly matching their geometry there are four primary coils connected in series made of Nb (cross area is 5 μm × 500 nm) that create the ac exciting magnetic field.

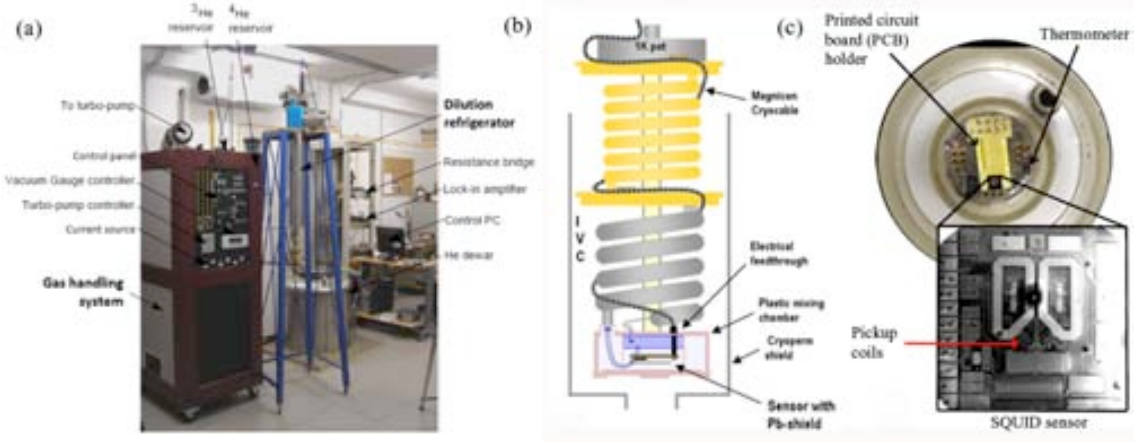

Figure 7.16 (a) Minikelvin 126-TOF dilution refrigerator by Leiden Cryogenics located in the Low Temperature Laboratory of the ICMA. (b) Schematic illustration of the lower part of the dilution refrigerator insert. The sensor lies inside the mixing chamber immersed in the ^{3}He-^{4}He mixture, with the PCB holder plugged into electrical feedthroughs connected to the cryocable in the inner vacuum chamber. (c) Bottom view of the mixing chamber with a SQUID susceptometer chip mounted in place. The inset shows an enlarged SEM view of the sensor, the size of which is 3 mm × 3 mm. Images reproduced from ref.[283].

Sensors are mounted on printed circuit board (PCB) holders and installed in direct contact with ^{3}He– ^{4}He mixture inside the mixing chamber of a dilution refrigerator adapted to this end. This configuration ensures a good thermalization of the sample at very low temperature and provides a friendly tool capable of ac susceptibility measurements under extreme conditions of frequencies (1 mHz – 1 MHz) and temperatures ($T \approx 13$ mK) (**Figure 7.16**). Dr. M. J. Martínez-Pérez and co-workers experimentally measured the spin sensitivity of this susceptometer using a calibration Pb spherical sample of 45 μm in diameter giving ~ $3 \cdot 10^4$ $\mu_B \cdot Hz^{-1/2}$ at 13 mK.[283, 426] Typically, the samples measured using this type of sensors show sizes comparable with the size of the pickup coil loop. These samples of micrometer size can be easily placed onto the pickup coils, gluing them with vacuum grease and with the help of a micromanipulator (**Figure 7.17**). However, thanks to their high sensitivity, these susceptometers should also enable the detection of single layers of molecular nanomagnets, therefore providing a relatively simple tool to ascertain if these materials preserve their interesting magnetic properties on the surface. The aim was to deposit dots of a controlled amount of ferritin particles at the most sensitive areas of the sensor by using direct-write AFM lithography in order to maximize the coupling between sample and coil. However, before patterning was performed, the sensitive areas of the sensor were identified by Dr. M. J. Martínez-Pérez and co-workers, as described next.[283, 284]

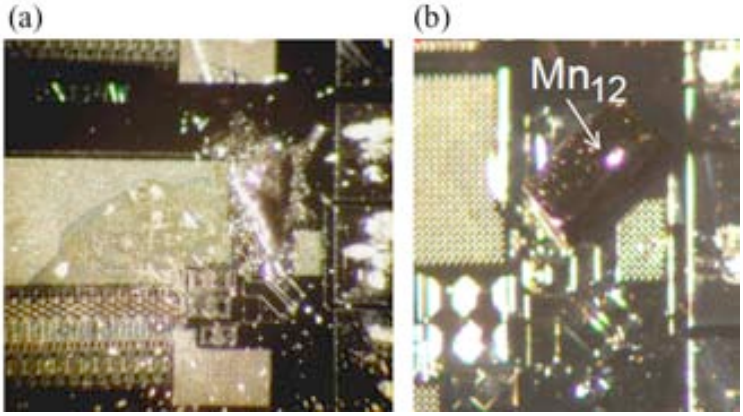

Figure 7.17 Optical image of the microSQUID susceptometer and a sample attached to it with vacuum grease. The deposition of the sample onto the pickup coils was performed with a micromanipulator and with the help of an optical microscope. Samples consists in (a) lyophilized ferritin displaying an internal core made of ~ 3 nm CoO and (b) a Mn_{12}bz single crystal. Images obtained by Dr. M. J. Martínez-Pérez.

With the aim of identifying the pickup coil "active" or most sensitive areas, Dr. M. J. Martínez-Pérez and co-workers performed calculations of the magnetic flux $\phi_{coupled}$ generated by a sample located at a particular position with respect to the coils boundaries.[283] A susceptometer provides a signal proportional to the susceptibility of a sample located within the pickup coils, that is, to the magnetic moment induced in the sample by the field created by the primary coil (B_P) along its direction. The coupling factor α, is defined by:

$$\alpha = \frac{\phi_{coupled}}{\mu_i} \frac{B_P}{i_P} \qquad (7.1)$$

where μ_i is the magnetic moment induced by the excitation magnetic field B_p, and i_p is the electrical current circulating via the primary coil. The calculation was performed using finite element method software (COMSOL Multiphysics) to simulate the magnetic field on a plane perpendicular to the coils. First $\frac{\phi_{coupled}}{\mu_i}$ was calculated using the reciprocity theorem.[428] This theorem states that calculating the flux coupled to the pickup coil per unit of magnetic moment is equivalent to calculating the magnetic field, generated at the location of the magnetic moment, per unit of current circulating through the SQUID pickup coil. Therefore, this problem is reduced to the evaluation of the magnetic field created by a current flowing through the pickup coil. For this, the actual shape of the SQUID loops was approximated to a circular shaped pickup coil having the same area. The second value $\frac{B_P}{i_P}$ is referred to the fact that the magnetic moment of the sample is induced by the magnetic field B_P created by a current that circulates through the primary coil (i_P), and is calculated using the same procedure.

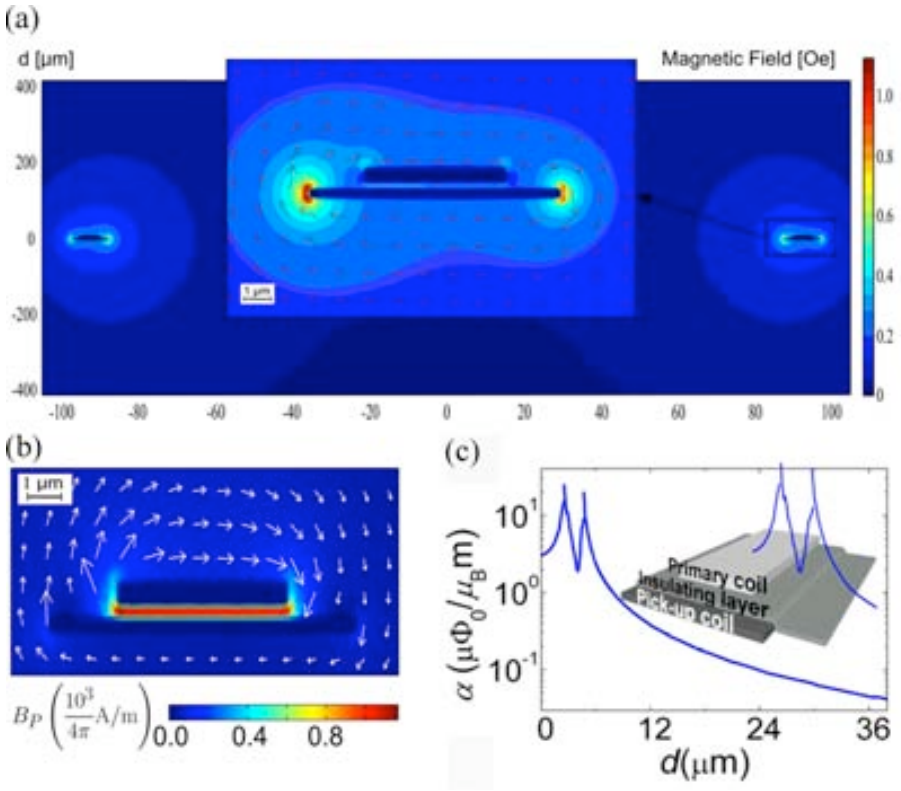

Figure 7.18 (a) Finite element calculations of the magnetic field created by the pickup coil (approximated to a circular spire) with a driving current of 500 μA. The current circulating in the primary coil is forced to be zero. The inset shows an amplification of the region near to the wire. (b) Finite element calculation of the excitation magnetic field (B_p) created by an i_p = 500 μA current flowing through the primary coil, approximated by a circular spire. (c) Numerical calculations of the coupling factor (α) as a function of the distance from the center of the pickup coil wire towards the center of the coil, approximated also by a circular spire. The inset shows a 3-D cross section of the pickup and primary coil wires, where the coupling factor (α) profile has been superimposed. Images reproduced from ref.[283].

As shown in **Figure 7.18**a,b, the magnetic field becomes largest in the vicinity of the coils, which imply an enhancement of the coupling factor. Therefore, these regions will be referred to

as the "active areas" or most sensitive areas of the sensor. Figure 7.18c shows numerical calculations of the coupling factor as a function of the distance from the pickup coil wire towards center of the coil. The enhanced sensitive areas are schematically shown in the inset of Figure 7.18c and correspond to the closest position to the coil wire edges where the magnetic field lines concentrate.

7.4.1.3 *2nd generation microSQUIDs*

The sensor used in Chapter 4 forms part of a second generation of microSQUID susceptometers, recently developed within the collaboration of Dr. J. Sesé, Dr. F. Luis and co-workers from INA and ICMA, with Dr. D. Drung and T. Schurig from the PTB. Similar to the first generations of sensors described above, they used the SQUID technological process of the PTB (from Magnicon GbR) as starting point for the fabrication of the new susceptometer.

Their purpose with this second generation of microSQUIDs was to design a SQUID-susceptometer from the very beginning instead of using the modification of an existing design. That allowed the freedom to miniaturize the size of the pickup coils in order to further increase the coupling factor with the magnetic sample and hence, improve the sensitivity of the sensor to measure very small magnetic signals. The sensor consists of two circular-shaped pickup coils in parallel with gradiometric design that forms part of the SQUID loop itself (see **Figure 7.19**). The cross area of the coil wire is 5 μm × 450 nm. In this case, the primary coils are not matching the geometry of secondary coils. Instead, the primary coils are larger and surround the secondary coils as shown in Figure 7.19. This design allows creating very homogeneous magnetic fields perpendicular to the sensor surface and increasing up to two orders of magnitude the magnetic field that can be applied to the sample with respect to the first generation of sensors.

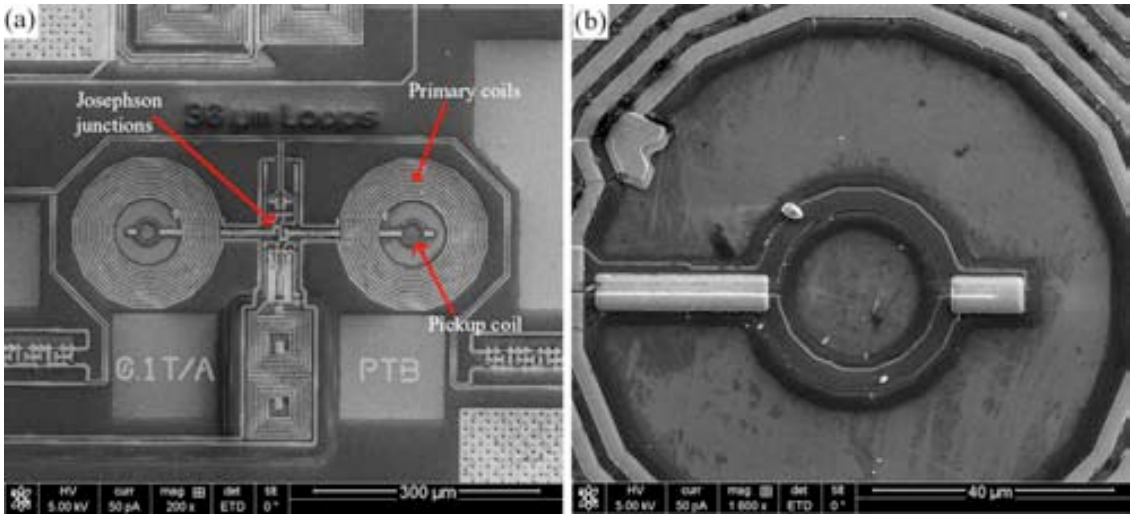

Figure 7.19 SEM images of the second generation of microSQUID susceptometers. (a) The gradiometric design is shown. The Josephson junctions, primary coils and pickup coils are indicated with labeled arrows. (b) Detail of one of the pickup coils with a diameter of 30 μm. Images obtained by Dr. J. Sesé.

Preliminary ac susceptibility measurements were performed at 4.2 K using a helium transport dewar. For this purpose, Dr. M. J. Marínez-Pérez and co-workers fabricated a so-called *dip stick*. This instrument consists of a stainless steel stick terminated in a celotex platform where the sensors can be plugged (see **Figure 7.20**). The sensor was mounted on printed circuit board (PCB) holders that were installed on the *dip stick* and introduced directly into the helium dewar. Dr. J. Sesé and co-workers characterized the intrinsic response of showing a very low flux noise of the sensors. Even though these are very promising results, to date no experimental measurements have been performed to evaluate the spin sensitivity of the susceptometer because of the performance of the first batch of sensors was damaged by electrostatic discharges (this delicate handling of these sensors was considered during the integration experiment, as described in Chapter 5). In addition, these experiments require depositing a sample on the pickup coil with high accuracy. However, this degree of control is not easily achieved by using a micromanipulator, as was performed with the first generation of sensors.

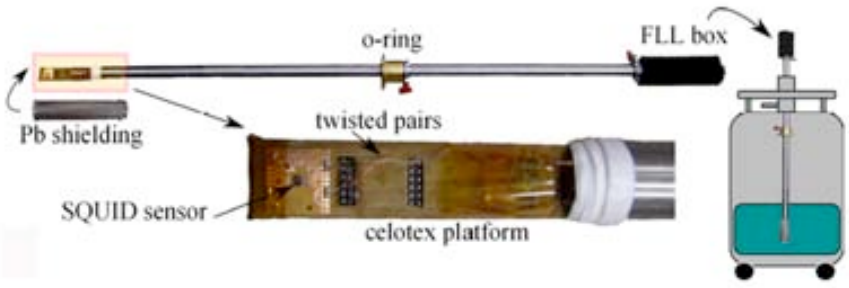

Figure 7.20 Image of the *dip stick* used to perform measurements at helium temperatures using a transport dewar. The bottom part of the figure shows an enlarged view of the celotex part where sensor is located. Reproduced from ref.[283].

At the moment of writing this manuscript, M. Jenkins and co-workers were performing calculations in order to identify the most sensitive areas of the pickup coil using COMSOL Multiphysics software in a similar manner as described above. Even though these calculations are a work still in progress, they estimate that the active areas should correspond to the closest position to the coil wire edges similarly to first generations of microSQUIDs.

7.4.2 Graphene-based nanoHall sensor

In Chapter 5 we developed a methodology for the integration of magnetic samples into graphene-based nanoHall sensors. In this section, a brief introduction to Hall sensor principles is given. Then, we describe the sensor used in this Thesis.

7.4.2.1 *Hall sensor principles*

Hall sensors are based on the principle of Hall effect and is referred to the appearance of a transverse voltage (called Hall voltage, V_H) when a perpendicular magnetic field crosses a charge current. The basic principle of the Hall effect is illustrated in **Figure 7.21**.

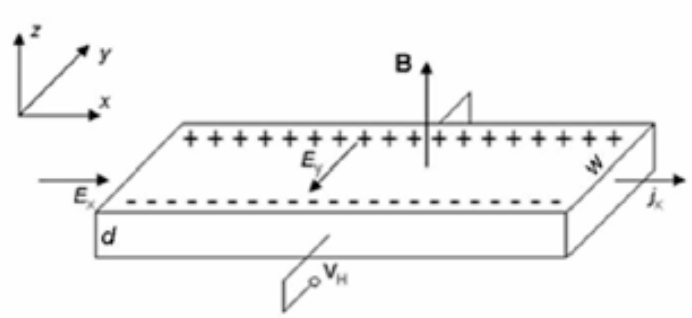

Figure 7.21 Schematic illustration of Hall effect in a thin sheet of semiconducting material (Hall element) through which current is passed. When a perpendicular magnetic field is present, the current distribution is disturbed resulting in a potential difference (voltage) across the output, the Hall voltage (V_H). Reproduced from ref.[429].

The Hall voltage V_H is given by $V_H = R_H \cdot I \cdot B_z$, where B_Z is the component of the magnetic field perpendicular to the Hall probe plane, I is the driven current and R_H is referred to the Hall coefficient and is defined as $R_H = 1/n \cdot e$ where n is the concentration of electrons or holes and e is the electron charge. Therefore Hall voltage is proportional to the current and magnetic field, and inversely proportional to the carrier density n of the conductor.

The Hall effect is often used to determine n and the sign of the charge carries in a material, however it can also be used to measure a magnetic field if n is known. The simplest geometry for a Hall sensor is the Hall cross and is shown in **Figure 7.22**. If a magnetic sample is placed near the sensing area of the sensor, then the Hall voltage will be proportional to the sum of the magnetic flux originated by the external magnetic field B and the stray field coming from the sample (i.e. referred to the magnetic field generated by the magnetization in the sample) that enters in the sensing area. Since the stray field is related to the magnetization of the sample, the device works as a magnetometer, based on the Hall effect. By measuring the resistance of the Hall probe it is quite straightforward to obtain the magnetization of the sample, and then a variety of measurements can be performed, such as magnetic hysteresis and relaxation experiments.[109, 430, 431] Typically, Hall probes are made of high mobility semiconductors (usually InSb for room temperature applications, GaAs/AlGaAs two dimensional electron gas (2DEG) for low temperatures). These materials are chosen for the special combination of low density of charge carriers and high mobility. The small value of n gives high Hall coefficient while high mobility means smaller resistance.

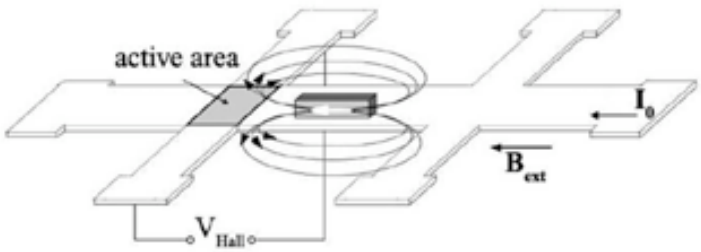

Figure 7.22 Principle of Hall sensor magnetometry. A magnetic sample is placed close to the sensing area of the Hall sensor, which corresponds to the cross area, and magnetized by an external field, B. The output signal will be proportional to the stray field generated by the sample's magnetization that enters in the Hall's sensitive region. Reproduced from ref.[429].

The Hall voltage is proportional to the average perpendicular stray field in the whole sensing area. Therefore, the reduction of the size of the sensing area towards the sample size offers a better coupling with the magnetic signal originated by the sample and can be used to measure small magnetic objects.

7.4.2.2 *Graphene-based nanoHall sensors*

In Chapter 5, we describe a methodology for the integration of NPs into graphene-based nanoHall sensors. These sensors were developed and fabricated by Prof. M. Affronte and co-workers at the CNR-Institute of NanoSciences S3 in collaboration with the Istituto Nazionale per la Fisica della Materia (CNR-INFM). CNR-INFM fabricates graphene-based nanosensors and employs them to detect the magnetization switching of NPs and magnetic molecules which are deposited on the surface using a random integration method, e.g. drop casting.

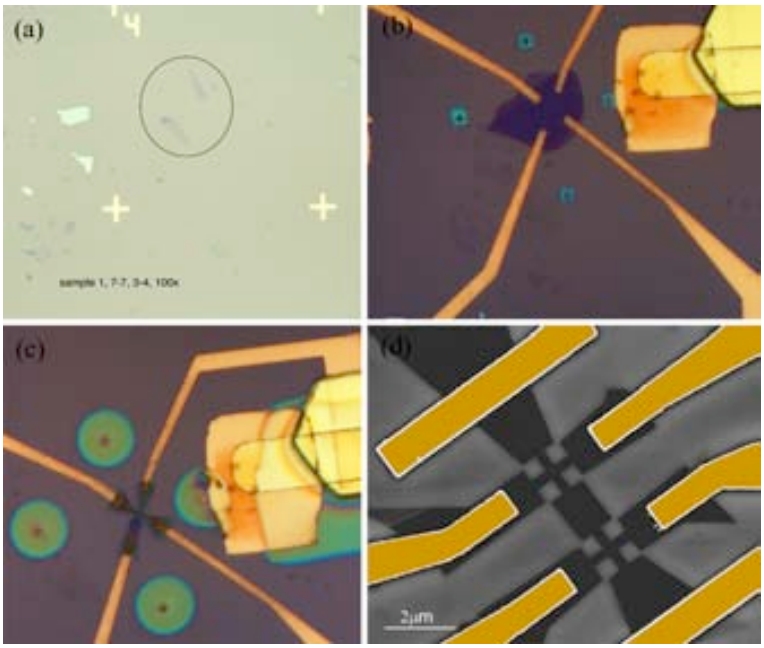

Figure 7.23 Optical images of the process of fabrication of the graphene-based sensors. (a) A graphene sheet deposited on a Si/SiO_2(300 nm) surface. (b) Fabrication of the electrical contacts. (c) Second step of the process to reduce the size of the graphene. (d) A representative example of a graphene-based nanoHall sensor. Images obtained by Prof. M. Affronte and co-workers.

Graphene is obtained with the micromechanical exfoliation method[399] from natural graphite (NGS GmbH, Germany) on top of 300 nm thick SiO_2 on highly doped Si substrate that they contacted from the bottom and then used as a backgate during transport measurements. Thin flakes were found with optical microscope and characterized with Raman spectroscopy to determine the exact number of layers (**Figure 7.23**a). After choosing the graphene flake, the electrical contacts (Ti-Pt) were patterned on the graphene flake by EBL, followed by e-beam metal evaporation and lift-off (Figure 7.23b). Prof. M. Affronte and co-workers performed room temperature measurements that reveal the good quality of their sensors, showing a carrier mobility between 2000 and 5000 $cm^2 \cdot V^{-1} \cdot s^{-1}$. In order to make sensors able to read out the spin state of a small number of molecules (and eventually a single one) they proceed with a second

step of EBL to reduce the size of the graphene flake with oxygen plasma etching to remove the unprotected graphene (Figure 7.23c). After the fabrication, thermal annealing under Ar flux at 300°C was performed to remove residues from the lithography processes. A typical example of a graphene-based nanoHall sensor is shown in Figure 7.23d. Following this method, they obtained reproducible Hall structures down to 100 nm whose charge carrier was modulated by gate voltage (see **Figure 7.24**).

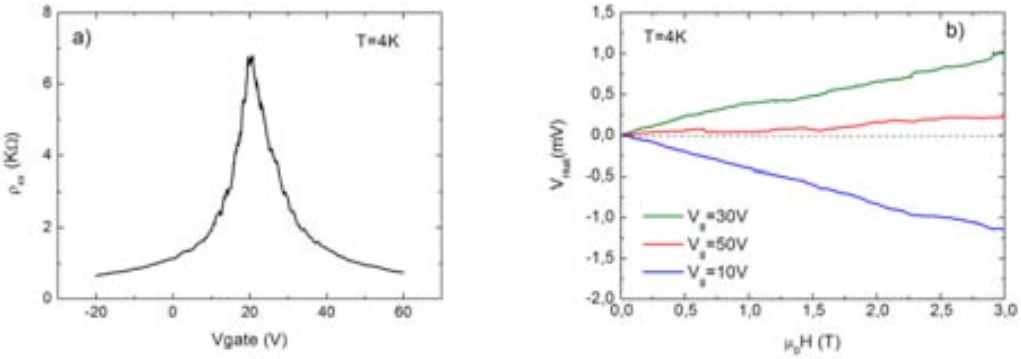

Figure 7.24 Graphene quality clearly reveals itself in a pronounced ambipolar electric field effect such that charge carriers and concentration can be controlled through electric fields gate. (a) Characteristic resistance peak in graphene, corresponding to the Dirac point. The shift on the Dirac point is due to unintentional chemical doping during the fabrication and storage in room temperature. (b) Change of sign in the Hall effect through electric field gate, confirming the change between electrons and holes type carriers. Data obtained by Prof. M. Affronte and co-workers.

Prof. M. Affronte and co-workers characterized the empty Hall sensors to evaluate their magnetic field sensitivity. Concerning the operation as magnetometer, they found that the optimal working conditions for the sensors at low temperatures were: (i) reduced sensing areas down to 100 nm in size, (ii) carrier density (tuneable with the backgate) ~ 1 - 5 · 10^{12} cm^{-2}, that correspond to a voltage applied to the backgate equal to ± 10 – 20 V with respect to the charge neutrality point; even if in principle a lower density of carrier results in an enhanced Hall coefficient R_H, it turned out that at low doping level the devices were more noisy. Under the abovementioned conditions, the fabricated sensors had similar characteristics with a Hall coefficient R_H ~ 1200 Ω/T.

To avoid a huge background signal from the external field, the measurements were typically in the parallel field configuration, i.e. with the magnetic field applied along the plane of the graphene, to be sensitive only to the stray field generated by the magnetic samples deposited on the surface. It is expected, under optimal conditions, a sensor sensitivity down to 10 – 50 μ_B if the sample is placed directly on top of the graphene sensing area.

References

1. D. L. Leslie-Pelecky and R. D. Rieke, *Chem. Mater.*, 1996, **8**, 1770-1783.
2. D. E. Speliotis, *J. Magn. Magn. Mater.*, 1999, **193**, 29-35.
3. S. Sun, C. B. Murray, D. Weller, L. Folks and A. Moser, *Science*, 2000, **287**, 1989-1992.
4. C. A. Ross, *Annu. Rev. Mater. Res.*, 2001, **31**, 203-235.
5. C. Chappert, A. Fert and F. N. Van Dau, *Nat. Mater.*, 2007, **6**, 813-823.
6. P. K. Gupta, C. T. Hung, F. C. Lam and D. G. Perrier, *Int. J. Pharm.*, 1988, **43**, 167-177.
7. V. P. Torchilin, *Eur. J. Pharm. Sci.*, 2000, **11**, S81-S91.
8. H.-T. Song, J.-s. Choi, Y.-M. Huh, S. Kim, Y.-w. Jun, J.-S. Suh and J. Cheon, *J. Am. Chem. Soc.*, 2005, **127**, 9992-9993.
9. B. Bonnemain, *J. Drug Target.*, 1998, **6**, 167-174.
10. U. I. Tromsdorf, N. C. Bigall, M. G. Kaul, O. T. Bruns, M. S. Nikolic, B. Mollwitz, R. A. Sperling, R. Reimer, H. Hohenberg, W. J. Parak, S. Förster, U. Beisiegel, G. Adam and H. Weller, *Nano Lett.*, 2007, **7**, 2422-2427.
11. E. S. Day, J. G. Morton and J. L. West, *J. Biomech. Eng.*, 2009, **131**, 074001.
12. A.-H. Lu, E. L. Salabas and F. Schüth, *Angew. Chem., Int. Ed.*, 2007, **46**, 1222-1244.
13. N. A. Frey, S. Peng, K. Cheng and S. Sun, *Chem. Soc. Rev.*, 2009, **38**, 2532-2542.
14. M.-P. Pileni and A.-T. Ngo, *ChemPhysChem*, 2005, **6**, 1027-1034.
15. R. D. L. Carlin, ed., *Magnetochemistry*, Springer-Verlag, Berlin, 1986.
16. R. D. Willet, D. Gatteschi and O. Kahn, eds., *Magneto-structural Correlations in Exchange Coupled Systems*, Reidel Publishing, Dordrecht, The Netherlands, 1983.
17. O. Kahn, ed., *Molecular Magnetism*, VCH, Weinheim, Germany, 1993.
18. D. Gatteschi, R. Sessoli and J. Villain, *Molecular Nanomagnets*, Oxford University Press, Oxford, UK, 2006.
19. D. Maspoch, N. Domingo, D. Ruiz-Molina, K. Wurst, J. Tejada, C. Rovira and J. Veciana, *J. Am. Chem. Soc.*, 2004, **126**, 730-731.
20. D. Maspoch, N. Domingo, D. Ruiz-Molina, K. Wurst, G. Vaughan, J. Tejada, C. Rovira and J. Veciana, *Angew. Chem., Int. Ed.*, 2004, **43**, 1828-1832.
21. D. Maspoch, N. Domingo, N. Roques, K. Wurst, J. Tejada, C. Rovira, D. Ruiz-Molina and J. Veciana, *Chem. – Eur. J.*, 2007, **13**, 8153-8163.
22. E. Evangelio and D. Ruiz-Molina, *Eur. J. Inorg. Chem.*, 2005, **2005**, 2957-2971.
23. R. Sessoli, D. Gatteschi, A. Caneschi and M. A. Novak, *Nature*, 1993, **365**, 141-143.
24. D. Gatteschi and R. Sessoli, *Angew. Chem., Int. Ed.*, 2003, **42**, 268-297.
25. R. Sessoli, H. L. Tsai, A. R. Schake, S. Wang, J. B. Vincent, K. Folting, D. Gatteschi, G. Christou and D. N. Hendrickson, *J. Am. Chem. Soc.*, 1993, **115**, 1804-1816.
26. J. R. Friedman, M. P. Sarachik, J. Tejada and R. Ziolo, *Phys. Rev. Lett.*, 1996, **76**, 3830-3833.
27. L. Thomas, F. Lionti, R. Ballou, D. Gatteschi, R. Sessoli and B. Barbara, *Nature*, 1996, **383**, 145-147.
28. J. M. Hernández, X. X. Zhang, F. Luis, J. Bartolomé, J. Tejada and R. Ziolo, *EPL (Europhysics Letters)*, 1996, **35**, 301-306.
29. D. Maspoch, D. Ruiz-Molina, K. Wurst, N. Domingo, M. Cavallini, F. Biscarini, J. Tejada, C. Rovira and J. Veciana, *Nat. Mater.*, 2003, **2**, 190-195.
30. F. Prins, M. Monrabal-Capilla, E. A. Osorio, E. Coronado and H. S. J. van der Zant, *Adv. Mater.*, 2011, **23**, 1545-1549.
31. N. Crivillers, M. Mas-Torrent, J. Vidal-Gancedo, J. Veciana and C. Rovira, *J. Am. Chem. Soc.*, 2008, **130**, 5499-5506.

32. M. Mannini, F. Pineider, P. Sainctavit, C. Danieli, E. Otero, C. Sciancalepore, A. M. Talarico, M.-A. Arrio, A. Cornia, D. Gatteschi and R. Sessoli, *Nat. Mater.*, 2009, **8**, 194-197.
33. M. Affronte, *J. Mater. Chem.*, 2009, **19**, 1731-1737.
34. E. M. Chudnovsky and J. Tejada, eds., *Macroscopic quantum tunneling of the magnetic moment*, Cambridge University Press, Cambridge, 1998.
35. M. N. Leuenberger and D. Loss, *Nature*, 2001, **410**, 789-793.
36. J. Lehmann, A. Gaita-Arino, E. Coronado and D. Loss, *J. Mater. Chem.*, 2009, **19**, 1672-1677.
37. J. Camarero and E. Coronado, *J. Mater. Chem.*, 2009, **19**, 1678-1684.
38. M. Evangelisti and E. K. Brechin, *Dalton Trans.*, 2010, **39**, 4672-4676.
39. A. Cornia, M. Mannini, P. Sainctavit and R. Sessoli, *Chem. Soc. Rev.*, 2011, **40**, 3076-3091.
40. M. P. Pileni, *Acc. Chem. Res.*, 2007, **40**, 685-693.
41. L. Vitali, S. Fabris, A. M. Conte, S. Brink, M. Ruben, S. Baroni and K. Kern, *Nano Lett.*, 2008, **8**, 3364-3368.
42. D. Gatteschi, A. Cornia, M. Mannini and R. Sessoli, *Inorg. Chem.*, 2009, **48**, 3408-3419.
43. M. Mannini, P. Sainctavit, R. Sessoli, C. Cartier dit Moulin, F. Pineider, M.-A. Arrio, A. Cornia and D. Gatteschi, *Chem.-Eur. J.*, 2008, **14**, 7530-7535.
44. M. Mannini, F. Pineider, C. Danieli, F. Totti, L. Sorace, P. Sainctavit, M. A. Arrio, E. Otero, L. Joly, J. C. Cezar, A. Cornia and R. Sessoli, *Nature*, 2010, **468**, 417-421.
45. W. Wernsdorfer, *Supercond. Sci. Technol.*, 2009, **22**, 064013.
46. J. Tejada, E. M. Chudnovsky, E. d. Barco, J. M. Hernandez and T. P. Spiller, *Nanotechnology*, 2001, **12**, 181.
47. R. L. Fagaly, *Rev. Sci. Instrum.* , 2006, **77**, 101101.
48. C. P. Foley and H. Hilgenkamp, *Supercond. Sci. Technol.*, 2009, **22**, 064001.
49. J. Gallop, *Supercond. Sci. Technol.*, 2003, **16**, 1575.
50. C. Granata, E. Esposito, A. Vettoliere, L. Petti and M. Russo, *Nanotechnology*, 2008, **19**.
51. A. Vettoliere, C. Granata, E. Esposito, R. Russo, L. Petti, B. Ruggiero and M. Russo, *IEEE Trans. Appl. Supercond.*, 2009, **19**, 702-705.
52. L. Hao, J. C. Macfarlane, J. C. Gallop, D. Cox, J. Beyer, D. Drung and T. Schurig, *Appl. Phys. Lett.*, 2008, **92**, 192507.
53. M. B. Ketchen, T. Kopley and H. Ling, *Appl. Phys. Lett.*, 1984, **44**, 1008-1010.
54. D. D. Awschalom, J. R. Rozen, M. B. Ketchen, W. J. Gallagher, A. W. Kleinsasser, R. L. Sandstrom and B. Bumble, *Appl. Phys. Lett.*, 1988, **53**, 2108-2110.
55. W. Wernsdorfer, *Superconductor science and technology*, 2009, **22**, 064013.
56. J. Gallop, P. W. Josephs-Franks, J. Davies, L. Hao and J. Macfarlane, *Phys. C*, 2002, **368**, 109-113.
57. C. I. Pakes, P. W. Josephs-Franks, R. P. Reed, S. G. Corner and M. S. Colclough, *IEEE Trans. Instrum. Meas.*, 2001, **50**, 310-313.
58. W. Wernsdorfer, K. Hasselbach, D. Mailly, B. Barbara, A. Benoit, L. Thomas and G. Suran, *J. Magn. Magn. Mater.*, 1995, **145**, 33-39.
59. A. G. P. Troeman, H. Derking, B. Borger, J. Pleikies, D. Veldhuis and H. Hilgenkamp, *Nano Lett.*, 2007, **7**, 2152-2156.
60. S. K. H. Lam, *Supercond. Sci. Technol.*, 2006, **19**, 963.
61. S. K. H. Lam and D. L. Tilbrook, *Appl. Phys. Lett.*, 2003, **82**, 1078-1080.
62. V. Bouchiat, *Supercond. Sci. Technol.*, 2009, **22**, 064002.
63. C. Granata, A. Vettoliere, P. Walke, C. Nappi and M. Russo, *J. Appl. Phys.*, 2009, **106**, 5.
64. D. L. Tilbrook, *Supercond. Sci. Technol.*, 2009, **22**, 064003.
65. W. Wernsdorfer, E. B. Orozco, K. Hasselbach, A. Benoit, B. Barbara, N. Demoncy, A. Loiseau, H. Pascard and D. Mailly, *Phys. Rev. Lett.*, 1997, **78**, 1791-1794.

66. B. Schleicher, U. Tapper, E. I. Kauppinen, M. Martin, L. Roschier, M. Paalanen, W. Wernsdorfer and A. Benoit, *Appl. Organomet. Chem.*, 1998, **12**, 315-320.
67. W. Wernsdorfer, B. Doudin, D. Mailly, K. Hasselbach, A. Benoit, J. Meier, J. P. Ansermet and B. Barbara, *Phys. Rev. Lett.*, 1996, **77**, 1873.
68. W. Wernsdorfer, E. Bonet Orozco, K. Hasselbach, A. Benoit, D. Mailly, O. Kubo, H. Nakano and B. Barbara, *Phys. Rev. Lett.*, 1997, **79**, 4014.
69. J. L. O'Brien, S. R. Schofield, M. Y. Simmons, R. G. Clark, A. S. Dzurak, N. J. Curson, B. E. Kane, N. S. McAlpine, M. E. Hawley and G. W. Brown, *Phys. Rev. B*, 2001, **64**, 161401.
70. P. H. Beton, A. W. Dunn and P. Moriarty, *Appl. Phys. Lett.*, 1995, **67**, 1075-1077.
71. T. R. Ramachandrany, C. Baur, A. Bugacov, A. Madhukar, B. E. Koel, A. Requicha and C. Gazen, *Nanotechnology*, 1998, **9**, 237.
72. M. Martin, L. Roschier, P. Hakonen, U. Parts, M. Paalanen, B. Schleicher and E. I. Kauppinen, *Appl. Phys. Lett.*, 1998, **73**, 1505-1507.
73. C. I. Pakes, D. P. George, S. Ramelow, A. Cimmino, D. N. D. N. Jamieson and S. Prawer, *J. Magn. Magn. Mater.*, 2004, **272-276**, E1231-E1233.
74. M. Jamet, W. Wernsdorfer, C. Thirion, D. Mailly, V. Dupuis, P. Mélinon and A. Pérez, *Phys. Rev. Lett.*, 2001, **86**, 4676-4679.
75. M. Faucher, P. O. Jubert, O. Fruchart, W. Wernsdorfer and V. Bouchiat, *Supercond. Sci. Technol.*, 2009, **22**, 064010.
76. L. Hao, C. Assmann, J. C. Gallop, D. Cox, F. Ruede, O. Kazakova, P. Josephs-Franks, D. Drung and T. Schurig, *Appl. Phys. Lett.*, 2011, **98**, 092504.
77. P. F. Vohralik and S. K. H. Lam, *Supercond. Sci. Technol.*, 2009, **22**, 064007.
78. S. K. H. Lam, W. R. Yang, H. T. R. Wiogo and C. P. Foley, *Nanotechnology*, 2008, **19**, 285303.
79. J. P. Cleuziou, W. Wernsdorfer, V. Bouchiat, T. Ondarcuhu and M. Monthioux, *Nat. Nanotechnol.*, 2006, **1**, 53-59.
80. L. Bogani, C. Danieli, E. Biavardi, N. Bendiab, A.-L. Barra, E. Dalcanale, W. Wernsdorfer and A. Cornia, *Angew. Chem., Int. Ed.*, 2009, **48**, 746-750.
81. M. Urdampilleta, S. Klyatskaya, J. P. Cleuziou, M. Ruben and W. Wernsdorfer, *Nat. Mater.*, 2011, **10**, 502-506.
82. L. Bogani and W. Wernsdorfer, *Inorg. Chim. Acta*, 2008, **361**, 3807-3819.
83. R. Singh, T. Premkumar, J.-Y. Shin and K. E. Geckeler, *Chem.-Eur. J.*, 2010, **16**, 1728-1743.
84. D. Shi, Y. Guo, Z. Dong, J. Lian, W. Wang, G. Liu, L. Wang and R. C. Ewing, *Adv. Mater.*, 2007, **19**, 4033-4037.
85. V. Georgakilas, D. Gournis, V. Tzitzios, L. Pasquato, D. M. Guldi and M. Prato, *J. Mater. Chem.*, 2007, **17**, 2679-2694.
86. D. A. Britz and A. N. Khlobystov, *Chem. Soc. Rev.*, 2006, **35**, 637-659.
87. A. Giusti, G. Charron, S. Mazerat, J.-D. Compain, P. Mialane, A. Dolbecq, E. Rivière, W. Wernsdorfer, R. Ngo Biboum, B. Keita, L. Nadjo, A. Filoramo, J.-P. Bourgoin and T. Mallah, *Angew. Chem., Int. Ed.*, 2009, **48**, 4949-4952.
88. L. Bogani, R. Maurand, L. Marty, C. Sangregorio, C. Altavilla and W. Wernsdorfer, *J. Mater. Chem.*, 2010, **20**, 2099-2107.
89. I. Rod, O. Kazakova, D. C. Cox, M. Spasova and M. Farle, *Nanotechnology*, 2009, **20**, 335301.
90. A. Saywell, G. Magnano, C. J. Satterley, L. M. A. Perdigó, A. J. Britton, N. Taleb, M. del Carmen Giménez-López, N. R. Champness, J. N. O'Shea and P. H. Beton, *Nat. Commun.*, 2010, **1**, 75.
91. A. Saywell, Andrew J Britton, Nassiba Taleb, Maria del Carmen Giménez-López, Neil R Champness, P. H. Beton and J. N. O'Shea, *Nanotechnology*, 2011, **22**, 075704.
92. R. Moroni, R. Buzio, A. Chincarini, U. Valbusa, F. B. d. Mongeot, L. Bogani, A. Caneschi, R. Sessoli, L. Cavigli and M. Gurioli, *J. Mater. Chem.*, 2008, **18**, 109-115.
93. M. Konczykowski and et al., *Supercond. Sci. Technol.*, 1991, **4**, S331.

94. A. D. Kent, S. von Molnar, S. Gider and D. D. Awschalom, *J. Appl. Phys.*, 1994, **76**, 6656-6660.
95. F. G. Monzon, D. S. Patterson and M. L. Roukes, *J. Magn. Magn. Mater.*, 1999, **195**, 19-25.
96. G. Meier, D. Grundler, K. B. Broocks, C. Heyn and D. Heitmann, *J. Magn. Magn. Mater.*, 2000, **210**, 138-142.
97. J. G. S. Lok, A. K. Geim, J. C. Maan, S. V. Dubonos, L. T. Kuhn and P. E. Lindelof, *Phys. Rev. B*, 1998, **58**, 12201.
98. Y. Li, P. Xiong, S. von Molnar, S. Wirth, Y. Ohno and H. Ohno, *Appl. Phys. Lett.*, 2002, **80**, 4644-4646.
99. A. D. Kent, T. M. Shaw, S. von Molnar and D. D. Awschalom, *Science*, 1993, **262**, 1249-1252.
100. S. Wirth and S. v. Molnár, *Appl. Phys. Lett.*, 2000, **76**, 3283-3285.
101. K. S. Novoselov, S. V. Morozov, S. V. Dubonos, M. Missous, A. O. Volkov, D. A. Christian and A. K. Geim, *J. Appl. Phys.*, 2003, **93**, 10053-10057.
102. J. Jin and X.-Q. Li, *Appl. Phys. Lett.*, 2005, **86**, 143504-143503.
103. A. Candini and et al., *Nanotechnology*, 2006, **17**, 2105.
104. M. Gabureac and et al., *Nanotechnology*, 2010, **21**, 115503.
105. P.-A. Besse, G. Boero, M. Demierre, V. Pott and R. Popovic, *Appl. Phys. Lett.*, 2002, **80**, 4199-4201.
106. A. Sandhu, Y. Kumagai, A. Lapicki, S. Sakamoto, M. Abe and H. Handa, *Biosens. Bioelectron.*, 2007, **22**, 2115-2120.
107. G. Landry, M. M. Miller, B. R. Bennett, M. Johnson and V. Smolyaninova, *Appl. Phys. Lett.*, 2004, **85**, 4693-4695.
108. G. Mihajlovic, P. Xiong, S. v. Molnár, K. Ohtani, H. Ohno, M. Field and G. J. Sullivan, *Appl. Phys. Lett.*, 2005, **87**, 112502.
109. P. Manandhar, K. S. Chen, K. Aledealat, G. Mihajlovic, C. S. Yun, M. Field, G. J. Sullivan, G. F. Strouse, P. B. Chase, S. von Molnar and P. Xiong, *Nanotechnology*, 2009, **20**, 355501.
110. K. S. Novoselov, A. K. Geim, S. V. Morozov, D. Jiang, M. I. Katsnelson, I. V. Grigorieva, S. V. Dubonos and A. A. Firsov, *Nature*, 2005, **438**, 197-200.
111. A. K. Geim and K. S. Novoselov, *Nat. Mater.*, 2007, **6**, 183-191.
112. A. A. Balandin, S. Ghosh, W. Bao, I. Calizo, D. Teweldebrhan, F. Miao and C. N. Lau, *Nano Lett.*, 2008, **8**, 902-907.
113. A. K. Geim, *Science*, 2009, **324**, 1530-1534.
114. C. Girit, V. Bouchiat, O. Naamanth, Y. Zhang, M. F. Crommie, A. Zetti and I. Siddiqi, *Nano Lett.*, 2009, **9**, 198-199.
115. S. Pisana, P. M. Braganca, E. E. Marinero and B. A. Gurney, *Nano Lett.*, 2010, **10**, 5.
116. M. Lopes, A. Candini, M. Urdampilleta, A. Reserbat-Plantey, V. Bellini, S. Klyatskaya, L. t. Marty, M. Ruben, M. Affronte, W. Wernsdorfer and N. Bendiab, *ACS Nano*, 2010, **4**, 7531-7537.
117. A. Candini, S. Klyatskaya, M. Ruben, W. Wernsdorfer and M. Affronte, *Nano Lett.*, 2011, **11**, 2634-2639.
118. A. Candini, S. Klyatskaya, M. Ruben, W. Wernsdorfer and M. Affronte, *Nano Lett.*, 2011, **11**, 2634–2639.
119. A. D. Kent, S. von Molnar, S. Gider and D. D. Awschalom, *Journal of Applied Physics*, 1994, **76**, 6656-6660.
120. R. D. Piner, J. Zhu, F. Xu, S. Hong and C. A. Mirkin, *Science*, 1999, **283**, 661-663.
121. B. Basnar and I. Willner, *Small*, 2009, **5**, 28-44.
122. M. Jaschke and H.-J. Butt, *Langmuir*, 1995, **11**, 1061-1064.
123. R. D. Piner and C. A. Mirkin, *Langmuir*, 1997, **13**, 6864-6868.
124. D. S. Ginger, H. Zhang and C. A. Mirkin, *Angew. Chem., Int. Ed.*, 2004, **43**, 30-45.
125. J. Loos, *Adv. Mater.*, 2005, **17**, 1821-1833.
126. R. Garcia, R. V. Martinez and J. Martinez, *Chem. Soc. Rev.*, 2006, **35**, 29-38.
127. R. Garcia, M. Calleja and F. Perez-Murano, *Appl. Phys. Lett.*, 1998, **72**, 2295-2297.

128. L. G. Rosa and J. Liang, *J. Phys.: Condens. Matter.*, 2009, **21**, 483001.
129. X. N. Xie, H. J. Chung, C. H. Sow and A. T. S. Wee, *Mater. Sci. Eng. R*, 2006, **54**, 1-48.
130. G. Binnig and H. Rohrer, *Rev. Mod. Phys.*, 1987, **59**, 615.
131. G. Binnig, C. F. Quate and C. Gerber, *Phys. Rev. Lett.*, 1986, **56**, 930.
132. Y. F. Dufrene, *J. Bacteriol.*, 2002, **184**, 5205-5213.
133. F. J. Giessibl, *Rev. Mod. Phys.*, 2003, **75**, 949.
134. P. Eaton and P. West, eds., *Atomic Force Microscopy*, Oxford University Press Inc., New York, 2010.
135. C. Bustamante and D. Keller, *Phys. Today*, 1995, **48**, 32-38.
136. A. San Paulo and R. García, *Biophys. J.*, 2000, **78**, 1599-1605.
137. C. Möller, M. Allen, V. Elings, A. Engel and D. J. Müller, *Biophys. J.*, 1999, **77**, 1150-1158.
138. F. J. Giessibl, *Science*, 1995, **267**, 68-71.
139. Y. Sugawara, M. Ohta, H. Ueyama and S. Morita, *Science*, 1995, **270**, 1646-1648.
140. A. Martínez-Otero, J. Hernando, D. Ruiz-Molina and D. Maspoch, *Small*, 2008, **4**, 2131-2135.
141. R. García and R. Pérez, *Surf. Sci. Rep.*, 2002, **47**, 197-301.
142. R. W. Carpick and M. Salmeron, *Chem. Rev.*, 1997, **97**, 1163-1194.
143. D. Rugar, H. J. Mamin, P. Guethner, S. E. Lambert, J. E. Stern, I. McFadyen and T. Yogi, *J. Appl. Phys.*, 1990, **68**, 1169-1183.
144. H.-J. Butt, *Biophys. J.*, 1991, **60**, 777-785.
145. M. Nonnenmacher, M. P. O'Boyle and H. K. Wickramasinghe, *Appl. Phys. Lett.*, 1991, **58**, 2921-2923.
146. A. Majumdar, *Annu. Rev. Mater. Sci.*, 1999, **29**, 505-585.
147. Y. Cai and B. M. Ocko, *J. Am. Chem. Soc.*, 2005, **127**, 16287-16291.
148. J.-M. Chen, S.-W. Liao and Y.-C. Tsai, *Synth. Met.*, 2005, **155**, 11-17.
149. X. Liu, L. Fu, S. Hong, V. P. Dravid and C. A. Mirkin, *Adv. Mater.*, 2002, **14**, 231-234.
150. J. C. Garno, Y. Yang, N. A. Amro, S. Cruchon-Dupeyrat, S. Chen and G.-Y. Liu, *Nano Lett.*, 2003, **3**, 389-395.
151. W. K. Lee, Z. Dai, W. P. King and P. E. Sheehan, *Nano Lett.*, 2009, **10**, 129-133.
152. D. L. Wilson, R. Martin, S. Hong, M. Cronin-Golomb, C. A. Mirkin and D. L. Kaplan, *Proc. Natl. Acad. Sci.*, 2001, **98**, 13660-13664.
153. Zhou, A. Bruckbauer, Ying, C. Abell and D. Klenerman, *Nano Lett.*, 2003, **3**, 1517-1520.
154. B. Rezek, E. Ukraintsev, L. Michalíková, A. Kromka, J. Zemek and M. Kalbacova, *Diamond Relat. Mater.*, 2009, **18**, 918-922.
155. R. V. Martínez, J. Martínez, M. Chiesa, R. Garcia, E. Coronado, E. Pinilla-Cienfuegos and S. Tatay, *Adv. Mater.*, 2010, **22**, 588-591.
156. M. Su, X. Liu, S.-Y. Li, V. P. Dravid and C. A. Mirkin, *J. Am. Chem. Soc.*, 2002, **124**, 1560-1561.
157. J. N. Garno and C. Jayne, *Anal. Chem.*, 2008, **80**, 1361-1369.
158. W. P. King, T. W. Kenny, K. E. Goodson, G. Cross, M. Despont, U. Durig, H. Rothuizen, G. K. Binnig and P. Vettiger, *Appl. Phys. Lett.*, 2001, **78**, 1300-1302.
159. S. Xu and G.-y. Liu, *Langmuir*, 1997, **13**, 127-129.
160. L. Santinacci, T. Djenizian, H. Hildebrand, S. Ecoffey, H. Mokdad, T. Campanella and P. Schmuki, *Electrochim. Acta*, 2003, **48**, 3123-3130.
161. J. Hu, Y. Zhang, H. Gao, M. Li and U. Hartmann, *Nano Lett.*, 2001, **2**, 55-57.
162. L. Roschier, J. Penttila, M. Martin, P. Hakonen, M. Paalanen, U. Tapper, E. I. Kauppinen, C. Journet and P. Bernier, *Appl. Phys. Lett.*, 1999, **75**, 728-730.
163. P. E. Sheehan and C. M. Lieber, *Science*, 1996, **272**, 1158-1161.
164. Y. Sugimoto, M. Abe, S. Hirayama, N. Oyabu, O. Custance and S. Morita, *Nat. Mater.*, 2005, **4**, 156-159.
165. M. Péter, X.-M. Li, J. Huskens and D. N. Reinhoudt, *J. Am. Chem. Soc.*, 2004, **126**, 11684-11690.

166. S. Rozhok, R. Piner and C. A. Mirkin, *J. Phys. Chem. B*, 2002, **107**, 751-757.
167. S. Rozhok, P. Sun, R. Piner, M. Lieberman and C. A. Mirkin, *J. Phys. Chem. B*, 2004, **108**, 7814-7819.
168. J. Haaheim, R. Eby, M. Nelson, J. Fragala, B. Rosner, H. Zhang and G. Athas, *Ultramicroscopy*, 2005, **103**, 117-132.
169. S. Hong, J. Zhu and C. A. Mirkin, *Science*, 1999, **286**, 523-525.
170. S. Hong and C. A. Mirkin, *Science*, 2000, **288**, 1808-1811.
171. Y. Li, B. W. Maynor and J. Liu, *J. Am. Chem. Soc.*, 2001, **123**, 2105-2106.
172. G. Gundiah, N. S. John, P. J. Thomas, G. U. Kulkarni, C. N. R. Rao and S. Heun, *Appl. Phys. Lett.*, 2004, **84**, 5341-5343.
173. K. Salaita, Y. Wang and C. A. Mirkin, *Nat. Nano.*, 2007, **2**, 145-155.
174. A. Ivanisevic, K. V. McCumber and C. A. Mirkin, *J. Am. Chem. Soc.*, 2002, **124**, 11997-12001.
175. Y. Zhang, K. Salaita, J.-H. Lim, K.-B. Lee and C. A. Mirkin, *Langmuir*, 2004, **20**, 962-968.
176. H. Zhou, Z. Li, A. Wu, G. Wei and Z. Liu, *Appl. Surf. Sci.*, 2004, **236**, 18-24.
177. D. Nyamjav and A. Ivanisevic, *Chem. Mater.*, 2004, **16**, 5216-5219.
178. M. Su, M. Aslam, L. Fu, N. Wu and V. P. Dravid, *Appl. Phys. Lett.*, 2004, **84**, 4200-4202.
179. A. Noy, A. E. Miller, J. E. Klare, B. L. Weeks, B. W. Woods and J. J. DeYoreo, *Nano Lett.*, 2001, **2**, 109-112.
180. L. Qin, S. Park, L. Huang and C. A. Mirkin, *Science*, 2005, **309**, 113-115.
181. W. M. Wang, R. M. Stoltenberg, S. Liu and Z. Bao, *ACS Nano*, 2008, **2**, 2135-2142.
182. L. Ding, Y. Li, H. Chu, X. Li and J. Liu, *J. Phys. Chem. B*, 2005, **109**, 22337-22340.
183. J. Li, C. Lu, B. Maynor, S. Huang and J. Liu, *Chem. Mater.*, 2004, **16**, 1633-1636.
184. L. Fu, X. Liu, Y. Zhang, V. P. Dravid and C. A. Mirkin, *Nano Lett.*, 2003, **3**, 757-760.
185. K.-B. Lee, J.-H. Lim and C. A. Mirkin, *J. Am. Chem. Soc.*, 2003, **125**, 5588-5589.
186. J.-H. Lim, D. S. Ginger, K.-B. Lee, J. Heo, J.-M. Nam and C. A. Mirkin, *Angew. Chem., Int. Ed.*, 2003, **42**, 2309-2312.
187. Y. Cho and A. Ivanisevic, *J. Phys. Chem. B*, 2005, **109**, 6225-6232.
188. Y. Cho and A. Ivanisevic, *J. Phys. Chem. B*, 2004, **108**, 15223-15228.
189. H. Jiang and S. I. Stupp, *Langmuir*, 2005, **21**, 5242-5246.
190. S. Lenhert, P. Sun, Y. Wang, H. Fuchs and C. A. Mirkin, *Small*, 2007, **3**, 71-75.
191. L. M. Demers, D. S. Ginger, S.-J. Park, Z. Li, S.-W. Chung and C. A. Mirkin, *Science*, 2002, **296**, 1836-1838.
192. S.-W. Chung, D. S. Ginger, M. W. Morales, Z. Zhang, V. Chandrasekhar, M. A. Ratner and C. A. Mirkin, *Small*, 2005, **1**, 64-69.
193. S. E. Kooi, L. A. Baker, P. E. Sheehan and L. J. Whitman, *Adv. Mater.*, 2004, **16**, 1013-1016.
194. X. Liu, Y. Zhang, D. K. Goswami, J. S. Okasinski, K. Salaita, P. Sun, M. J. Bedzyk and C. A. Mirkin, *Science*, 2005, **307**, 1763-1766.
195. G. Agarwal, R. R. Naik and M. O. Stone, *J. Am. Chem. Soc.*, 2003, **125**, 7408-7412.
196. Y. Wang, W. Wei, D. Maspoch, J. Wu, V. P. Dravid and C. A. Mirkin, *Nano Lett.*, 2008, **8**, 3761-3765.
197. K.-B. Lee, S.-J. Park, C. A. Mirkin, J. C. Smith and M. Mrksich, *Science*, 2002, **295**, 1702-1705.
198. H. Zhang, S.-W. Chung and C. A. Mirkin, *Nano Lett.*, 2002, **3**, 43-45.
199. S. Matsubara, H. Yamamoto, K. Oshima, E. Mouri and H. Matsuoka, *Chem. Lett.*, 2002, **31**, 886-887.
200. E. J. Peterson, B. L. Weeks, J. J. De Yoreo and P. V. Schwartz, *J. Phys. Chem. B*, 2004, **108**, 15206-15210.
201. J. Jang, G. C. Schatz and M. A. Ratner, *Phys. Rev. Lett.*, 2004, **92**, 085504.
202. J. Jang, G. C. Schatz and M. A. Ratner, *J. Chem. Phys*, 2002, **116**, 3875-3886.
203. J. R. Hampton, A. A. Dameron and P. S. Weiss, *J. Am. Chem. Soc.*, 2006, **128**, 1648-1653.

204. B. L. Weeks, A. Noy, A. E. Miller and J. J. De Yoreo, *Phys. Rev. Lett.*, 2002, **88**, 255505.
205. J. Jang, S. Hong, G. C. Schatz and M. A. Ratner, *J. Chem. Phys.*, 2001, **115**, 2721-2729.
206. D. M. Heo, M. Yang, S. Hwang and J. Jang, *J. Phys. Chem. C*, 2008, **112**, 8791-8796.
207. H. Jung, C. K. Dalal, S. Kuntz, R. Shah and C. P. Collier, *Nano Lett.*, 2004, **4**, 2171-2177.
208. G. Jutz and A. Böker, *Polymer*, 2011, **52**, 211-232.
209. M. T. Klem, M. Young and T. Douglas, *Mater. Today*, 2005, **8**, 28-37.
210. I. Yamashita, *J. Mater. Chem.*, 2008, **18**, 3813-3820.
211. M. Young, W. Debbie, M. Uchida and T. Douglas, *Annu. Rev. Phytopathol.*, 2008, **46**, 361-384.
212. E. Dujardin, C. Peet, G. Stubbs, J. N. Culver and S. Mann, *Nano Lett.*, 2003, **3**, 413-417.
213. M. Kobayashi, M. Seki, H. Tabata, Y. Watanabe and I. Yamashita, *Nano Lett.*, 2010, **10**, 773-776.
214. R. Tsukamoto, M. Muraoka, M. Seki, H. Tabata and I. Yamashita, *Chem. Mater.*, 2007, **19**, 2389-2391.
215. I. Yamashita, K. Iwahori and S. Kumagai, *Biochim. Biophys. Acta, Gen. Subj.*, 2010, **1800**, 846-857.
216. M. Allen, D. Willits, J. Mosolf, M. Young and T. Douglas, *Adv. Mater.*, 2002, **14**, 1562-1565.
217. M. Allen, D. Willits, M. Young and T. Douglas, *Inorg. Chem.*, 2003, **42**, 6300-6305.
218. P. M. Harrison and P. Arosio, *Biochim. Biophys. Acta, Bioenerg.*, 1996, **1275**, 161-203.
219. T. Takahashi and S. Kuyucak, *Biophys. J.*, 2003, **84**, 2256-2263.
220. X. Yang, P. Arosio and N. D. Chasteen, *Biophys. J.*, 2000, **78**, 2049-2059.
221. E. A. Deliyanni, D. N. Bakoyannakis, A. I. Zouboulis and K. A. Matis, *Chemosphere*, 2003, **50**, 155-163.
222. X. Lopez and V. M. Castaño, *J. Nanosci. and Nanotechnol.*, 2009, **8**, 5733-5738.
223. E. C. Theil, H. Takagi, G. W. Small, L. He, A. R. Tipton and D. Danger, *Inorg. Chim. Acta*, 2000, **297**, 242-251.
224. N. Gálvez, B. n. Fernández, P. n. Sánchez, R. Cuesta, M. Ceolín, M. Clemente-León, S. Trasobares, M. López-Haro, J. J. Calvino, O. Stéphan and J. M. Domínguez-Vera, *J. Am. Chem. Soc.*, 2008, **130**, 8062-8068.
225. K. Iwahori and I. Yamashita, *J. Cluster Sci.*, 2007, **18**, 358-370.
226. F. Meldrum, B. Heywood and S. Mann, *Science*, 1992, **257**, 522-523.
227. M. J. Martínez-Pérez, R. de Miguel, C. Carbonera, M. Martinez-Julvez, A. Lostao, C. Piquer, C. Gomez-Moreno, J. Bartolome and F. Luis, *Nanotechnology*, 2010, **21**, 465707.
228. R. Tsukamoto, K. Iwahori, M. Muraoka and I. Yamashita, *Bull. Chem. Soc. Jpn.*, 2005, **78**, 2075-2081.
229. T. Douglas and V. T. Stark, *Inorg. Chem.*, 2000, **39**, 1828-1830.
230. F. C. Meldrum, T. Douglas, S. Levi, P. Arosio and S. Mann, *J. Inorg. Biochem.*, 1995, **58**, 59-68.
231. M. T. Klem, J. Mosolf, M. Young and T. Douglas, *Inorg. Chem.*, 2008, **47**, 2237-2239.
232. N. Galvez, P. Sanchez and J. M. Dominguez-Vera, *Dalton Trans.*, 2005, 2492-2494.
233. T. Ueno, M. Suzuki, T. Goto, T. Matsumoto, K. Nagayama and Y. Watanabe, *Angew. Chem., Int. Ed.*, 2004, **43**, 2527-2530.
234. N. Galvez, P. Sanchez, J. M. Dominguez-Vera, A. Soriano-Portillo, M. Clemente-Leon and E. Coronado, *J. Mater. Chem.*, 2006, **16**, 2757-2761.
235. B. Warne, O. I. Kasyutich, E. L. Mayes, J. A. L. Wiggins and K. K. W. Wong, *IEEE Trans. Magn.*, 2000, **36**, 3009-3011.
236. I. Yamashita, J. Hayashi and M. Hara, *Chem. Lett.*, 2004, **33**, 1158-1159.
237. K. Iwahori, K. Yoshizawa, M. Muraoka and I. Yamashita, *Inorg. Chem.*, 2005, **44**, 6393-6400.

238. T. Hikono, Y. Uraoka, T. Fuyuki and I. Yamashita, *Jpn. J. Appl. Phys.*, 2003, **42**, L398-L399.
239. I. Yamashita, *Thin Solid Films*, 2001, **393**, 12-18.
240. E. Adachi and K. Nagayama, *Langmuir*, 1996, **12**, 1836-1839.
241. Z. Yuan, D. N. Petsev, B. G. Prevo, O. D. Velev and P. Atanassov, *Langmuir*, 2007, **23**, 5498-5504.
242. K. Won, M. J. Park, H. H. Yoon and J. H. Kim, *Ultramicroscopy*, 2008, **108**, 1342-1347.
243. B. L. Scott and D. C. Zapien, *Electroanalysis*, 2010, **22**, 379-383.
244. J. M. Domínguez-Vera, L. Welte, N. Gálvez, B. Fernández, J. Gómez-Herrero and F. Zamora, *Nanotechnology*, 2008, **19**, 025302.
245. J.-W. Kim, S. H. Choi, P. T. Lillehei, S.-H. Chu, G. C. King and G. D. Watt, *J. Electroanal. Chem.*, 2007, **601**, 8-16.
246. T. Matsui, N. Matsukawa, K. Iwahori, K.-I. Sano, K. Shiba and I. Yamashita, *Langmuir*, 2007, **23**, 1615-1618.
247. Y. Ikezoe, Y. Kumashiro, K. Tamada, T. Matsui, I. Yamashita, K. Shiba and M. Hara, *Langmuir*, 2008, **24**, 12836-12841.
248. K. Uto, K. Yamamoto, N. Kishimoto, M. Muraoka, T. Aoyagi and I. Yamashita, *J. Mater. Chem.*, 2008, **18**, 3876-3884.
249. M. Tominaga, M. Matsumoto, K. Soejima and I. Taniguchi, *J. Colloid Interface Sci.*, 2006, **299**, 761-765.
250. K. Yamada, S. Yoshii, S. Kumagai, I. Fujiwara, K. Nishio, M. Okuda, N. Matsukawa and I. Yamashita, *Jpn. J. Appl. Phys.*, 2006, **45**, 4259-4264.
251. S. Daniels, J. Ngunjiri and J. Garno, *Anal. Bioanal. Chem.*, 2009, **394**, 215-223.
252. F. Zhang, R. J. Gates, V. S. Smentkowski, S. Natarajan, B. K. Gale, R. K. Watt, M. C. Asplund and M. R. Linford, *J. Am. Chem. Soc.*, 2007, **129**, 9252-9253.
253. Y. X. Hu, D. A. Chen, S. Park, T. Emrick and T. P. Russell, *Adv. Mater.*, 2010, **22**, 2583-2587.
254. J.-K. Chen, Z.-Y. Chen, H.-C. Lin, P.-D. Hong and F.-C. Chang, *ACS Appl. Mater. Interfaces*, 2009, **1**, 1525-1532.
255. K.-I. Sano, S. Yoshii, I. Yamashita and K. Shiba, *Nano Lett.*, 2007, **7**, 3200-3202.
256. K. Yamashita, H. Kirimura, M. Okuda, K. Nishio, K. I. Sano, K. Shiba, T. Hayashi, M. Hara and Y. Mishima, *Small*, 2006, **2**, 1148-1152.
257. K. Ishikawa, K. Yamada, S. Kumagai, K. I. Sano, K. Shiba, I. Yamashita and M. Kobayashi, *Appl. Phys. Express*, 2008, **1**, 034006.
258. N. Matsukawa, K. Nishio, K. Sano, K. Shiba and I. Yamashita, *Langmuir*, 2009, **25**, 3327-3330.
259. S. Yoshii, S. Kumagai, K. Nishio, A. Kadotani and I. Yamashita, *Appl. Phys. Lett.*, 2009, **95**, 133702.
260. S. Kumagai, S. Yoshii, K. Yamada, N. Matsukawa, I. Fujiwara, K. Iwahori and I. Yamashita, *Appl. Phys. Lett.*, 2006, **88**, 153103.
261. S. Kumagai, T. Ono, S. Yoshii, A. Kadotani, R. Tsukamoto, K. Nishio, M. Okuda and I. Yamashita, *Appl. Phys. Express*, 2010, **3**, 015101.
262. T. Yoshinobu, J. Suzuki, H. Kurooka, W. C. Moon and H. Iwasaki, *Electrochim. Acta*, 2003, **48**, 3131-3135.
263. E. Manning and S.-T. Yau, *J. Vac. Sci. Technol., B*, 2005, **23**, 2309-2313.
264. R. V. Martínez, J. Martínez, M. Chiesa, R. Garcia, E. Coronado, E. Pinilla Cienfuegos and S. Tatay, *Advanced Materials*, 2010, **22**, 588-591.
265. C.-C. Wu, D. N. Reinhoudt, C. Otto, V. Subramaniam and A. H. Velders, *Small*, 2011, **7**, 989-1002.
266. A. J. Senesi, D. I. Rozkiewicz, D. N. Reinhoudt and C. A. Mirkin, *ACS Nano*, 2009, **3**, 2394-2402.
267. I. Kuljanishvili, D. A. Dikin, S. Rozhok, S. Mayle and V. Chandrasekhar, *Small*, 2009, **5**, 2523-2527.

268. H.-T. Wang, O. A. Nafday, J. R. Haaheim, E. Tevaarwerk, N. A. Amro, R. G. Sanedrin, C.-Y. Chang, F. Ren and S. J. Pearton, *Appl. Phys. Lett.*, 2008, **93**, 143105.
269. B. Li, C. F. Goh, X. Zhou, G. Lu, H. Tantang, Y. Chen, C. Xue, F. Y. C. Boey and H. Zhang, *Adv. Mater.*, 2008, **20**, 4873-4878.
270. M. Ben Ali, T. Ondarçuhu, M. Brust and C. Joachim, *Langmuir*, 2002, **18**, 872-876.
271. M. Tominaga, M. Matsumoto, K. Soejima and I. Taniguchi, *Journal of Colloid and Interface Science*, 2006, **299**, 761-765.
272. M. S. Wagner and D. G. Castner, *Appl. Surf. Sci.*, 2004, **231-232**, 366-376.
273. M. Mannini, D. Bonacchi, L. Zobbi, F. M. Piras, E. A. Speets, A. Caneschi, A. Cornia, A. Magnani, B. J. Ravoo, D. N. Reinhoudt, R. Sessoli and D. Gatteschi, *Nano Lett.*, 2005, **5**, 1435-1438.
274. F. Zhang, R. J. Gates, V. S. Smentkowski, S. Natarajan, B. K. Gale, R. K. Watt, M. C. Asplund and M. R. Linford, *Journal of the American Chemical Society*, 2007, **129**, 9252-9253.
275. R. N. S. Sodhi, *Analyst*, 2004, **129**, 483-487.
276. R. Michel and D. G. Castner, *Surf. Interface Anal.*, 2006, **38**, 1386-1392.
277. M. S. Wagner and D. G. Castner, *Langmuir*, 2001, **17**, 4649-4660.
278. J. Cook and B. Skikne, *Am. J. Clin. Nutr.*, 1982, **35**, 1180-1185.
279. A. K. Panwar, S. K. Barthwal and S. Ray, *J. Adhes. Sci. Technol.*, 2003, **17**, 1321-1329.
280. L. Xu and M. Salmeron, in *Nano-Surface Chemistry*, ed. M. Rosoff, Marcel Dekker, Inc., New York - Basel 2001, pp. 243-286.
281. J. Arcamone, E. Dujardin, G. Rius, F. Pérez-Murano and T. Ondarçuhu, *J. Phys. Chem. B*, 2007, **111**, 13020-13027.
282. R. D. Deegan, O. Bakajin, T. F. Dupont, G. Huber, S. R. Nagel and T. A. Witten, *Nature*, 1997, **389**, 827-829.
283. M. J. Martínez-Pérez, Ph.D. Thesis. Instituto de Ciencia de Materiales de Aragón. Universidad de Zaragoza, 2011.
284. M. J. Martínez-Pérez, E. Bellido, R. d. Miguel, J. Sesé, A. Lostao, C. Gómez-Moreno, D. Drung, T. Schurig, D. Ruiz-Molina and F. Luis, *Appl. Phys. Lett.*, 2011, **99**, 032504.
285. D. Gatteschi, R. Sessoli and J. Villain, eds., *Molecular Nanomagnets*, Oxford University Press, Oxford, UK, 2006.
286. T. Lis, *Acta Crystallogr., Sect. B*, 1980, **36**, 2042-2046.
287. K. M. Mertes, Y. Suzuki, M. P. Sarachik, Y. Myasoedov, H. Shtrikman, E. Zeldov, E. M. Rumberger, D. N. Hendrickson and G. Christou, *Solid State Commun.*, 2003, **127**, 131-139.
288. M. Clemente-León, H. Soyer, E. Coronado, C. Mingotaud, C. J. Gómez-García and P. Delhaès, *Angew. Chem., Int. Ed.*, 1998, **37**, 2842-2845.
289. M. Clemente-León, E. Coronado, A. Soriano-Portillo, C. Mingotaud and J. M. Dominguez-Vera, *Adv. Colloid Interface Sci.*, 2005, **116**, 193-203.
290. A. Nait, J. P. Bucher, G. Ph, P. Rabu and M. Drillon, *Adv. Mater.*, 2005, **17**, 1612-1616.
291. J. Gomez-Segura, I. Diez-Perez, N. Ishikawa, M. Nakano, J. Veciana and D. Ruiz-Molina, *Chem. Commun.*, 2006, 2866-2868.
292. D. M. Seo, V. Meenakshi, W. Teizer, H. Zhao and K. R. Dunbar, *J. Magn. Magn. Mater.*, 2006, **301**, 31-36.
293. G. Otero, E. Evangelio, C. Rogero, L. Vázquez, J. Gómez-Segura, J. A. M. Gago and D. Ruiz-Molina, *Langmuir*, 2009, **25**, 10107-10115.
294. B. Fleury, V. Huc, L. Catala, P. Jegou, L. Baraton, C. David, S. Palacin and T. Mallah, *CrystEngComm*, 2009, **11**, 2192-2197.
295. A. Cornia, A. C. Fabretti, M. Pacchioni, L. Zobbi, D. Bonacchi, A. Caneschi, D. Gatteschi, R. Biagi, U. del Pennino, V. De Renzi, L. Gurevich and H. S. J. Van der Zant, *J. Magn. Magn. Mater.*, 2004, **272-276**, E725-E726.
296. L. Zobbi, M. Mannini, M. Pacchioni, G. Chastanet, D. Bonacchi, C. Zanardi, R. Biagi, U. D. Pennino, D. Gatteschi, A. Cornia and R. Sessoli, *Chem. Commun.*, 2005, 1640-1642.

297. F. Pineider, M. Mannini, R. Sessoli, A. Caneschi, D. Barreca, L. Armelao, A. Cornia, E. Tondello and D. Gatteschi, *Langmuir*, 2007, **23**, 11836-11843.
298. A. Nait, J. P. Bucher, P. Rabu, O. Toulemonde, M. Drillon and P. Gerbier, *J. Appl. Phys.*, 2004, **95**, 7345-7347.
299. M. Burgert, S. Voss, S. Herr, M. Fonin, U. Groth and U. Rudiger, *J. Am. Chem. Soc.*, 2007, **129**, 14362-14366.
300. E. Coronado, A. Forment-Aliaga, F. M. Romero, V. Corradini, R. Biagi, V. De Renzi, A. Gambardella and U. del Pennino, *Inorg. Chem.*, 2005, **44**, 7693-7695.
301. J. Gomez-Segura, O. Kazakova, J. Davies, P. Josephs-Franks, J. Veciana and D. Ruiz-Molina, *Chem. Commun.*, 2005, 5615-5617.
302. H. Sun, W. Li, L. Wollenberg, B. Li, L. Wu, F. Li and L. Xu, *J. Phys. Chem. B*, 2009, **113**, 14674-14680.
303. M. Cavallini, F. Biscarini, J. Gomez-Segura, D. Ruiz and J. Veciana, *Nano Lett.*, 2003, **3**, 1527-1530.
304. M. Cavallini, J. Gomez-Segura, C. Albonetti, D. Ruiz-Molina, J. Veciana and F. Biscarini, *J. Phys. Chem. B*, 2006, **110**, 11607-11610.
305. M. Cavallini, J. Gomez-Segura, D. Ruiz-Molina, M. Massi, C. Albonetti, C. Rovira, J. Veciana and F. Biscarini, *Angew. Chem., Int. Ed.*, 2005, **44**, 888-892.
306. K. Kim, A. Ford, V. Meenakshi, W. Teizer, H. Zhao and K. R. Dunbar, *J. Appl. Phys.*, 2007, **102**, 094306.
307. K. Kim, D. M. Seo, J. Means, V. Meenakshi, W. Teizer, H. Zhao and K. R. Dunbar, *Appl. Phys. Lett.*, 2004, **85**, 3872-3874.
308. V. Corradini, U. d. Pennino, R. Biagi, V. De Renzi, A. Gambardella, G. C. Gazzadi, A. Candini, L. Zobbi and A. Cornia, *Surf. Sci.*, 2007, **601**, 2618-2622.
309. R. V. Martínez, F. García, R. García, E. Coronado, A. Forment-Aliaga, F. M. Romero and S. Tatay, *Adv. Mater.*, 2007, **19**, 291-295.
310. P. Krukowski, Z. Klusek, W. Olejniczak, R. Klepaczko, M. Puchalski, P. Dabrowski, P. J. Kowalczyk and K. Gwozdzinski, *Appl. Surf. Sci.*, 2009, **255**, 8769-8773.
311. L. Bogani, C. Danieli, E. Biavardi, N. Bendiab, A.-L. Barra, E. Dalcanale, W. Wernsdorfer and A. Cornia, *Angew. Chem., Int. Ed.*, 2009, **48**, 746-750.
312. S. Kyatskaya, J. R. Galan-Mascaros, L. Bogani, F. Hennrich, M. Kappes, W. Wernsdorfer and M. Ruben, *J. Am. Chem. Soc.*, 2009, **131**, 15143-15151.
313. G. Charron, A. Giusti, S. Mazerat, P. Mialane, A. Gloter, F. Miserque, B. Keita, L. Nadjo, A. Filoramo, E. Riviere, W. Wernsdorfer, V. Huc, J. P. Bourgoin and T. Mallah, *Nanoscale*, 2010, **2**, 139-144.
314. A. Caneschi, D. Gatteschi, R. Sessoli, A. L. Barra, L. C. Brunel and M. Guillot, *J. Am. Chem. Soc.*, 1991, **113**, 5873-5874.
315. S. M. J. Aubin, Z. Sun, H. J. Eppley, E. M. Rumberger, I. A. Guzei, K. Folting, P. K. Gantzel, A. L. Rheingold, G. Christou* and D. N. Hendrickson*, *Polyhedron*, 2001, **20**, 1139-1145.
316. N. E. Chakov, S.-C. Lee, A. G. Harter, P. L. Kuhns, A. P. Reyes, S. O. Hill, N. S. Dalal, W. Wernsdorfer, K. A. Abboud and G. Christou, *J. Am. Chem. Soc.*, 2006, **128**, 6975-6989.
317. E. M. Rumberger, E. d. Barco, J. Lawrence, S. Hill, A. D. Kent, L. N. Zakharov, A. L. Rheingold and D. N. Hendrickson, *Polyhedron*, 2005, **24**, 2557-2561.
318. J. Gomez-Segura, J. Campo, I. Imaz, K. Wurst, J. Veciana, P. Gerbier and D. Ruiz-Molina, *Dalton Trans.*, 2007, 2450-2456.
319. D. Ruiz-Molina, P. Gerbier, E. Rumberger, D. B. Amabilino, I. A. Guzei, K. Folting, J. C. Huffman, A. Rheingold, G. Christou, J. Veciana and D. N. Hendrickson, *J. Mater. Chem.*, 2002, **12**, 1152-1161.
320. P. Gerbier, D. Ruiz-Molina, J. Gómez, K. Wurst and J. Veciana, *Polyhedron*, 2003, **22**, 1951-1955.
321. J. Gomez-Segura, E. Lhotel, C. Paulsen, D. Luneau, K. Wurst, J. Veciana, D. Ruiz-Molina and P. Gerbier, *New J. Chem.*, 2005, **29**, 499-503.
322. A. Saywell and et al., *Nanotechnology*, 2011, **22**, 075704.

323. N. Domingo, B. E. Williamson, J. Gómez-Segura, P. Gerbier, D. Ruiz-Molina, D. B. Amabilino, J. Veciana and J. Tejada, *Phys. Rev. B*, 2004, **69**, 052405.
324. K. H. Yu, J. M. Rhee, Y. Lee, K. Lee and S.-C. Yu, *Langmuir*, 2000, **17**, 52-55.
325. C. Carbonera, F. Luis, J. Campo, J. Sánchez-Marcos, A. Camón, J. Chaboy, D. Ruiz-Molina, I. Imaz, J. van Slageren, S. Dengler, M. González, *Phys. Rev. B*, 2010, **81**, 014427.
326. D.-L. Long, R. Tsunashima and L. Cronin, *Angew. Chem., Int. Ed.*, 2010, **49**, 1736-1758.
327. D.-L. Long and L. Cronin, *Chem.-Eur. J.*, 2006, **12**, 3698-3706.
328. A. Müller, P. Kögerler and A. W. M. Dress, *Coord. Chem. Rev.*, 2001, **222**, 193-218.
329. S. Liu, D. G. Kurth, B. Bredenkötter and D. Volkmer, *J. Am. Chem. Soc.*, 2002, **124**, 12279-12287.
330. C. L. Polyoxometalates special issue: Hill, *Chem. Rev.*, 1998, **98**, 1-387.
331. A. Muller, E. Diemann, C. Kuhlmann, W. Eimer, C. Serain, T. Tak, A. Knochel and P. K. Pranzas, *Chem. Commun.*, 2001, 1928-1929.
332. T. Liu, E. Diemann, H. Li, A. W. M. Dress and A. Muller, *Nature*, 2003, **426**, 59-62.
333. T. Liu, *Langmuir*, 2010, **26**, 9202-9213.
334. G. Liu, T. Liu, S. S. Mal and U. Kortz, *J. Am. Chem. Soc.*, 2006, **128**, 10103-10110.
335. J. Zhang, D. Li, G. Liu, K. J. Glover and T. Liu, *J. Am. Chem. Soc.*, 2009, **131**, 15152-15159.
336. J. M. Pigga, M. L. Kistler, C.-Y. Shew, M. R. Antonio and T. Liu, *Angew. Chem., Int. Ed.*, 2009, **48**, 6538-6542.
337. P. P. Mishra, J. Jing, L. C. Francesconi and T. Liu, *Langmuir*, 2008, **24**, 9308-9313.
338. G. Liu, M. Cons and T. Liu, *J. Mol. Liq.*, 2005, **118**, 27-29.
339. A. A. Verhoeff, M. L. Kistler, A. Bhatt, J. Pigga, J. Groenewold, M. Klokkenburg, S. Veen, S. Roy, T. Liu and W. K. Kegel, *Phys. Rev. Lett.*, 2007, **99**, 066104.
340. M. L. Kistler, K. G. Patel and T. Liu, *Langmuir*, 2009, **25**, 7328-7334.
341. T. Liu, B. Imber, E. Diemann, G. Liu, K. Cokleski, H. Li, Z. Chen and A. Müller, *J. Am. Chem. Soc.*, 2006, **128**, 15914-15920.
342. T. Liu, *J. Am. Chem. Soc.*, 2002, **124**, 10942-10943.
343. G. Liu and T. Liu, *J. Am. Chem. Soc.*, 2005, **127**, 6942-6943.
344. G. Liu, M. L. Kistler, T. Li, A. Bhatt and T. Liu, *J. Cluster Sci.*, 2006, **17**, 427-443.
345. M. A. AlDamen, J. M. Clemente-Juan, E. Coronado, C. Martí-Gastaldo and A. Gaita-Ariño, *J. Am. Chem. Soc.*, 2008, **130**, 8874-8875.
346. M. A. AlDamen, S. Cardona-Serra, J. M. Clemente-Juan, E. Coronado, A. Gaita-Ariño, C. Martí-Gastaldo, F. Luis and O. Montero, *Inorg. Chem.*, 2009, **48**, 3467-3479.
347. F. Luis, M. J. Martínez-Pérez, O. Montero, E. Coronado, S. Cardona-Serra, C. Martí-Gastaldo, J. M. Clemente-Juan, J. Sesé, D. Drung and T. Schurig, *Phys. Rev. B*, 2010, **82**, 060403.
348. T. Liu, *J. Am. Chem. Soc.*, 2002, **125**, 312-313.
349. J. H. Fendler, *Chem. Mater.*, 1996, **8**, 1616-1624.
350. G. M. Whitesides and B. Grzybowski, *Science*, 2002, **295**, 2418-2421.
351. V. Aleksandrovic, D. Greshnykh, I. Randjelovic, A. Frö msdorf, A. Kornowski, S. V. Roth, C. Klinke and H. Weller, *ACS Nano*, 2008, **2**, 1123-1130.
352. M. I. Bodnarchuk, M. V. Kovalenko, S. Pichler, G. Fritz-Popovski, G. n. Hesser and W. Heiss, *ACS Nano*, 2009, **4**, 423-431.
353. K. Butter, P. H. H. Bomans, P. M. Frederik, G. J. Vroege and A. P. Philipse, *Nat. Mater.*, 2003, **2**, 88-91.
354. F. X. Redl, C. T. Black, G. C. Papaefthymiou, R. L. Sandstrom, M. Yin, H. Zeng, C. B. Murray and S. P. O'Brien, *J. Am. Chem. Soc.*, 2004, **126**, 14583-14599.
355. C. Altavilla, E. Ciliberto, D. Gatteschi and C. Sangregorio, *Adv. Mater.*, 2005, **17**, 1084-1087.
356. B. Fleury, F. Volatron, L. Catala, D. Brinzei, E. Rivière, V. Huc, C. David, F. Miserque, G. Rogez, L. Baraton, S. Palacin and T. Mallah, *Inorg. Chem.*, 2008, **47**, 1898-1900.

357. C. Altavilla, E. Ciliberto, A. Aiello, C. Sangregorio and D. Gatteschi, *Chem. Mater.*, 2007, **19**, 5980-5985.
358. B. t. P. Pichon, A. Demortière, M. Pauly, K. Mougin, A. Derory and S. Bégin-Colin, *J. Phys. Chem. C*, 2010, **114**, 9041-9048.
359. A. C. C. Yu, M. Mizuno, Y. Sasaki, M. Inoue, H. Kondo, I. Ohta, D. Djayaprawira and M. Takahashi, *Appl. Phys. Lett.*, 2003, **82**, 4352-4354.
360. S. Kinge, T. Gang, W. J. M. Naber, W. G. van der Wiel and D. N. Reinhoudt, *Langmuir*, 2010, **27**, 570-574.
361. J. Legrand, A. T. Ngo, C. Petit and M. P. Pileni, *Adv. Mater.*, 2001, **13**, 58-62.
362. M. P. Pileni, *Adv. Funct. Mater.*, 2001, **11**, 323-336.
363. A. T. Ngo and M. P. Pileni, *New J. Phys.*, 2002, **4**, 87.81-87.88.
364. S. Palacin, P. C. Hidber, J.-P. Bourgoin, C. Miramond, C. Fermon and G. M. Whitesides, *Chem. Mater.*, 1996, **8**, 1316-1325.
365. L. An, W. Li, Y. Nie, B. Xie, Z. Li, J. Zhang and B. Yang, *J. Colloid Interface Sci.*, 2005, **288**, 503-507.
366. O. Yildirim, T. Gang, S. Kinge, D. Reinhoudt, D. Blank, W. van der Wiel, G. Rijnders and J. Huskens, *Int. J. Mol. Sci.*, 2010, **11**, 1162-1179.
367. Q. Guo, X. Teng, S. Rahman and H. Yang, *J. Am. Chem. Soc.*, 2002, **125**, 630-631.
368. Q. Guo, X. Teng and H. Yang, *Adv. Mater.*, 2004, **16**, 1337-1341.
369. J.-I. Park, W.-R. Lee, S.-S. Bae, Y. J. Kim, K.-H. Yoo, J. Cheon and S. Kim, *J. Phys. Chem. B*, 2005, **109**, 13119-13123.
370. M. Cavallini, E. Bystrenova, M. Timko, M. Koneracka, V. Zavisova and P. Kopcansky, *J. Phys.: Condens. Matter.*, 2008, **20**, 204144.
371. X. Yang, C. Liu, J. Ahner, J. Yu, T. Klemmer, E. Johns and D. Weller, *J. Vac. Sci. Technol. B*, 2004, **22**, 31-34.
372. I. Seo, C. W. Kwon, H. H. Lee, Y. S. Kim, K. B. Kim and T. S. Yoon, *Electrochem. Solid-State Lett.*, 2009, **12**, K59-K62.
373. G. Chen, M. I. Bodnarchuk, M. V. Kovalenko, G. Springholz, W. Heiss, W. Jantsch, E. Platzgummer, H. Loeschner and J. Schotter, *Adv. Mater.*, 2010, **22**, 1364-1368.
374. A. Mari, E. Agostinelli, D. Fiorani, A. Flamini, S. Laureti, D. Peddis, A. M. Testa, G. Varvaro, M. V. Mansilla, A. Mezzi and S. Kaciulis, *Superlattices Microstruct.*, 2009, **46**, 95-100.
375. M. Chen, D. E. Nikles, H. Yin, S. Wang, J. W. Harrell and S. A. Majetich, *J. Magn. Magn. Mater.*, 2003, **266**, 8-11.
376. B. Basnar, J. Xu, D. Li and I. Willner, *Langmuir*, 2007, **23**, 2293-2296.
377. S. Hoeppener, A. S. Susha, A. L. Rogach, J. Feldmann and U. S. Schubert, *Curr. Nanosci.*, 2006, **2**, 135-141.
378. Y. Sasaki, M. Mizuno, A. C. C. Yu, T. Miyauchi, D. Hasegawa, T. Ogawa, M. Takahashi, B. Jeyadevan, K. Tohji, K. Sato and S. Hisano, *IEEE Trans. Magn.*, 2005, **41**, 660-664.
379. M. Cavallini, F. C. Simeone, F. Borgatti, C. Albonetti, V. Morandi, C. Sangregorio, C. Innocenti, F. Pineider, E. Annese, G. Panaccione and L. Pasquali, *Nanoscale*, 2010, **2**, 2069-2072.
380. P. E. Sheehan, L. J. Whitman, W. P. King and B. A. Nelson, *Appl. Phys. Lett.*, 2004, **85**, 1589-1591.
381. C. Lee, X. Wei, J. W. Kysar and J. Hone, *Science*, 2008, **321**, 385-388.
382. S. Guo and S. Dong, *Chem. Soc. Rev.*, 2011, **40**, 2644-2672.
383. F. Bonaccorso, Z. Sun, T. Hasan and A. C. Ferrari, *Nat. Photon.*, 2010, **4**, 611-622.
384. A. H. Castro Neto, F. Guinea, N. M. R. Peres, K. S. Novoselov and A. K. Geim, *Rev. Mod. Phys.*, 2009, **81**, 109-162.
385. N. Tombros, C. Jozsa, M. Popinciuc, H. T. Jonkman and B. J. van Wees, *Nature*, 2007, **448**, 571-574.
386. X. Huang, Z. Yin, S. Wu, X. Qi, Q. He, Q. Zhang, Q. Yan, F. Boey and H. Zhang, *Small*, 2011, **7**, 1876-1902.

387. G. M. Scheuermann, L. Rumi, P. Steurer, W. Bannwarth and R. Mü lhaupt, *J. Am. Chem. Soc.*, 2009, **131**, 8262-8270.
388. A. Cao, Z. Liu, S. Chu, M. Wu, Z. Ye, Z. Cai, Y. Chang, S. Wang, Q. Gong and Y. Liu, *Adv. Mater.*, 2010, **22**, 103-106.
389. Y. Lin, K. Zhang, W. Chen, Y. Liu, Z. Geng, J. Zeng, N. Pan, L. Yan, X. Wang and J. G. Hou, *ACS Nano*, 2010, **4**, 3033-3038.
390. X. Geng, L. Niu, Z. Xing, R. Song, G. Liu, M. Sun, G. Cheng, H. Zhong, Z. Liu, Z. Zhang, L. Sun, H. Xu, L. Lu and L. Liu, *Adv. Mater.*, 2010, **22**, 638-642.
391. J. Liu, S. Fu, B. Yuan, Y. Li and Z. Deng, *J. Am. Chem. Soc.*, 2010, **132**, 7279-7281.
392. J. Lee, S. Shim, B. Kim and H. S. Shin, *Chem. Eur. J.*, 2011, **17**, 2381-2387.
393. F. Schedin, E. Lidorikis, A. Lombardo, V. G. Kravets, A. K. Geim, A. N. Grigorenko, K. S. Novoselov and A. C. Ferrari, *ACS Nano*, 2010, **4**, 5617-5626.
394. A. Courty, C. Fermon and M. P. Pileni, *Adv. Mater.*, 2001, **13**, 254-258.
395. K. S. Novoselov, D. Jiang, F. Schedin, T. J. Booth, V. V. Khotkevich, S. V. Morozov and A. K. Geim, *Proc. Natl. Acad. Sci.*, 2005, **102**, 10451-10453.
396. L. M. Malard, M. A. Pimenta, G. Dresselhaus and M. S. Dresselhaus, *Phys. Rep.*, 2009, **473**, 51-87.
397. A. C. Ferrari, J. C. Meyer, V. Scardaci, C. Casiraghi, M. Lazzeri, F. Mauri, S. Piscanec, D. Jiang, K. S. Novoselov, S. Roth and A. K. Geim, *Phys. Rev. Lett.*, 2006, **97**, 187401.
398. M. S. Dresselhaus, A. Jorio and R. Saito, *Annu. Rev. Condens. Matter. Phys.*, 2010, **1**, 89-108.
399. K. S. Novoselov, A. K. Geim, S. V. Morozov, D. Jiang, Y. Zhang, S. V. Dubonos, I. V. Grigorieva and A. A. Firsov, *Science*, 2004, **306**, 666-669.
400. M. Ishigami, J. H. Chen, W. G. Cullen, M. S. Fuhrer and E. D. Williams, *Nano Lett.*, 2007, **7**, 1643-1648.
401. J. Moser, A. Verdaguer, D. Jimenez, A. Barreiro and A. Bachtold, *Appl. Phys. Lett.*, 2008, **92**, 123507.
402. M. Lafkioti, B. Krauss, T. Lohmann, U. Zschieschang, H. Klauk, K. v. Klitzing and J. H. Smet, *Nano Lett.*, 2010, **10**, 1149-1153.
403. R. de Miguel, Ph.D. Thesis. Instituto Universitario de Nanociencia de Aragón. Universidad de Zaragoza, 2011.
404. K. K. W. Wong, T. Douglas, S. Gider, D. D. Awschalom and S. Mann, *Chem. Mater.*, 1998, **10**, 279-285.
405. M. J. Martínez-Pérez and et al., *Nanotechnology*, 2010, **21**, 465707.
406. G. A. Clegg, J. E. Fitton, P. M. Harrison and A. Treffry, *Prog. Biophys. Mol. Biol.*, 1981, **36**, 53-86.
407. D. M. Lawson, A. Treffry, P. J. Artymiuk, P. M. Harrison, S. J. Yewdall, A. Luzzago, G. Cesareni, S. Levi and P. Arosio, *FEBS Letters*, 1989, **254**, 207-210.
408. D. M. Lawson, P. J. Artymiuk, S. J. Yewdall, J. M. A. Smith, J. C. Livingstone, A. Treffry, A. Luzzago, S. Levi, P. Arosio, G. Cesareni, C. D. Thomas, W. V. Shaw and P. M. Harrison, *Nature*, 1991, **349**, 541-544.
409. R. Tsukamoto, K. Iwahori, M. Muraoka and I. Yamashita, *Bulletin of the Chemical Society of Japan*, 2005, **78**, 2075-2081.
410. C. Carbonera, I. Imaz, D. Maspoch, D. Ruiz-Molina and F. Luis, *Inorg. Chim. Acta*, 2008, **361**, 3951-3956.
411. I. Creaser, M. C. Heckel, R. J. Neitz and M. T. Pope, *Inorg. Chem.*, 1993, **32**, 1573-1578.
412. R. Shiozaki, A. Inagaki, A. Nishino, E. Nishio, M. Maekawa, H. Kominami and Y. Kera, *J. Alloys Compd.*, 1996, **234**, 193-198.
413. S. Cardona, Ph.D. Thesis. Instituto de Ciencia Molecular. Universidad de Valencia, 2011.
414. V. F. Puntes, K. M. Krishnan and A. P. Alivisatos, *Science*, 2001, **291**, 2115-2117.
415. M. Varón, L. Peña, L. Balcells, V. Skumryev, B. Martinez and V. Puntes, *Langmuir*, 2009, **26**, 109-116.

416. U. Wiedwald, J. Lindner, M. Spasova, Z. Frait and M. Farle, *Phase Transitions*, 2005, **78**, 85-104.
417. J. B. Tracy, D. N. Weiss, D. P. Dinega and M. G. Bawendi, *Phys. Rev. B*, 2005, **72**, 064404.
418. I. Horcas, R. Fernández, J. M. Gómez-Rodríguez, J. Colchero, J. Gómez-Herrero and A. M. Baro, *Rev. Sci. Instrum.* , 2007, **78**, 013705.
419. K. Iwahori and I. Yamashita, *J. Cluster Sci.*, 2007, **18**, 358-370.
420. J. Clarke and A. I. Braginski, eds., *The SQUID Handbook: Fundamentals and Technology of SQUIDs and SQUID Systems, Volume I*, Wiley-VCH Verlag GmbH & Co. KGaA, 2005.
421. J. Clarke and A. I. Braginski, eds., *The SQUID Handbook: Fundamentals and Technology of SQUIDs and SQUID Systems, Volume I*, Wiley-VCH Verlag GmbH & Co. KGaA, 2005.
422. F. Luis and et al., *EPL (Europhysics Letters)*, 2006, **76**, 142.
423. J. M. Hernández and et al., *EPL (Europhysics Letters)*, 1996, **35**, 301.
424. E. M. Chudnovsky and J. Tejada, *Macroscopic Quantum Tunneling of the Magnetic Moment*, Cambridge University Press, Cambridge, 1998.
425. M. J. Martínez-Pérez, J. Sesé, F. Luis, D. Drung and T. Schurig, *Rev. Sci. Instrum.* , 2010, **81**, 016108.
426. M. J. Martinez-Perez, J. Sese, F. Luis, R. Cordoba, D. Drung, T. Schurig, E. Bellido, R. de Miguel, C. Gomez-Moreno, A. Lostao and D. Ruiz-Molina, *IEEE Trans. Appl. Supercond.*, 2011, **21**, 345-348.
427. D. Drung, C. Assmann, J. Beyer, A. Kirste, M. Peters, F. Ruede and T. Schurig, *IEEE Trans. Appl. Supercond.*, 2007, **17**, 699-704.
428. V. Bouchiat, *Superconductor Science and Technology*, 2009, **22**, 064002.
429. A. Candini, Università degli studi di Modena e Reggio Emilia, 2008.
430. A. D. Kent, S. v. Molnár, S. Gider and D. D. Awschalom, *J. Appl. Phys.*, 1994, **76**, 6656-6660.
431. Y. Li, P. Xiong, S. v. Molnár, S. Wirth, Y. Ohno and H. Ohno, *Appl. Phys. Lett.*, 2002, **80**, 4644-4646.